

# INVESTIGATIONS OF COLLECTIVITY IN SMALL AND LARGE COLLISION SYSTEMS AT THE LHC WITH ALICE

by *Katarína Gajdošová*

ACADEMIC ADVISORS:

*Prof. Jens Jørgen Gaardhøje*

AND

*Dr. You Zhou*

HIGH ENERGY HEAVY-ION GROUP

NIELS BOHR INSTITUTE  
UNIVERSITY OF COPENHAGEN

UNIVERSITY OF  
COPENHAGEN



---

THIS PHD THESIS HAS BEEN SUBMITTED TO THE PHD SCHOOL OF THE FACULTY OF  
SCIENCE, UNIVERSITY OF COPENHAGEN ON 23RD OF JULY 2018



# Abstract

Collisions of heavy ions at ultrarelativistic energies aim to recreate a hot and dense form of matter, called the Quark-Gluon Plasma (QGP), where quarks and gluons are in a deconfined state. One of the most suitable probes to study the properties of the QGP are the flow coefficients  $v_n$ , which quantifies the anisotropic particle distributions in the final state. Experimental measurements of  $v_n$  together with their good description by hydrodynamic calculations demonstrate that the QGP is an almost ideal fluid which undergoes a collective expansion into the surrounding vacuum. This collectivity exhibits itself in the form of long-range multi-particle correlations, which originate from a common source.

Small collision systems, such as proton-proton and proton-lead, aim to provide the reference data for collisions of heavy nuclei. However, inspection of high multiplicity pp and p-Pb interactions revealed surprising features, usually attributed to collective effects in heavy-ion collisions. Thus, one of the main goals of this thesis is to understand these unexpected observations.

In this work, measurements of flow coefficients and their correlations using the cumulant method are obtained as a function of multiplicity in pp collisions at  $\sqrt{s} = 13$  TeV, p-Pb collisions at  $\sqrt{s_{NN}} = 5.02$  TeV, Xe-Xe collisions at  $\sqrt{s_{NN}} = 5.44$  TeV, and finally Pb-Pb collisions at  $\sqrt{s_{NN}} = 5.02$  TeV, from the LHC Run 2 data taking using the ALICE experiment. The ability of the novel subevent technique to suppress non-flow effects was examined with the experimental measurements and found to be crucial for the interpretation of the results in small collision systems. Exploration of the measurements presented in this thesis further implies that long-range multi-particle correlations prevail in small collision systems. Comparison of the pp data to PYTHIA 8 calculations shows that non-flow cannot fully explain the observed collectivity. Hydrodynamic calculations IP-Glasma+MUSIC+UrQMD could not reproduce the pp results either, while they provided a successful description of Pb-Pb, Xe-Xe and p-Pb collisions. The broad spectrum of measured observables from various collision systems and their comparison to theoretical models provide an exhaustive set of information, which sheds more insight into the mechanisms responsible for the collectivity seen in different collision systems.



# Dansk resumé

Sammenstød mellem tunge ioner ved ultrarelativistiske energier søger at genskabe en varm og tæt form for stof, kaldet Kvarke-Gluon-Plasma (QGP), hvor kvarker og gluoner er i en ubunden tilstand. En af de bedst egnede prober til at studere QGP's egenskaber er flow koefficienterne  $v_n$ , som kvantificerer de anisotrope partikelfordelinger i sluttilstanden. Eksperimentelle målinger af  $v_n$ , sammenholdt med disses gode overensstemmelse med hydrodynamiske beregninger viser, at QGP opfører sig som en næsten ideel væske, som gennemgår en kollektiv ekspansion i det omgivende vakuum. Denne kollektivitet viser sig i form af langrækkende flerpartikkelkorrelationer, der stammer fra en fælles kilde.

Små kollisionssystemer, såsom proton-proton og proton-bly, har til formål at give referencedata til kollisioner af tunge kerner. Imidlertid viste inspektion af pp og p-Pb stød med høj multiplicitet overraskende egenskaber, som normalt kun tilskrives kollektive effekter i tung-ionkollisioner. Et af hovedformålene med denne afhandling er at forstå disse uventede observationer.

I denne afhandling opnås målinger af flow koefficienter og deres korrelationer ved anvendelse af den kumulative metode som en funktion af multiplicitet i pp kollisioner ved  $\sqrt{s} = 13$  TeV, p-Pb kollisioner ved  $\sqrt{s_{NN}} = 5.02$  TeV, Xe-Xe kollisioner ved  $\sqrt{s_{NN}} = 5.44$  TeV og endelig Pb-Pb kollisioner ved  $\sqrt{s_{NN}} = 5.02$  TeV, fra LHC Run 2 data med ALICE eksperimentet. Den nye subevent-tekniks evne til at undertrykke non-flow effekter blev undersøgt med de eksperimentelle målinger og viste sig at være afgørende for fortolkningen af resultaterne i småkollisionssystemer. Undersøgelse af målingerne fremlagt i denne afhandling indebærer yderligere, at langdistansekorrelationer med flere partikler er dominerende i småkollisionssystemer. Sammenligning af pp data med PYTHIA 8 beregninger viser, at non-flow ikke helt er i stand til at forklare den observerede kollektivitet. Hydrodynamiske beregninger IP-Glasma + MUSIC + UrQMD kunne heller ikke reproducere pp-resultaterne, mens de gav en vellykket beskrivelse af Pb-Pb, Xe-Xe og p-Pb kollisioner. Det brede spektrum af målte observable fra forskellige kollisionssystemer og deres sammenligning med teoretiske modeller giver et omfattende sæt af informationer, som giver større indsigt i de mekanismer, der er ansvarlige for kollektiviteten, der ses i forskellige kollisionssystemer.





LHC, taken from: <http://cds.cern.ch/record/2261828>

## Preface

In September of 2015, I joined ALICE experiment at CERN and started to learn about one of the most suitable probes of the QGP properties: the anisotropic flow.

At the beginning, my Ph.D. project was supposed to be dedicated to data analysis and measurements of anisotropic flow in heavy-ion collisions, especially with the newly collected Pb–Pb collisions at  $\sqrt{s_{NN}} = 5.02$  TeV. The analysis technique that I used were cumulants calculated with two- and multi-particle correlations. Not long before I joined the HEHI group, the members of the group have developed the Generic Framework, which would calculate any type of correlation including the corrections in the acceptance of the detector. After the implementation of this new framework to my code, I have begun with measurements of flow coefficients  $v_n$  as a function of centrality and  $p_T$ , and studies of flow fluctuations via ratios of higher order cumulants. These studies were done on a fraction of the new data, and once the full data set would be available, they were aiming to be a part of an extensive ALICE publication. However, data reconstruction of the large Pb–Pb sample took too long. When the data became available, I was already fully dedicated to another topic. These results were later completed by collaborators and published (*arXiv:1804.02944 [nucl-ex]*).

During the absence of  $\sqrt{s_{NN}} = 5.02$  TeV Pb–Pb data, I have participated in analyses of Pb–Pb collisions at  $\sqrt{s_{NN}} = 2.76$  TeV from Run 1, lead by my supervisor You Zhou: measurements of  $p_T$ -dependent flow vector fluctuations and measurements of linear and non-linear flow modes. The first analysis measured the ratio of  $v_n$  coefficients  $v_n\{2\}/v_n[2]$ . A deviation of this ratio from 1 should indicate  $p_T$ -dependent flow vector fluctuations. This was indeed found, especially in central heavy-ion collisions. This paper was published in *JHEP 1709 (2017) 032*. In heavy-ion collisions, the initial spatial anisotropies are transformed into the final momentum anisotropies of particles via the strongly interacting medium. The flow coefficients  $v_2$  and  $v_3$  are linearly connected to the initial spatial eccentricities  $\epsilon_2$  and  $\epsilon_3$ . However, higher order flow coefficients are in addition affected by the non-linear components

from lower order  $v_n$ . These measurements, especially the non-linear mode coefficients  $\chi_{n,mk}$ , have shown additional sensitivity to different initial conditions or transport properties of the QGP. The results were published in *PLB* 773 (2017) 68. Finally, I have also contributed to a review paper on recent theoretical and experimental progress on collective flow at the LHC, in particular in the overview of the method and some experimental measurements, published in *Nucl.Sci.Tech.* 28 (2017) 99.

In between these studies of heavy-ion collisions, my own project started to crystallise, which is the investigation of collectivity in small collision systems. Since mid 2016, I have been working on the measurements of two- and multi-particle cumulants in small collision systems, using the Generic Framework. I obtained results from  $\sqrt{s} = 13$  TeV pp collisions, which I have compared to the measurements from Run 1 p-Pb and Pb-Pb collisions at  $\sqrt{s_{NN}} = 5.02$  TeV and  $\sqrt{s_{NN}} = 2.76$  TeV, respectively (At that time, the Run 2 Pb-Pb data were not fully available yet and the Run 2 p-Pb collisions were in a planning stage.) The search for collectivity in small collision systems is challenging due to dominating non-flow effects. Therefore, my main struggle was to avoid the contamination of such effects in the measurements. I have first tried to enhance the possible flow by increasing the cut on minimum  $p_T$ . The desired effect was observed in Pb-Pb and also in p-Pb collisions, however it wasn't enough to reveal collectivity in pp collisions. An opposite approach was to suppress non-flow correlations in the measurements. This was achieved with the idea of my supervisor to implement a new method to multi-particle cumulants, called the subevent method, and include it into the Generic Framework. Using this new approach, I obtained measurements of four-particle cumulants with  $|\Delta\eta|$  gap (or subevent), capable of further suppression of non-flow. However, collectivity could not be observed even with this method. These results were accepted by ALICE collaboration as preliminary and I had a chance to present them at Quark Matter 2017 (eventually leading to published conference proceedings in *Nucl.Phys. A* 967 (2017) 437). Together with the ATLAS collaboration, we have presented the first measurements of multi-particle cumulants with a subevent method at this conference.

During the rest of the year of 2017, I have continued in these studies. Results presented at Quark Matter 2017 were an inspiration to focus on effects of the subevent method in Symmetric Cumulants,  $SC(m, n)$ . I have presented my work at the XII Workshop on Particle Correlations and Femtoscopy and the XLVII International Symposium on Multiparticle Dynamics. Jiangyong Jia and his students (who had shown the nice results on collectivity in small collision systems at Quark Matter 2017) have also continued with applying the subevent method to the  $SC(m, n)$  measurements. This resulted in a common publication on the effects of the subevent method on  $SC(m, n)$  studied with PYTHIA and HIJING simulations, which was published in *PLB* 777 (2018) 201. In the meantime, the reconstruction of the new ALICE data was progressing fast, so I could collect much more statistics than I had in hand the year before. Moreover, I could use the new Run 2 data from p-Pb, Pb-Pb and even the new Xe-Xe collisions. With these data and with the high multiplicity trigger using the forward V0 detector, I was finally able to observe collectivity in pp collisions. In order to investigate the origin of this collectivity, I have also measured the  $SC(m, n)$  calculated with the subevent method, since it was shown that non-flow effects largely affect these measurements in small collision systems. All these results have been again successfully accepted by ALICE collaboration as preliminary, and I presented them at Quark Matter 2018 conference. Apart from that, these measurements are also planned to be published this year. Our paper proposal have been

accepted and the draft is now under the review within the collaboration.

## Acknowledgements

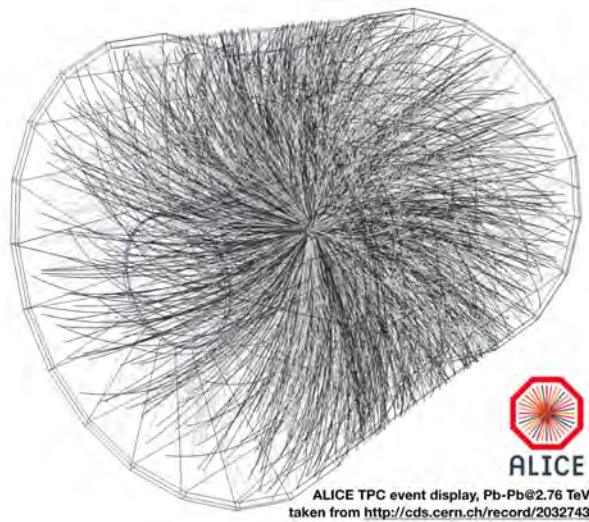
In summary, I definitely wasn't bored during the 3 years of my Ph.D. studies. However, I would never be able to achieve all this if I wouldn't have the right people by my side. My very first big thanks belongs to my supervisors. To Jens Jørgen Gaardhøje for his absolute support at any time and in any decision I made. To You Zhou for being there for me every day, guiding me to my results, discussing with me any little detail that I needed to know, and being online until the late night during the hard times of approvals when I needed it. His belief in me and my achievements was enormous, which can be seen e.g. on the fact that it was his idea to submit the abstract to QM17, even though I was only starting my second year of the Ph.D. studies. I can only hope that I will continue to be able to perform like this in my future career, where I won't have his guidance anymore, and where he won't come every morning, asking what is new :) My analysis would never move forward without the great help of Michele Floris, who shared his excellent knowledge of the data, and showed strong interest in my analysis. I would also like to thank Børge, Ian, Christian, Kristjan, Hans, who were always kind and at hand when I needed help, and Marek, who didn't forget us and kept visiting from the outside world of industry.

I will never forget our czecho-slovak office, which I shared with Vojtěch Pacík. I really enjoyed the early lunches and our czecho-slovak discussions, it really felt like at home. I am very grateful for his willingness to help at any time. Thanks to him, I have learned many new tips and tricks in programming and in the labyrinth of the ALICE software that I used during the data analysis. I want to thank to all my Master, Ph.D. and Posdoc colleagues which have always made my day better, were very supportive and very persuasive in beer consumption, even though I always had something to finish :) Laís, Meera, Freja, Chrisitan, Fabian, Helene and Vytautas, thank you.

Finally, my big thanks goes to my family. I want to thank my parents, Margita and Pavel, who would climb mountains to help and make my studies easier, my grandmother Emília, who showed an infinite support that I will really miss in my future career, and my sister Zuzana, which is the best sister I could wish for: always ready to talk, laugh, listen and support. My very last thanks goes to my soon-to-be-husband Filip, who have kept my mental health on good level even during the bad times that every Ph.D. student sometimes goes through. He was always able to cheer me up, support me, understand me, and make my life here complete.

I have spent 3 long unforgettable years gaining a lot of new experience and knowledge, which resulted in lots of (hopefully) fruitful results. I have summarised the most important achievements in this thesis. There is nothing more I would like to say here, so, I wish you a happy reading.

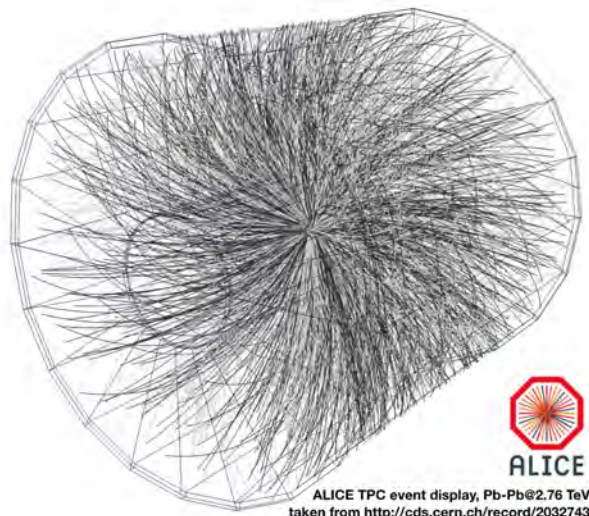




## List of publications

- 1. Investigations on anisotropic flow using multi-particle correlations in pp, p-Pb, Xe-Xe and Pb-Pb collisions**  
ALICE Collaboration, PC members: K. Gajdošová (chair), Y. Zhou, V. Pacík and C. Loizides  
within internal collaboration review, aiming for *Phys. Rev. Lett.*
- 2. ALICE measurements of flow coefficients and their inner correlations in small (pp and p-Pb) and large (Xe-Xe and Pb-Pb) collision systems**  
K. Gajdošová (for the ALICE Collaboration)  
Quark Matter 2018 conference proceedings, submitted to *Nucl. Phys. A*, arXiv:1807.02998 [nucl-ex] (2018).
- 3. Energy dependence and fluctuations of anisotropic flow in Pb-Pb collisions at  $\sqrt{s_{NN}} = 5.02$  and 2.76 TeV**  
ALICE Collaboration, PC members: J. Margutti (chair), A. Dobrin, Y. Zhou, K. Gajdošová, I. Selyuzhenkov, R. Snellings, S. Voloshin  
accepted by JHEP, arXiv:1804.02944 [nucl-ex] (2018).
- 4. Importance of non-flow in mixed-harmonic multi-particle correlations in small collision systems**  
P. Huo, K. Gajdošová, J. Jia and Y. Zhou  
*Phys. Lett. B* 777 (2018) 201-206.
- 5. Investigations of anisotropic collectivity using multi-particle correlations in pp, p-Pb and Pb-Pb collisions**  
K. Gajdošová (for the ALICE Collaboration)  
Quark Matter 2017 conference proceedings, *Nucl. Phys. A* 967 (2017) 437-440.

6. **Linear and non-linear flow modes in Pb-Pb collisions at  $\sqrt{s_{\text{NN}}} = 2.76$  TeV**  
ALICE Collaboration, PC members: Y. Zhou (chair), K. Gajdošová and D.J. Kim  
Phys. Lett. B773 (2017) 68-80.
  
7. **Searches for transverse momentum dependent flow vector fluctuations in Pb-Pb and p-Pb collisions at the LHC**  
ALICE Collaboration, PC members: Y. Zhou (chair), A. Dobrin, R. Snellings and K. Gajdošová  
JHEP 1709 (2017) 032.
  
8. **Collective flow and hydrodynamics in large and small systems at the LHC**  
H. Song, Y. Zhou and K. Gajdošová  
Nucl. Sci. Tech. 28 (2017) 99.



# Contents

	<b>Recreating tiny Universe ?</b> .....	<b>1</b>
<b>1</b>	<b>Ultrarelativistic collisions</b> .....	<b>3</b>
1.1	<b>Heavy-ion collisions</b>	<b>5</b>
1.1.1	The QCD phase diagram .....	6
1.2	<b>Current theoretical understanding of heavy-ion collisions</b>	<b>7</b>
1.2.1	Color Glass Condensate and Glasma .....	7
1.2.2	Initial conditions .....	9
1.2.3	Final state description .....	9
1.3	<b>Anisotropic flow as a probe of the QGP</b>	<b>12</b>
1.3.1	Summary of relevant anisotropic flow results .....	14
1.4	<b>Small collision systems</b>	<b>17</b>
1.4.1	Collectivity in small systems ? .....	17
<b>2</b>	<b>Analysis techniques</b> .....	<b>23</b>
2.1	<b>Standard method of azimuthal correlations</b>	<b>23</b>
2.1.1	Multi-particle azimuthal correlations .....	23
2.1.2	From correlations to observables .....	26

<b>2.2</b>	<b>Subevent method</b>	<b>28</b>
2.2.1	Subevent method on cumulant level	28
2.2.2	Subevent method in Generic Framework	33
<b>2.3</b>	<b>Performance of the subevent method in simulations</b>	<b>34</b>
<b>3</b>	<b>Experimental setup</b>	<b>37</b>
<b>3.1</b>	<b>The Large Hadron Collider (LHC)</b>	<b>37</b>
<b>3.2</b>	<b>A Large Ion Collider Experiment (ALICE)</b>	<b>39</b>
3.2.1	Inner Tracking System (ITS)	40
3.2.2	Time Projection Chamber (TPC)	41
3.2.3	VZERO (V0)	43
3.2.4	Capabilities of the ALICE detector	44
<b>4</b>	<b>Data processing and selection</b>	<b>47</b>
<b>4.1</b>	<b>Event selection</b>	<b>49</b>
4.1.1	Rejection of background and pileup events	49
4.1.2	Collision vertex selection	50
4.1.3	Effects of the high multiplicity trigger in pp collisions	51
<b>4.2</b>	<b>Track selection</b>	<b>52</b>
<b>4.3</b>	<b>Compatibility between different periods</b>	<b>54</b>
4.3.1	pp collisions	54
4.3.2	p–Pb collisions	55
<b>5</b>	<b>Analysis of data</b>	<b>57</b>
<b>5.1</b>	<b>Non-uniform acceptance correction</b>	<b>57</b>
<b>5.2</b>	<b>Efficiency correction based on Monte Carlo simulations</b>	<b>60</b>
<b>5.3</b>	<b>Correction of the <math>x</math>-axis</b>	<b>61</b>
<b>5.4</b>	<b>Estimation of systematic uncertainties</b>	<b>63</b>
5.4.1	Uncertainty from variations of event and track cuts	65
5.4.2	Monte Carlo closure test	68
<b>6</b>	<b>Results and discussion</b>	<b>71</b>
<b>6.1</b>	<b>Non-flow effects</b>	<b>72</b>
6.1.1	Suppression of non-flow in two-particle cumulant measurements	72
6.1.2	Suppression of non-flow in multi-particle cumulant measurements	76

<b>6.2</b>	<b>Comparison of results of <math>v_2\{m\}</math> for <math>m \geq 2</math></b>	<b>82</b>
<b>6.3</b>	<b>Direct comparison of small and large collision systems</b>	<b>84</b>
6.3.1	Flow coefficients $v_n$ measured with two-particle cumulants . . . . .	84
6.3.2	Flow coefficients $v_n$ measured with multi-particle cumulants . . . . .	87
6.3.3	$SC(m,n)$ measured with multi-particle cumulants . . . . .	89
<b>7</b>	<b>Conclusions</b> . . . . .	<b>93</b>
	<b>Appendices</b> . . . . .	<b>105</b>
<b>A</b>	<b>Non-uniform acceptance</b> . . . . .	<b>107</b>
A.1	p–Pb collisions	107
A.2	Xe–Xe and Pb–Pb collisions	107
<b>B</b>	<b>Efficiency correction</b> . . . . .	<b>111</b>
B.1	p–Pb collisions	111
B.2	Xe–Xe and Pb–Pb collisions	111
<b>C</b>	<b>Correction of the <math>x</math>-axis</b> . . . . .	<b>117</b>
<b>D</b>	<b>Systematic uncertainties</b> . . . . .	<b>119</b>
<b>E</b>	<b>Earlier studies of collectivity</b> . . . . .	<b>123</b>
E.1	Data sets	123
E.2	Results	125
E.2.1	Enhancing the flow signal . . . . .	126
E.2.2	Suppression of non-flow effects . . . . .	129
E.2.3	Summary . . . . .	131
<b>F</b>	<b>PYTHIA 8 simulation setup</b> . . . . .	<b>133</b>



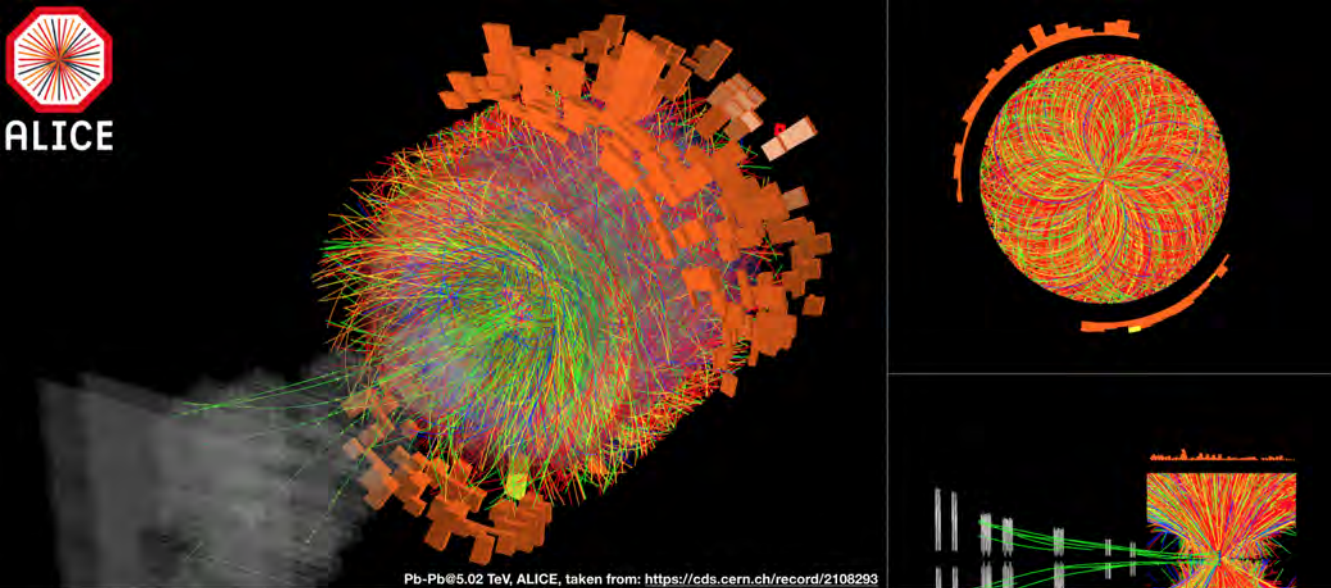


by the emitted particles. Thanks to the measurements of  $v_n$ , we understand that the QGP is probably the most perfect fluid in nature: its resistance to flow is very small. Collisions at the LHC occur in an almost perfect vacuum. Thus, when the QGP is created, it tends to equilibrate with the surrounding vacuum, as everything in nature, leading to its expansion. Because the QGP is a fluid, all its constituents move (flow) collectively with the overall medium. Particles that are eventually created, are composed of quarks and gluons that took part in this flow of the medium. Therefore, they will also exhibit signs of collectivity, which we can measure.

In order to say whether the QGP is responsible for measurements performed in heavy-ion collisions, it is necessary to compare them to collisions, which do not create this hot and dense medium. Collisions of small systems, such as proton-proton or proton-nucleus, are naïvely considered to happen without the QGP phase. Thus, they are supposed to provide a reference measurements for those in heavy-ion collisions. It was a great surprise when features, usually understood to come from collective effects of the QGP in heavy-ion collisions, were also seen in pp and p–Pb interactions, with a large number of created particles. These unexpected observations are a mystery to the heavy-ion community. Thus, one of our main goals is to answer the question of whether we can create a small droplet of the QGP even in the smallest type of collisions.

This thesis will try to provide explanation to these confusing phenomena.

First, Chapter 1 will start with an introduction to the physics of heavy-ion collisions and the QGP, followed by a description of models and experimental measurements that help us to understand this medium. This Chapter will end with providing a closer look to the measurements that led to the excitement about small collision systems. Observables that are measured in this thesis and methods used to calculate them will be described in Chapter 2, including a new method that proved to be important in reducing effects that contaminate the measurements in small collision systems. ALICE detector, that was used to collect the data from collisions at the LHC, will be presented in Chapter 3. Details regarding the processing of data and performing the analysis are summarised in Chapters 4 and 5. Finally, Chapter 6 reports the measurements of flow coefficients and their correlations in pp collisions at  $\sqrt{s} = 13$  TeV, p–Pb at  $\sqrt{s_{NN}} = 5.02$  TeV, Xe–Xe at  $\sqrt{s_{NN}} = 5.44$  TeV, and finally Pb–Pb collisions at  $\sqrt{s_{NN}} = 5.02$  TeV. Moreover, the results will be compared to theoretical calculations. The important findings made in this work will be summarised in Chapter 7, and it will be revealed whether collectivity is observed in small collision systems, and if yes, what is its origin.



Pb-Pb@5.02 TeV, ALICE, taken from: <https://cds.cern.ch/record/2108293>

# 1. Ultrarelativistic collisions

The Standard Model of particle physics describes two groups of fundamental particles, *quarks* and *leptons*, which can interact with each other via three fundamental forces: electromagnetic, weak, and strong. The forces are transmitted via force carriers. In particular, *photons* are exchanged between particles in case of an electromagnetic interaction, bosons  $W^\pm$  or  $Z$  are the carriers of the weak force, and finally *gluons* are responsible for the strong interaction. There are six quarks and six leptons (and their anti-particles). Quarks can be identified based on their flavour: *up*, *down*, *strange*, *charm*, *bottom* and *top*. We distinguish the following leptons: *electron* and *electron neutrino*, *muon* and *muon neutrino*, and finally *tauon* and *tauon neutrino*. All these fundamental particles are summarised in Fig. 1.1. This figure includes one more particle, which is the Higgs boson, responsible for giving mass to the particles.

The forces are distinguished based on their characteristic behaviour. The well known electromagnetic force is mediated between particles which carry an electric charge. The weak force is responsible for the nuclear decays thanks to its ability to change the flavour of quarks and leptons. Finally, the strong force is only exerted on particles carrying a *colour charge*, which are quarks and gluons.

The theory describing the strong force is the Quantum Chromodynamics (QCD), whose name is derived from the colour charges of particles affected by the strong interaction. In particular, there are three charges: **red**, **green** and **blue**. Each quark can only have one colour charge, while a gluon has two charges. Gluons can also interact with themselves thanks to the possession of a charge, as opposed to the carriers of the electromagnetic force, photons, which do not have an electric charge, thus are not allowed to interact with each other. The strength of the force can be quantified by a coupling constant  $\alpha_{QCD}$ . At large distances (or low energies), the  $\alpha_{QCD}$  increases, while at small distances (or large energies), the  $\alpha_{QCD}$  approaches asymptotically to zero. This is opposite to the behaviour of the familiar electromagnetic force which is strongest at small distances and becomes very weak at large

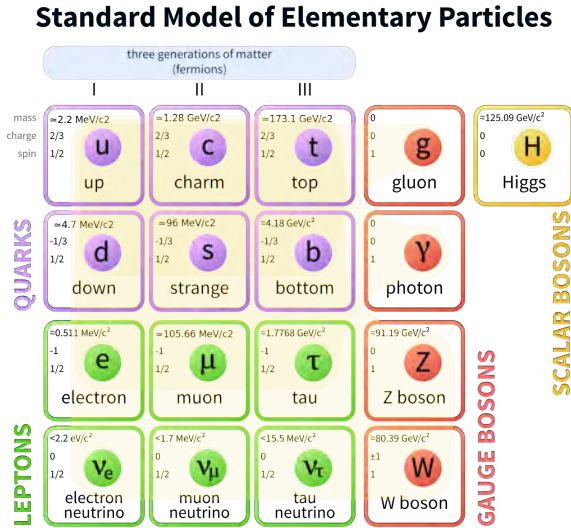


**Figure 1.1:** Standard model of elementary particles. Figure taken from [1].

distances. The properties of the coupling constant in QCD result in two main features of the strong interaction: *colour confinement* and *asymptotic freedom*.

The color confinement is in principle responsible for holding the matter together. The increasing  $\alpha_{QCD}$  with the distance between two quarks results in more and more energy would have to be applied in order to move the two quarks farther away from each other. At some point, there would be enough energy to create a new quark–antiquark pair from the vacuum. Therefore, no free quarks can be observed in Nature at normal conditions. Instead, all quarks are confined inside the so-called *hadrons*. All hadrons contain a quark composition such that the resulting colour charge is neutral. This leaves us with two types of hadrons: baryons and mesons. Baryons are composed of three quarks, each carrying different colour charge which would combine into a neutral colour in an analogy to the red, green and blue light being combined into a colour neutral light beam. Mesons are formed of a quark–antiquark pair with a charge of certain colour and its anticolour.

On the other hand, at the limit of a small distance between quarks (or large energies), the strong interaction becomes weak such that quarks are no longer bound inside hadrons, but they are almost free. This effect is called asymptotic freedom. A few microseconds after the Big Bang at very high temperature and density, the Universe was composed of such deconfined matter, which we now call *Quark–Gluon Plasma* (QGP). The understanding of this extreme state of matter is the main purpose of the ultrarelativistic heavy-ion collisions, which will be described below.

## 1.1 Heavy-ion collisions

At the two largest hadron colliders, the Relativistic Heavy-Ion Collider (RHIC) and the Large Hadron Collider (LHC), the heavy nuclei (e.g. gold at RHIC and lead at the LHC) are accelerated to almost the speed of light. At such high velocities, the nuclei are Lorentz contracted into narrow disks (often called “pancakes”) characterised by high densities with large gluon occupation.

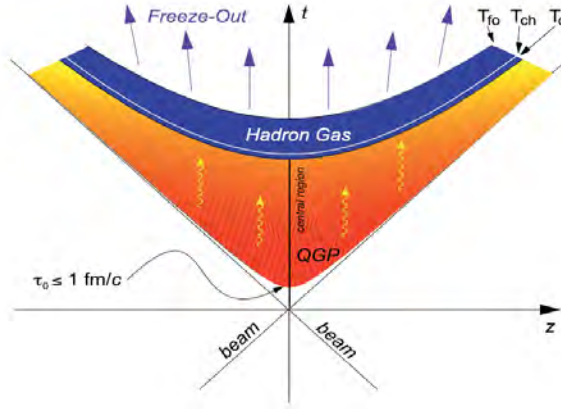


**Figure 1.2:** Diagram of the evolution of a heavy-ion collision. Figure taken from [2].

The two nuclei are then brought into collision. At the point of a collision, the nuclei pass through each other, leaving behind a system which cools down and expands. It was suggested already by Bjorken in [3] that at the beginning, the expansion occurs mainly in the longitudinal direction. This allows us to describe the stages of the evolution of this system in terms of the light cone variables, time  $t$  and direction of the incoming beams of particles  $z$ , see Fig. 1.2. The proper time  $\tau = \sqrt{t^2 - z^2}$  is situated on space-time hyperbolas of the diagram. The evolution of the created system after the collision can be divided into the following stages [4]:

1. **Pre-equilibrium phase:** The receding nuclei leave behind colour flux tubes (as illustrated in Fig. 1.4 (right)), which lead to the production of partons that further interact with each other. At this stage, high momentum transfer scatterings occur which give rise to the production of jets or heavy quarks.
2. **Thermal equilibrium:** The created system approaches a local thermal equilibrium thanks to the interactions of individual partons, where their mean free path is smaller than the overall size of the system. This leads to the creation of the Quark Gluon Plasma around a formation time  $\tau_0 \approx 1 \text{ fm}/c$ . At this stage, the matter behaves as strongly interacting almost perfect fluid which can be described by hydrodynamics. This system then expands to the surrounding vacuum and cools down.
3. **Phase transition:** When the system cools down to its critical temperature  $T_c$  at approxi-

mately  $\tau \approx 10 \text{ fm}/c$ , it undergoes a phase transition to the hadronic matter, where quarks and gluons are no longer free, but become confined in hadrons instead. In the regimes of the highest energy collisions performed at RHIC or the LHC accelerators, the phase transition is in the form of a *cross-over*, which resembles a smooth transition between the two phases. Therefore, there is no well-defined separation of phases, but it can instead be estimated from the point where the thermodynamic properties change rapidly.

4. **Chemical freeze-out:** The system continues to expand and cool down, and the hadrons continue to interact with each other. The so-called chemical freeze-out is the point where the inelastic processes cease and the chemical composition of the system (i.e., composition of hadrons) does not change anymore. This occurs almost at the same time as the hadronization, i.e. the phase transition to the hadron gas.
5. **Kinetic freeze-out:** Hadrons might still interact via elastic scatterings until the point of a kinetic freeze-out at  $\tau \approx 20 \text{ fm}/c$ , where the density of the system is small enough to cease the particle scatterings. Then, the created particles fly into the vacuum and are detected by experiments.

### 1.1.1 The QCD phase diagram

During the intermediate stages of a heavy-ion collision, the created hot and dense matter undergoes a phase transition to a hadron gas. This process can be expressed in a form of a phase diagram, in analogy to a phase diagram of ordinary water which describes the conditions at which different phases of water exist (water vapour, water liquid and ice).

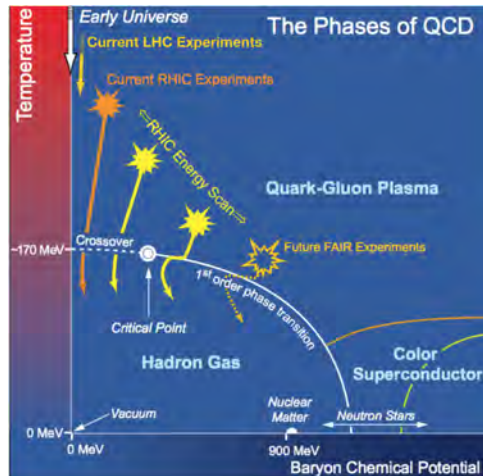


**Figure 1.3:** Phase diagram of nuclear matter. Figure adapted from [5].

The phase diagram in Fig. 1.3 is drawn in terms of temperature on the  $y$ -axis, and the so-called baryon chemical potential  $\mu_B$  on the  $x$ -axis. The  $\mu_B$  can be understood as the difference

of baryons minus anti-baryons (i.e., matter minus anti-matter). When  $\mu_B = 0$ , baryons are equally present as anti-baryons. On the other hand, when  $\mu_B > 0$ , baryons dominate over anti-baryons. Collisions of heavy ions at high energies (such as those performed at RHIC and the LHC) belong to the low values of  $\mu_B$ . Even though there is an excess of baryons (the colliding nuclei are composed of protons and neutrons), this number becomes negligible next to the overwhelming number of newly created particles, which are composed of both matter and anti-matter. On the other hand, collisions at lower energies would move in the phase diagram towards larger values of  $\mu_B$  since the original number of nucleons brought into the collision becomes significant.

A first order phase transition between the QGP and the phase of confined hadron gas happens at higher  $\mu_B$  and lower temperatures, while the cross-over is believed to mark the boundary between the hadron gas and the QGP at low  $\mu_B$  and high  $T$ . The hadron gas undergoes a phase transition to the deconfined state of matter when sufficient energy density and temperature are reached, which is estimated with Lattice QCD to be  $\varepsilon \approx 0.18 - 0.5$  GeV/fm<sup>3</sup> [6] and  $T_c \approx 145 - 165$  MeV [6]. The determination of the phase transition is a place of a lot of scientific effort. A dedicated program at RHIC called the Beam Energy Scan (BES) [7] is focused on the study of this boundary, in particular in finding the point where the first order phase transition becomes a cross-over. The scan of the boundary of the phase transition is performed by lowering the energy of collisions of heavy nuclei. Heavy-ion collisions at the highest possible energy at RHIC and the LHC lie at the very top left part of this phase diagram, at the region of almost zero  $\mu_B$  and very high  $T$ .

## 1.2 Current theoretical understanding of heavy-ion collisions

As was mentioned above, the creation of the QGP occurs at very early times after a heavy-ion collision. On top of that, its subsequent expansion and transition into a hadron gas which would eventually freeze out into final particles takes only a very short time of the order of  $\tau \approx 20$  fm/c [4]. With our current measuring capabilities, we cannot probe the QGP directly, but rather analyse the properties of the final particles that reach our detectors. In order to understand the effects behind the distributions of particles that we measure, we need to be able to describe the whole evolution of a heavy-ion collision, and try to depict those that are related to the QGP phase, which we are mainly interested in. This is not an easy task, since every stage of a collision is a complex many-body system. Moreover, each stage of a collision can affect the adjacent one. If our models do not correctly describe the early stages, it might result in an inaccurate determination of the parameters of the next stage (i.e., hydrodynamic phase), eventually leading to misguided final particle distributions and comparison to experimental data. Therefore, a proper description of each of the stages of a heavy-ion collision is the goal of the current theoretical efforts. In the following, models describing various stages of a collision will be presented. These models can then be combined into a hybrid framework which, by comparison to experimental data, can provide the information on the properties of the QGP.

### 1.2.1 Color Glass Condensate and Glasma

The Color Glass Condensate (CGC) is the effective field theory describing scatterings in QCD at the high energy limit [4, 8–10]. This model is suitable for describing the initial stage

of a lepton-hadron, hadron-hadron, and even heavy-ion collisions. In particular, this model describes the matter created inside the nuclei right before they collide. Since the nuclei are accelerated to ultrarelativistic energies, we are probing a region with a very small  $x$ , which is defined as a fraction of the momentum of the colliding nucleon. Under such circumstances, the nuclei are no longer described as being composed of nucleons and their constituent quarks. Instead, they are seen as being filled with a large number of gluons. This can be inferred from the parton distribution function PDF  $f_i(x, Q^2)$ , which determines, at a fixed momentum transfer  $Q^2$ , a probability of finding a parton  $i$  carrying a fraction  $x$  of the momentum of a nucleon, shown in Fig. 1.4 (left) [11]. At large  $x \approx 1/3$ , nucleons are predominantly formed of 3 constituent valence quarks. Therefore, their  $f_{u_v}$  and  $f_{d_v}$  are the most significant in Fig. 1.4. Moving to small  $x$ , it becomes clear that the largest contribution to the composition of the nucleon belongs to gluons (and less importantly to sea quarks). These gluons are interacting weakly due to the small  $\alpha_{QCD}$  at the asymptotic region of the QCD reached at the high energies of the heavy-ion collisions and small distances between the closely packed gluons within the nucleons. Because the CGC theory describes the evolution of a dense gluon system, it can be universally applied to any type of a collision involving a hadron. It therefore reveals the collective dynamics of the QCD at high parton densities.

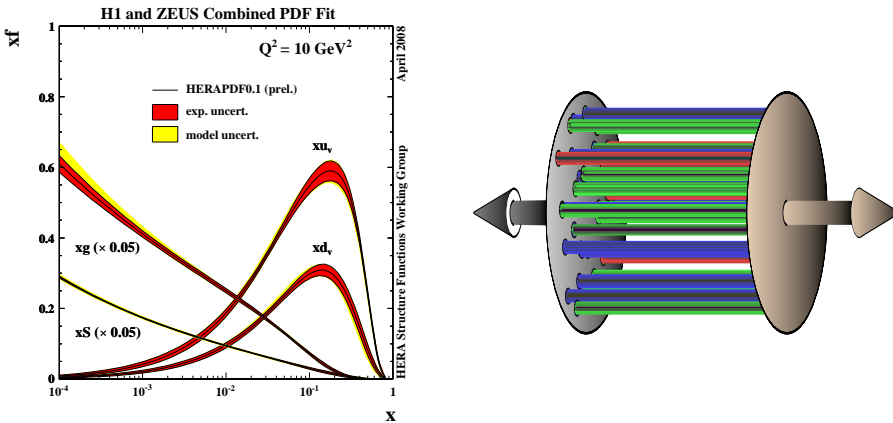


**Figure 1.4:** Left: Parton distribution functions PDFs of the valence  $u$  and  $d$  quarks, the sea quarks  $S$  and gluons  $g$ . Figure taken from [11]. Right: Illustration of the Glasma phase of a heavy-ion collision, with the colour electric and magnetic fields spanning across long range in rapidity. Figure taken from [8].

The pre-equilibrium stage of a heavy-ion collision, between the domains of the CGC and the QGP type of matter, is composed of a medium called the Glasma [4, 10, 11]. Immediately after the collision, the fields originally contained within the nuclei, are now spread longitudinally between the receding sheets of the Lorentz contracted nuclei in the form of colour electric and magnetic field tubes. This is shown in Fig. 1.4 (right). Each of the flux tubes can produce particles along the longitudinal direction. Therefore, the Glasma fields are long-range in rapidity, and can be responsible for later observations of the “ridge” in the near-side long-range two-particle correlations of final produced particles (described later on

in section 1.3.1).

### 1.2.2 Initial conditions

Before continuing with the description of final state models (describing the QGP created at the equilibrium stage of a heavy-ion collision), this section addresses selected initial state models. Due to the finite size of the colliding nuclei in the transverse plane (perpendicular to the collision axis), they can collide at various geometries. The models described below are often used to generate the initial density profiles of this overlap collision geometry for the initialization of the subsequent evolution of the QGP phase. These models either exploit the CGC framework, or they are just a simple geometric models, which also give satisfactory results.

#### MC-Glauber

A simple MC-Glauber [12] model simulates a collision of two heavy nuclei in terms of their nucleon constituents. Each collision occurs with a random impact parameter  $b$ , and is treated as a sequence of independent binary nucleon-nucleon collisions. The position of nucleons inside the nuclei vary event-by-event, which is randomly generated based on the Wood-Saxon distribution. The resulting initial density profile is composed of nucleons that suffered from at least one collision.

#### MC-KLN

The MC-KLN model [13, 14] exploits the formalism of the CGC, a theory based on a dense gluon environment inside the colliding nuclei at high energy. Apart from the collisions of nucleons distributed inside a nucleus via a nuclear density distribution (Woods-Saxon), it also takes into account the distribution of gluon fields inside the nuclei.

#### IP-Glasma

The IP-Glasma model [15, 16] is also based on the description of the interaction between the gluon fields inside the colliding nucleus (CGC). This model gained its importance thanks to its successful simultaneous implementation of fluctuating distributions of nucleons inside nuclei, plus fluctuations in the colour charges inside nucleons. This results in a “lumpy” initial state that varies event-by-event. Another improvement compared to the previous models is the more realistic inclusion of a pre-equilibrium flow, which can smoothen the initial density profiles before the onset of the adjacent simulation of the QGP phase.

The difference between the initial conditions of all three models described here is shown in Fig. 1.5. It is clear that going from the simplest MC-Glauber model (left panel) through the MC-KLN (middle panel), until the IP-Glasma model (right panel), the structure of the initial condition becomes more complex, and apparently successful. Hydrodynamic models that include the IP-Glasma initial conditions are outstanding in describing the experimental data [17].

### 1.2.3 Final state description

There are two most common approaches to the description of the QGP phase. The use of relativistic viscous hydrodynamics, or a Multi-Phase Transport Model (AMPT). Both will be briefly introduced in the following.

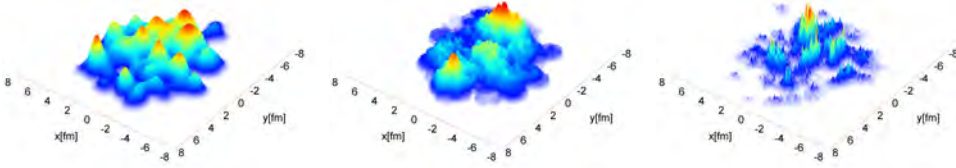


**Figure 1.5:** Initial energy densities in the transverse plane of the overlapping region of the colliding heavy nuclei. Going from left to right: MC-Glauber, MC-KLN and IP-Glasma models. Figures taken from [15].

### Hydrodynamics

Relativistic hydrodynamics describes the medium created in a heavy-ion collision from a macroscopic point of view [18, 19]. This type of description can be only used under certain circumstances. The system has to be in (near) a local thermal equilibrium<sup>\*</sup>, which means that the mean free path of partons cannot exceed the size of the medium. As was mentioned earlier during the description of the evolution of a heavy-ion collision, such a condition is only satisfied after some formation time  $\tau_0 \approx 1 \text{ fm}/c$ . Therefore, the initial state models, briefly described above, have to be employed in order to obtain the input distribution of the transverse density profile which will be fed into the hydrodynamic model.

The hydrodynamic simulation of the evolution of the created medium consists of numerically solving a set of equations. In particular, the equations express the local conservation of the energy and momentum at a position  $x$  of the fluid cell

$$\partial_\mu T^{\mu\nu}(x) = 0, \quad (1.1)$$

and the local conservation of currents

$$\partial_\mu N_i^\mu(x) = 0. \quad (1.2)$$

The  $T^{\mu\nu}$  is the energy-momentum tensor, where the diagonal contains the energy  $e$  and pressure  $p$  of a fluid cell, and in case of a moving relativistic fluid, it also has non-zero off-diagonal terms, such as momentum density and energy flux. The  $N_i^\mu$  is the  $i$ -th conserved current, such as the electric charge, or net baryon number. The set of equations is completed with an additional input from the equation of state  $p = p(e, n_i)$ , also obtained from models or Lattice QCD calculations.

Because the system created in a heavy-ion collision immediately starts expanding, the local thermal equilibrium of the system can only be an approximation. Therefore, the relativistic viscous hydrodynamics, that studies deviations from local thermal equilibrium, has to be applied to describe such a system. In this framework, the  $T^{\mu\nu}$  and  $N_i^\mu$  will be extended with additional terms containing parameters called transport coefficients. These parameters involve the *shear viscosity*  $\eta$  and *bulk viscosity*  $\zeta$ .

The shear viscosity measures the resistance of the fluid to deformations caused by shear stress, or in other words, it is a friction between the fluid cells. Low viscosity thus implies

<sup>\*</sup>Although the necessity of this condition was questioned recently [20]

a strongly interacting fluid, while large values of the shear viscosity are characteristic to a weakly interacting gas. This quantity can be constrained by experimental data from heavy-ion collisions, in particular the ratio of the shear viscosity to entropy density,  $\eta/s$ . The shear viscosity washes out small structures in the initial anisotropies, which would reduce the observed final momentum anisotropy in terms of flow coefficients  $v_n$  (more details on this observable are provided in section 1.3). Comparisons to these data indicate that the values are  $\eta/s \approx 0.08 - 0.20$ , close to the boundary  $\eta/s \geq \hbar/4\pi k_B$ , that was conjectured by string theory methods [21]. The shear viscosity can depend on the temperature of the QGP,  $\eta/s(T)$ . This indeed seems to hold, since smaller values of  $\eta/s$  describe the RHIC data, while larger  $\eta/s$  is necessary in order to describe the LHC results [17, 22]. The temperature dependence has recently been extracted via an advanced Bayesian analysis [23, 24]. Based on the extracted values of the  $\eta/s$ , it is clear that the QGP is the most “perfect” fluid known so far.

The bulk viscosity  $\zeta$  has effect on the radial expansion of the QGP, which in turn affects the transverse momentum of the emitted particles. It was mainly neglected in hydrodynamic simulations, however it gradually became clear that its non-zero value is necessary in order to describe measurements of flow and mean transverse momentum [25].

The hydrodynamic simulation is finished when the local equilibrium of the system is no longer maintained: the system is now more dilute and the mean free paths become larger than the system size. At this stage, the hydrodynamic description is changed to a hadron cascade simulation around  $T_c$  of the phase transition from the QGP to a hadron gas, which ensures a realistic description of a heavy-ion collision evolution. At the transition point, the output from hydrodynamic simulation is used to generate particles, which are then described by a hadron cascade model. One of the most used models is the Ultra-relativistic Quantum Molecular Dynamics (UrQMD) [26], which further simulates the evolution of the hadron gas via elastic or inelastic scatterings and resonance decays until the freeze-out. The output composed of the final produced hadrons can then be used to calculate observables which can be compared to experimental data.

### A Multi-Phase Transport Model

The final state evolution of a heavy-ion collision during the QGP phase can also be fairly well described by A Multi-Phase Transport Model (AMPT) model [27]. As opposed to hydrodynamics, the AMPT is a microscopic model trying to describe all stages of a collision. This includes initial conditions, initial parton scatterings, their hadronization and subsequent interactions via hadronic scatterings, all combined into a single model.

This model comes in two versions. A default AMPT, and the AMPT with the so-called string melting mechanism. Both approaches start with the initial excited strings and minijets. In the default AMPT model, the partons from minijets that first undergo a Zhang’s Parton Cascade (ZPC), are recombined with the parent strings and converted to the hadronic phase via the Lund string fragmentation mechanism. On the other hand, the AMPT model with string melting mechanism first fragments all the excited strings and mini-jets into partons, which interact with each other in the ZPC phase. Then, the quark coalescence model combines nearby partons into hadrons. The later approach is more successful in describing the anisotropic flow measurements from heavy-ion collisions than the default AMPT.

### 1.3 Anisotropic flow as a probe of the QGP

Models that attempt to describe the evolution of a heavy-ion collision, in particular those involving the QGP, are constrained by the comparison to experimental data. Suitable probes that are sensitive to various stages of the collision, or different properties of the QGP, need to be examined in order to pin down the values of the unknown model parameters, or even the whole model.

There are several different probes that can be used to study the QGP. They can in general be divided into hard and soft probes. This is based on the momentum scale of the given probe. One of the most remarkable phenomena corresponding to hard probes that provide strong evidence for the presence of the QGP is the modification of jets in the medium. High- $p_T$  partons are created at very early stages of the collision during the hard scatterings. These partons then fragment into di-jets. If this occurs near the edge of the created medium, one jet immediately fragments into final particles in the surrounding vacuum, while the opposite jet travels through the QGP. Since the QGP is a strongly interacting medium, the jet will interact with the constituents of the QGP, thus losing its energy and eventually dissolving into the medium. Such processes end up in a suppression of high- $p_T$  particles in the final observations, compared to the same measurements from proton-proton collisions without the presence of the QGP.

The properties of the QGP can also be extracted from one of the most prominent observables of the soft probes: the anisotropic flow. As was mentioned above, due to the finite size of the colliding nuclei in the transverse direction perpendicular to the collision axis, they can collide at various geometric configurations. It is possible to characterize the type of a collision based on the so-called impact parameter  $b$ , which is the distance between the centers of the two nuclei in the transverse plane. We can distinguish a central collision with  $b \approx 0$ , a semi-central collision with  $b > 0$ , and a peripheral collision when  $b \gg 0$ . In a central collision, almost all the nucleons inside a nucleus participate in the collision, while in a peripheral collision, only a small fraction of the nucleons collide. Different types of heavy-ion collisions thus imply different geometries of the overlapping area. A central collision results in an almost circular geometry, while the geometry of a peripheral collision resembles an almond shape.

Anisotropies in the initial geometry lead to steeper pressure gradients along the shorter axis of the geometry. A particular case of a peripheral collision with a roughly elliptic shape is shown in Fig. 1.6 (left). In this case, the pressure gradient will be larger along the  $x$  direction than along the  $y$  axis. The medium will then prefer to expand more along this direction. Due to the strong interactions between partons inside the QGP, these initial geometries are transmitted to the final particle distributions. Eventually, we will observe more particles flying out along the  $x$  direction than in the other direction. Thus, by exploiting the final distribution of particles in azimuthal direction, one can infer the properties of the QGP, since it was at this phase where the initial spatial anisotropies were imparted into the final particle anisotropies in momentum space.

In reality, the geometry of the overlapping region is not a perfect ellipse, nor a smooth almond shape. Because the colliding nuclei are compound objects composed of nucleons whose positions may fluctuate in each collision, the resulting initial geometry is irregular, as can be seen in Fig. 1.6 (right). Such a shape can be expressed as a superposition of various

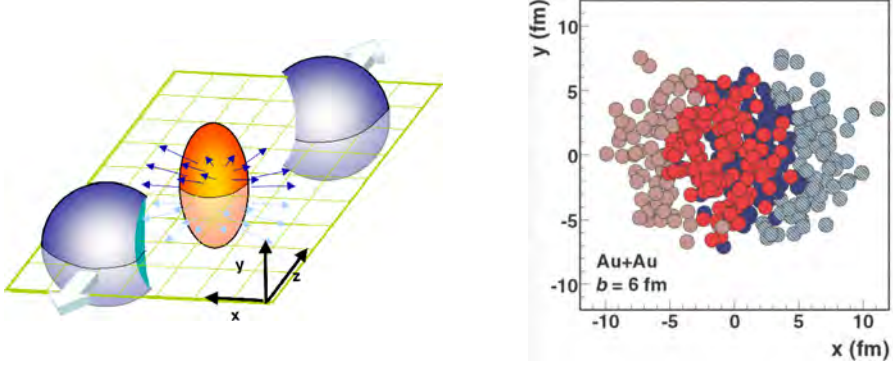


**Figure 1.6:** Left: Illustration of a peripheral collision with almond shaped overlap region. Figure taken from [28]. Right: Glauber simulation of a heavy-ion collision with constituent nucleons, showing that the overlap geometry does not have a perfect elliptic-like shape, but it contains several geometries combined together which can be studied with Fourier decomposition. Figure taken from [12].

geometries.

In an experimental measurement, the Fourier decomposition of azimuthal particle distribution with respect to a symmetry plane angle is used to characterise the final anisotropies [29]:

$$\frac{dN}{d\varphi} \propto 1 + 2 \sum_{n=1}^{\infty} v_n e^{in(\varphi - \Psi_n)}. \quad (1.3)$$

In this equation,  $\varphi$  is the azimuthal angle of particles,  $\Psi_n$  is the symmetry plane angle of  $n$ -th harmonic, and  $v_n$  are flow coefficients corresponding to a harmonic  $n$ :

$$v_n = \langle \cos [n(\varphi - \Psi_n)] \rangle, \quad (1.4)$$

where  $\langle \cdot \rangle$  is the average over a sample of (usually similar type) collisions. Based on the above equation, the  $v_n$  can be understood as a correlation of particles with respect to a common symmetry plane. In case of a peripheral collision with a pronounced elliptic shape, the most significant flow coefficient from the Fourier series is the so-called elliptic flow,  $v_2$ . On the other hand, in a central collision, higher order flow coefficients might become significant if the overlap geometry is completely driven by the fluctuations in nucleon positions inside the nuclei.

The flow coefficients  $v_n$  depend on the collision centrality due to their connection to the initial anisotropies. At the same time, they exhibit a dependence on transverse momentum  $p_T$ , pseudorapidity  $\eta$ , or different particle species. Even though it was presented here that the  $v_n$  are connected to the initial collision geometries  $\varepsilon_n$ , a linear correlation is only provided by  $v_2$  and  $v_3$ . Higher order flow coefficients  $v_n$  (for  $n > 3$ ) are affected by both  $\varepsilon_n$  and lower order anisotropies. Finally, the symmetry planes  $\Psi_n$  might also change with  $p_T$  and  $\eta$ . All these measurements have been explored experimentally during the recent years and have provided an enormous amount of information for the determination of model parameters. In the next section, these results will be discussed briefly.

### 1.3.1 Summary of relevant anisotropic flow results

This section attempts to summarise the measurements of flow coefficients demonstrating their ability to constrain theoretical models and thus gain information on the properties of the system created in heavy-ion collisions. The focus of this section will be given on the measurements of anisotropic flow of charged particles with the ALICE experiment. The method to calculate the flow coefficients will be described in more details in chapter 2. However, it should be noted already here that the symmetry plane  $\Psi_n$  cannot be reliably obtained in each collision. Instead, flow coefficients are calculated from correlations among the produced particles (two, four-, six- or eight-particle correlations), which result in cumulants of the flow distribution. Under the assumption of the factorization of  $m$ -particle distribution into a product of single-particle distributions, the value of  $v_n$  can be extracted from these measurements.

Starting from the correlations between two charged particles, measurements of “di-hadron” correlations as a function of their relative difference in azimuth  $\Delta\phi$  and pseudorapidity  $\Delta\eta$  show a nice, intuitive illustration of the appearance of azimuthal anisotropy in heavy-ion collisions. These measurements were later some of the first measurements attracting the attention to the investigations on collectivity in small collision systems. Typical di-hadron correlation structures in heavy-ion collisions are shown in Fig. 1.7. In these measurements, the so-called *near-side* region is found at  $\Delta\phi \approx 0$ , while on the other hand, the *away-side* region means  $\Delta\phi \approx \pi$ . Also, notations of *short-range* and *long-range* are widely used in the heavy-ion community, meaning  $\Delta\eta \approx 0$  and  $|\Delta\eta| \gg 0$ , respectively.

The strong peak in the near-side region in Fig. 1.7 (left) originates mainly from the correlations of particles from high- $p_T$  resonance decays or particles within a jet cone, etc. The so-called *ridge* structure spanning over the whole rapidity range at the away-side comes from low- $p_T$  resonance decays and from correlations of particles between the two cones of a di-jet. The ridge observed at the near-side in heavy-ion collisions is understood as a result of the collective expansion of the system leading to the anisotropic flow. If the near-side jet peak, dominated by effects not originating from anisotropic flow, is removed by cutting the whole section at  $|\Delta\eta| > 1.0$ , the remaining structure can be described by a combination of different contributions from  $v_n$ , as is illustrated in Fig. 1.7 (right).

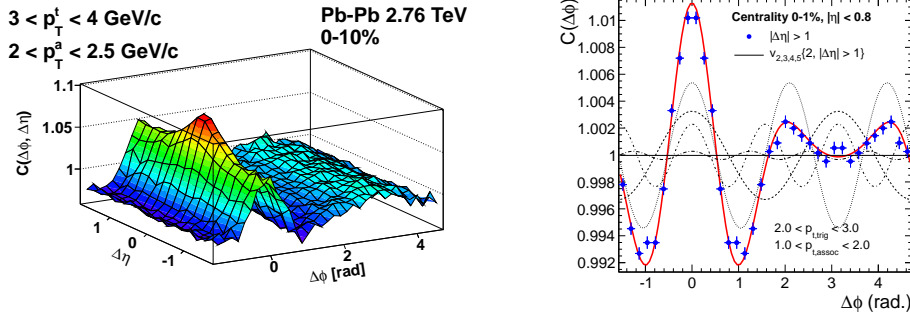


**Figure 1.7:** Left: Di-hadron correlation in 2.76 TeV Pb–Pb collisions, measured as a function of relative difference in azimuthal angle  $\phi$  and pseudorapidity  $\eta$ . Figure taken from [30]. Right: Projection of the di-hadron correlation in 2.76 TeV Pb–Pb collisions onto the  $\Delta\phi$  plane. The near-side jet peak was removed with  $a|\Delta\eta| > 1.0$ . Figure taken from [31].

Flow coefficients can be also extracted from the measurements of multi-particle cumulants (defined later in chapter 2), which are related to different moments of the  $v_n$  distribution. In Fig. 1.8, the centrality dependence of the integrated  $v_2$ ,  $v_3$  and  $v_4$  of charged particles is presented. The left hand-side region of the figure correspond to the central collisions where the two colliding nuclei are almost fully overlapped, while large values of the centrality percentile represent peripheral collisions with a little overlap. The central collisions have almost circular geometry, therefore any space anisotropy comes predominantly from the fluctuations in the positions of nucleons inside the colliding nuclei. The measurements indeed show that comparable elliptic, triangular and quadrangular asymmetries are present. On the other hand, the measured anisotropies become more pronounced in semi-central to peripheral collisions. In particular, the  $v_2$  significantly rises towards larger centralities, which is in agreement to the assumption of an almond shaped overlap region of the colliding nuclei.

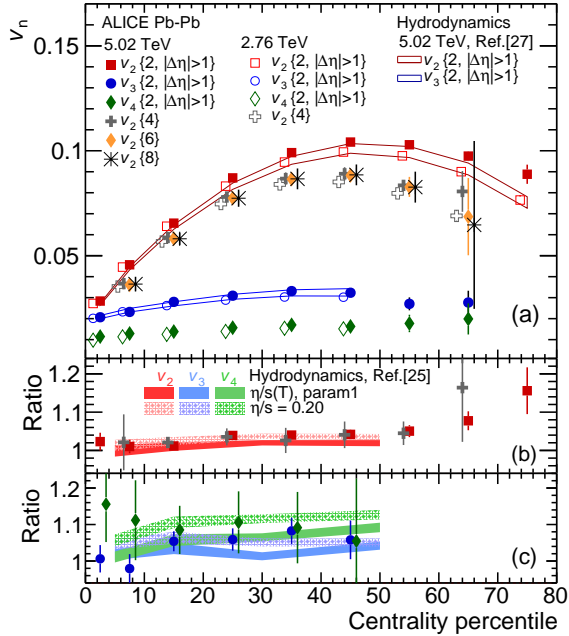


**Figure 1.8:** Flow coefficients as a function of collision centrality in  $\sqrt{s_{\text{NN}}} = 5.02$  TeV Pb–Pb collisions. Measurements are compared to hydrodynamic calculations. Figure taken from [32].

It can be noticed in Fig. 1.8 that the measurements of elliptic flow obtained from two-particle correlations,  $v_2\{2\}$ , are higher than  $v_2$  calculated with higher order correlations,  $v_2\{m\}$  for ( $m > 2$ ). This is caused by flow fluctuations of the  $v_n$  p.d.f. distribution, which contribute differently to cumulants. The contribution of flow fluctuations in two-particle cumulants is positive, while the contribution in higher order cumulants is negative. Additional comparisons between higher order cumulants can serve for more detailed investigations of the shape of the  $v_n$  distribution, as examined e.g. in [33, 34].

More detailed measurements of azimuthal particle correlations can provide tighter constraints on theoretical models. Differential flow measurements [32, 35], as well as decorrelation of the flow vector (which includes  $v_n$  fluctuations and decorrelations of  $\Psi_n$ ) [36–38], flow measurements of identified hadrons [39], or measurements of the linear and non-linear response of flow coefficients [40], have good potentials to differentiate between various scenarios of model descriptions. Finally, direct measurements of correlations between different orders of flow coefficients  $v_n$  [41] also have good ability to provide additional constraints to theoretical models. Since these measurements will be shown later in relation to the small systems, they are presented here in more details.

Correlations between flow coefficients  $v_n$  and  $v_m$  can be measured by the so-called Symmetric Cumulants  $SC(m, n)$  [42]. In particular, correlation between  $v_2$  and  $v_3$  are sensitive to different initial conditions, due to their above mentioned linear response to initial eccentricities  $\epsilon_n$ . On the other hand, correlations with higher order  $v_n$  can bring more insight into the hydrodynamic response. Figure 1.9 (left) shows measurements of  $SC(3, 2)$  and  $SC(4, 2)$  in Pb–Pb collisions at  $\sqrt{s_{NN}} = 2.76$  TeV as a function of collision centrality. The negative sign of  $SC(3, 2)$  indicates an anti-correlation between  $v_2$  and  $v_3$ , while a positive correlation between  $v_2$  and  $v_4$  is found.

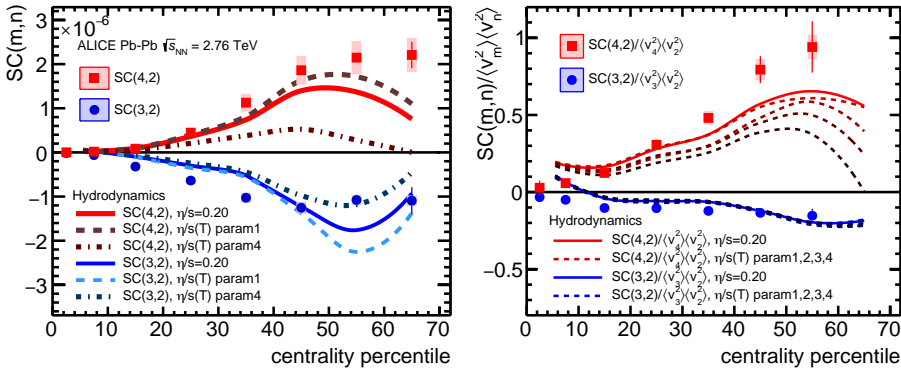


**Figure 1.9:** Left: Measurements of Symmetric Cumulants  $SC(m, n)$  as a function of collision centrality in Pb–Pb collisions at  $\sqrt{s_{NN}} = 2.76$  TeV. Right: Measurements of normalised Symmetric Cumulants  $SC(m, n)$  as a function of collision centrality in Pb–Pb collisions at  $\sqrt{s_{NN}} = 2.76$  TeV. Both measurements are compared to hydrodynamic models with different parametrisations of  $\eta/s$ . Figures taken from [43].

The right panel of Fig. 1.9 presents the normalised Symmetric Cumulants  $NSC(m, n)$ . This observable is obtained by dividing the  $SC(m, n)$  by  $\langle v_n^2 \rangle \langle v_m^2 \rangle$ , which eliminates the dependence on individual flow coefficients. These measurements are at the same time compared to hydrodynamic calculations with different setting of the  $\eta/s(T)$  parametrisations. It is clear that the model cannot quantitatively reproduce the measurements, even though it was successful in describing the individual flow coefficients. This proves that more detailed investigation of the relation between different orders of flow coefficients are more powerful in constraining the model parameters. In addition, the fact that  $NSC(4, 2)$  is more sensitive to

different  $\eta/s$  scenarios of the hydrodynamic model than  $NSC(3,2)$  confirms the assumption of additional non-linear hydrodynamic response of the higher order  $v_n$ .

The wealth of the experimental measurements in heavy-ion collisions gathered during the last years together with the great improvement in theoretical descriptions of the data helped our understanding of the physics of heavy-ion collisions. Measurements of flow coefficients have brought an important insight into the collective effects of the QGP. The chapter will now continue with the introduction to small collision systems, which is the core topic of this thesis. The approach in investigations of the new surprising phenomena in small collision systems should be more clear with the information that was presented in this section.

## 1.4 Small collision systems

Collisions between protons, or a proton with a heavy ion, are commonly denoted as collisions of small systems. The main purpose of pp collisions in the field of heavy-ion physics is to provide baseline measurements for those performed in heavy-ion collisions. In a pp collision, the produced partons evolve without interacting until the final produced particles, therefore they do not suffer from the strongly interacting medium effects. A modification of the observables in heavy-ion collisions with respect to the pp collisions suggests a presence of the QGP. However, initial state effect arising from gluon interactions inside the nuclei during the early stages of a collision might survive during the whole system evolution and affect final observables, both in pp and heavy-ion collisions. For this purpose, asymmetric collisions of proton and a heavy nucleus were performed in order to identify and characterise these so-called Cold Nuclear Matter effects.

During the recent years, this simple picture of small collision systems has been challenged. Measurements considered as an indication of the emergence of the QGP have been revealed in collisions of small systems, too. This triggered lots of discussions about the nature of the observed collective phenomena in small collision systems and how it affects our understanding of large collision systems.

### 1.4.1 Collectivity in small systems ?

Measurements of azimuthal particle correlations in small collision systems have gained a lot of interest. In heavy-ion collisions, measurements of flow coefficients, which quantify the degree of azimuthal anisotropy, are understood as a consequence of an initial spatial anisotropy being transferred via a hydrodynamic expansion of the system to final particle distributions. In other words, it is the collective expansion (flow) of the system that results in a correlated multiparticle production with a common origin.

Similar observations in small collision systems do not necessarily have the same origin as in heavy-ion collisions. Effects of the initial stage, as well as interactions in the hadronic stage, might also result in final particle anisotropy. In order to distinguish various explanations of the experimental observations, a careful comparison between data and theory is in place. Extensive studies in heavy-ion collisions proved the existence of the QGP and its fluid-like character to be responsible for the reported results. It is one of the main interests nowadays to put similar efforts into the understanding of the phenomena observed in (high multiplicity) collisions of small systems.

First, it needs to be determined whether the observations indeed are of a collective nature. Azimuthal anisotropy of final state particles can also be generated by e.g. a di-jet. Nevertheless, the origin of this anisotropy, though common to the particles within the jet, is not connected to the global collective evolution of all particles. Therefore, it needs to be clear what kind of effects we are looking for in order to establish the presence of collectivity in small collision systems. Based on the experience that we have gained in collisions of heavy-nuclei, collective effects usually span across a long range in pseudorapidity. That is, even particles that are separated in rapidity are correlated with each other. At the same time, signs of collectivity should persist to correlations of many particles: no matter how many particles we choose to correlate, the observation should not change. Thus, the “definition” of collectivity is long-range multi-particle correlations.

Anything that does not satisfy the definition of collectivity should be denoted as *non-flow*. Small collision systems are highly dominated by non-flow effects, which can mimic signatures of collectivity. Therefore, it is crucial to study the ways of suppressing non-flow effects in the measurements.

In case collectivity in small collision systems is established, it is natural to continue with the exploration of its origin and establish whether it arises from initial state effects, final state effects, or a combination of the two.

Below, measurements that triggered the discussion about small collision systems will be presented. The main focus will be on the multiplicity dependent measurements of two- or multi-particle correlations of charged particles.

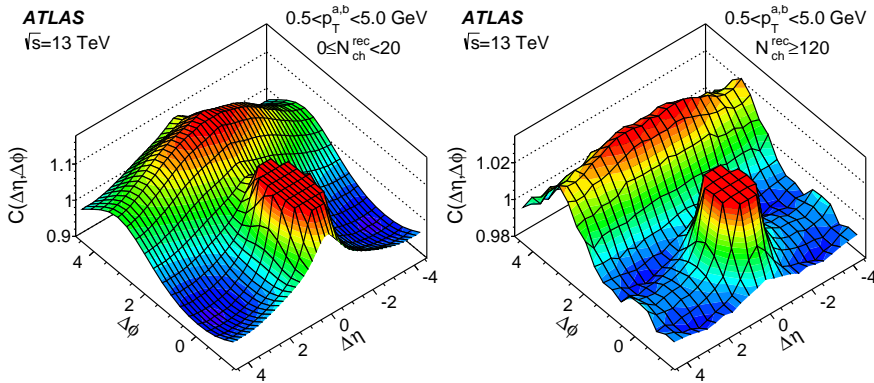


**Figure 1.10:** Di-hadron correlations in 13 TeV pp collisions, measured as a function of relative difference in azimuthal angle  $\phi$  and pseudorapidity  $\eta$ . Left: Measurements from minimum bias pp collisions. Right: Measurements from high multiplicity pp collisions, showing the ridge structure at near side. Figure taken from [44].

Correlations between pairs of charged particles plotted as a function of their relative difference in azimuthal angle  $\Delta\phi$  and pseudorapidity  $\Delta\eta$  show distinct features in heavy-ion collisions, as was shown above in Fig. 1.7. Similar type of measurement performed in low multiplicity pp collisions is clearly different, see Fig. 1.10 (left). The ridge structure spanning over a large range in pseudorapidity at near-side ( $\Delta\phi$ ), considered to be the effect of collective expansion of the matter during the QGP phase in heavy-ion collisions, is not revealed in

low multiplicity pp collisions. However, looking at high multiplicity pp collisions, the ridge appears at near-side for the first time in 7 TeV [45], and also persists at 13 TeV, as can be seen in Fig. 1.10 (right). Even though the ridge is significantly smaller compared to that observed in heavy-ion collisions, it was definitely not expected and needs to be investigated further. The same measurement was performed in low multiplicity and high multiplicity p–Pb collisions (Fig. 1.11) with similar conclusions as in pp collisions: a clear ridge at near-side can be only seen at high multiplicity p–Pb collisions. Moreover, it has more pronounced signal than in pp collisions.

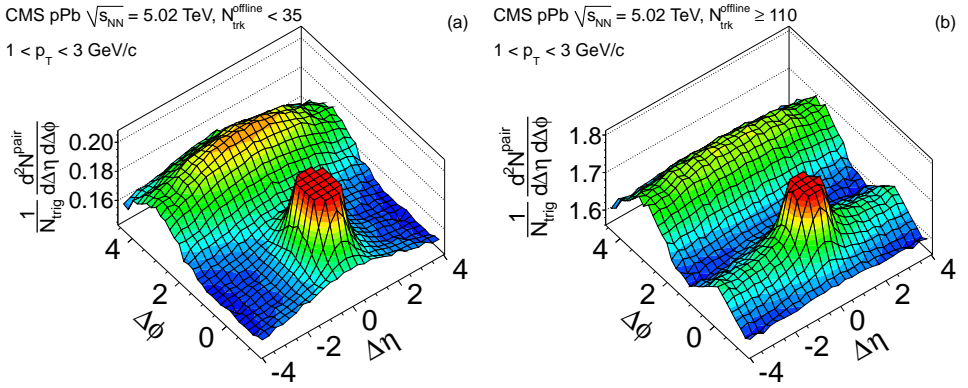


**Figure 1.11:** Di-hadron correlations in 5.02 TeV p–Pb collisions, measured as a function of relative difference in azimuthal angle  $\phi$  and pseudorapidity  $\eta$ . Left: Measurements from minimum bias p–Pb collisions. Right: Measurements from high multiplicity p–Pb collisions, showing the ridge structure at near side. Figure taken from [46].

After these observations, it was clear that the possible presence of collectivity in small collision systems needs to be probed further. Whether the observed long-range two-particle correlations come from collective effects, understood as effects common to essentially all particles in the bulk of a collision, can be studied with the measurements of multi-particle correlations involving more than just pairs of two particles. The multi-particle cumulants and their properties will be described in more details in the next Chapter 2. Here, it is sufficient to note that negative sign of the four-particle cumulant is usually attributed to the presence of the collective hydrodynamic expansion of the QGP in heavy-ion collisions, and it is not expected to be found in small collision systems, without any collective effects. However, results of multi-particle cumulants in p–Pb collisions have revealed similar features as those in peripheral Pb–Pb collisions [47–49]. This is illustrated in Fig. 1.12, where the four-particle cumulant as a function of multiplicity is shown for Pb–Pb and p–Pb collisions. A clear negative sign is seen in Pb–Pb collisions. Significant negative  $c_2\{4\}$  is reported in high-multiplicity p–Pb collisions too, although with smaller magnitude.

During the recent years, such measurements were obtained even in pp collisions. Collectivity in this smallest collision system was announced by CMS after observing a clear negative sign of the four-particle cumulant [50]. However, since then it was understood that

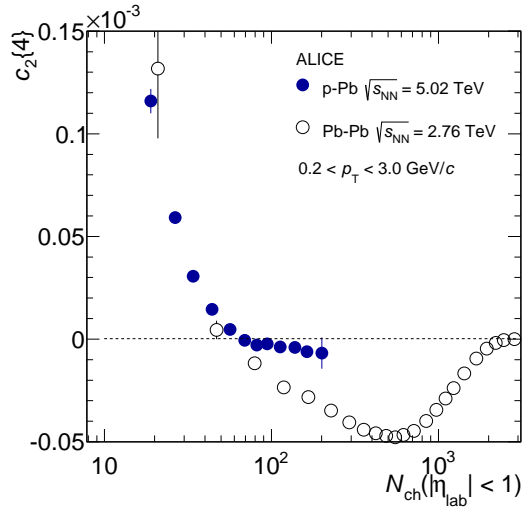


**Figure 1.12:** Four-particle cumulant as a function of multiplicity in Pb–Pb and p–Pb collisions. Figure taken from [47].

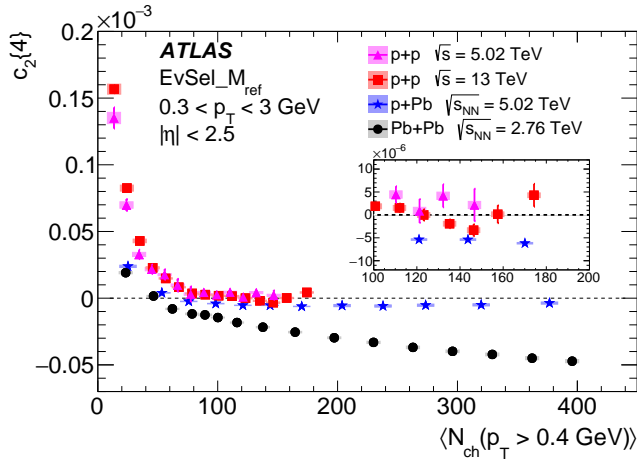


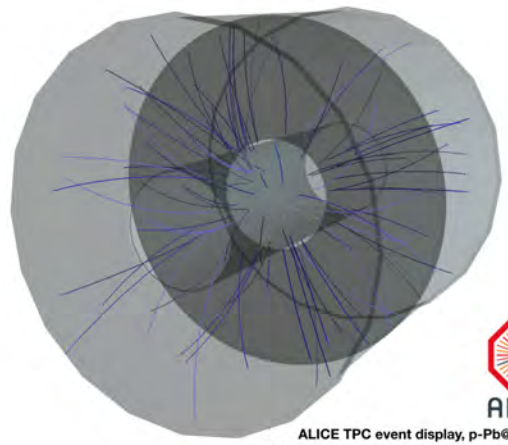
**Figure 1.13:** Multiplicity dependence of four-particle cumulant in 5.02 and 13 TeV pp collisions, 5.02 TeV p–Pb and 2.76 TeV Pb–Pb collisions. Negative  $c_2\{4\}$  can be seen in Pb–Pb and p–Pb collisions, while no negative sign is observed in pp collisions. Figure taken from [49].

the non-flow effects, which dominate in small collision systems, significantly affect not only two-particle correlations, but also multi-particle cumulant measurements. Therefore, their contribution to these measurements should not be neglected. In fact, non-flow correlations can mimic the features of the measurements usually attributed to collectivity, if the measurements are not calculated carefully. Results reported as a function of multiplicity can suffer from

non-flow fluctuations if the cumulants are not calculated in unit bins of multiplicity defined within the same kinematic range that was applied for particles used for the calculation of correlations. Using the correct method, free of such fluctuations, the collectivity was not confirmed in pp collisions [49]. This can be illustrated in Fig. 1.13 with the red and magenta markers representing the measurement of the four-particle cumulant  $c_2\{4\}$ , which is positive in the whole multiplicity range.

The search for collectivity in small collision systems has been given here in a rather brief and straight-forward way. Since the research presented in this thesis is dedicated to the search for collectivity in small collision systems, recent observations and successes in this field will be described in a more detailed way in the following chapters using the ALICE data. The aim of this section was to mediate the excitement and importance of this topic before the thesis continues with more technical details.





## 2. Analysis techniques

A variety of experimental methods exist to calculate the  $v_n$  observable. The most common methods were nicely summarised and discussed with their pros and cons in [51]. Out of the different approaches mentioned there, the method proposed in [51–55] is used to obtain the results in this thesis. In the following, the procedure of the Q-cumulant method will be introduced, and later its generalization into a Generic Framework [42] will be presented. Then, the chapter will continue with recent developments in terms of a suppression of non-flow effects, explaining the implementation into the Generic Framework formalism. The chapter will conclude with the test of performance of this new method on simulations.

### 2.1 Standard method of azimuthal correlations

In this section, the calculation of  $m$ -particle correlation and the procedure to obtain final observables from  $m$ -particle correlations will be described, using the full volume of the detector.

#### 2.1.1 Multi-particle azimuthal correlations

A single event  $m$ -particle correlation in harmonics  $n_1, n_2, \dots, n_m$  is expressed as

$$\langle m \rangle_{n_1, n_2, \dots, n_m} = \langle e^{i(n_1 \varphi_1 + n_2 \varphi_2 + \dots + n_m \varphi_m)} \rangle. \quad (2.1)$$

The  $\langle \cdot \rangle$  represents an average of all possible combinations of  $m$ -tuplets of particles from the overall  $M$  particles created in an event. Then, an event averaged correlation is obtained, generally denoted as

$$\langle\langle m \rangle\rangle_{n_1, n_2, \dots, n_m} = \langle\langle e^{i(n_1 \varphi_1 + n_2 \varphi_2 + \dots + n_m \varphi_m)} \rangle\rangle, \quad (2.2)$$

where  $\langle\langle \cdot \rangle\rangle$  represents the weighted average over many events.

One way to calculate correlations among particles created in a collision is using the so-called *nested loops*. In case of a 2-particle correlation, it is required to have 2 loops over all particles, where the second loop is contained within the first one, therefore resulting in  $M$  loops. A scheme of such a calculation is shown below:

```

for(int i=0; i<M; i++)
{
    for(int j=0; j<M; j++)
    {
        if(i==j) continue;
    }
}

```

Correlating each particle with all the remaining particles in a collision in the form of nested loops can consume a lot of computational power. The consumption increases especially when calculating the  $m$ -particle correlations of higher orders ( $m > 2$ ).

### Q-cumulant

A new method to calculate  $m$ -particle correlations, called the Q-cumulant method, was developed in [51, 55]. This method introduces the so-called  $Q$ -vector  $Q_n$  for harmonic  $n$  defined as:

$$Q_n = \sum_{k=1}^M e^{in\phi_k}. \quad (2.3)$$

This enables the calculation of any order of  $m$ -particle correlation using just one loop over the particles in a collision.

A simple example of the calculation of a single event-averaged 2-particle correlation  $\langle\langle 2 \rangle\rangle_{n_1, n_2}$  exploiting the  $Q$ -vector for the case when  $n_1 = n_2 = n$  is shown in (2.4):

$$\langle\langle 2 \rangle\rangle_n = \frac{|Q_n|^2 - M}{M(M-1)}. \quad (2.4)$$

The product  $|Q_n|^2 = Q_n \cdot Q_n^* = \sum_{i,j} e^{in(\phi_i - \phi_j)}$  represents all the combinations of two-particle correlations, including the auto-correlation terms when the same particle is being correlated with itself ( $i = j$ ). For this purpose, a factor  $M$ , which represents the number of diagonal terms of  $|Q_n|^2$  when  $i = j$ , is subtracted from  $|Q_n|^2$ . The number of terms in the formulas for higher order correlations are significantly increasing, thus they are not explicitly shown here. The equations can be found in [51, 55].

### Generic Framework

The results presented in this thesis are calculated using the Generic Framework [42], therefore it will be described here in more details.

Analysis based on azimuthal correlations of particles is vulnerable to non-uniform acceptance of the used detector. Inefficient particle detection in some regions of the detector results in biased final correlation. In such a case, additional terms would appear in eq. (2.4) to correct for non-uniform acceptance effects, as described in [55]. Correcting for such terms

is challenging, especially for higher orders of  $m$ -particle correlations, where the number of correction terms rapidly increases.

The Generic Framework [42] is a universal method to calculate any type of  $m$ -particle correlation in an exact and efficient way. It can correct for non-uniform acceptance effects on the level of the  $Q$ -vector with an accessible way by introducing a weight  $w$ :

$$Q_{n,p} = \sum_{k=1}^M w_k^p e^{in\phi_k} \quad Q_{-n,p} = Q_{n,p}^* \quad (2.5)$$

For instance, if a region of the detector in azimuth exhibits lower detection efficiency, larger emphasis will be put on particles from this region in order to account for losses caused by the detector inefficiency. All particles will thus have weight  $w = 1$ , except for the lower performance detector region, where  $w > 1$ . The weight can depend not only on the azimuthal angle  $\phi$ , but also on any other variable, depending on the dimension in which the inefficiency is present (such as  $\eta$  or  $p_T$ ). The procedure to obtain the weight will be described in details in Chapter 5.

Similarly to the  $Q$ -cumulant method, only a single pass over particles in an event is necessary to get the  $Q$ -vector for various combinations of harmonic  $n$  and power  $p$ . A compact prescription of the general formulas of  $m$ -particle correlations based just on the operations with the  $Q$ -vectors allows for efficient and direct calculation of any type of observable. A generic formula for any  $m$ -particle correlation can be written as [42]:

$$\langle m \rangle_{n_1, n_2, \dots, n_m} = \frac{N \langle m \rangle_{n_1, n_2, \dots, n_m}}{D \langle m \rangle_{n_1, n_2, \dots, n_m}} = \frac{N \langle m \rangle_{n_1, n_2, \dots, n_m}}{N \langle m \rangle_{0, 0, \dots, 0}} \quad (2.6)$$

Formulas for  $N \langle m \rangle_{n_1, n_2, \dots, n_m}$ , where  $m \leq 4$ , are shown explicitly in eq. (2.7), (2.8) and (2.9) [42]:

$$N \langle 2 \rangle_{n_1, n_2} = Q_{n_1, 1} Q_{n_2, 1} - Q_{n_1+n_2, 2} \quad (2.7)$$

$$\begin{aligned} N \langle 3 \rangle_{n_1, n_2, n_3} &= Q_{n_1, 1} Q_{n_2, 1} Q_{n_3, 1} - Q_{n_1+n_2, 2} Q_{n_3, 1} - Q_{n_2, 1} Q_{n_1+n_3, 2} \\ &\quad - Q_{n_1, 1} Q_{n_2+n_3, 2} + 2Q_{n_1+n_2+n_3, 3} \end{aligned} \quad (2.8)$$

$$\begin{aligned} N \langle 4 \rangle_{n_1, n_2, n_3, n_4} &= Q_{n_1, 1} Q_{n_2, 1} Q_{n_3, 1} Q_{n_4, 1} - Q_{n_1+n_2, 2} Q_{n_3, 1} Q_{n_4, 1} \\ &\quad - Q_{n_2, 1} Q_{n_1+n_3, 2} Q_{n_4, 1} - Q_{n_1, 1} Q_{n_2+n_3, 2} Q_{n_4, 1} \\ &\quad + 2Q_{n_1+n_2+n_3, 3} Q_{n_4, 1} - Q_{n_2, 1} Q_{n_3, 1} Q_{n_1+n_4, 2} \\ &\quad + Q_{n_2+n_3, 2} Q_{n_1+n_4, 2} - Q_{n_1, 1} Q_{n_3, 1} Q_{n_2+n_4, 2} \\ &\quad + Q_{n_1+n_2, 2} Q_{n_2+n_4, 2} + 2Q_{n_3, 1} Q_{n_1+n_2+n_4, 3} \\ &\quad - Q_{n_1, 1} Q_{n_2, 1} Q_{n_3+n_4, 2} + Q_{n_1+n_2, 2} Q_{n_3+n_4, 2} \\ &\quad + 2Q_{n_2, 1} Q_{n_1+n_3+n_4, 3} + 2Q_{n_1, 1} Q_{n_2+n_3+n_4, 3} \\ &\quad - 6Q_{n_1+n_2+n_3+n_4, 4} \end{aligned} \quad (2.9)$$

Higher order correlations contain a largely growing number of terms (203 for 6-particle correlation, or 4140 for 8-particle correlation). Therefore, they are not explicitly presented here. However, the authors of [42] provide a recursive, or recurrent algorithm to produce any order of  $m$ -particle correlation by exploiting the lower order correlations. For the analysis presented in this thesis, the recurrent formula was used to obtain the higher order correlations, shown below in the form of a pseudocode:

```

N⟨1⟩n1 : return Qn1,1
N⟨m⟩n1,...,nm :
  C ← 0
  for k ← (m - 1), 1 do
    for each combination c = c1, ..., ck of n1, ..., nm-1 do
      q ← ∑j not in c nj
      C ← C + (-1)m-k (m - k - 1)! × N⟨k⟩c1,...,ck × Qq,m-k
    end for each c
  end for k
  return C.

```

(2.10)

### 2.1.2 From correlations to observables

The amount of possible observables which exploit the  $m$ -particle azimuthal correlations have been growing during the recent years. Integrated or differential measurements of flow coefficients  $v_n$  can be calculated from  $m$ -particle correlations using the same harmonic ( $n_1 = n_2 = \dots = n_m = n$ ). On the other hand, measurements of correlations between different flow coefficients (Symmetric Cumulants), or measurements of linear and non-linear flow modes, can fully benefit from the generic formulas presented above by using different harmonics ( $n_1 \neq n_2 \neq \dots \neq n_m$ ). In this section, the description of the observables later presented in the final results of this thesis, and of the procedure to obtain these observables, will be shown.

#### The case when $n_1 = n_2 = \dots = n_m = n$

The standard measurements of flow coefficients are obtained from the  $m$ -particle correlations for the same order of harmonic  $n$ . First, the event-averaged  $m$ -particle correlations are used to calculate the  $m$ -particle cumulants  $c_n\{m\}$ :

$$\begin{aligned}
c_n\{2\} &= \langle\langle 2 \rangle\rangle_{n,-n} \\
c_n\{4\} &= \langle\langle 4 \rangle\rangle_{n,n,-n,-n} - 2 \cdot \langle\langle 2 \rangle\rangle_{n,-n}^2 \\
c_n\{6\} &= \langle\langle 6 \rangle\rangle_{n,n,n,-n,-n,-n} - 9 \cdot \langle\langle 2 \rangle\rangle_{n,-n} \cdot \langle\langle 4 \rangle\rangle_{n,n,-n,-n} + 12 \cdot \langle\langle 2 \rangle\rangle_{n,-n}^3 \\
c_n\{8\} &= \langle\langle 8 \rangle\rangle_{n,n,n,n,-n,-n,-n,-n} - 16 \cdot \langle\langle 6 \rangle\rangle_{n,n,n,-n,-n,-n} \cdot \langle\langle 2 \rangle\rangle_{n,-n} \\
&\quad - 18 \cdot \langle\langle 4 \rangle\rangle_{n,n,-n,-n}^2 + 144 \cdot \langle\langle 4 \rangle\rangle_{n,n,-n,-n} \cdot \langle\langle 2 \rangle\rangle_{n,-n}^2 - 144 \cdot \langle\langle 2 \rangle\rangle_{n,-n}^4
\end{aligned}
\tag{2.11}$$

where the curly brackets  $\{\cdot\}$  represent the order of the  $m$ -particle correlation. The two-particle cumulant is directly equal to  $\langle\langle 2 \rangle\rangle_{n,-n}$ . However, higher order cumulants have more complex

formulas in order to obtain the genuine  $m$ -particle correlation by subtraction of contributions from lower order correlations.

Eventually, the flow coefficients are retrieved from cumulants, as is written in eq. (2.12):

$$\begin{aligned} v_n\{2\} &= \sqrt{c_n\{2\}}, & v_n\{4\} &= \sqrt[4]{-c_n\{4\}}, \\ v_n\{6\} &= \sqrt[6]{\frac{1}{4}c_n\{6\}}, & v_n\{8\} &= \sqrt[8]{-\frac{1}{33}c_n\{8\}}. \end{aligned} \quad (2.12)$$

The curly brackets  $\{\cdot\}$  again denote the way of how the given  $v_n$  was estimated (order of the  $m$ -particle correlation). It is important to notice the requirements imposed on cumulants based on the formulas in (2.12): in order to obtain real values of  $v_n$  observables, the sign of the 2- and 6-particle cumulant is required to be positive, while the 4- and 8-particle cumulant negative.

An example of cumulant measurements in Pb–Pb collisions at  $\sqrt{s_{NN}} = 5.02$  TeV can be seen in Fig. 2.1. The sign of the cumulants (positive for the two- and six-particle cumulant and negative for the four- and eight-particle cumulant) allows to extract the real measurements of flow coefficients in these collisions.

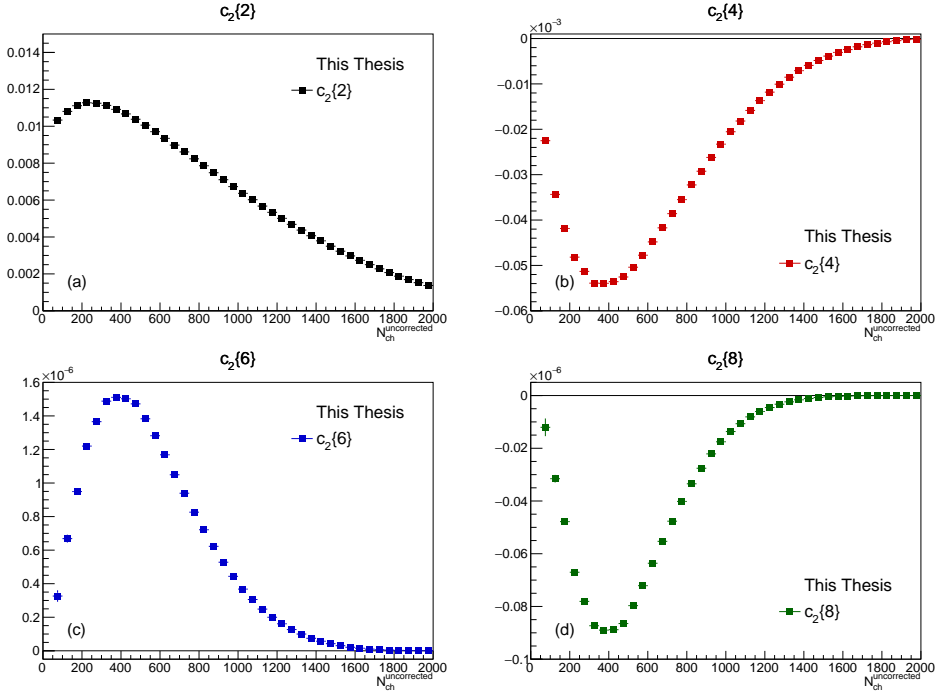


**Figure 2.1:** Measurements of  $m$ -particle cumulants in  $\sqrt{s_{NN}} = 5.02$  TeV Pb–Pb collisions. (a)  $c_2\{2\}$ , (b)  $c_2\{4\}$ , (c)  $c_2\{6\}$  and (d)  $c_2\{8\}$ .

### The case when $n_1 \neq n_2 \neq \dots \neq n_m$

Correlations between different harmonics can be used in a variety of observables. One of the most recent examples was published in [40], measuring the non-linear flow modes, non-linear mode coefficients, and correlations between different orders of the symmetry planes. Here, the Symmetric Cumulants,  $SC(m, n)$ , proposed in [42] and measured for the first time by ALICE [43], are briefly summarised.

Symmetric Cumulants measure the correlation between different orders of flow coefficients  $v_n$  and  $v_m$ . It is defined as

$$SC(m, n) = \langle v_n^2 \cdot v_m^2 \rangle - \langle v_n^2 \rangle \cdot \langle v_m^2 \rangle, \quad (2.13)$$

where the  $\langle \cdot \rangle$  represents the event average.

In order to calculate the  $SC(m, n)$ , a formula similar to the calculation of the 4-particle cumulant is used, but with  $m \neq n$ :

$$SC(m, n) = \langle \langle 4 \rangle \rangle_{m, n, -m, -n} - \langle \langle 2 \rangle \rangle_{m, -m} \cdot \langle \langle 2 \rangle \rangle_{n, -n}. \quad (2.14)$$

Moreover, in contrast with the  $c_n\{4\}$  formula (2.11), the product of the 2-particle correlation is not multiplied by a factor 2, because the presence of two different harmonics,  $m$  and  $n$ , does not allow for more permutations of the possible grouping of particles. If there is no correlation between  $v_n$  and  $v_m$ , the  $\langle v_n^2 \cdot v_m^2 \rangle$  would factorise, thus resulting in a zero signal of  $SC(m, n)$ . In case of a correlation between  $v_n$  and  $v_m$ , the  $SC(m, n)$  will be non-zero. Therefore, this observable can provide an information on whether finding  $v_n$  larger than  $\langle v_n \rangle$  in an event will increase/decrease the probability of finding the  $v_m$  larger than  $\langle v_m \rangle$ .

## 2.2 Subevent method

Measurements related to the azimuthal flow coefficients are often contaminated by the so-called *non-flow* processes, which do not have a connection to a global symmetry plane. These are typically correlations between few particles, characterised by small opening angles. Such effects might for example arise from correlations between particles in jets, or resonance decays. A back-to-back jet can also produce a large signal of  $v_2$ , because the particles within the jet are correlated with respect to the jet symmetry plane. However, the jet symmetry plane might be different from the global collision symmetry plane, common to all the particles in the bulk of a collision. Therefore, measurements of  $m$ -particle correlations might include contributions from such non-flow effects, which introduce a contamination to the measurements.

The so-called subevent method is able to suppress non-flow in  $m$ -particle correlations. In this section, its usage in the measurements of two-particle cumulants, and its successful recent extension to higher order cumulants, will be presented. First, the general idea is shown with supporting illustrations and then, the implementation of this idea into the Generic Framework is explained.

### 2.2.1 Subevent method on cumulant level

#### Two-particle cumulant

By default, the calculation of the two-particle correlation is performed between particles within a certain detector acceptance. A sketch of a side view of a detector volume, together

with an example of a two-particle correlation, is shown in Fig. 2.2. In the standard case of the two-particle correlation when the whole detector acceptance is used, one would also include particles being close to each other, which might originate from the above mentioned non-flow type of processes, giving rise to a strong two-particle correlation. As was explained above, such particles are indeed correlated with each other, given that they originate from the same source. However, they do not correspond to the global correlation with respect to a symmetry plane common to all particles in a collision.

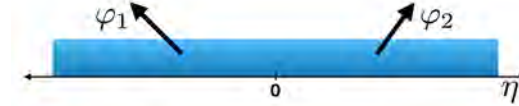


**Figure 2.2:** Sketch of the side view of a detector, showing an example of a two-particle correlation without the subevent method.

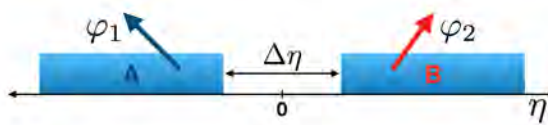


**Figure 2.3:** Sketch of the side view of a detector, showing an example of two-particle correlation using the 2-subevent method with an additional  $|\Delta\eta|$  gap between the subevents.

To suppress the non-flow effects, one can split the detector acceptance into two subevents (as illustrated in Fig.2.3) and calculate the two-particle correlation as written in eq. (2.15):

$$\langle\langle 2 \rangle\rangle_{n,2\text{-sub}} = \langle\langle e^{in(\varphi_1 - \varphi_2)} \rangle\rangle. \quad (2.15)$$

A condition for each pair of particles that are being correlated is applied, where one particle is taken from the subevent A indicated with the blue color, while the second particle is taken from the subevent B represented by the red color. This is the so-called 2-subevent method. Compared to the case without the subevent method, in this procedure it is less probable that one would select a pair of particles where both originate from a non-flow correlation, because a space separation (in pseudorapidity  $\eta$ ) is enforced between them. This method should not be mistaken for the  $\Delta\eta$  cut used in the measurements of two-particle correlation function, usually plotted as a function of  $\Delta\varphi$  and  $\Delta\eta$  (e.g. [44]). In that analysis, the pseudorapidity gap is imposed between each pair of particles. Since cumulants are calculated from the  $Q$ -vectors (sum over all particles in an event), it is not possible to put a gap between individual two particles that are used for correlation. Instead, the pseudorapidity gap is imposed on the region from which the particles, forming the  $Q$ -vector, are selected. Particles from the region excluded by the pseudorapidity gap are not used in the measurement. Therefore, the number of pairs in the correlation decreases with increasing  $|\Delta\eta|$  gap, causing larger statistical uncertainties.

In a simple case, where the detector is just divided into two subevents, it is still possible to include short-range correlations at the common edge of the subevents. In order to further suppress short range correlations, a larger  $\Delta\eta$  gap should be imposed between the subevents, as is shown in Fig. 2.3. In general, this means that the larger the  $\Delta\eta$  gap, the larger the suppression of non-flow effects there is. It is assumed that the point where applying a larger  $\Delta\eta$  gap does not cause a further decrease of the signal of the two-particle correlation, is when the non-flow contribution is best suppressed.

### Multi-particle cumulants

By construction, higher order  $m$ -particle cumulants ( $m > 2$ ) are less sensitive to non-flow effects originating from correlations between  $k$  particles, where  $k < m$  [52, 53]. However, contamination with the non-flow from correlations of similar order remain. These effects play a significant role especially in small collision systems dominated by non-flow effects, or also in larger collision systems with low number of created particles. It is therefore important to investigate the possibility to further suppress non-flow contamination in multi-particle cumulants.

As can be seen from eq. (2.11),  $c_n\{4\}$  is obtained from the event averaged two- and four-particle correlations. The subevent method for two-particle correlations was already described above. In a similar way, we can enforce a  $\Delta\eta$  separation between the four particles that are being correlated in the way that is illustrated in Fig. 2.4. The way to obtain the 4-particle cumulant with the two-subevent method is written in eq. (2.16).

$$\begin{aligned}
\langle\langle 4 \rangle\rangle_{n,2\text{-sub}} &= \langle\langle e^{in(\varphi_1 + \varphi_2 - \varphi_3 - \varphi_4)} \rangle\rangle \\
\langle\langle 2 \rangle\rangle_{n,2\text{-sub}}^{1-3} \cdot \langle\langle 2 \rangle\rangle_{n,2\text{-sub}}^{2-4} &= \langle\langle e^{in(\varphi_1 - \varphi_3)} \rangle\rangle \cdot \langle\langle e^{in(\varphi_2 - \varphi_4)} \rangle\rangle \\
\langle\langle 2 \rangle\rangle_{n,2\text{-sub}}^{1-4} \cdot \langle\langle 2 \rangle\rangle_{n,2\text{-sub}}^{2-3} &= \langle\langle e^{in(\varphi_1 - \varphi_4)} \rangle\rangle \cdot \langle\langle e^{in(\varphi_2 - \varphi_3)} \rangle\rangle \\
c_n\{4\}_{2\text{-sub}} &= \langle\langle 4 \rangle\rangle_{n,2\text{-sub}} - \langle\langle 2 \rangle\rangle_{n,2\text{-sub}}^{1-3} \cdot \langle\langle 2 \rangle\rangle_{n,2\text{-sub}}^{2-4} \\
&\quad - \langle\langle 2 \rangle\rangle_{n,2\text{-sub}}^{1-4} \cdot \langle\langle 2 \rangle\rangle_{n,2\text{-sub}}^{2-3} \\
&= \langle\langle 4 \rangle\rangle_{n,2\text{-sub}} - 2 \cdot \langle\langle 2 \rangle\rangle_{n,2\text{-sub}}^2
\end{aligned} \tag{2.16}$$

One has to ensure that the four-particle correlation is calculated such that  $\varphi_1$  and  $\varphi_2$  (both with a positive sign) are in the subevent A, while the  $\varphi_3$  and  $\varphi_4$  (both with a negative sign) are in the subevent B. If  $\varphi_1$  and  $\varphi_3$  originate from a non-flow correlation, having them in the same subevent would introduce a fake flow signal  $\approx \langle \cos n(\varphi_1 - \varphi_3) \rangle$ . The two-particle correlation should also be calculated with a subevent method, keeping the layout of the subevents the same as for the four-particle correlation.

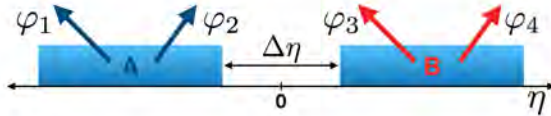


**Figure 2.4:** Sketch of the side view of a detector, showing an example of a four-particle correlation with the 2-subevent method. An additional  $|\Delta\eta|$  gap is applied between the subevents.

The 2-subevent method has a potential to further suppress non-flow contamination, however it would not be able to suppress cases when e.g. a jet produces particles in opposite directions such that each would end up in one of the two subevents. Such effects can be suppressed with a 3-subevent method. In this case, the detector acceptance is divided into three subevents, as illustrated in Fig. 2.5. The particles  $\varphi_1$  and  $\varphi_2$  (positive sign terms) are taken from the middle subevent A, while the  $\varphi_3$  is taken from the left subevent B, and the  $\varphi_4$  from the right subevent C, shown with blue, red and yellow color, respectively. The correlations entering the calculation of  $c_2\{4\}$  are written in eq. (2.17):

$$\begin{aligned}
\langle\langle 4 \rangle\rangle_{n,3\text{-sub}} &= \langle\langle e^{in(\varphi_1+\varphi_2-\varphi_3-\varphi_4)} \rangle\rangle \\
\langle\langle 2 \rangle\rangle_{n,AB} \cdot \langle\langle 2 \rangle\rangle_{n,AC} &= \langle\langle e^{in(\varphi_1-\varphi_3)} \rangle\rangle \cdot \langle\langle e^{in(\varphi_2-\varphi_4)} \rangle\rangle \\
\langle\langle 2 \rangle\rangle_{n,AC} \cdot \langle\langle 2 \rangle\rangle_{n,AB} &= \langle\langle e^{in(\varphi_1-\varphi_4)} \rangle\rangle \cdot \langle\langle e^{in(\varphi_2-\varphi_3)} \rangle\rangle \\
c_n\{4\}_{3\text{-sub}} &= \langle\langle 4 \rangle\rangle_{n,3\text{-sub}} - 2 \cdot \langle\langle 2 \rangle\rangle_{n,AB} \cdot \langle\langle 2 \rangle\rangle_{n,AC}. \quad (2.17)
\end{aligned}$$

The formulas are similar as for the calculation of the standard  $c_n\{4\}$  and  $c_n\{4\}_{2\text{-sub}}$ , the only difference are the subevents from which the particles originate.

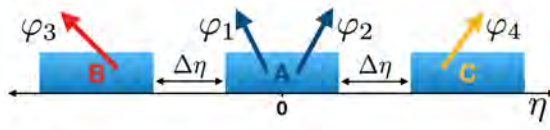


**Figure 2.5:** Sketch of the side view of a detector, showing an example of a four-particle correlation with the 3-subevent method with an additional  $|\Delta\eta|$  gap between the subevents.

Apart from the “BAC” configuration of the three subevents shown in Fig. 2.5, there is also a possibility to permute the position of the subevent A, namely as “ABC” and “BCA”. In this way, it is possible to fully, or partially, recover for the lost statistics (number of particle multiplets) in the 3-subevent method, or the 3-subevent method with a  $|\Delta\eta|$  gap between the subevents, respectively.

The subevent method applied to Symmetric Cumulants is performed in a very similar way as in the case of  $c_n\{4\}$ , except for the fact that  $SC(m,n)$  observable exploits cross-harmonic correlations. Following the illustration of a 2-subevent method drawn in Fig. 2.4, the  $SC(m,n)_{2\text{-sub}}$  can be calculated as (2.18):

$$\begin{aligned}
\langle\langle 4 \rangle\rangle_{m,n,2\text{-sub}} &= \langle\langle e^{i(n\varphi_1+m\varphi_2-n\varphi_3-m\varphi_4)} \rangle\rangle \\
\langle\langle 2 \rangle\rangle_{n,2\text{-sub}} \cdot \langle\langle 2 \rangle\rangle_{m,2\text{-sub}} &= \langle\langle e^{in(\varphi_1-\varphi_3)} \rangle\rangle \cdot \langle\langle e^{im(\varphi_2-\varphi_4)} \rangle\rangle \\
SC(m,n)_{2\text{-sub}} &= \langle\langle 4 \rangle\rangle_{m,n,2\text{-sub}} - \langle\langle 2 \rangle\rangle_{n,2\text{-sub}} \cdot \langle\langle 2 \rangle\rangle_{m,2\text{-sub}} \quad (2.18)
\end{aligned}$$

The fact that  $m \neq n$  in  $SC(m,n)$  results in two possibilities to arrange the  $m$ -particle correlations in the case of the 3-subevent method. They are shown in eq. (2.19) and (2.20):

$$\begin{aligned}
\langle\langle 4 \rangle\rangle_{m,n,3\text{-sub}}^I &= \langle\langle e^{i(n\varphi_1+m\varphi_2-n\varphi_3-m\varphi_4)} \rangle\rangle \\
\langle\langle 2 \rangle\rangle_{n,AB}^I \cdot \langle\langle 2 \rangle\rangle_{m,AC}^I &= \langle\langle e^{in(\varphi_1-\varphi_3)} \rangle\rangle \cdot \langle\langle e^{im(\varphi_2-\varphi_4)} \rangle\rangle \\
SC(m,n)_{3\text{-sub}}^I &= \langle\langle 4 \rangle\rangle_{m,n,3\text{-sub}}^I - 2 \cdot \langle\langle 2 \rangle\rangle_{n,AB}^I \cdot \langle\langle 2 \rangle\rangle_{m,AC}^I \quad (2.19)
\end{aligned}$$

$$\begin{aligned}
\langle\langle 4 \rangle\rangle_{m,n,3\text{-sub}}^{II} &= \langle\langle e^{i(n\varphi_1+m\varphi_2-m\varphi_3-n\varphi_4)} \rangle\rangle \\
\langle\langle 2 \rangle\rangle_{m,AB}^{II} \cdot \langle\langle 2 \rangle\rangle_{n,AC}^{II} &= \langle\langle e^{in(\varphi_1-\varphi_4)} \rangle\rangle \langle\langle e^{im(\varphi_2-\varphi_3)} \rangle\rangle \\
SC(m,n)_{3\text{-sub}}^{II} &= \langle\langle 4 \rangle\rangle_{m,n,3\text{-sub}}^{II} - 2 \cdot \langle\langle 2 \rangle\rangle_{m,AB}^{II} \langle\langle 2 \rangle\rangle_{n,AC}^{II} \quad (2.20)
\end{aligned}$$

If  $SC(m,n)_{3\text{-sub}}^I \approx SC(m,n)_{3\text{-sub}}^{II}$ , they are combined to form the final measurement  $SC(m,n)_{3\text{-sub}}$ . At the same time, each of the two possibilities have additional freedom to have 3 different permutations of the subevents, just like the  $c_n\{4\}_{3\text{-sub}}$ .

In a similar way, the subevent method can be extended further to  $m > 4$  order of the cumulants. The illustration and corresponding formulas for  $c_n\{6\}$  can be seen in Fig. 2.6 and in eq. (2.21), and for  $c_n\{8\}$  in Fig. 2.7 and in eq. (2.22).

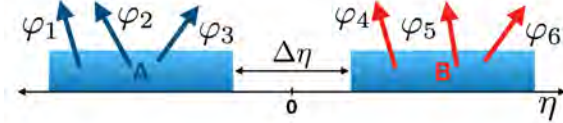


**Figure 2.6:** Sketch of the side view of a detector, showing example of six-particle correlation with 2-subevent method with an additional  $|\Delta\eta|$  gap between the subevents.

$$c_n\{6\}_{2\text{-sub}} = \langle\langle 6 \rangle\rangle_{n,2\text{-sub}} - 9 \cdot \langle\langle 2 \rangle\rangle_{n,2\text{-sub}} \cdot \langle\langle 4 \rangle\rangle_{n,2\text{-sub}} + 12 \cdot \langle\langle 2 \rangle\rangle_{n,2\text{-sub}}^3 \quad (2.21)$$

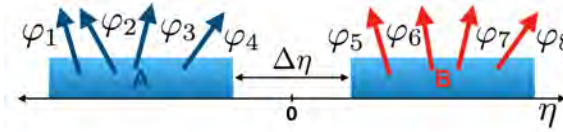


**Figure 2.7:** Sketch of the side view of a detector, showing example of eight-particle correlation with 2-subevent method with an additional  $|\Delta\eta|$  gap between the subevents.

$$\begin{aligned}
c_n\{8\}_{2\text{-sub}} &= \langle\langle 8 \rangle\rangle_{n,2\text{-sub}} - 16 \cdot \langle\langle 6 \rangle\rangle_{n,2\text{-sub}} \langle\langle 2 \rangle\rangle_{n,2\text{-sub}} - 18 \cdot \langle\langle 4 \rangle\rangle_{n,2\text{-sub}}^2 \\
&\quad + 144 \cdot \langle\langle 4 \rangle\rangle_{n,2\text{-sub}} \langle\langle 2 \rangle\rangle_{n,2\text{-sub}}^2 - 144 \cdot \langle\langle 2 \rangle\rangle_{n,2\text{-sub}}^4 \quad (2.22)
\end{aligned}$$

### 2.2.2 Subevent method in Generic Framework

The calculation of the standard  $m$ -particle correlation in the case where the whole detector acceptance is used is implemented in the Generic Framework [42]. This formalism was extended to the subevent case, as described in this section, and used for the analysis presented in this thesis in the following chapters.

#### Two-particle correlation

The simplest calculation is the one of the two-particle correlation. In case of a full detector acceptance, it is calculated as a product of two  $Q$ -vectors, from which the auto-correlation term is subtracted, see eq. (2.7).

However, in the subevent method, the 2-particle correlation is performed between particles where each comes from a different subevent. For this reason, it is not needed to subtract any auto-correlation term. The formula (2.7) can be rewritten in a simpler format shown in (2.23):

$$N\langle 2 \rangle_{n_1, n_2} = Q_{n_1, 1}^A Q_{n_2, 1}^B, \quad (2.23)$$

where A and B represent the subevents. When using the 2-subevent method, it is crucial to distinguish the  $Q$ -vectors from different subevents:

$$Q_{n,p}^A = \sum_{k=1}^{M^A} w_k^p e^{in\varphi_k^A} \quad Q_{n,p}^B = \sum_{k=1}^{M^B} w_k^p e^{in\varphi_k^B}, \quad (2.24)$$

where  $M^A$  represents the multiplicity in subevent A, and  $M^B$  the multiplicity in subevent B.

#### Multi-particle correlations

It is possible to remove the auto-correlation terms from the formula for the four-particle correlation in eq. (2.9) in a similar way to what was done above. The formula to calculate the four-particle correlation with the 2-subevent method using the Generic Framework can be written as:

$$\begin{aligned} N\langle 4 \rangle_{n_1, n_2, n_3, n_4} = & Q_{n_1, 1}^A Q_{n_2, 1}^A Q_{n_3, 1}^B Q_{n_4, 1}^B - Q_{n_1+n_2, 2}^A Q_{n_3, 1}^B Q_{n_4, 1}^B \\ & - Q_{n_1, 1}^A Q_{n_2, 1}^A Q_{n_3+n_4, 2}^B + Q_{n_1+n_2, 2}^A Q_{n_3+n_4, 2}^B. \end{aligned} \quad (2.25)$$

In comparison with the standard formula in (2.9), 11 out of the 15 terms could be removed. For example, the auto-correlation term  $Q_{n_2, 1} Q_{n_1+n_3, 2} Q_{n_4, 1}$  no longer contributes to the four-particle correlation formula in eq. (2.25), because  $\varphi_1$  and  $\varphi_3$  do not share a common subevent, therefore there is no auto-correlation left to be subtracted.

In the case of the 3-subevent method, even more auto-correlation terms can be removed from the four-particle correlation formula, since now even  $\varphi_3$  and  $\varphi_4$  do not share a common subevent:

$$N\langle 4 \rangle_{n_1, n_2, n_3, n_4} = Q_{n_1, 1}^A Q_{n_2, 1}^A Q_{n_3, 1}^B Q_{n_4, 1}^C - Q_{n_1+n_2, 2}^A Q_{n_3, 1}^B Q_{n_4, 1}^C \quad (2.26)$$

All the time it is important to have different  $Q$ -vectors for subevents A and B in the 2-subevent method, and A, B and C in the 3-subevent method.

While in the two- and four-particle correlations it was possible to manually identify and remove the auto-correlation terms, doing that in higher order cumulants, where the amount of terms rapidly increases up to 4140 terms in the 8-particle correlation [42], could lead to mistakes or forgotten terms. Fortunately, there is another way to obtain the formulas for the subevent method within the Generic Framework. It will be first demonstrated on the four-particle correlation, showing that using the optimised method will lead to the same formulas as in (2.25) and (2.26).

This method consists of using lower order correlations to construct the final formula for the  $m$ -particle correlation. In order to obtain equation (2.25), one only needs to multiply two two-particle correlations from (2.7),  $N\langle 2 \rangle_{n_1, n_2}^A$  and  $N\langle 2 \rangle_{n_1, n_2}^B$ , where each was calculated independently in subevent A and B. It is again important, that the  $Q$ -vectors entering the formula  $N\langle 2 \rangle_{n_1, n_2}^A$  are only calculated within the subevent A, and  $Q$ -vectors entering the formula  $N\langle 2 \rangle_{n_1, n_2}^B$  are only calculated within the subevent B. Also, the signs of  $n_1$  and  $n_2$  should be the same in subevent A and B, e.g. both positive in A, and both negative in B, or viceversa. The detailed derivation of this formalism is shown in (2.27).

$$\begin{aligned}
N\langle 4 \rangle_{n_1, n_2, n_3, n_4} &= N\langle 2 \rangle_{n_1, n_2}^A \cdot N\langle 2 \rangle_{n_3, n_4}^B = \\
&= (Q_{n_1, 1}^A Q_{n_2, 1}^A - Q_{n_1+n_2, 2}^A) \cdot (Q_{n_3, 1}^B Q_{n_4, 1}^B - Q_{n_3+n_4, 2}^B) = \\
&= Q_{n_1, 1}^A Q_{n_2, 1}^A Q_{n_3, 1}^B Q_{n_4, 1}^B - Q_{n_1+n_2, 2}^A Q_{n_3, 1}^B Q_{n_4, 1}^B \\
&\quad - Q_{n_1, 1}^A Q_{n_2, 1}^A Q_{n_3+n_4, 2}^B + Q_{n_1+n_2, 2}^A Q_{n_3+n_4, 2}^B
\end{aligned} \tag{2.27}$$

Similarly, the 3-subevent method can be obtained as follows:

$$\begin{aligned}
N\langle 4 \rangle_{n_1, n_2, n_3, n_4} &= N\langle 2 \rangle_{n_1, n_2}^A \cdot Q_{n_3}^B \cdot Q_{n_4}^C \\
&= (Q_{n_1, 1}^A Q_{n_2, 1}^A - Q_{n_1+n_2, 2}^A) \cdot Q_{n_3}^B \cdot Q_{n_4}^C \\
&= Q_{n_1, 1}^A Q_{n_2, 1}^A Q_{n_3, 1}^B Q_{n_4, 1}^C - Q_{n_1+n_2, 2}^A Q_{n_3, 1}^B Q_{n_4, 1}^C
\end{aligned} \tag{2.28}$$

It is clear that this procedure results in the same formulas as in (2.25) and (2.26).

Finally, following the strategy introduced above, one can write down the formula for the six- and eight-particle correlations with the subevent method. In eq. (2.29) and (2.30) the 2-subevent methods within the Generic Framework are shown, where the three- and four-particle correlations are in the form of (2.8) and (2.9), respectively.

$$N\langle 6 \rangle_{n_1, n_2, n_3, n_4, n_5, n_6} = N\langle 3 \rangle_{n_1, n_2, n_3}^A \cdot N\langle 3 \rangle_{n_4, n_5, n_6}^B \tag{2.29}$$

$$N\langle 8 \rangle_{n_1, n_2, n_3, n_4, n_5, n_6, n_7, n_8} = N\langle 4 \rangle_{n_1, n_2, n_3, n_4}^A \cdot N\langle 4 \rangle_{n_5, n_6, n_7, n_8}^B \tag{2.30}$$

## 2.3 Performance of the subevent method in simulations

The subevent method was tested on PYTHIA 8 simulation [56, 57] of pp collisions at  $\sqrt{s} = 13$  TeV taken from the ALICE Monte Carlo productions. This is a purely non-flow driven model,

i.e there is no collective flow. Therefore, if the subevent method is able to suppress non-flow contributions, in general, we expect the values of the measurements to decrease.

In Fig. 2.8 (left) the effect of the subevent method on the two-particle cumulant is shown. A clear decrease of  $c_2\{2\}$  can be observed with an increasing  $|\Delta\eta|$  gap. In an ideal case of a complete removal of non-flow contamination, the signal should be suppressed down to 0. These results thus suggest that  $|\Delta\eta| > 1.4$  gap is not enough to remove the short-range correlations completely.

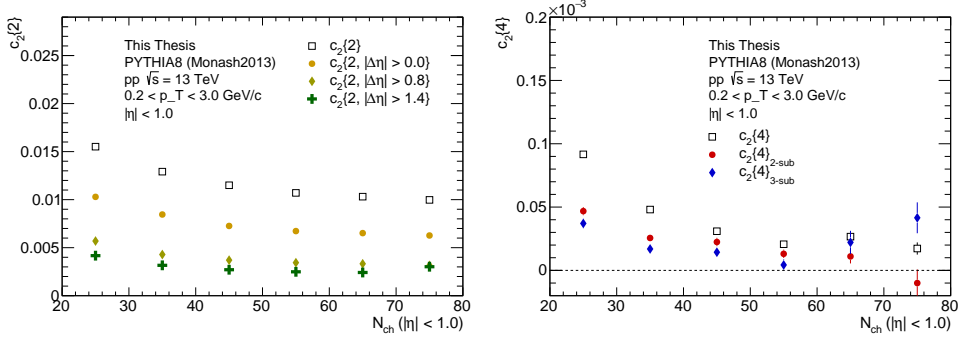


**Figure 2.8:** Left: Multiplicity dependence of  $c_2\{2\}$  (open marker) and  $c_2\{2,|\Delta\eta|\}$  (filled markers) in PYTHIA 8 simulations of  $\sqrt{s} = 13$  TeV pp collisions. A decrease of the signal with increasing  $|\Delta\eta|$  gap is observed. Right: Multiplicity dependence of  $c_2\{4\}$  (open markers),  $c_2\{4\}_{2\text{-sub}}$  (filled red markers) and  $c_2\{4\}_{3\text{-sub}}$  (filled blue markers) in PYTHIA 8 simulations of  $\sqrt{s} = 13$  TeV pp collisions. A decrease of the  $c_2\{4\}$  with the subevent method can be seen.

The right panel of Fig. 2.8 presents the effects of the subevent method on the 4-particle cumulant. A clear decrease of  $c_2\{4\}$  can be seen with the 2-subevent method, and even a further decrease with the 3-subevent method, which shows the ability of this method to suppress non-flow contamination in multi-particle cumulants. The remaining positive signal of  $c_2\{4\}$  suggests that complete removal of non-flow was not achieved. Further increase of the  $|\Delta\eta|$  gap between the subevents, or a 4-subevent method, might remove all non-flow. Such methods are however statistically demanding, and not feasible within the small acceptance  $|\eta| < 1.0$ . In [58], the authors performed these studies on PYTHIA 8 simulation with an artificially injected flow signal of  $v_2 = 0.04$ . They showed that while the standard and the 2-subevent method were not able to reproduce the flow signal, the 3-subevent method is sensitive enough to detect a flow signal as small as 4%.

Similar test was performed with the  $SC(m,n)$  measurements. The results shown in Fig. 2.9 validate the ability of the subevent method to suppress non-flow. On the left, comparison of the standard  $SC(m,n)$  and  $SC(m,n)_{2\text{-sub}}$  is shown. The signal of both  $SC(3,2)$  and  $SC(4,2)$  clearly decreases when the subevent method is employed. The 3-subevent method was tested as well. Its comparison to the results with the 2-subevent method is shown in a separate plot on the right panel for clarity. Within the statistical uncertainties, no significant further decrease is found between the 2- and the 3-subevent method. In [59], larger number of generated events and larger pseudorapidity acceptance allowed to test the method up to 4-subevents. The effects of the subevent method differ from the ones reported here, probably due to the

difference in kinematic cuts. However, the main conclusion is similar to what was made here: the subevent method is able to largely suppress non-flow in the  $SC(m,n)$  measurements.

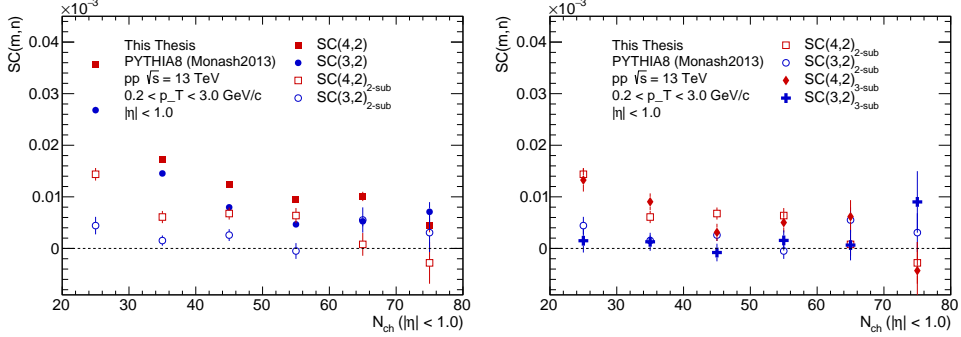
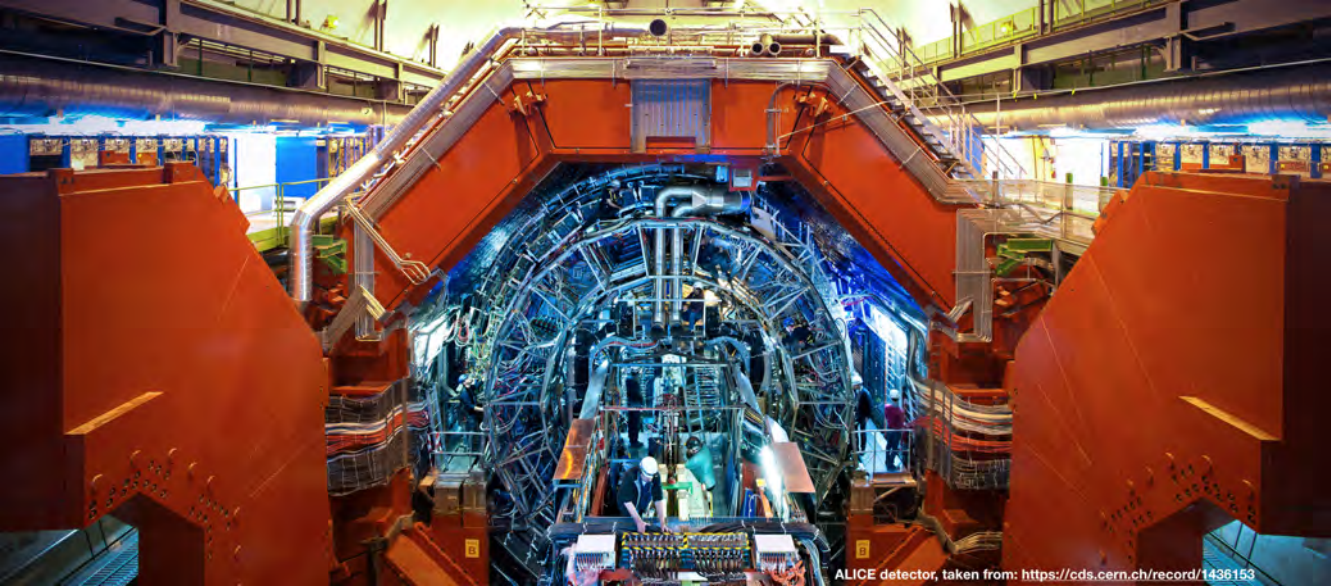


**Figure 2.9:** Left: Multiplicity dependence of  $SC(m,n)$  and  $SC(m,n)_{2\text{-sub}}$  in PYTHIA 8 simulations of  $\sqrt{s} = 13$  TeV pp collisions. A clear decrease of the signal is observed. Right: Multiplicity dependence of  $SC(m,n)_{2\text{-sub}}$  and  $SC(m,n)_{3\text{-sub}}$  in PYTHIA 8 simulations of  $\sqrt{s} = 13$  TeV pp collisions. The two methods produce compatible results within the statistical uncertainties.

The test shown in this section confirms the importance of the subevent method in the measurements exploiting the multi-particle cumulants. The study shown here was using the subevent method implemented in the Generic Framework. Using this particular method in real data analysis has the important advantage of the ability to correct for inefficiencies in the performance of the detector in an efficient way. Simulations with larger  $\eta$  acceptance were also performed in [58, 59].



## 3. Experimental setup

### 3.1 The Large Hadron Collider (LHC)

The data which will be used for the analysis presented in this thesis were taken at the Large Hadron Collider (LHC) [60, 61]. It is the largest hadron accelerator built so far, with a circumference of 26.7 km. It is located in the old tunnel used for a former Large Electron-Positron Collider (LEP) 100 m below the surface (on average), at the border between France and Switzerland, as a part of the CERN accelerator complex. The layout of the LHC is not a perfect circle. Rather, it consists of eight straight sectors and eight arcs. Particles are accelerated in one of the straight sectors, and their trajectory is bent in the arcs. It started its operation in 2009, and since then it almost completed two periods of data taking, called Run1 and Run2, out of at least 5 planned periods.

The LHC performs collisions of protons, protons with lead ions, and collisions of lead ions. The highest energy achieved in a proton-proton collision is  $\sqrt{s} = 13$  TeV, the collision energy of proton-lead is  $\sqrt{s_{NN}} = 5.02$  and 8.16 TeV, and collisions of lead ions have increased the energy from  $\sqrt{s_{NN}} = 2.76$  TeV to  $\sqrt{s_{NN}} = 5.02$  TeV during Run2. Recently, the LHC provided few hours of Xe–Xe collisions at  $\sqrt{s_{NN}} = 5.44$  TeV. Due to the fact that the LHC collides hadrons with the same sign, there are two separate beam pipes in which protons or heavy nuclei circulate separately. The beam pipes intersect at eight different points and in four of these the beams are brought to collide in the four large experiments located at the LHC: ATLAS, CMS, LHCb and ALICE. The first two experiments are dedicated to study rare processes which are accessible in pp collisions and LHCb focuses on detailed studies of B mesons, which contain the heavy  $b$  quark. The ALICE experiment is the only dedicated heavy-ion experiment with the purpose of studying the QGP. It will be described in more details below.

Particles circulate inside the LHC in groups of  $\approx 1.10^{11}$  protons or  $\approx 7.10^7$  lead ions,

called bunches. The LHC can simultaneously accelerate and circulate up to 2808 proton bunches or, alternatively, 600 lead ion bunches. Particles are accelerated to almost the speed of light, thus bunches pass through the intersection points roughly 10000 times per second. Just before the crossing point, bunches are squeezed down to smaller cross sections to increase the probability of a collision. For example, 20 proton collisions occur on average during one bunch crossing at the intersection point in ATLAS and CMS.

Particles are accelerated by an electric field which is contained in the so-called radiofrequency (RF) cavities, distributed along a straight section of the LHC. The trajectories of the particles are bent into a circular path by dipole magnets in the arc sections of the LHC, and quadrupole magnets are necessary to focus the beam. Other types of magnets are used for further corrections, beam injection into the LHC, or further squeezing of the beam immediately before a crossing point. The magnets used at the LHC are superconductive, thus they require constant cooling, which is achieved by a distribution system of liquid helium with the temperature of 1.9 K. In addition, the interior of the beam pipes has to contain as few gas molecules as possible in order to avoid interactions with the particle beam. Therefore, a very high vacuum is maintained inside the beam pipes and at the intersection points where the collisions take place.

An illustration of the layout of the LHC is shown in Fig. 3.1 with highlighted intersection points where the four main experiments are located.



**Figure 3.1:** Illustration of the layout of the Large Hadron Collider [62]. It has 26.7 km long circumference and crosses the border between France and Switzerland. It is buried 100 m below the surface (on average). The LHC provides data to four main experiments, ALICE, ATLAS, CMS and LHCb.

## 3.2 A Large Ion Collider Experiment (ALICE)

ALICE is the only dedicated heavy-ion experiment at the LHC [63]. Its primary goal is to study the QCD matter at extreme conditions of high temperatures and energy densities, where quarks and gluons are no longer confined inside hadrons (the QGP). Such matter can be created in collisions of lead nuclei. ALICE also collects data from pp and p-Pb collisions as a reference to Pb-Pb measurements. The detector is composed of central barrel part located inside a large solenoid magnet with magnetic field up to 0.5 T, and a forward muon spectrometer. Both parts consist of several subdetectors as is schematically shown in Fig. 3.2. The mid-rapidity detectors of the central barrel are the Inner Tracking System (ITS), Time-Projection Chamber (TPC), Transition Radiation Detector (TRD), Time-Of-Flight (TOF), High-Momentum Particle Identification Detector (HMPID), PHOTon Spectrometer (PHOS), ElectroMagnetic CALorimeter (EMCal), and ALICE COsmic Radiation DETector (ACORDE). This list is completed with forward detectors Zero Degree Calorimeter (ZDC), Photon Multiplicity Detector (PMD), Forward Multiplicity Detector (FMD), V0 detector and T0 detector.

Below, the technical parameters of main subdetectors used for the analysis presented in this thesis will be described in detail. Then, a basic description of the track reconstruction and trigger system of ALICE will be given.

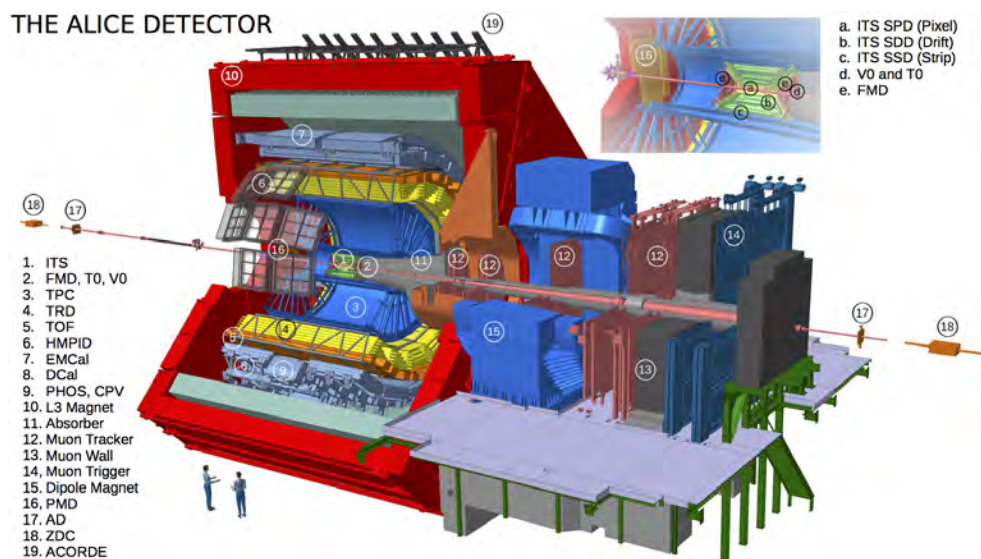


**Figure 3.2:** Schematic view of the ALICE detector during the Run2 data taking [64]. It consists of a central barrel and a forward muon arm. The central part of the detector is contained within a large magnet. The main detectors that will be used for the analysis described in this thesis are the ITS, TPC and V0.

### 3.2.1 Inner Tracking System (ITS)

The Inner Tracking System (ITS) [63, 65] is located in close proximity to the beam pipe, surrounding it in whole azimuth, and having coverage in pseudorapidity of  $|\eta| < 0.9$ . Its main purpose is to estimate the precise position of the primary (i.e. collision) vertex, to improve the resolution of tracks reconstructed in the TPC, to detect decay vertices of heavy flavor particles, such as  $D$  and  $B$  mesons, and also track particles with low momentum, or particles which enter the dead regions of the TPC. It is also able to provide particle identification via the energy loss information,  $dE/dx$ , at low momenta. Apart from these offline capabilities, the inner layers of the ITS are also one of the trigger detectors providing information to the very first level in the trigger decision process (described below in section 3.2.4).

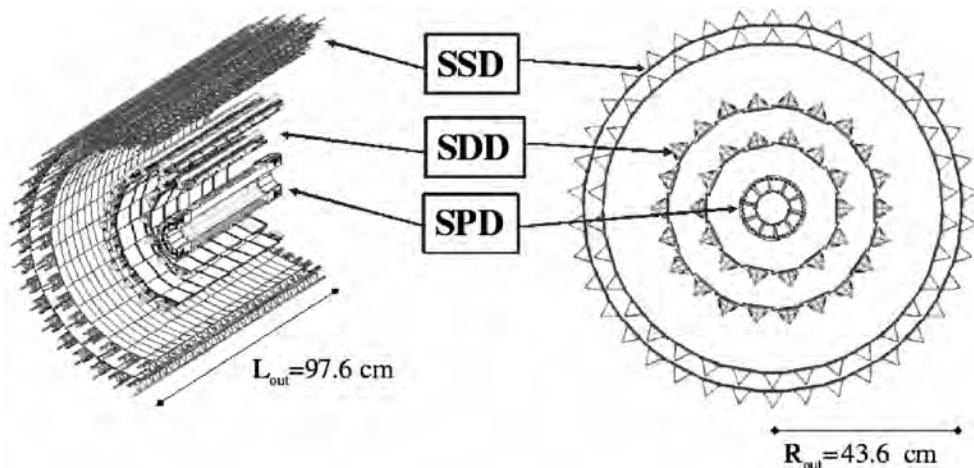


**Figure 3.3:** Schematic view of the ALICE Inner Tracking System (ITS) detector [66]. It is composed of three detectors: the Silicon Pixel Detector (SPD) closely surrounding the beam pipe, then the Silicon Drift Detector (SDD) and finally the Silicon Strip Detector (SSD), furthest from the beam pipe. Each detector consists of 2 layers.

The ITS is composed of 3 different types of detectors, Silicon Pixel Detector (SPD), Silicon Drift Detector (SDD) and Silicon Strip Detector (SSD), each consisting of 2 cylindrical layers with increasing radii, as shown in Fig. 3.3. As already implied by their names, all detectors are based on the principle of a silicon semiconductor detector. The general working principle is the following: an n-type semiconductor detector volume is connected to a reversed bias voltage in order to clean the volume from free charges. When a particle passes through the detector, it transfers energy to the valence electrons of the material which are then able to cross the energy gap to the conduction band. These electrons can then be collected by anodes at the edges of the detector, creating a signal to be read out. In the ITS, different designs of detectors were chosen based on the expected particle density, which is largest at the collision point, and decreasing with increasing radius.

The SPD lies closest to the beam pipe with an average distance of its first layer from the beam pipe of 3.9 cm, and with the second layer at 7.6 cm. The basic building structure of the SPD is a pixel which is split into a matrix of sensitive detector cells connected to a readout

chip, with a dimension of one cell being  $50 \mu\text{m}$  ( $r\phi$ ) by  $425 \mu\text{m}$  ( $z$ ). This cell size is suitable for the high particle density environment where the SPD is located. If a hit is detected in one of the cells, it is assumed to originate from a single particle. Therefore, the SPD is using a binary readout, i.e. output value is 0 unless an incoming signal crosses a set threshold, which changes the output to 1. This fast readout of the SPD provides a good baseline for prompt trigger decisions at the level L0 (described in more detail in section 3.2.4).

The SSD forms the last two layers of the ITS with a radius of 38.0 and 43.0 cm. This detector is important for a smooth continuation of the track reconstruction in the TPC. The principle of this detector is similar to the SPD, only now the low particle density doesn't require the small pixel layout of silicon detectors. The basic element of the SSD is split into strips of a rectangular shape ( $73 \times 40 \text{ mm}^2$ ), each being read out on the edges of the strip. Assuming that a hit in one strip corresponds to one particle, the SSD provides a good spatial precision in the region of lower particle densities.

Finally, the intermediate two layers of the ITS of radius 15.0 and 23.9 cm belong to the SDD. In contrast to the previously described detectors, the SDD is able to provide a two-dimensional spatial information in moderate particle density without the necessity of separation into small pixel cells. One dimension is obtained from the signal readout along the anode strip, and second dimension is obtained from the drift time of the electrons towards the anode. Both SDD and SSD have an analogue readout, which enables to detect the magnitude of deposited charge, as opposed to the simple 1/0 digital signal in the SPD. Therefore, the last four layers of the ITS can be used for measurements of the energy loss,  $dE/dx$ , used for particle identification.

### 3.2.2 Time Projection Chamber (TPC)

The Time Projection Chamber (TPC) [63, 67] is the main and the biggest ALICE detector, whose purpose is to reconstruct particle tracks (thus also to estimate the collision vertex), and to identify particles via  $dE/dx$  measurements. The TPC is a cylinder surrounding the ITS, with its inner radius of about 85 cm, outer radius 250 cm and the length of 500 cm. The TPC covers the whole azimuth, except for small dead regions between its 18 sectors of trapezoidal shape. The pseudorapidity range is  $|\eta| < 0.9$ , which ensures good quality tracks with a lot of space points when combined with the ITS, TRD or TOF detectors. The volume of the TPC is filled with a  $Ne/CO_2/N_2$ , or  $Ar/CO_2$  gas combination. A schematic picture of the TPC layout is shown in Fig. 3.4.

The working principle of the TPC is the following: when a charged particle traverses the volume of the TPC it ionises the gas molecules, thus creating pairs of electrons and positive ions along its trajectory. A uniform electrostatic field is maintained inside the TPC, which causes drift of the created charges; electrons towards the endcap readout chambers, and positive ions towards the central cathode.

The readout chambers of the TPC are based on the Multi-Wire Proportional Chamber detectors with cathode pad readout. The anode wire grid and cathode pads are responsible for the readout of the signal. The electric field close to the anodes is stronger, therefore the drifting electrons will gain enough energy to ionise the gas as well, creating an avalanche onto the anode wire. A corresponding signal is generated on the adjacent cathode pads by capacitive coupling. During the avalanche, significant amount of positive ions are created, which would distort the local electric field or travel back to the sensitive volume of the

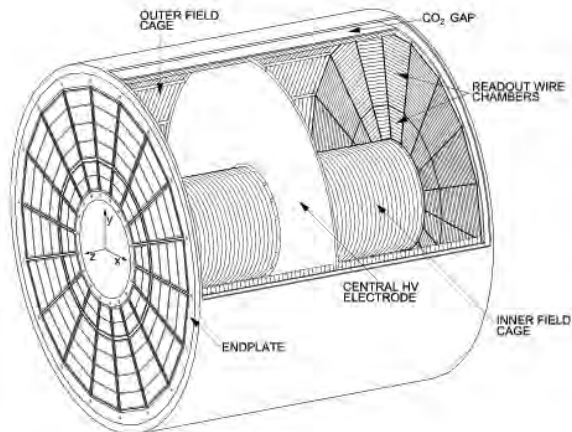


**Figure 3.4:** Schematic view of the TPC [68]. It has a cylindrical shape with inner radius of 85 cm, outer radius 250 cm, and a length of 500 cm. A high voltage cathode is placed in the center, and readout chambers are located at both sides of the TPC. A resistive coating of  $CO_2$  surrounds the TPC in order to isolate the rest of the ALICE detectors from the large electric field inside of the TPC.

detector. Therefore, a grid of cathode wires is placed in front of the anode plane to collect the positive charges created during the avalanche. Finally, a gating grid is placed in front of the cathode plane. This grid opens in case a collision needs to be recorded and electrons from the drift region can enter the amplification region to be read out, otherwise it remains closed and prevents electrons from entering. A set of cathode pads are associated with each anode wire, therefore they provide a projected  $r - \phi$  plane information (see example in Fig. 3.5). The dimension along the beam direction is given by the drift time of the electrons. In this way, the TPC can provide up to 159 space points corresponding to one track. Based on the detected signal strength, it is also possible to measure the energy loss of the incident particle, used for particle identification.

The choice of a suitable gas mixture is crucial in order to ensure an undisturbed drift of the electrons towards the readout chambers. In ALICE, the components of the gas provide good transport properties for the drifting electrons, quenching capability to absorb high energy photons from the avalanche which might have enough energy to further ionise gas molecules, and a potential to have high gas gain, thus high signal amplification. The gas is constantly circulating and cleaned in order to flush away impurities, such as oxygen, which would attach the drifting electrons and cause a loss of signal. During the years of ALICE operation, the gas mixture has been changed few times from  $Ne/CO_2/N_2$  to the combination of  $Ar$  and  $CO_2$ . The Argon component has been chosen to maintain better high voltage stability. However, problems with drift field distortions arose and caused that the electrons did not drift towards the endcaps along a straight trajectory, thus affecting the readout precision. Based on the ALICE gas composition, the maximum electron drift time might vary, but usually it is around  $90 \mu s$ .

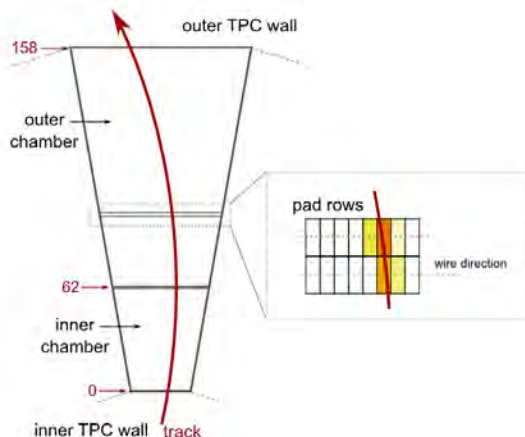


**Figure 3.5:** Illustration of the signal readout in the TPC (side view on the transverse  $r - \phi$  plane) [69]. The incident particle (track) traverses the TPC and ionises the gas molecules. The created electrons drift towards the endcap readout chambers, where the position of the signal is determined from the position of the anode wire and the readout pad.

The drift velocity can vary depending on the temperature and pressure conditions (especially sensitive for the gas mixture used in ALICE) or imperfections of the electric field inside the TPC. A regular calibration of the TPC coordinate in the  $z$  direction (direction of the beam) is therefore important in order to provide precise coordinates to the readout. This is done by the TPC laser system, which distributes straight laser lines through the whole TPC volume in planes perpendicular to the  $z$  direction. The photons of the laser do not have enough energy to ionise the original gas mixture, but the energy of two photons is enough to ionise the gas impurities and to create charges which drift towards the endcaps and are detected. Because of the well known positions of the laser planes, a pre-defined drift time is expected, and drift variations with respect to the default time are then measured and used for calibration.

### 3.2.3 VZERO (V0)

The V0 detector [63, 70] is composed of two scintillator arrays, V0A and V0C. The arrays are located on the opposite sides of the collision point in the  $z$  direction at the distance of 329 cm for the V0A and -86 cm for the V0C. The V0A covers the pseudorapidity range of  $2.8 < \eta < 5.1$ , and the V0C  $-3.7 < \eta < -1.7$ . Both arrays of the V0 are composed of four rings in the radial direction divided into 32 segments in total, as shown in Fig. 3.6. The minimum and maximum radii of the V0A are 4.3 cm and 42.2 cm, and 4.5 cm and 32 cm for the V0C. The V0A and V0C arrays are not placed symmetrically around the collision vertex due to the spatial constraints imposed by the hadron absorber of the muon arm. The main purpose of the V0 is to provide a minimum-bias trigger (in Run2 also the high multiplicity trigger in pp collisions) for the central barrel detectors, help to reject events not originating from a collision (e.g. interaction of the beam with the residual gas in beam pipe), determine

centrality of a collision, and help to measure the beam luminosity.

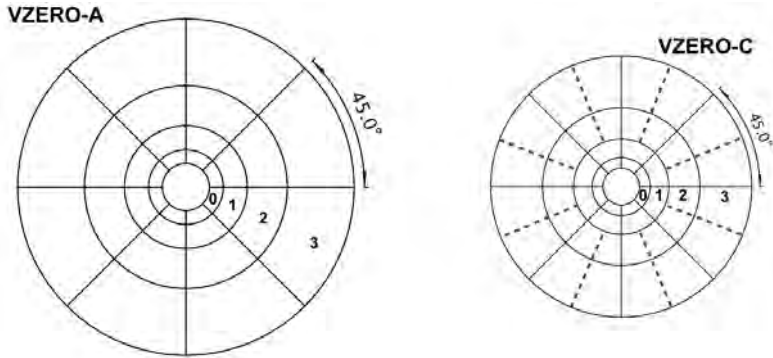


**Figure 3.6:** Illustration of the layout of the V0 detector rings [70]. Both V0A and V0C rings are scintillator counters divided into 4 rings, where each is further divided into 8 segments. The V0C is located closer to the interaction point and has smaller diameter due to spatial constraints from the hadron absorber of the muon arm. The scintillator segments split by the dashed lines are connected to the same photomultiplier.

When a particle traverses the scintillator counter of the V0, it excites the material, which emits photons at deexcitation. These photons are transmitted to a photomultiplier (PMT), where they are converted to an electric signal, which can then be read out. The response of scintillating detectors is fast, which makes them suitable trigger detectors. The PMT consists of a photocathode, a system of dynodes, and finally an anode which is connected to the readout electronic system. The photocathode is optically connected to the scintillating material via optic fibers. It is adjusted to the typical photon wavelength of the scintillating material in order to convert the incoming photon to an electron via the photoelectric effect. High voltage applied inside the PMT then directs the electron towards the system of dynodes. The electron transfers some energy to a dynode, causing more electrons to be emitted, which repeat the process at the next dynode, etc. In this way, the original signal is amplified and read out once the electrons hit the collection anode.

### 3.2.4 Capabilities of the ALICE detector

#### Track reconstruction

The main detector designed for the track reconstruction in ALICE is the TPC, which occupies a large fraction of the volume of the ALICE detector. In addition, more information provided by the ITS improves the reconstruction of decay vertices of heavy flavor and strange particles and tracking of particles with low momentum. Usually, the tracking includes both the ITS and the TPC. The tracking algorithm starts with the determination of the collision vertex using the hits information in the SPD by a linear extrapolation to the ALICE center. Once the vertex is established, the tracking begins in the outer part of the TPC with lower track density by connecting the space points (seeds) towards the ITS. This process is done using the Kalman filter [71], which consists of careful point-to-point extrapolation of the track. At the innermost edge of the TPC the track propagation continues to the ITS, until it reaches the innermost

layer of the SPD. Then, the procedure is reversed and the track finding algorithm continues from the ITS towards the outer radius of the TPC, this time having more precise information. At this stage, the tracking might continue beyond the TPC, including TOF, TRD, HMPID or PHOS matching. Eventually, the procedure is reversed for the last time, and the found tracks are refitted all the way to the reconstructed collision vertex, providing information about the distance of closest approach of the track to the vertex [63].

### Triggering

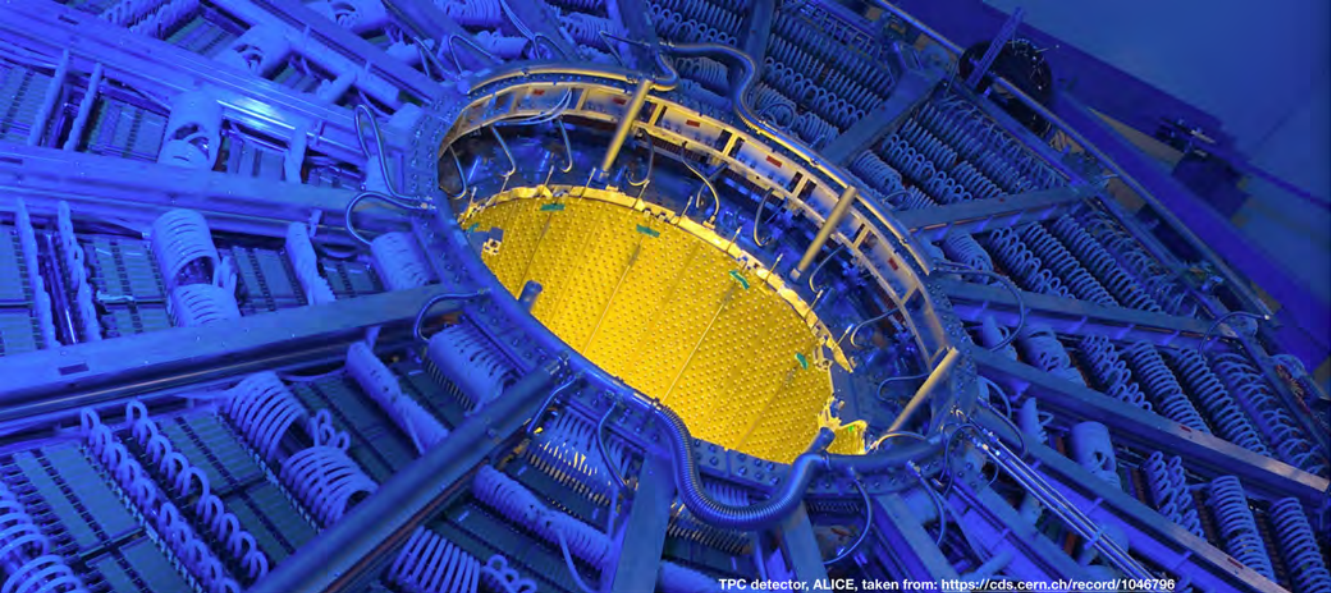
Collisions at the LHC occur at a high rate, which in combination with different detector readout times and speed of the electronics readout systems, not to mention the limited storage for the data, makes it impossible to record every single collision. For this purpose, a trigger system was developed in order to select and store only interesting physics events. In ALICE, the trigger system [63, 72] can operate at collision rates of roughly 8 kHz for Pb-Pb collisions and up to 300 kHz for pp collisions. It has to be adjusted not only to the different rates, but also to different multiplicities and thus size of the data from different collisions, taking into account different detector response times.

The main part of the ALICE trigger system is the Central Trigger Processor (CTP), which collects input data from the trigger detectors, makes a decision about whether to take or reject the event, and in case of a positive decision sends the signal back to the detectors to start the readout. Considering the very high collision rate, such decisions have to be made in a short time period. In ALICE, the trigger decision is split into 3 levels: L0, L1 and L2. The L0 trigger level makes its decision based on only a small amount of information from a fraction of detectors with fast response, and sends the decision back to detectors in  $1.2 \mu\text{s}$ . The L1 trigger decision is based on all remaining fast detector inputs, and the trigger decision arrives back into detectors in  $6.5 \mu\text{s}$ . The final L2 trigger level waits for all the detector readouts, including the slowest TPC detector, thus it happens in about  $90 \mu\text{s}$  time. The L2 trigger level also includes a so-called past-future protection which makes sure that the event selected by the L0 and L1 trigger is not contaminated by pile-up events (multiple events that occur within a short time window, thus have an interaction vertex within the ALICE acceptance and tracks from such events are mixed with tracks from the triggered event).

During the data taking, the trigger system can be set to more than just one configuration, i.e. a trigger class. A trigger class defines which trigger detectors are required to have a certain logical combination of a signal in order to select an interesting event of some specific properties, thus it defines the input to the CTP. It is convenient to have several trigger classes active during the data taking: while waiting for a rare type of collision such as high multiplicity pp collisions, we can take e.g. more common minimum-bias type of events.

Finally, once an event passes all the trigger decisions of the CTP, it is further sent to the Data Acquisition System (DAQ) which redistributes it for more detailed processing and compression of the final data, which will then be stored on a permanent storage and become available for the final user analysis.





TPC detector, ALICE, taken from: <https://cds.cern.ch/record/1046796>

## 4. Data processing and selection

The LHC experiments produce on average 30GB of data per second [73]. This is already after the trigger selection of only collisions of interest, as was described in the previous Chapter 3. It would not be possible to process and store such a large amount of data at a single computing centre. Therefore, the LHC experiments share many computing centres distributed in different countries around the world, which are coordinated by the Worldwide LHC Computing Grid (WLCG) [73], or simply Grid. It consists both of storage and computing centres. All the data coming from the experiments are first directed to the so-called Tier-0 centre, the largest of the WLCG computing centres, which is located at CERN. Recently, an extension of the Tier-0 has been constructed at the Wigner Research Centre for Physics in Budapest. Here, the raw data are stored at the permanent data storage consisting of magnetic tapes called CASTOR. Also, the first data processing is performed at the Tier-0. A copy of this data is immediately transferred, re-processed and stored at the Tier-1 centres located outside of CERN. Further data reduction, simulations and final user analyses are done at Tier-2 centres. There are 13 Tier-1 centres and around 160 Tier-2 centres around the world.

The data that arrive from the detectors are in the form of the detector outputs from the electronics, the so-called *raw data*. These need to be further processed, e.g. by doing the track reconstruction in the TPC, as was described previously in section 3.2.4. The collected information are eventually stored in the form of Event Summary Data, commonly referred to as ESD files, or ESDs. In general, ESD format can be used for end-user analyses. However, ESDs still contain large amount of information, which consume large amount of memory on the storage disks, and negatively affect the performance of analysis calculations. The ESDs are then compressed and stored into Analysis Object Data (AOD), which are a preferred format for the final user analysis. The data are saved and read by the ROOT program based on the C++ language, which was developed for the purpose of the collider experiments. One ROOT file usually contains information about several thousands of events and its size is up

to a few hundred MB. In a data analysis, usually hundreds, or thousands of such files are used. Local computing power or memory is not enough to perform calculations over such a large amount of files. Therefore, user analysis is also done on the Grid by distributing the user tasks on small fractions of the overall data sample in the form of jobs that are processed at the above mentioned Tier-2 centres. Every day, almost 2 million jobs are running on the Grid. The final output of the user analysis is then usually small enough (few hundred KB or MB) to be stored locally and used for the final physics interpretation. For the purpose of data reconstruction and user analyses, individual collaborations usually develop their own ROOT extensions to account for detector-specific requirements. In case of ALICE, two separated frameworks are developed, AliRoot and AliPhysics. AliRoot is used during data processing and reconstruction, and contains common classes used by every user analysis, while AliPhysics stores codes of individual tasks of final users. In AliPhysics, each user task is implemented as a single C++ class object. AliPhysics is updated daily, while updates of AliRoot happen less frequently.

The final user analysis task must always specify the desired AOD (ESD) files. The files are logically organised according to a scheme which is going to be described here. During the data taking, when the LHC is colliding bunches of protons or heavy ions, the experiments are ready and collecting these collisions, called *events*. However, sometimes it can happen that a detector experiences problems, such as overheating of the electronics. In that case, the data taking has to be interrupted in order to recover the affected detector. Apart from these unexpected interruptions, intended breaks in the data taking are also made in case some modifications in the software or detector settings needs to be done. A period when the experiment is recording collisions, is called *run* with a specific set of six identifying numbers. When the experiment is ready to take data again, a new run with a new identifier is began. The runs are further grouped into *periods*, which usually define a time segment in the data taking with specific settings. For example, this might include a change in the colliding system, or collision energy. The list of available periods and corresponding run numbers are summarised and checked for quality by experts, and then provided to the users.

In the analysis presented in this thesis, data from pp collisions at  $\sqrt{s} = 13$  TeV, p-Pb at  $\sqrt{s_{NN}} = 5.02$  TeV, Xe-Xe at  $\sqrt{s_{NN}} = 5.44$  TeV, and Pb-Pb collisions at  $\sqrt{s_{NN}} = 5.02$  TeV are used, all collected during the LHC Run 2 data taking. The periods used for each collision system are summarised in Table 4.1.

Collision system	Collision energy	Period
pp	$\sqrt{s} = 13$ TeV	LHC16k, LHC16l, LHC16o LHC17m, LHC17o
p-Pb	$\sqrt{s_{NN}} = 5.02$ TeV	LHC16q, LHC16t
Xe-Xe	$\sqrt{s_{NN}} = 5.44$ TeV	LHC17n
Pb-Pb	$\sqrt{s_{NN}} = 5.02$ TeV	LHC15o

**Table 4.1:** List of collision systems and corresponding periods used for the analysis presented in this thesis.

## 4.1 Event selection

Events collected during the data taking were selected based only on very basic information in order to allow for fast trigger decisions. Further offline selection is done based on the quality assurance (QA) for each detector participating in the run to check for apparent faults in data. Events that are stored should serve for all possible types of analyses, therefore more thorough selection is done at the user level to suit the purpose of the particular analysis. In ALICE, a common framework of event cuts suitable for most of the analyses has been developed to facilitate the work. It will be described in more details in this section.

First, events with the desired trigger type are selected. In this analysis, the minimum-bias trigger was chosen for most of the data sets. In pp collisions, a dedicated high multiplicity trigger is chosen in order to reach higher range of multiplicity in the analysis. The minimum-bias trigger (kINT7) selects events based on at least one hit in both arrays of the V0 detector (V0A and V0C). In addition, the high multiplicity trigger (kHighMultV0) requires that the number of hits in V0A and V0C are above a certain threshold. The triggered events are further cleaned up from a remaining contamination by an additional set of cuts in the offline selection. All the event cuts that will be described below are implemented in a common framework called AliPhysicsSelection and AliEventCuts, which is maintained by experts centrally within ALICE to keep consistent event selection for most of the analyses.

### 4.1.1 Rejection of background and pileup events

Events that are not suitable for data analysis can be divided into two groups. Background events which originate from interactions of the beam with the remaining gas in the beam pipe, and pileup events which occur within the short time window of the reconstruction of the triggered event, resulting in mixing particles from different collisions. The later can be further grouped into same-bunch and out-of-bunch pileup. As the name suggests, the same-bunch pileup are events occurring during the same bunch crossing, and out-of-bunch pileup are events that come from different bunch crossings shortly after/before the triggered event.

#### Rejection of background events

A background interaction usually occurs outside of the central region of the detector, therefore the tracks originating from these events will cross the SPD almost parallel to its layers. This results in a large number of SPD pixels being hit, forming a large number of clusters. The tracks which would be reconstructed from these clusters would not point to the main collision vertex in the center of the detector. It is assumed that an event with a small number of tracks but a large number of clusters in the SPD would thus come from background effects. Therefore, correlation between the number of fired clusters in the SPD and so-called tracklets in the SPD (simple tracks obtained by fitting the signal in the two SPD layers and the position of the collision vertex) will help to reject background events. Further rejection can be done using the information from the V0 detector. An event with a low number of SPD tracklets but a large multiplicity in the V0 is a candidate for background interaction occurring far away from the ALICE central interaction point. Therefore, another set of cuts using the correlation between the multiplicity in V0 and the SPD tracklets, and the correlation between the multiplicity in the three inner and one outer ring of the V0, are applied.

### Rejection of pileup events

Due to the high interaction rate during the data taking, triggered events cannot be completely isolated from the pileup, thus additional offline event selection is necessary to determine which tracks correspond to the desired triggered event. The following set of cuts is applied in pp and p–Pb collisions, because they suffer from pileup the most. The out-of-bunch pileup can be rejected by exploiting the fact that the V0 detector is able to record  $\pm 10$  events around the triggered event. Thus, if an additional activity is observed in the V0 within the SPD readout time, that event is rejected. In addition, another 2 cuts to remove out-of-bunch pileup are applied using two of the trigger detectors, V0 and SPD. We distinguish online and offline signals of these detectors. The online signal is fast, used for the L0 trigger decision evaluations (described in section 3.2.4). The offline signal contains the full information after the total charge collection whose evaluation requires more time, thus it can catch signal from another incoming collision. Therefore, the correlation between the online and offline V0 signal, and the correlation between the online and offline SPD signal, are used to reject pileup events. Finally, same-bunch pileup events can be removed based on multiple reconstructed collision vertices with the SPD detector. Tracks that do not originate in the vertex of the triggered event are then used to estimate another possible vertex. If more than one vertex satisfying a set of criteria (number of tracks that point to the vertex, distance from the main vertex, etc.) is found, the event is rejected as a pileup event. Finally, a similar cut using full tracks reconstructed in the ITS and TPC is applied for further pileup rejection.

In heavy-ion collisions, a set of cleanup cuts is applied based on the correlation between different centrality estimators, or different track type multiplicities. Cut on the correlation between the number of ESD tracks and the number of tracks using only the TPC information removes events with worse tracking performance, which is caused by a large number of TPC clusters that are fired by tracks from pileup events. A cut on the correlation between the number of tracks with ITS+TPC information and the same tracks with additional matching with the TOF detector is used to reject tracks originating from an out-of-bunch pileup event. Such tracks will be shifted in the slow drift detectors like the TPC, therefore events with a large number of tracks not matched with the TOF detector are rejected.

#### 4.1.2 Collision vertex selection

The collision vertex is determined from reconstructed tracks in the detector by estimating their common point of origin. A cut on the number of track contributors to the vertex estimation to be  $> 1$  rejects events without any collision vertex. The vertex can be estimated either by using the fully reconstructed tracks (including the TPC information), or based on only the SPD, which is closest to the collision point. In a properly reconstructed vertex these two approaches should yield similar result. Thus, a cut on the correlation between collision vertices estimated using these two methods is applied. Finally, vertices with poor spatial resolution below a set threshold are removed.

After the event cuts,  $310 \cdot 10^6$  high multiplicity pp collisions were selected for the analysis, as well as  $230 \cdot 10^6$  p–Pb,  $1.3 \cdot 10^6$  Xe–Xe and  $55 \cdot 10^6$  Pb–Pb minimum-bias collisions.

### 4.1.3 Effects of the high multiplicity trigger in pp collisions

In pp collisions, events with large multiplicity are of special interest. In order to enhance the abundance of high multiplicity events, a dedicated trigger has been used. However, the fact that events with high multiplicities were selected using the V0 detector at forward rapidity has an effect on the cumulant measurements presented in this thesis which was done using the ITS and TPC information (i.e. the mid-rapidity region). The reason is that in small collision systems the number of particles at mid-rapidity is weakly correlated (with large spread) with the number of particles detected at forward rapidity. The lack of correlation is illustrated in Fig. 4.1, by plotting the number of tracks in  $|\eta| < 0.8$ ,  $M(|\eta| < 0.8)$ , as a function of the multiplicity in the V0 detector normalised to the mean V0 multiplicity,  $V0M/\langle V0M \rangle$ . The left panel shows kINT7 triggered events in order to demonstrate the full scale of the relation between the multiplicities, while the right panel shows the kHighMultV0 trigger. The large spread of the correlation between the observables is apparent. It can also be observed that the kHighMultV0 selects high multiplicity events above a preset threshold of the multiplicity in the V0 detector, which can be translated as  $V0M/\langle V0M \rangle > 4$  (from the right panel of Fig. 4.1).

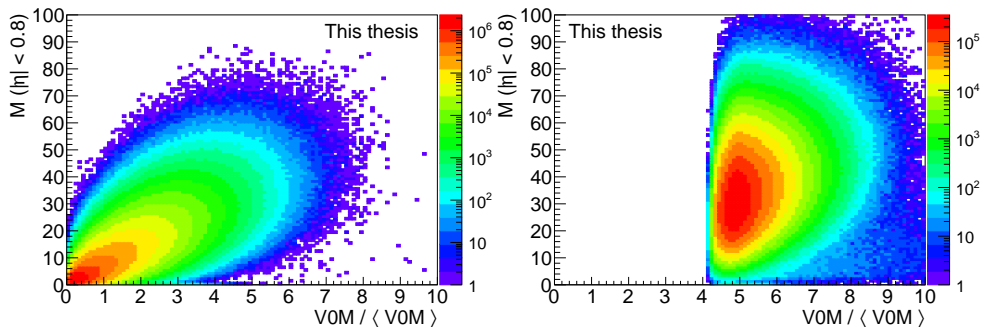


**Figure 4.1:** Distribution of the number of tracks at mid-rapidity,  $M(|\eta| < 0.8)$ , vs.  $V0M/\langle V0M \rangle$  for the kINT7 trigger (left) and for the kHighMultV0 trigger (right). The cut on  $V0M/\langle V0M \rangle > 4$  in kHighMultV0 is apparent.

The naïve procedure to enhance the high multiplicity region for results presented as a function of multiplicity at mid-rapidity (as is done in this thesis) would be to determine the point from where the results from the minimum-bias trigger can be extended with the results from the high multiplicity trigger. In other words, the observable, or the multiplicity distribution from both triggers, should start to overlap at some point. This is not the case in Fig. 4.2, where the multiplicity distribution at mid-rapidity is shown for kINT7 and kHighMultV0 trigger on the left panel, and their ratio on the right panel. The distributions on the left are normalised to the integral between  $M = (60, 80)$  in order to demonstrate the difference in the slopes at high multiplicity. This is shown better with the ratio of multiplicities from the kINT7 to the kHighMultV0 on the right, which does not reach a flat multiplicity dependence at any point. These figures show that the high multiplicity trigger results cannot be simply appended to the minimum-bias results. Instead, the measurements from the high multiplicity trigger can

be treated as measurements with an additional event selection of  $V0M/\langle V0M \rangle > 4$ . The effect of this selection on an actual measurement can be seen in Fig. 4.3 (left), where a measurement of two-particle cumulant,  $c_2\{2\}$ , as a function of multiplicity at mid-rapidity is shown for the two triggers. As in the case of the multiplicity distributions, the  $c_2\{2\}$  measurements do not overlap at any point.

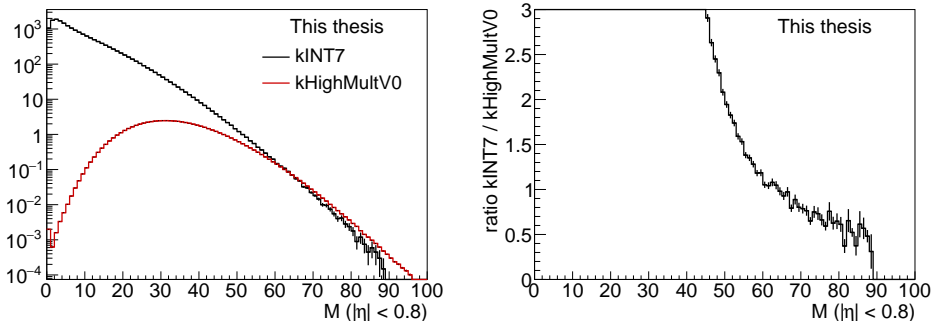


**Figure 4.2:** Left: Distribution of number of particles (tracks in ITS+TPC) from the kINT7 trigger (black color) and the kHighMultV0 trigger (red color). The distributions are scaled by the integral between  $M = (60, 80)$ . Right: Ratio of the number of particles from the kINT7 trigger to the kHighMultV0 trigger. The ratio is not constant, showing that there is no region of multiplicity where the two triggers would give similar results.

In order to demonstrate that the results from the kHighMultV0 trigger can indeed be considered as events with one additional event cut, the high multiplicity trigger was replayed in the minimum-bias data sample and compared to the results from the kHighMultV0 trigger. The trigger was mimicked by applying the above mentioned cut  $V0M/\langle V0M \rangle > 4$  to the kINT7 data. The result of this selection on the measurements of  $c_2\{2\}$  is shown in Fig. 4.3 (right). While the result from default minimum-bias data sample was different from the high-multiplicity triggered sample on the left panel, the measurements are compatible with each other after the additional event selection (right panel). This shows that indeed the effect of the high multiplicity selection with the V0 detector can be explained by the additional event cut  $V0M/\langle V0M \rangle > 4$ . The same check that was done for the  $c_2\{2, |\Delta\eta| > 1.4\}$ . After the suppression of non-flow with the  $|\Delta\eta|$  gap, results from the kINT7 and kHighMultV0 triggers are roughly compatible (left panel of Fig. 4.4). With the additional mimicked high multiplicity event selection in the minimum-bias data, the results remain being compatible (right panel of Fig. 4.4), although with large statistical fluctuations in the kINT7 results. This observation suggests that the high multiplicity trigger is able to suppress non-flow correlations.

## 4.2 Track selection

After the event selection, a selection of tracks, suitable for the desired analysis, follows. Tracks with high quality can be selected based on a set of cuts which are going to be described in the following. The so-called *global tracks* are chosen for the analysis presented in this

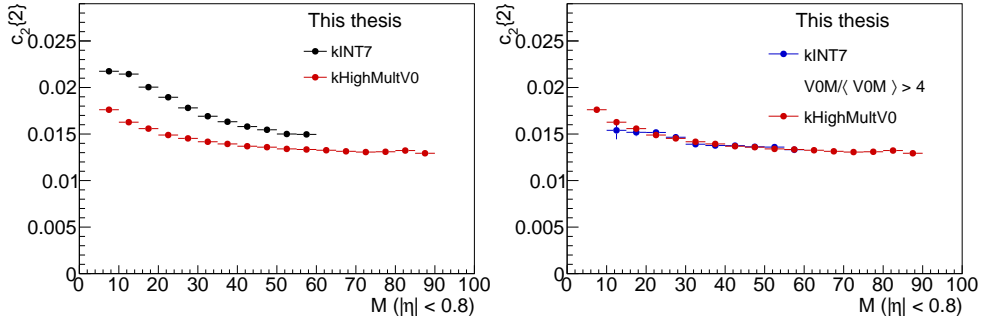


**Figure 4.3:** Left:  $c_2\{2\}$  as a function of multiplicity at mid-rapidity for the kINT7 and the kHighMultV0 trigger. The results of kINT7 trigger are systematically higher than from the kHighMultV0 trigger. Right:  $c_2\{2\}$  for the kHighMultV0 trigger and the kINT7 trigger after the cut  $V0M/\langle V0M \rangle > 4$ .

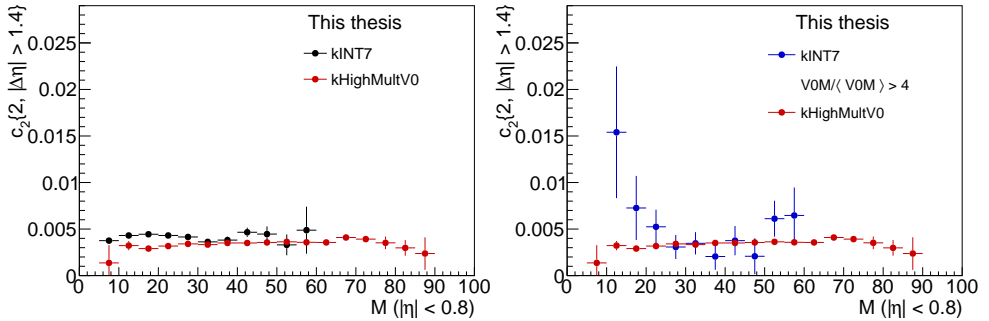


**Figure 4.4:** Left:  $c_2\{2, |\Delta\eta| > 1.4\}$  as a function of multiplicity at mid-rapidity for the kINT7 and the kHighMultV0 trigger. Right:  $c_2\{2, |\Delta\eta| > 1.4\}$  for the kHighMultV0 trigger and the kINT7 trigger after the cut  $V0M/\langle V0M \rangle > 4$ .

thesis, which require information from both ITS and TPC detectors. Tracks that provide good approximations to the real particle trajectory are selected by the following cuts, implemented in the ALICE software:

- Minimum number of 70 TPC clusters used for the track fit
- Maximum  $\chi^2$  of 4 of the track fit per TPC cluster
- At least one hit in the SPD detector
- Maximum  $\chi^2$  of 36 of the track fit per ITS cluster
- Cut on the distance of closest approach in the longitudinal direction  $|DCA_z| < 2$  cm

- Cut on the distance of closest approach in the transverse plane  $|DCA_{xy}| < 0.0182 + 0.0350/p_T^{1.1}$
- Requirements of a converged track fit during the final step in the track reconstruction procedure.

In addition to the quality assurance of the tracks, kinematic cuts of  $|\eta| < 0.8$  and  $0.2 < p_T < 3.0$  GeV/ $c$  are applied. The cut in pseudorapidity is used in order to assure that the whole volume of the TPC will be used for the data analysis without a significant drop of efficiency at the edges, which would require larger corrections to the results. The lower  $p_T$  cut is applied in order to reject tracks with low tracking performance, and the upper  $p_T$  cut is used to remove contributions from hard processes to the analysis results. The distributions of the basic variables for tracks that will be used in the analysis are shown in Fig. 4.5.

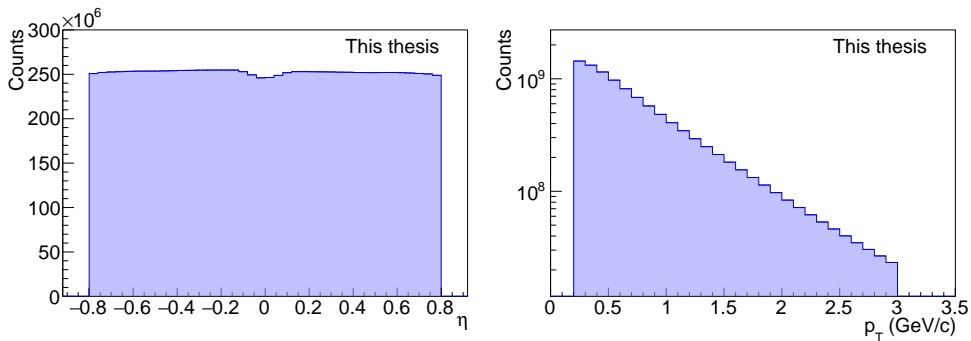


**Figure 4.5:** Track distributions from 13 TeV pp collisions after all the event and track cuts. Left: Distribution of pseudorapidity  $\eta$ . Right: Distribution of the transverse momentum  $p_T$ .

## 4.3 Compatibility between different periods

If multiple periods for a given collision system are available, it is desirable to combine them in order to increase the statistical stability of the results. However, division of the collected data into periods is usually caused by a change in the data taking conditions, as was explained at the beginning of this chapter. Therefore, before the data samples from different periods are combined together, it is necessary to check whether the measurements are compatible with each other. The data used in this analysis consist of 2 periods of p–Pb collisions, and several periods of pp collisions. Below, the compatibility of results from these periods will be checked individually for the two collision systems. The Xe–Xe and Pb–Pb collisions were taken within a single period. Therefore, they are not included here.

### 4.3.1 pp collisions

The high multiplicity trigger selects events based on the multiplicity in the V0 detector, as was discussed in section 4.1.3. This detector however suffers from ageing effects, which causes a

degradation of the trigger efficiency. For this purpose, thresholds for the high multiplicity trigger have been adjusted by increasing the cut on  $VOM/\langle VOM \rangle$ . In section 4.1.3 it was shown that cutting on  $VOM/\langle VOM \rangle$  has effects on the results presented in this thesis. Thus, it is natural to check whether the changes of the trigger threshold, which usually happens in different periods, have any significant effect on the observables.

In Fig. 4.6 (left) the ratio of  $c_2\{2\}$  from different periods with respect to the LHC16k period, which has a large number of events, is shown as a function of multiplicity at mid-rapidity. Small deviations of the order of few percent can be observed in some periods, rising up to 4% for the LHC16p period. Periods which show less than 1% of deviation with respect to the LHC16k period were considered for the data analysis. The selection of these periods was also based on whether they contain a significant amount of collected statistics, and whether their full reconstruction was available at the time of performing the analysis. These periods are: LHC16k, LHC16l, LHC16o, LHC17m and LHC17o. These periods account for  $\approx 80\%$  of the statistics available at the time of performing this analysis. In Fig. 4.6 (right), it is shown that the reported difference in  $c_2\{2\}$  is caused by the change in the trigger threshold. In this figure, the  $VOM/\langle VOM \rangle$  distribution normalised to the integral between  $VOM/\langle VOM \rangle = (6, 10)$  is shown for different periods: while all the periods selected for the data analysis are compatible, the rest of the periods have a different starting point.

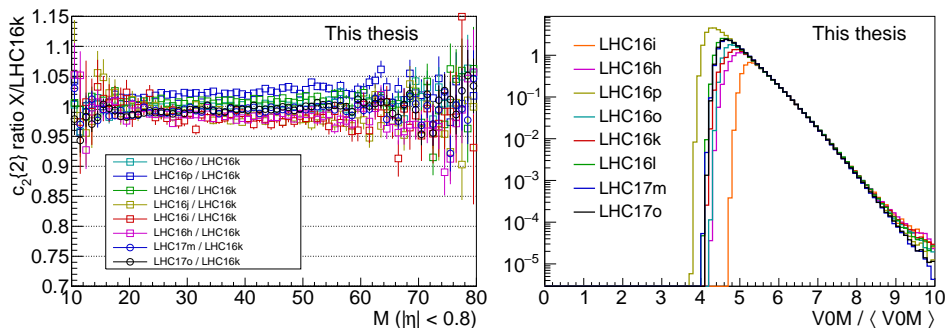


**Figure 4.6:** Left: Ratio of  $c_2\{2\}$  from different periods to the LHC16k period. The effect of the rising trigger threshold due to V0 ageing is visible based on the deviations of the measurements from different periods with respect to the chosen default LHC16k period. Right: Comparison of  $VOM/\langle VOM \rangle$  distributions for different periods. Periods which were chosen to be combined for final data analysis show similar thresholds of the high multiplicity trigger.

### 4.3.2 p–Pb collisions

The data sample of collisions of a proton and a lead nucleus do not suffer from the V0 ageing effects since the data were taken only with the minimum-bias trigger, which does not include any threshold on the V0 multiplicity. This dataset consists of two periods, which are separated by a few weeks time, because the LHC machine was running the p–Pb collisions at  $\sqrt{s_{NN}} = 8.16$  TeV in the meantime. Due to this interruption, it is necessary to check whether the results from the two periods, LHC16q and LHC16t, are compatible.

Figure 4.7 (left) shows the ratio of  $c_2\{2\}$  from LHC16t to LHC16q period as a function of multiplicity at mid-rapidity. Even though some statistical fluctuations are present due to the small amount of events collected in the LHC16t period, the ratio is compatible with unity. Therefore, the datasets can be combined and used for the analysis. For completeness, the distribution of the  $V_0M/\langle V_0M \rangle$  for the two periods is shown in right panel of Fig. 4.7. Since there is no selection applied on the  $V_0$  multiplicity, the distributions can be shown down to low multiplicities. Similar to  $c_2\{2\}$ , the  $V_0M/\langle V_0M \rangle$  distributions are compatible for the two periods in p–Pb collisions.

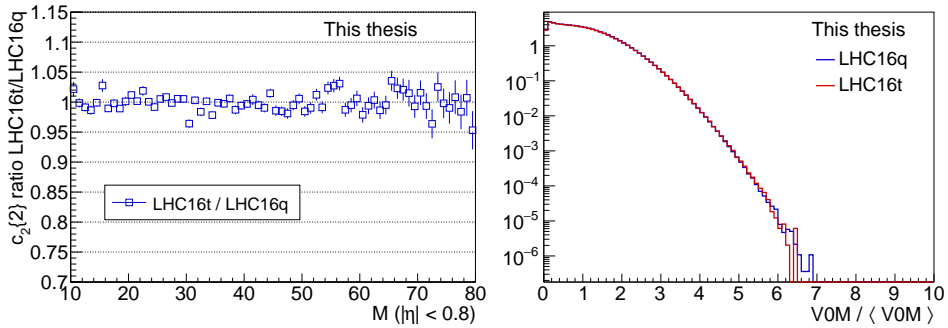
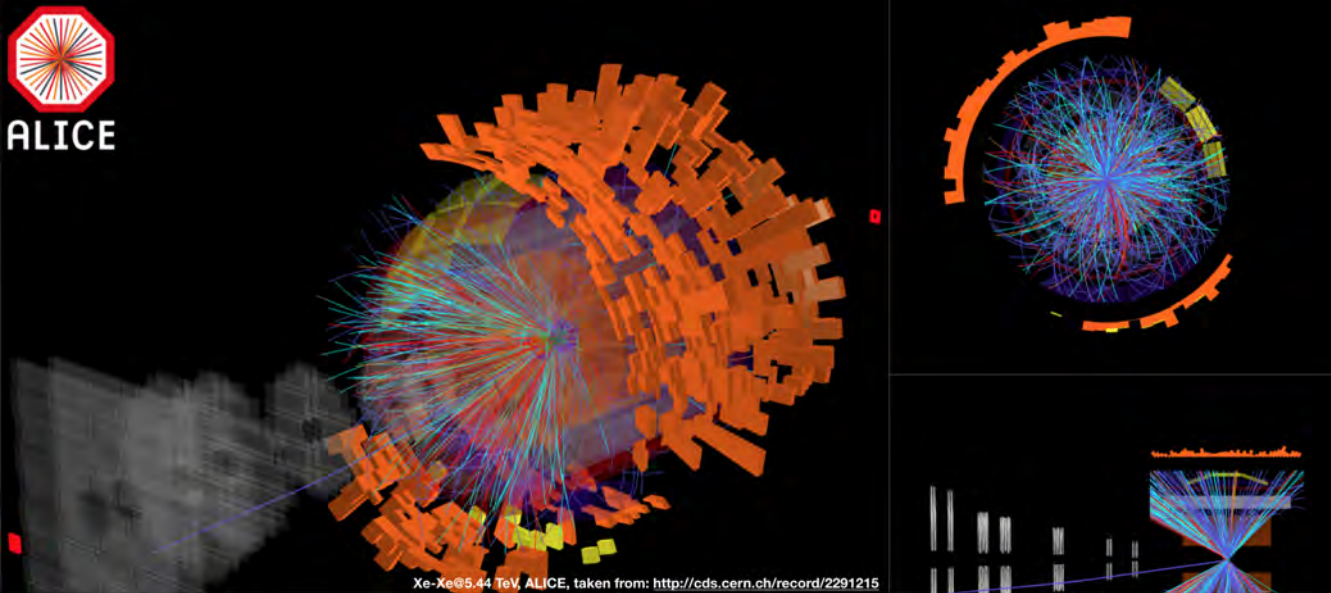


**Figure 4.7:** Left: Ratio of  $c_2\{2\}$  from LHC16t to LHC16q period. The results are compatible with each other, thus the periods can be combined for the final data analysis. Right: Comparison of  $V_0M/\langle V_0M \rangle$  distributions for LHC16q and LHC16t periods. The distributions are consistent.



## 5. Analysis of data

In this thesis, measurements of flow coefficients and their correlations are presented as a function of multiplicity at mid-rapidity for different collision systems: pp, p–Pb, Xe–Xe and Pb–Pb collisions. The strategy to perform the analysis is common to all the collision systems, therefore it is going to be shown on an example of pp collisions in this chapter.

The method of measuring  $m$ -particle correlations is presented in Chapter 2 and the experiment and data sets in Chapters 3 and 4. The correlations  $\langle\langle m \rangle\rangle_{n_1, n_2, \dots, n_m}$  obtained from each event are stored in a `TProfile` in unit bins of the number of tracks,  $N_{\text{tracks}}$ , containing the same tracks that entered the calculation of correlations. The subsequent computation of the observables from these correlations is still performed in unit bins of  $N_{\text{tracks}}$ . Only then are the final results re-binned to the desired bin width. This procedure is crucial in the analysis of azimuthal particle correlations, especially in small collision systems, due to the influence from multiplicity fluctuations. Furthermore, the measurements are corrected for detector inefficiencies, and eventually the systematic uncertainty is estimated. This is going to be described in this Chapter.

### 5.1 Non-uniform acceptance correction

Measurements of azimuthal correlations are sensitive to detector inefficiencies in the azimuthal direction, which can give rise to false correlations and bias the final results. Whether a detector has a lower performance in some particular region can be revealed by looking at the event-averaged azimuthal distribution of the tracks,  $dN_{\text{tracks}}/d\varphi$  (after the event and track cuts, described in Chapter 4, are applied). Because the direction of the symmetry plane  $\Psi_n$  of a collision, and therefore the  $\varphi$  distribution of particles with respect to this plane, fluctuates event-by-event, the harmonic modulation of the  $\varphi$  distribution of particles vanishes when averaged over all events. Thus, in an ideal case of a fully efficient detector, the event-averaged

$\varphi$  particle distribution will be uniform.

Non-uniform features in the event-averaged azimuthal distributions are present in all collision systems in the data sets used for this analysis, as shown on an example in Fig. 5.1 (left) for the LHC16k period. The correction for the non-uniform acceptance is implemented in the Generic Framework in the form of per-particle weight  $w$ , as was already introduced in Chapter 2 in eq. (2.5). Since the correction is fully data-driven, one needs to measure the azimuthal distribution first, calculate the corresponding weights, and then perform the analysis using the obtained correction. Therefore, it requires two runs over the data sample. The advantage of the data-driven correction is that it does not rely on a Monte Carlo simulation, as it is usually the case in other analyses. The simulation might not describe the exact condition of the detector during the data taking properly, resulting in unprecise corrections.

The weights are calculated from the event-averaged  $\varphi$  distribution as  $w_i = N_{max}/N_i$ , where  $N_{max}$  is the maximum value in the  $\varphi$  distribution, and  $N_i$  is the value in the  $i^{th}$  bin of the  $\varphi$  distribution. Thus, the weights are always  $w_i > 1$ . The final event-averaged  $\varphi$  distribution will be constant over the whole azimuth after applying the weight. In Fig. 5.1 (right) the azimuthal distribution from the LHC16k period after the weight correction is shown. The distribution is uniform, as was intended.

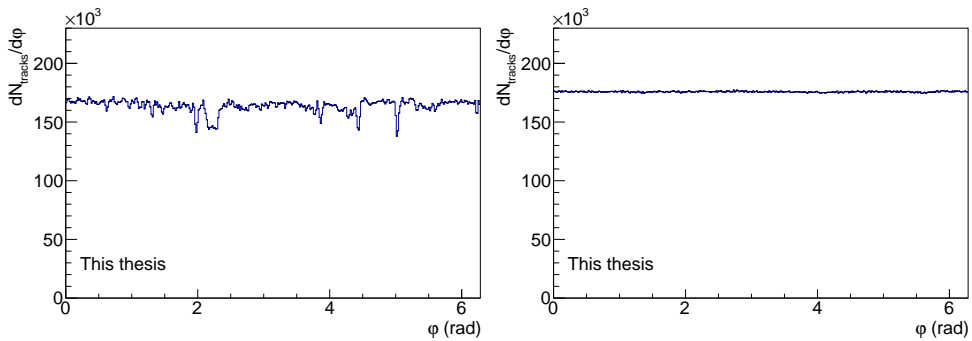


**Figure 5.1:** Left: Event-averaged  $\varphi$  distribution of the LHC16k period of pp collisions. The regions with non-uniform acceptance can be clearly seen. Right: The same  $\varphi$  distribution after the weight application to account for non-uniform acceptance. The distribution is uniform, as was intended.

The azimuthal distribution was checked for inconsistencies between different data taking periods. The comparison of the distributions from all the periods of pp collisions is shown in Fig. 5.2 (left), and ratios of different periods to the LHC16k period is shown on the right panel. It can be seen that the correction is period-dependent. Similar comparison was done for different run numbers, but no significant dependences were found. Thus, a universal acceptance correction is applied within a period in pp collisions. Similar checks were done for all the considered collision systems. It was found that a run dependent correction is necessary for p–Pb and Pb–Pb collisions. Comparison of azimuthal distributions from different runs in both systems is shown in the Appendix A.

Sectors of the detector with lower efficiency in azimuth might vary in longitudinal direction, i. e. along the beam. The azimuthal distribution was therefore further checked for

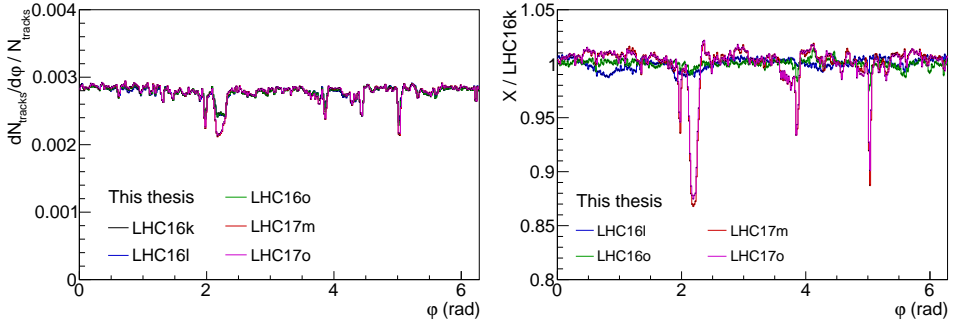


**Figure 5.2:** Left:  $\phi$  distribution from different periods of pp collisions. The distributions are normalised with the number of entries (i.e. tracks). The  $\phi$  distributions from different periods are incompatible. Right: Ratio of  $\phi$  distributions of all pp periods to the LHC16k period. The distributions are first normalised with number of entries. The necessity for a period dependent acceptance correction is apparent.

the dependence on pseudorapidity  $\eta$  or collision vertex in the direction of the beam  $V_z$ . A two-dimensional map in  $\phi - \eta$  and  $\phi - V_z$  coordinates is shown in Fig. 5.3 for the LHC16k period. It is clear from the figure, that the correction indeed needs to be calculated as a function of  $\eta$  and  $V_z$ . The procedure to obtain a multi-dimensional weight is the same as was described above: for each slice in  $\eta$  and  $V_z$ , a maximum  $N_{max}(\eta, V_z)$  of that  $\phi$  distribution is found. Then, the weight is calculated in each  $\phi$  bin as  $w_i(\eta, V_z) = N_{max}(\eta, V_z) / N_i(\eta, V_z)$ . In this way, the non-uniformities in the azimuthal direction will be corrected, while not disturbing the  $\eta$  or  $V_z$  distributions of the tracks (corrections in terms of  $\eta$  and  $V_z$  are described below in the next section). The same procedure was performed in p–Pb, Xe–Xe and Pb–Pb collisions.

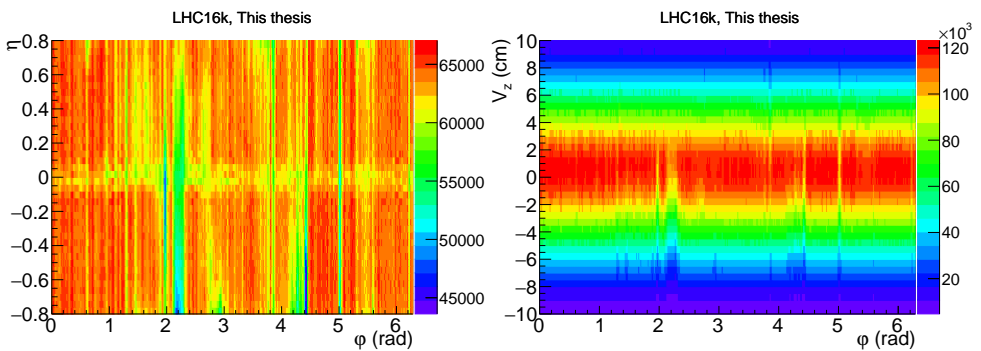


**Figure 5.3:** Left: Distribution of  $\eta$  vs.  $\phi$  of the LHC16k period of pp collisions. Right: Distributions of  $V_z$  vs.  $\phi$  of the LHC16k period in pp collisions. The necessity for  $\eta$  and  $V_z$  dependent acceptance correction is apparent.

## 5.2 Efficiency correction based on Monte Carlo simulations

In this section, efficiency corrections calculated from Monte Carlo (MC) simulations are described. In particular, the calculation of the correction as a function of  $p_T$ ,  $\eta$  and  $V_z$  are shown.

The shape of true  $p_T$ ,  $\eta$  and  $V_z$  distributions without any detector effects is not as predictable as in the previous case of  $dN_{\text{tracks}}/d\phi$ , i.e., they are not “flat” (thus, one cannot simply invert the distribution and obtain the weights in the way that was done in the previous section 5.1). For this reason, simulation is used to calculate these corrections. Different collision systems will use different models that are suitable to describe the particle production in the given type of a collision. The correction in pp collisions, which will be described here, was calculated using the PYTHIA 8 [56, 57] simulation provided by ALICE common data repositories. Each period of the reconstructed data has its corresponding simulation datasets, which are anchored to that particular period and its run numbers. First, a pure simulation of a pp collision is performed and stored as the so-called MC-truth sample. In the next stage, generated particles are propagated through the detector using the GEANT3 simulation tool [74], which contains the exact geometry and state of the detector during the data taking. The output from the detector simulation has a similar type of information as the one from real data. Thus, the reconstruction of the simulated output can be performed using the same software as in real data processing. This results in the so-called MC-reconstructed sample. The final track distributions in the MC-reconstructed sample should coincide with those in real data. This is checked centrally within ALICE in the end of the simulation process before the official ALICE simulation production is made available to user analyses.

As explained above, particle distributions from the MC-reconstructed sample represent the real data, and distributions from the MC-truth sample represent the true distributions without any losses in the detector. Therefore, the correction to the MC-reconstructed sample is calculated such that the distributions after the correction match the MC-truth sample. The efficiency of the detector is obtained as a ratio of a given particle distribution from MC-reconstructed sample to the same distribution from the MC-truth sample:

$$\text{efficiency}(p_T, \eta, V_z) = \frac{\text{MC-reconstructed}}{\text{MC-truth}}. \quad (5.1)$$

Eventually, the correction is obtained in the form of weight  $w(p_T, \eta, V_z) = 1/\text{efficiency}(p_T, \eta, V_z)$ .

The efficiency as a function of  $p_T$ ,  $\eta$  and  $V_z$  in pp collisions is shown on the left panels in Fig. 5.4, respectively. The efficiency drops at low  $p_T$ , while it remains roughly constant at higher  $p_T$  at a value of  $\approx 80\%$ . The  $\eta$ - or  $V_z$ -dependent efficiency have a small modulation in the entire range, except for the edge regions where the efficiency starts to drop. This suggests that the edge of the detector was reached, resulting in poorer tracking efficiency.

Similarly to the non-uniform acceptance correction described above, this efficiency is calculated for each period separately. In addition, in case of p–Pb and Pb–Pb collisions, each run is considered separately. The comparison of efficiencies from various periods in pp collisions is shown on the right panels of Fig. 5.4. The efficiencies from the other the collision systems are included in the Appendix B.

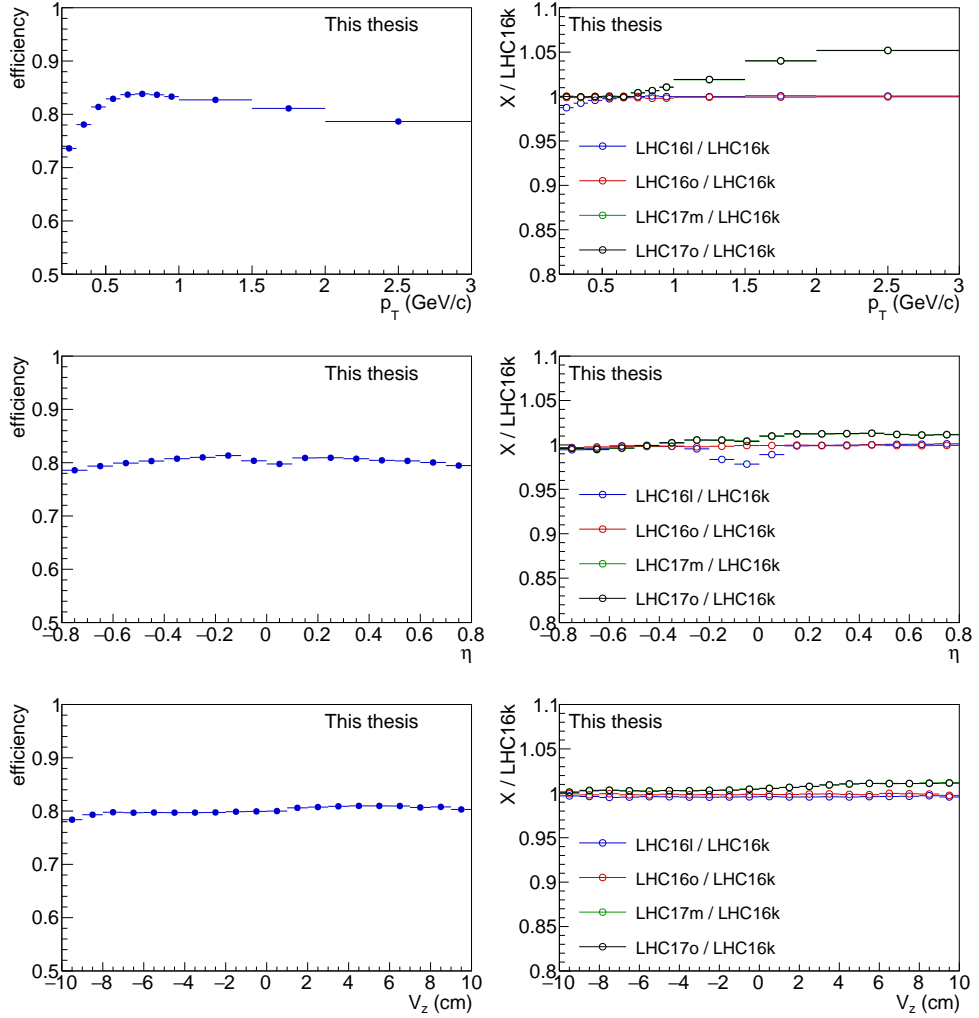


**Figure 5.4:** Left: Efficiency calculated from PYTHIA 8 simulation as a function of  $p_T$ ,  $\eta$  and  $V_z$  for the LHC16k period in pp collisions. Right: Ratio of efficiencies from different periods to the LHC16k period in pp collisions as a function of  $p_T$ ,  $\eta$  and  $V_z$ . The necessity for a period dependent correction is apparent.

### 5.3 Correction of the $x$ -axis

Observables in this analysis are measured as a function of the number of reconstructed tracks  $N_{\text{ch}}$  at mid-rapidity  $|\eta| < 0.8$ . Following the arguments discussed in this section, this observable also suffers from losses due to detector inefficiencies. In order to obtain the true number of particles in a created event corresponding to the given number of reconstructed

tracks, the Monte Carlo simulation is used. The correction is obtained from the correlation between the number of reconstructed tracks  $N_{\text{trk}}^{\text{reco}}$  from the MC-reconstructed sample and the number of true particles  $N_{\text{ch}}^{\text{truth}}$  from the MC-truth sample. An example of this correlation from pp collisions, denoted as a response matrix, is shown in Fig. 5.5.

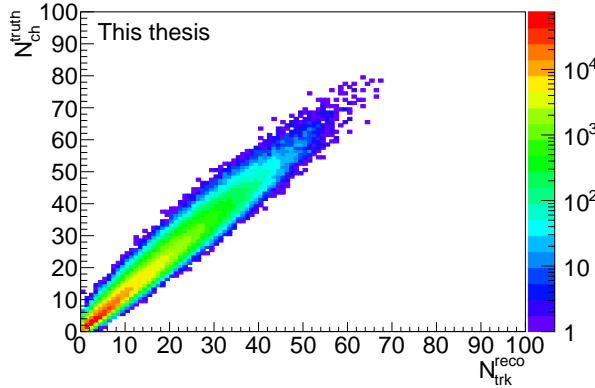


**Figure 5.5:** Response matrix: correlation between the number of generated particles  $N_{\text{ch}}^{\text{truth}}$  and the number of reconstructed tracks  $N_{\text{trk}}^{\text{reco}}$ . The matrix is taken from the PYTHIA 8 Monte Carlo simulation of pp collisions.

The correction is done as follows: in a given bin of  $N_{\text{trk}}^{\text{reco}}$ , chosen based on the desired binning of final results, a projection of the response matrix on the  $x$ -axis is done. Then, the mean of the projected distribution of  $N_{\text{trk}}^{\text{reco}}$ , the  $\langle N_{\text{trk}}^{\text{reco}} \rangle$ , is obtained. This will give the true mean value  $\langle N_{\text{trk}}^{\text{reco}} \rangle$  of the given bin, not necessarily identical to the centre of the bin. This is due to the steeply decreasing multiplicity distribution, especially in small collision systems. The  $\langle N_{\text{trk}}^{\text{reco}} \rangle$  is then mapped using a linear fit of the response matrix to give the  $\langle N_{\text{ch}}^{\text{truth}} \rangle$ .

Monte Carlo production is only available for minimum-bias data. In order to correct the results from high multiplicity trigger in pp collisions, the response matrix needs to be extended to larger multiplicities. For each unit bin of  $N_{\text{trk}}^{\text{reco}}$ , the matrix is projected on the  $y$ -axis, which gives the spread of  $N_{\text{ch}}^{\text{truth}}$  corresponding to the specific  $N_{\text{trk}}^{\text{reco}}$ . This distribution is then fitted with a Gaussian function. The mean  $\mu$  and width  $\sigma$  of these projections in each bin of  $N_{\text{trk}}^{\text{reco}}$ , taken from the fit parameters, are shown in the left and right panel of Fig. 5.6, respectively. Both distributions are then fitted with a linear function in order to estimate the dependence at high multiplicities.

Finally, the response matrix is extended by generating a Gaussian distribution representing the  $N_{\text{ch}}^{\text{truth}}$  in each bin of  $N_{\text{trk}}^{\text{reco}}$  from the linear fits to the mean and width from Fig. 5.6. Subsequently, new points are filled to the response matrix based on the new generated Gaussian functions. The final extended response matrix, which will be used to correct the  $x$ -axis of the measurements from the high multiplicity trigger in pp collisions, is shown in Fig. 5.7.

The response matrices used for the correction of the rest of the collision systems are shown in the Appendix C.

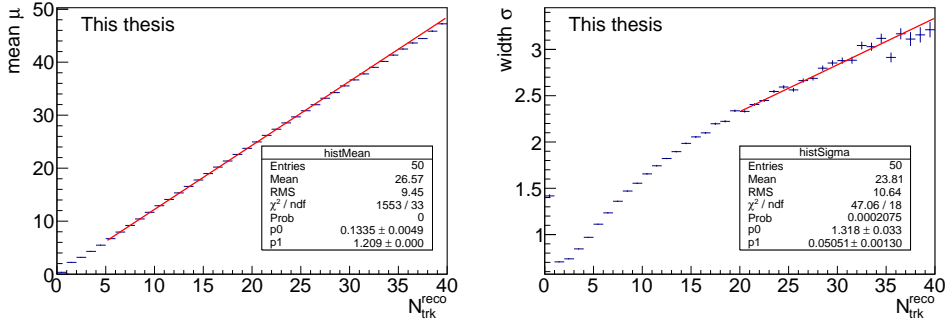


**Figure 5.6:** The mean  $\mu$  (left panel) and width  $\sigma$  (right panel) of a Gaussian fit to the y-axis projection of the response matrix in each bin of  $N_{\text{trk}}^{\text{reco}}$ . Both distributions are fitted with a linear function to estimate the dependence at high multiplicities.

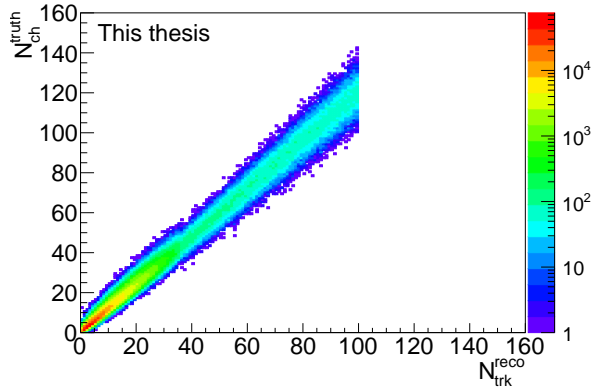


**Figure 5.7:** Extended response matrix: correlation between the number of generated particles ( $N_{\text{ch}}^{\text{truth}}$ ) and the number of reconstructed tracks ( $N_{\text{trk}}^{\text{reco}}$ ). This matrix will be used for the correction of x-axis of the measurements from the high multiplicity trigger in pp collisions.

## 5.4 Estimation of systematic uncertainties

A systematic uncertainty takes into account small deviations which might be caused by analysis method related choices, such as different event or track cuts. In this section studies of these effects on the final results are described in detail. The purpose of this study is to check how much the results change if events or tracks with better quality are used. For this reason, the cuts for this test are chosen to be tighter than the ones that were chosen as default. The uncertainty is estimated from the difference between results with default cuts and results where one of the cuts is changed. Every time only one cut from the overall set is varied. The whole analysis is repeated with the new tighter cut, and compared to the results obtained with default cuts.

All the cuts studied in order to get the systematic uncertainty are listed in Table 5.1.

The cut on the longitudinal position of the event vertex is changed from the default value of  $|V_z| < 10$  cm down to  $|V_z| < 5$  cm. The global type of tracks have been changed to the so-called *hybrid type* of tracks. These consist of a combination of different type of tracks with different quality in order to fill the low performance acceptance regions of the  $\varphi$  distribution. Therefore, it is not necessary to apply the non-uniform acceptance correction in azimuth when using the hybrid type of tracks. On the other hand, these tracks have looser cuts on the distance of closest approach (DCA) to the collision vertex and thus worse tracking efficiency. Another systematic check was based on the DCA in longitudinal,  $DCA_z$ , and transverse direction,  $DCA_{xy}$ . Both cuts are tightened for the studies. Finally, the cut on the minimum number of TPC clusters is changed from 70 up to 100. The last contribution to the systematic uncertainty comes from the so-called Monte Carlo closure test, which studies how much the corrected results approach the results obtained with the generated particles without any influence of the detector inefficiencies. This test, exploiting simulation calculations, will be described in more details below in section 5.4.2.

variable	default cut	changed cut
$ V_z $	$< 10$ cm	$< 7$ cm $< 6$ cm $< 5$ cm
type of tracks	global	hybrid
$ DCA_z $	$< 2$ cm	$< 1$ cm $< 0.5$ cm
$ DCA_{xy} $	$< 0.0182 + 0.0350/p_T^{1.1}$	$< 0.2$ cm $< 0.15$ cm
# of TPC clusters	$> 70$	$> 80$ $> 90$ $> 100$
Monte Carlo closure test		

**Table 5.1:** Cuts that were varied for systematic study in the analysis presented in this thesis.

The non-uniform acceptance and efficiency corrections were evaluated for each of the varied cuts separately and checked for any inconsistencies. In Fig. 5.8 (left) the  $\varphi$  distribution is shown for different cut variations. On the right panel the ratio of the distribution with varied cuts to the default  $\varphi$  distribution is plotted. It was found that special correction to non-uniform acceptance in the azimuthal direction has to be applied for different cuts on the number of TPC clusters, and that no correction is needed for hybrid tracks. The rest of the cases shared the same correction as was used for the default results. Because the non-uniform acceptance weights depend on  $V_z$ , no special correction was necessary for the variation of the  $V_z$  cut. The example shown in Fig. 5.8 is taken from LHC16k period of pp collisions. Analogous checks were performed for the rest of the periods and collision systems, yielding identical conclusions.

Similar check was performed for corrections obtained from the Monte Carlo simulations. This is illustrated in Fig. 5.9, where the efficiency as a function of  $p_T$ ,  $\eta$  and  $V_z$ , is plotted on the left panels for different variations of the cuts. Ratios of the correction with varied cuts to

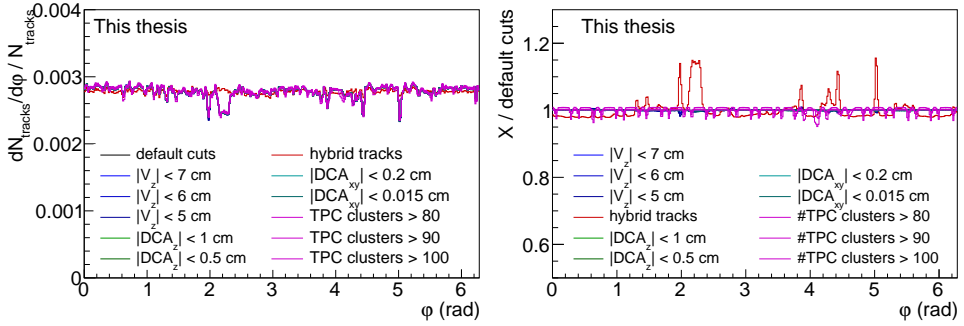


**Figure 5.8:** Left:  $\phi$  distribution for different variations of the cuts. The distributions are normalised with the number of entries (i.e. tracks). Right: Ratio of  $\phi$  distribution with different cut variations with respect to the default. No correction is necessary for the case of hybrid tracks, while a special correction is needed for different cuts on the minimum number of TPC clusters.

the correction with default cuts are plotted on the right panels of the figure. It was found that the correction is different for the hybrid type of tracks and for different cuts on the number of TPC clusters. Therefore, special Monte Carlo correction was applied for these cases of cut variations.

Since a special Monte Carlo efficiency had to be used in some cases of the cut variations, the same applies to the correction of the  $x$ -axis. Individual response matrix was obtained for each case of the cut variation. These matrices were then used to correct the  $x$ -axis of results with different cut variations. The effect of different correction can be seen below in Fig. 5.10, where the points of the same observable are shifted to slightly different values of  $N_{\text{ch}}$ , especially in case where hybrid tracks were used.

#### 5.4.1 Uncertainty from variations of event and track cuts

Systematic uncertainties from different variations of event and track cuts were evaluated in the following way:

1. Obtain results for each variation of the cut ( $V_z$ ,  $DCA_z$ , etc.) separately.
2. Perform the Barlow check bin-by-bin:

$$\frac{|x_1 - x_2|}{\sqrt{|\sigma_1^2 \pm \sigma_2^2|}} > 1 \quad (5.2)$$

- In case of correlated variables, the denominator will have a + sign, and viceversa.
- If the Barlow check is significant (that is, the ratio in eq. (5.2) is larger than 1), then a systematic uncertainty should be assigned.
- Bin-by-bin check might cause fluctuations of systematic uncertainties from point

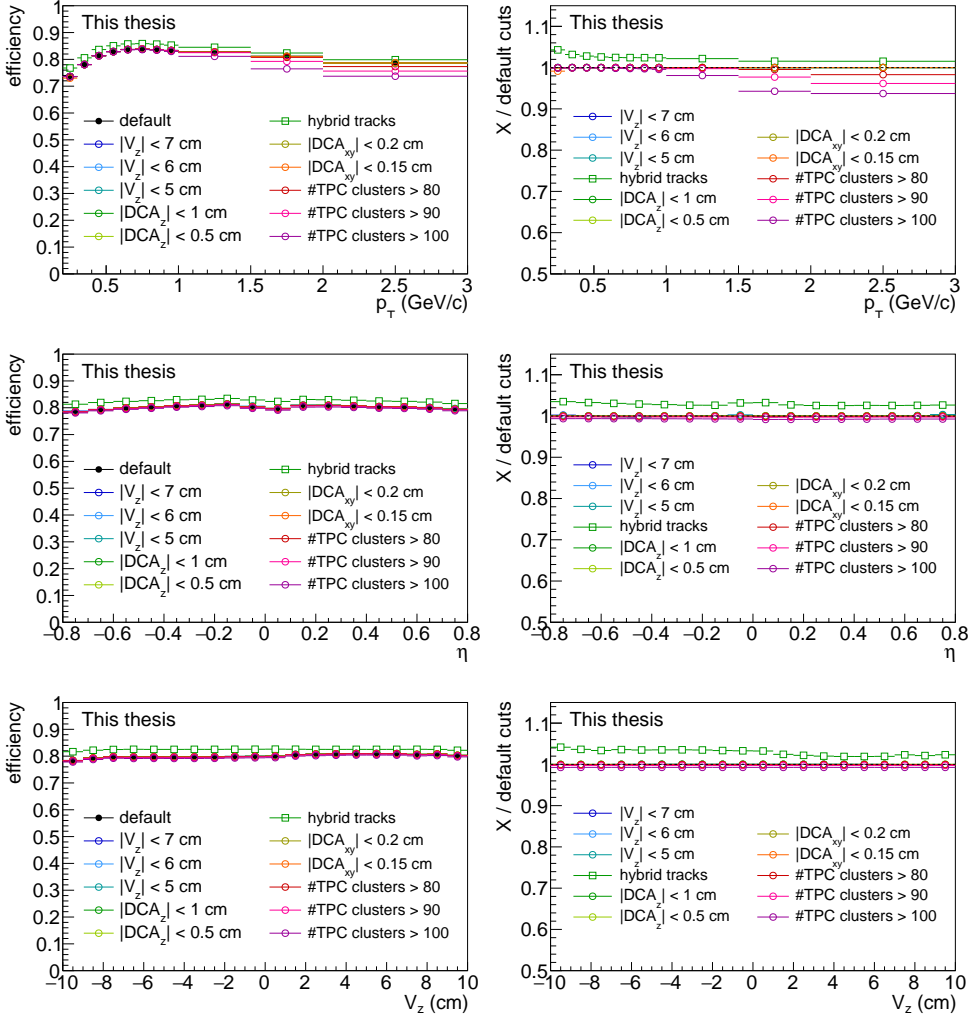


**Figure 5.9:** Left: Monte Carlo efficiency as a function of  $p_T$ ,  $\eta$  and  $V_z$  with different variations of the cuts. Right: Ratio of the efficiency with different variations of the cuts to the efficiency with default cuts, as a function of  $p_T$ ,  $\eta$  and  $V_z$ .

to point. Therefore, further smoothening of systematic uncertainties is necessary (described in the next point).

3. A polynomial fit to the ratio of the results with varied cut to results with default set of cuts is performed to estimate the relative uncertainty (polynomial function is chosen in order to describe a possible multiplicity dependence of the ratio).

- Some observables suffer from lack of statistics. It wouldn't be possible to evaluate systematic uncertainties based on the procedure described above. Therefore, the relative systematic uncertainty of related observables with no such problems was assigned to these results. Such measurements include:
  - observable  $v_2\{2, |\Delta\eta| > 1.4\}$  will use the relative systematic uncertainty from  $v_2\{2, |\Delta\eta| > 1.0\}$ ,
  - observables  $v_3\{2, |\Delta\eta| > 1.0\}$ ,  $v_3\{2, |\Delta\eta| > 0.8\}$  and  $v_3\{2, |\Delta\eta| > 0.4\}$  will use the relative systematic uncertainty from  $v_3\{2, |\Delta\eta| > 0.2\}$ ,
  - observables  $v_4\{2, |\Delta\eta| > 1.0\}$ ,  $v_4\{2, |\Delta\eta| > 0.8\}$  and  $v_4\{2, |\Delta\eta| > 0.4\}$  will use the relative systematic uncertainty from  $v_4\{2, |\Delta\eta| > 0.2\}$ ,
  - observables  $c_2\{4\}_{2\text{-sub}}$  and  $c_2\{4\}_{3\text{-sub}}$  will use the relative systematic uncertainty from  $c_2\{4\}$
  - observables  $SC(4,2)_{2\text{-sub}}$ ,  $SC(4,2)_{3\text{-sub}}$ ,  $SC(3,2)_{2\text{-sub}}$  and  $SC(3,2)_{3\text{-sub}}$  will use relative systematic uncertainty from  $SC(4,2)$  and  $SC(3,2)$ , respectively,
  - observables normalised  $SC(4,2)_{2\text{-sub}}$ ,  $SC(4,2)_{3\text{-sub}}$ ,  $SC(3,2)_{2\text{-sub}}$  and  $SC(3,2)_{3\text{-sub}}$  will use relative systematic uncertainty from normalised  $SC(4,2)$  and  $SC(3,2)$ , respectively.

4. Uncertainties from all variations of the cuts are added in quadrature to form the final systematic uncertainty.

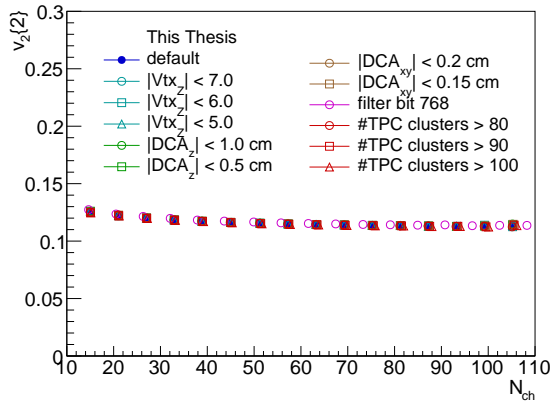


**Figure 5.10:** Comparison of  $v_2\{2\}$  results from pp collisions as a function of  $N_{\text{ch}}$  (corrected for inefficiencies) for default cuts, and different variations of these cuts.

In cases where a parameter would be varied more than once, only the one with the largest deviation with respect to default results is chosen to be assigned as systematic uncertainty. The contribution from the Monte Carlo closure test is also added in quadrature (the details of this study are described in the section 5.4.2). In the following, an example of the evaluation of systematic uncertainty is shown for  $v_2\{2\}$  in pp collisions.

First, results of  $v_2\{2\}$  with different variations of the cuts are obtained, as is shown in Fig. 5.10. Each of the cases is corrected using the corresponding weights, as was described above. All the results shown in Fig. 5.10 are then divided by the results with default cuts, shown in Fig. 5.11. It can be observed that the case which uses the hybrid tracks instead of the global tracks has the largest deviation from the default results. This is probably caused by the fact that the azimuthal inefficiencies in the detector were filled with tracks with loose DCA cuts, thus containing contamination from secondary (decayed) particles.

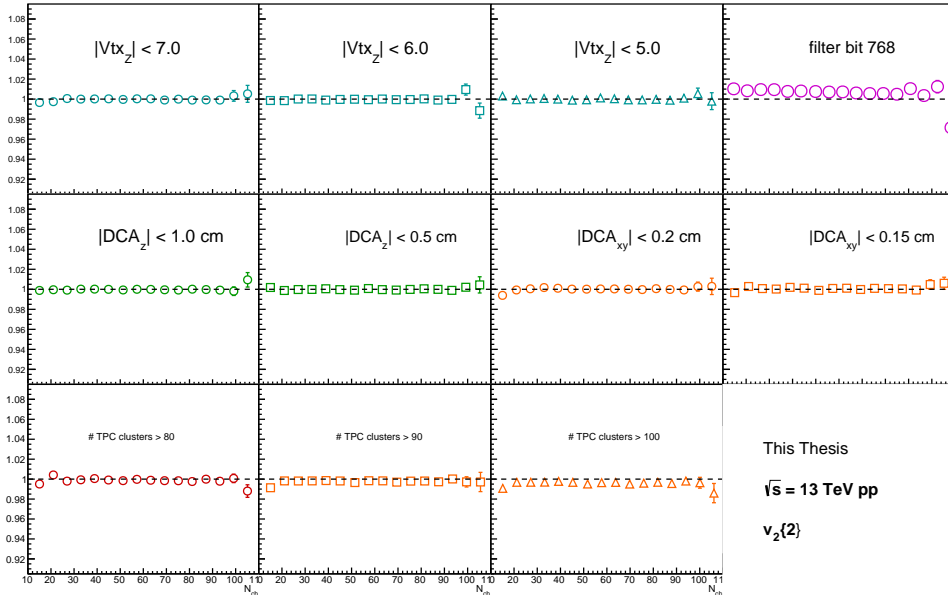


**Figure 5.11:** Ratio of  $v_2\{2\}$  results from pp collisions with variation of cuts to the results with default cuts, intended for systematic studies.

#### 5.4.2 Monte Carlo closure test

Monte Carlo closure test is the comparison of results from the following 2 simulations:

- Monte Carlo truth (MC-truth): pure simulation including the generation of events and particles, without any influence of the detector
- Monte Carlo reconstructed (MC-reconstructed): the generated particles from the MC-truth sample are propagated through the detector using GEANT3 [74], and recon-

reconstructed afterwards with the same reconstruction algorithm as was used in the real data reconstruction.

The MC-reconstructed sample should mimic the real data sample. Thus, exactly the same code with the same set of cuts that are used to perform the real data analysis can be used to analyse the simulation data from the MC-reconstructed sample. A slightly modified code is used to analyse the MC-truth sample. There, no event or track cuts which have connection with the detector response are used. Apart from the kinematic cuts applied on  $p_T$  and  $\eta$ , an additional cut to select only charged primary particles [75] was used in the MC-truth dataset.

Results from the MC-reconstructed sample, similarly to the real data analysis, are corrected for detector inefficiencies. The MC-reconstructed results are calculated as a function of the number of reconstructed tracks (as in the real data analysis), while the MC-truth results are obtained as a function of the real number of particles created in a collision. Thus, in order to make a proper comparison of results from these two simulation samples, the  $x$ -axis of the MC-reconstructed results is corrected in order to match the  $x$ -axis of the MC-truth results. Measurements from the MC-reconstructed sample with applied corrections should be compatible with the MC-truth sample. Deviations from the true results are taken as a systematic uncertainty.

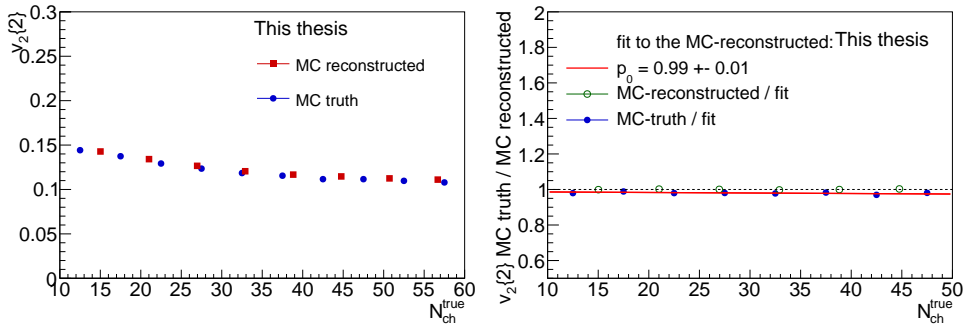
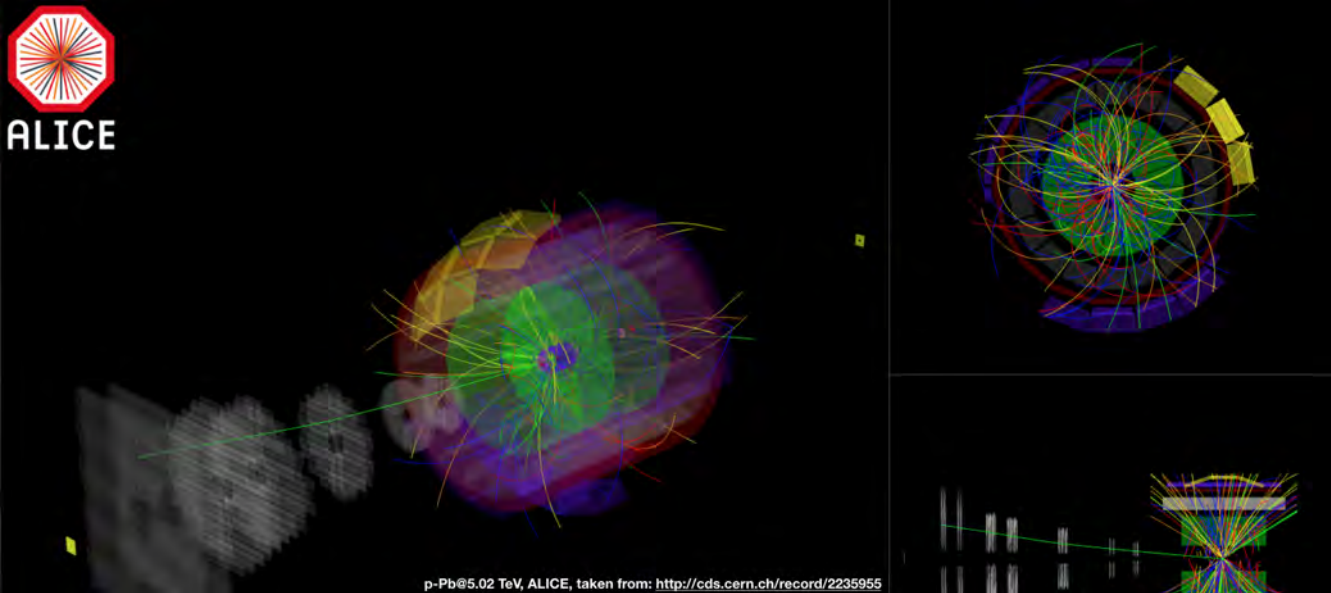


**Figure 5.12:** Left: Comparison of results of  $v_2\{2\}$  from the MC-truth (open blue circles) and the MC-reconstructed with corrections (open red squares) from PYTHIA 8 simulation of pp collisions. Right: Ratio of  $v_2\{2\}$  results from the MC-truth to the MC-reconstructed sample from PYTHIA 8 simulation of pp collisions (filled markers). The parameter of the fit to the ratio is taken as systematic uncertainty, which is in this case 1%. See text for more details on the open markers.

An example of a comparison of the MC-truth with the MC-reconstructed results is shown in Fig. 5.12 (left) for  $v_2\{2\}$ . In order to quantify the difference, the ratio of these results is shown in the right panel. Due to the fact that the points from the two data samples now correspond to different numbers on the  $x$ -axis, a direct bin-by-bin ratio is not possible. First, the MC-reconstructed result is fitted with an arbitrary function that describes the data points well. Then, the fit is evaluated in the  $N_{ch}$  bin that corresponds to the MC-truth data point, and a ratio to the MC-truth sample is calculated. This is shown in Fig. 5.12 (right). In order to check whether the fit of the MC-reconstructed sample is reasonable, the ratio to the same

MC-reconstructed results is shown in the figure with the open markers. It can be seen that the ratio is compatible with one, therefore the fit can be used to evaluate the difference between the MC-reconstructed and the MC-truth samples from their ratio, as is shown in the same figure with filled markers. The relative systematic uncertainty for this observable is obtained from the fit of this ratio, in order to smooth the final uncertainty. In the case shown in Fig. 5.12, the uncertainty is 1%. The same studies were performed for all observables separately.

The MC closure test was also done for the rest of the collision systems, but using different models most suitable to the given type of the collision system. In particular, the DPMJET [76] was used in p–Pb collisions, while HIJING [77] was employed in Xe–Xe collisions. At first, HIJING was used for Pb–Pb collisions too, however, the MC closure check was later redone using a new Monte Carlo production with the AMPT [27] model, that is more realistic for heavy-ion collisions. No AMPT production was available for Xe–Xe collisions at the time of performing this analysis. Summary of systematic uncertainties of all observables for all collision systems is shown in the Appendix D.



## 6. Results and discussion

Measurements of flow coefficients and their correlations in pp, p–Pb, Xe–Xe and Pb–Pb collisions will be shown in this chapter. These measurements will help in the investigation of collectivity in small collision systems by providing a complex set of information from a large number of measurements, which are compared between a wide range of collision systems, going from pp collisions up to Pb–Pb collisions. The large gap between the system size will be filled with comparison to p–Pb, and recently taken Xe–Xe collisions.

Large collision systems serve for the study of the properties of the QGP, while measurements in small collision systems were considered as a baseline because, naïvely thought, no hot and dense nuclear matter was created there. A typical measurement believed to originate from the presence of a collective medium in heavy-ion collisions is the ridge structure in the two-particle correlation function at  $\Delta\phi \approx 0$ , spanning over a wide range in pseudorapidity  $\eta$ . However, similar observations were seen in collisions of small systems with large multiplicities. It is important to understand where does the ridge structure in pp and p–Pb collisions come from, whether it originates from collective effects, and if yes, whether it means that a small sized QGP is created in such collisions, or whether it arises from other effects.

Before proceeding with investigations of collectivity, it is important to note how are the collective phenomena expected to be revealed in the measurements of azimuthal particle correlations. Based on the observations in flow dominated heavy-ion collisions, collectivity is understood as global correlations of many particles with respect to a common symmetry plane, where these correlations spread long range in pseudorapidity. Therefore, search for long-range multi-particle correlations in small collision systems will be the main focus of the measurements shown below.

Results will be presented as a function of multiplicity  $N_{\text{ch}}(|\eta| < 0.8)$ , which is commonly defined for all collision systems. This chapter will first investigate the effects of non-flow on the azimuthal particle correlation measurements using methods to suppress such effects.

Then, measurements in small collision systems (pp and p–Pb) will be compared to the results from large systems. Eventually, comparison to model calculations will provide further insight into the investigation of origins of collectivity in small collision systems.

## 6.1 Non-flow effects

One of the key challenges in this investigation is the dominance of non-flow effects, which affect the measurements exploiting the  $m$ -particle correlations. These effects predominantly come from short-range correlations among few particles, e.g. particles within a jet or daughter particles from resonance decays. The later is characterised by small opening angles, thus leading to a strong correlation. Particles from the jet share a common jet symmetry plane, therefore they also yield a significant flow signal. However, this plane might not be connected to the global symmetry plane of the bulk, thus such correlations contaminate the flow measurements. In the following, a new implementation of the cumulant method which can suppress such effects will be presented and the impact of this method on the final results will be discussed.

### 6.1.1 Suppression of non-flow in two-particle cumulant measurements

Non-flow effects in two-particle correlations can be suppressed by applying a  $|\Delta\eta|$  gap between the pair of particles that are being correlated. The procedure of this method and the way of how the pseudorapidity gap is used in the measurements have been described in Chapter 2. Below, the importance of this method in the azimuthal particle correlation measurements will be discussed for large and small collision systems.

#### Large collision systems

Measurements of different orders of flow coefficients  $v_n$ , obtained with the two-particle cumulant method with various sizes of  $|\Delta\eta|$  gaps as a function of multiplicity  $N_{\text{ch}}$ , are shown in Fig. 6.1 for Xe–Xe (left) and Pb–Pb (right) collisions. A logarithmic scale on the  $x$ -axis was chosen for clearer presentation of the details at low multiplicity. The maximum pseudorapidity gap for  $v_3$  and  $v_4$  is smaller than for  $v_2$  due to statistical limitations.

It can be seen that non-flow affects collisions of heavy ions mostly at low multiplicities, where the values of  $v_n$  significantly decrease with larger  $|\Delta\eta|$  gap, while the measurements saturate at high multiplicity. In addition, at the lowest multiplicity around  $N_{\text{ch}} < 100$ , the suppression of non-flow contribution influences the trend of the  $v_n\{2\}$  with multiplicity. The effect is most pronounced in the  $v_2$  measurement: the  $v_2\{2\}$  firstly decreases with multiplicity which resembles the naïvely expected non-flow dependence as  $\approx 1/N_{\text{ch}}$ . However, the slope changes with large  $|\Delta\eta|$  gap: it is increasing from low to intermediate  $N_{\text{ch}}$ .

The usage of  $|\Delta\eta|$  gap has a significant effect on  $v_3$  and  $v_4$  even at large multiplicities, where  $v_2$  already experienced saturation of the signal. This shows that higher order flow coefficients are more sensitive to non-flow effects, which is observed both in Xe–Xe and Pb–Pb collisions.

Eventually, a direct comparison of all orders of flow coefficients with the standard method,  $v_n\{2\}$ , and with pseudorapidity separation,  $v_n\{2, |\Delta\eta|\}$ , are shown in Fig. 6.2. The effect of  $|\Delta\eta|$  gap is apparent in both collision systems, although more details can be seen in the right panel for Pb–Pb collisions, where larger amount of collected data allowed for narrower

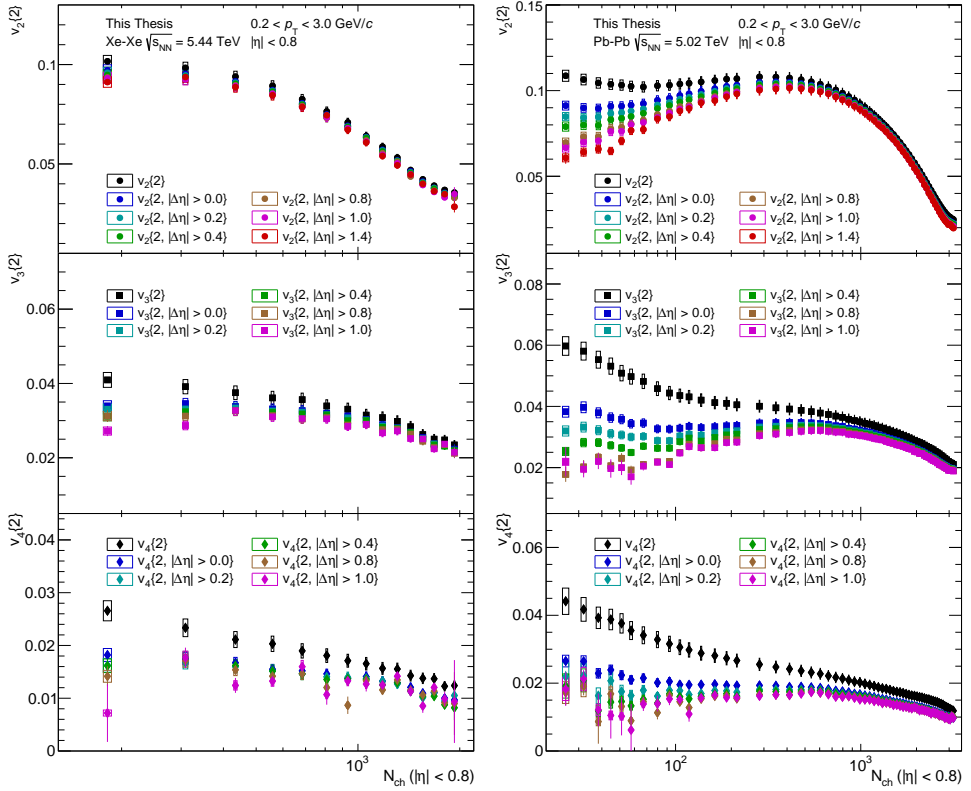


**Figure 6.1:** Multiplicity dependence of  $v_2\{2\}$ ,  $v_3\{2\}$  and  $v_4\{2\}$  for various pseudorapidity gaps in 5.44 TeV Xe–Xe collisions (left) and 5.02 TeV Pb–Pb collisions (right). A clear reduction of  $v_n$  with increasing  $|\Delta\eta|$  gap at low multiplicity, and a saturation of the signal at large multiplicity is observed.

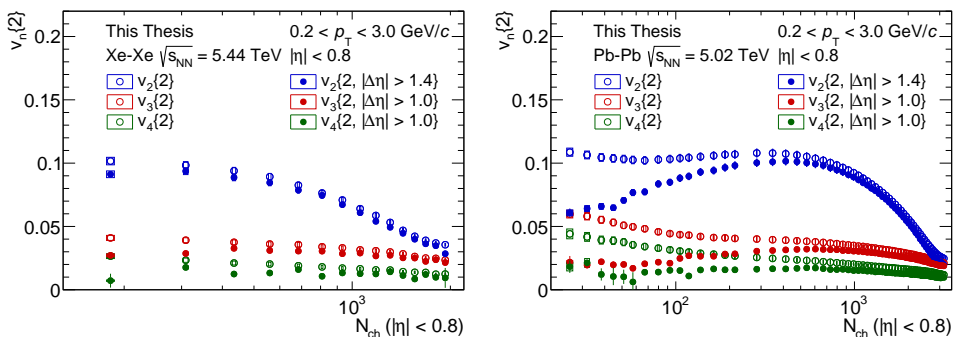


**Figure 6.2:** Multiplicity dependence of  $v_2\{2\}$ ,  $v_3\{2\}$  and  $v_4\{2\}$  compared to the same observables with the largest possible  $|\Delta\eta|$  gap in 5.44 TeV Xe–Xe collisions (left) and 5.02 TeV Pb–Pb collisions (right).

binning down to lower multiplicities. It can be clearly observed that the non-flow is largely suppressed at low multiplicities, based on the significant decrease in magnitude and the change of the decreasing trend of  $v_n$  with multiplicity to increasing with multiplicity.

The  $v_n$  measured with the two-particle cumulant method show, that large collision systems are dominated by flow, except for low  $N_{\text{ch}}$  region, where non-flow starts to prevail.

### Small collision systems

Figure 6.3 shows measurements of  $v_n$  as a function of  $N_{\text{ch}}$  in pp (left) and p–Pb (right) collisions, calculated using the two-particle cumulant method with various sizes of  $|\Delta\eta|$  gaps. The maximum pseudorapidity gap for  $v_3$  and  $v_4$  is smaller than for  $v_2$  due to statistical limitations. It is clear that the values of  $v_n$  significantly decrease with increasing  $|\Delta\eta|$  gap. This is observed for all orders of flow coefficients in both pp and p–Pb collisions. Large collision systems exhibit similar behaviour at the same multiplicity range. The reduction of  $v_n$  suggests that non-flow effects are suppressed with a  $|\Delta\eta|$  gap. However, some non-flow still remains, because a continuous decrease of the signal can be seen even with the  $|\Delta\eta| > 1.4$  gap. Within the acceptance chosen for this analysis, it is not possible to increase the separation even further. Therefore, based on the measurements of two-particle cumulants we cannot conclude whether the remaining signal of  $v_2\{2, |\Delta\eta| > 1.4\}$ ,  $v_3\{2, |\Delta\eta| > 1.0\}$  and  $v_4\{2, |\Delta\eta| > 1.0\}$ , is purely due to flow, or if it is still affected by non-flow effects.

Additional suppression could be achieved with the so-called non-flow subtraction method. This method is based on the assumption that the non-flow contribution is well described by correlation measurements of minimum-bias pp (or low multiplicity p–Pb) collisions. These measurements are subtracted from the measurements at high multiplicity pp or p–Pb collisions with a scaling factor usually taken as a ratio of the mean multiplicity in the low/high multiplicity event sample. This method is still a place of lots of discussions. Different analyses (either di-hadron correlations or two-particle cumulant method), as well as different experiments, use different techniques to remove non-flow contributions leading to incompatible results [49, 50]. However, measurements of multi-particle cumulants, which will be the main focus of this analysis, are able to suppress non-flow from these lower order correlations. Thus, the non-flow subtraction technique has not been investigated in these measurements yet.

Different orders of flow coefficients  $v_n$  are directly compared with each other in Fig. 6.4. The left panel presents the measurements of  $v_n\{2, |\Delta\eta|\}$  in  $\sqrt{s} = 13$  TeV pp collisions, while results from  $\sqrt{s_{\text{NN}}} = 5.02$  TeV p–Pb collisions are shown on the right. In order to suppress most of the non-flow contribution, the largest pseudorapidity gap that was possible to be used in the analysis, was chosen. Measurements are compared to results without  $|\Delta\eta|$  gap,  $v_n\{2\}$ , thus with a significant non-flow contribution. A decreasing dependence of  $v_n\{2\}$  on multiplicity is observed in both collision systems, although the trend is more pronounced in p–Pb collisions. Since non-flow is naïvely expected to be scaled as  $\approx 1/N_{\text{ch}}$ , the observed decreasing trend suggests that measurements using the standard method without  $|\Delta\eta|$  gap are strongly affected by non-flow. The measurements of  $v_n\{2\}$  in pp collisions reveal a very modest dependence on multiplicity. This is caused by the high multiplicity trigger which was used to obtain the pp results. It was indicated in section 4.1.3 that the selection of high multiplicity events in the forward region helps to further suppress non-flow. The measurements presented here support this observation. After a large  $\eta$  separation is

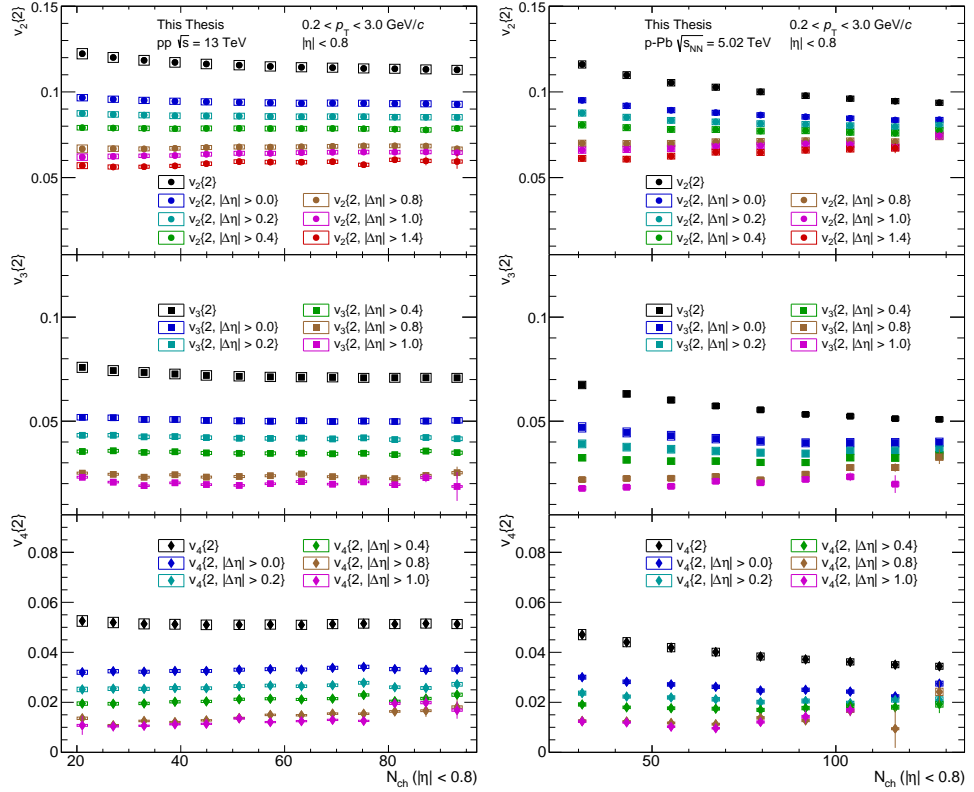


**Figure 6.3:** Multiplicity dependence of  $v_2\{2\}$ ,  $v_3\{2\}$  and  $v_4\{2\}$  for various pseudorapidity gaps in 13 TeV pp collisions (left) and 5.02 TeV p-Pb collisions (right). A clear reduction of the signal with increasing  $|\Delta\eta|$  gap is observed in both collision systems.

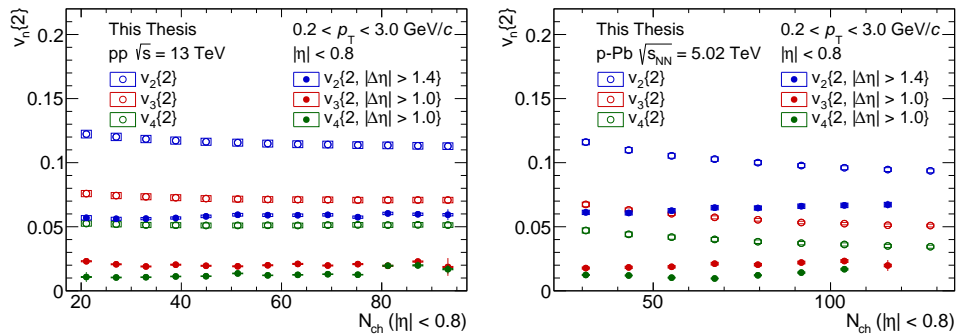


**Figure 6.4:** Multiplicity dependence of  $v_2\{2\}$ ,  $v_3\{2\}$  and  $v_4\{2\}$  compared to the same observables with the largest possible  $|\Delta\eta|$  gap in 13 TeV pp collisions (left) and 5.02 TeV p-Pb collisions (right).

enforced between two subevents, it can be seen that the multiplicity dependence of  $v_n$  changes, especially in p–Pb collisions where the  $v_n$  even starts to rise with multiplicity.

### Summary of non-flow effects in two-particle cumulant measurements

All the results presented in this section show that the  $|\Delta\eta|$  gap is able to suppress the few-particle short-range correlations. However, a non-negligible non-flow might still persist even with the largest possible  $|\Delta\eta|$  gap. Observables using more than just two-particle correlations are more robust against such effects, and are going to be presented in the next section.

## 6.1.2 Suppression of non-flow in multi-particle cumulant measurements

Multi-particle cumulants are less sensitive to the non-flow originating from lower order correlations. The measurements were therefore not considered to be significantly biased by non-flow effects. This is a good approximation for large collision systems due to the dominance of flow, as it will be shown below. However, in small collision systems, the azimuthal correlations are dominated by non-flow effects. Thus, multi-particle cumulant measurements in pp or p–Pb collisions might be still highly affected by multi-particle non-flow correlations, such as correlations among particles within the cones of a di-jet. The description of the subevent method in multi-particle cumulants, as well as the demonstration of its ability to further suppress non-flow in such measurements with PYTHIA 8 simulations, was shown in Chapter 2. Even though its idea seems to be very simple, the application of this method in multi-particle cumulants has been developed only recently by both ALICE and ATLAS collaborations independently. Early studies of multi-particle cumulants in pp, p–Pb and Pb–Pb collisions with ALICE, where the subevent method was employed for the first time in flow measurements, is described in Appendix E. Larger amount of collected data in the LHC Run 2 data taking allowed for more detailed investigation of non-flow effects in multi-particle cumulants, which will be discussed here.

### Large collision systems

In heavy-ion collisions, large multiplicities enable the calculation of multi-particle cumulants up to the 8-th order, i.e.  $c_n\{8\}$ . First, measurements of the four-particle cumulant, calculated with the standard, 2- and 3-subevent method for both Xe–Xe and Pb–Pb collisions, is shown in Fig. 6.5 (top). The measurements of  $c_2\{4\}$ ,  $c_2\{4\}_{2\text{-sub}}$  and  $c_2\{4\}_{3\text{-sub}}$  are compatible with each other, showing that non-flow contribution in heavy-ion collisions is well suppressed already with the standard method of the 4-particle cumulant. This observation implies a clear sign of collective effects. The same conclusion applies to measurements of 6- and 8-particle cumulants, shown in the middle and bottom panel of Fig. 6.5. Only the measurements with the standard method could be obtained for Xe–Xe collisions. However, the high statistics of Pb–Pb data allows to calculate the 6- and 8-particle cumulant with the 2-subevent method. No difference is observed when comparing the standard and the subevent method, as expected from the fact that Pb–Pb collisions are dominated by flow.

Another observable which exploits multi-particle correlations is the Symmetric Cumulant,  $SC(m,n)$ . It quantifies the correlation between different orders of flow coefficients  $v_m$  and  $v_n$ . Figure 6.6 presents measurements of  $SC(m,n)$  in Xe–Xe and Pb–Pb collisions as a function of  $N_{\text{ch}}$ . Similar to the cumulant measurements discussed above, these results are obtained down to lower multiplicities in Pb–Pb collisions than in Xe–Xe. In addition,

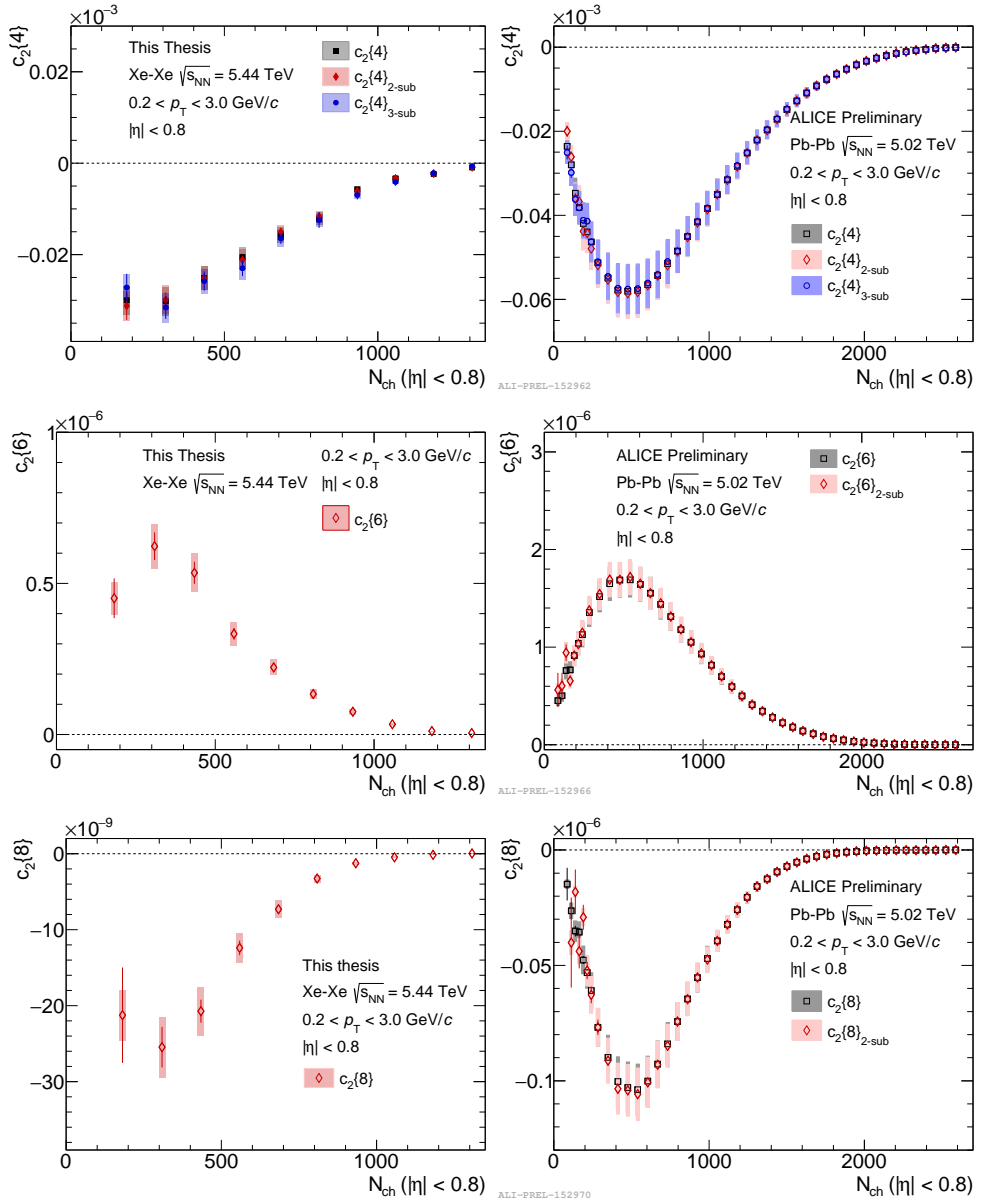


**Figure 6.5:** Multiplicity dependence of  $c_2\{4\}$ ,  $c_2\{4\}_{2-sub}$  and  $c_2\{4\}_{3-sub}$  (top),  $c_2\{6\}$  and  $c_2\{6\}_{2-sub}$  (middle), and  $c_2\{8\}$  and  $c_2\{8\}_{2-sub}$  (bottom) in 5.44 TeV Xe–Xe collisions (left) and in Pb–Pb collisions (right). Only  $c_2\{6\}$  and  $c_2\{8\}$  is shown in Xe–Xe collisions due to statistical limitations. The measurements obtained with different methods are compatible.

results calculated using the newly implemented 2- and 3-subevent method are presented as well. No significant difference between  $SC(m,n)$  and  $SC(m,n)_{\text{sub}}$  is observed within the uncertainties, confirming that large collision systems are dominated by flow. An ordering  $SC(m,n) \approx SC(m,n)_{3\text{-sub}} > SC(m,n)_{2\text{-sub}}$  can be seen in Pb–Pb collisions. One of the explanations might be the decorrelation of  $v_n$  coefficients in pseudorapidity  $\eta$ . In that case, the  $SC(m,n)$  measurements would depend on the choice of the subevents. An “opposite” ordering of  $SC(m,n)_{\text{sub}}$  is reported in small collision systems (as will be shown below in Fig. 6.10). Unfortunately, the large statistical fluctuations at low multiplicities of Pb–Pb collisions do not allow to check whether the observed behaviour persists at low  $N_{\text{ch}}$ .

In summary, the measurements of  $m$ -particle cumulants (for  $m > 2$ ) in large collision systems did not reveal a significant non-flow suppression with the subevent method, showing the strong dominance of final state collectivity.

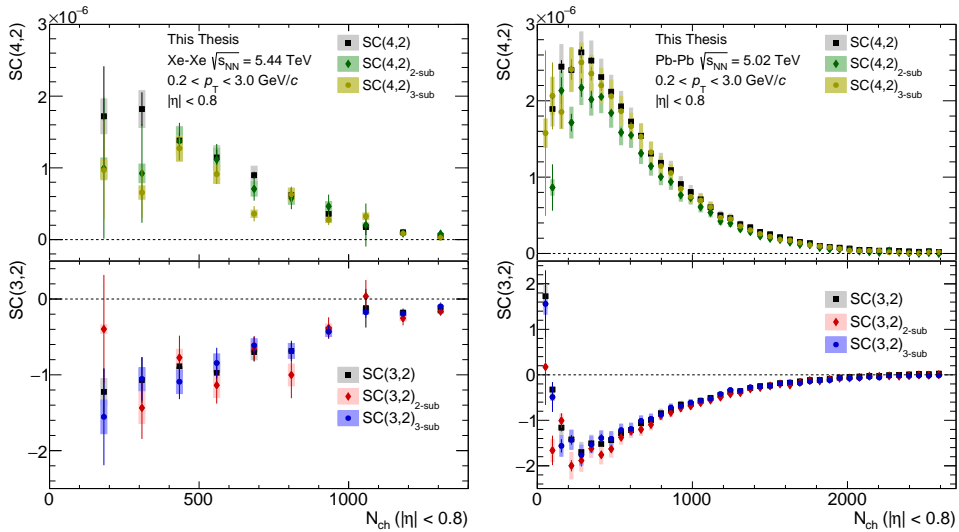


**Figure 6.6:** Multiplicity dependence of  $SC(4,2)$  (upper panels) and  $SC(3,2)$  (bottom panels) using the standard, 2- and 3-subevent method in 5.44 TeV Xe–Xe collisions (left) and in 5.02 TeV Pb–Pb collisions (right). The measurements using the different methods are compatible.

### Small collision systems

In small collision systems, the amount of used events for the analysis originally only allowed to calculate the four-particle cumulants, as can be seen in the Appendix E. However, with the collected data from the Run2 data taking, it is possible to calculate the four- and even the six-particle cumulant. In order to obtain a real-valued flow coefficient from multi-particle cumulants, the  $c_n\{4\}$  has to be negative, while the  $c_n\{6\}$  positive. In pp collisions, it is not possible to extract the  $v_n\{4\}$  even at high multiplicity events, where signatures of collectivity were revealed in other observables, e.g. the ridge structure at near-side in di-hadron correlation measurements. This is probably due to the large dominance of non-flow correlations. Non-flow effects have a positive contribution to the  $c_n\{4\}$ , while a negative contribution would be

generated by flow. Therefore, in a highly non-flow dominated system, the  $c_n\{4\}$  would be positive, not allowing for the calculation of  $v_n\{4\}$ . This doesn't necessarily mean that there is no  $v_2$ , but it suggests that the type of the underlying p.d.f. distribution of  $v_n$  is different from heavy-ion collisions. However, since the  $v_n$  distribution in small systems has not been investigated experimentally yet, one has to rely on the available measurements, i.e. the multi-particle cumulants. Models containing only non-flow exhibit a positive  $c_2\{4\}$ , or  $c_2\{4\}$  compatible with 0, as was shown e.g. in [47] for Pb–Pb collisions with HIJING calculations, or later in this thesis in Fig. 6.15 for pp collisions with PYTHIA 8 model. Positive  $c_2\{4\}$  was lately also generated with hydrodynamic simulations of pp collisions [78]. Therefore, in the search for collectivity in small systems, it is not possible to conclude anything if the  $c_n\{4\}$  is positive. On the other hand, once the  $c_n\{4\}$  turns negative, it is a hint of collectivity in small collision systems\*. Due to this property, the four-particle cumulant becomes a crucial observable in the investigation of collectivity in small collision systems.

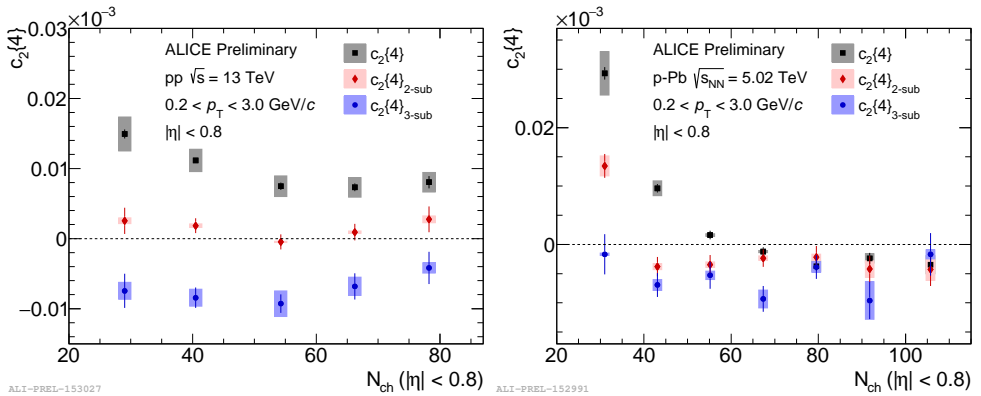


**Figure 6.7:** Multiplicity dependence of  $c_2\{4\}$ ,  $c_2\{4\}_{2-sub}$  and  $c_2\{4\}_{3-sub}$  in 13 TeV pp collisions (left) and 5.02 TeV p–Pb collisions (right). A clear reduction of  $c_2\{4\}$  with the subevent method is observed in both collision systems.

Even though the subevent method did not have a significant effect on multi-particle cumulant measurements in large collision systems, this might be different in small systems, where non-flow dominates. In Fig. 6.7, measurements of  $c_2\{4\}$  are shown as a function of multiplicity for pp collisions on the left panel, and p–Pb collisions on the right panel. In p–Pb collisions, the cumulant turns to be negative at  $N_{ch}(|\eta| < 0.8) \approx 60$ , which indicates the existence of collectivity in high multiplicity p–Pb collisions. Nevertheless, non-flow can still be largely suppressed in p–Pb collisions, demonstrated by the reduction of the  $c_2\{4\}$  to more negative values. Moreover, the subevent method resulted in a shift of the point, which is showing the crossing from positive to negative  $c_2\{4\}$ , down to lower  $N_{ch}$ .

In pp collisions, the  $c_2\{4\}$  is positive in the reported multiplicity region in Fig. 6.7. This might be due to the fact that non-flow contamination is larger in pp than in p–Pb collisions at the similar multiplicity range. In the same figure, four-particle cumulant measurements

\*Under the assumption that the measurements are free from e.g. multiplicity fluctuations, which were able to fake the negative  $c_2\{4\}$  in pp collisions [49].

with the 2- and 3-subevent method are shown as well. A clear decrease of the  $c_2\{4\}$  value can be seen in pp collisions, showing that non-flow effects can be largely suppressed in multi-particle cumulants using this method. The  $c_2\{4\}_{2\text{-sub}}$  is not yet negative, but compatible with 0 instead. However, the 2-subevent method would not be able to remove cases of e.g. back-to-back jets with emitted particles in the two subevents. With the 3-subevent method, an additional significant suppression was achieved in pp collisions, revealing a negative sign of the  $c_2\{4\}_{3\text{-sub}}$ . The negative four-particle cumulant is observed for the first time with ALICE, confirming the ATLAS findings [79]. This observation is an indication of multi-particle correlations present in pp collisions.

The negative  $c_2\{4\}_{3\text{-sub}}$  in pp collisions could only be obtained with the high multiplicity trigger. This can be seen in Fig. 6.8 (left), where the results from high multiplicity trigger (shown in Fig. 6.7) are compared to the results from the minimum-bias trigger. The decrease of the signal with the subevent method is clear also in minimum-bias collisions, however, even the  $c_2\{4\}_{3\text{-sub}}$  measurement with reduced non-flow contribution does not reveal a negative sign. Only further selection of events with the high multiplicity trigger based on the multiplicity in the forward region enabled to observe the negative  $c_2\{4\}_{3\text{-sub}}$ . This supports the fact that the event selection using the forward multiplicity might be able to further suppress non-flow, which was suggested in Chapter 4.1.3.

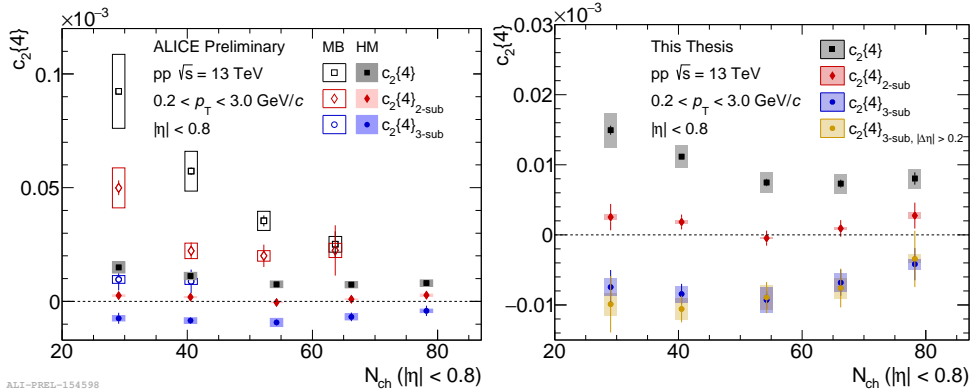


**Figure 6.8:** Left: Comparison of  $c_2\{4\}$ ,  $c_2\{4\}_{2\text{-sub}}$  and  $c_2\{4\}_{3\text{-sub}}$  results from high multiplicity and minimum-bias triggered pp events. Right: Multiplicity dependence of  $c_2\{4\}$ ,  $c_2\{4\}_{2\text{-sub}}$ ,  $c_2\{4\}_{3\text{-sub}}$  and  $c_2\{4\}_{3\text{-sub}, |\Delta\eta| > 0.2}$  in pp collisions. No significant further decrease is observed by putting  $|\Delta\eta| > 0.2$  gap between the subevents.

Even though there is a clear decrease of the value of four-particle cumulant in p-Pb collisions after applying the 2-subevent method, it seems to saturate with the 3-subevent method within the uncertainties. On the other hand, the difference in the non-flow suppression between the 2- and 3-subevent method in pp collisions is still very clear. Thus, it is natural to examine whether the 3-subevent method was already able to suppress most of the non-flow. This was studied with measurements of  $c_2\{4\}_{3\text{-sub}}$  with an additional  $|\Delta\eta| > 0.2$  gap between the subevents. The results for pp collisions are shown in Fig. 6.8 (right). Considering the small acceptance used in this analysis, splitting it into 3 subevents and applying a pseudorapidity gap

between them significantly reduces the amount of correlation  $m$ -tuplets, which in turn results in large statistical uncertainties. Within the error bars, no significant further suppression is observed with an additional gap  $|\Delta\eta| > 0.2$ . The measurement of  $c_2\{4\}_{3\text{-sub}}$  therefore represents a lower limit on the flow signal in pp collisions.

As mentioned above, with the amount of data collected during the LHC Run2 so far, it was possible to calculate the six-particle cumulant in both pp and p–Pb collisions. Measurements as a function of multiplicity are shown in Fig. 6.9 for pp collisions on the left, and p–Pb collisions on the right panel. Both collision systems show a non-zero positive value of  $c_2\{6\}$ , which allows to extract  $v_2\{6\}$ . However, this measurement is not as indicative in the investigation of collectivity as the  $c_2\{4\}$ , since both flow and non-flow have positive contributions to the six-particle cumulant. Nevertheless, comparisons of the  $v_n$  obtained from  $c_2\{m\}$  (where  $m = 4$  or  $6$ ), shown later on, are important to study the presence of multi-particle correlations. Finally, it would be interesting to check how strong is the non-flow contamination in the six-particle cumulant in small systems by measuring the  $c_2\{6\}_{2\text{-sub}}$ . Unfortunately, it was not possible to calculate such measurement with the available statistics.

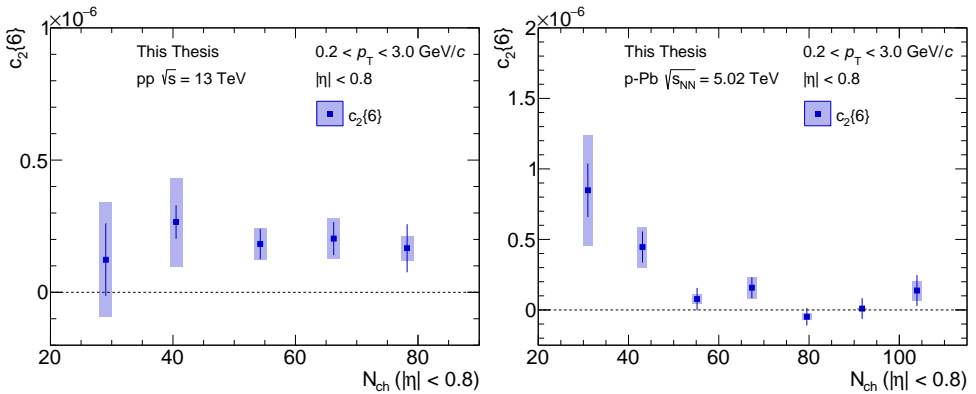


**Figure 6.9:** Left: Multiplicity dependence of  $c_2\{6\}$  in 13 TeV pp collisions (left) and in 5.02 TeV p–Pb collisions (right). Both collision systems show a non-zero positive value of  $c_2\{6\}$ .

Before this section is concluded,  $SC(m, n)$  are going to be examined here with the subevent method. The CMS experiment have measured the  $SC(3, 2)$  and  $SC(4, 2)$  in pp, p–Pb and low multiplicity Pb–Pb collisions [80]. However, their measurements were studied with the standard cumulant method without the subevent. Since it was shown that  $c_2\{4\}$  is affected by non-flow effects in small collision systems [59], the  $SC(m, n)$  might be affected by non-flow as well. The results of Symmetric Cumulants with the standard and the subevent method, measured in pp and p–Pb collisions, are shown in Fig. 6.10. In both collision systems, a large positive correlation is recognized between  $v_2$  and  $v_4$ , and between  $v_2$  and  $v_3$ . However, the strength of this correlation decreases after the reduction of a significant amount of non-flow effects thanks to the subevent method. Similarly, the measurements from ATLAS [81] and CMS experiments, which were presented at Quark Matter 2018 conference together with these ALICE results discussed here [82], show a strong further suppression of non-flow effects with the subevent method.

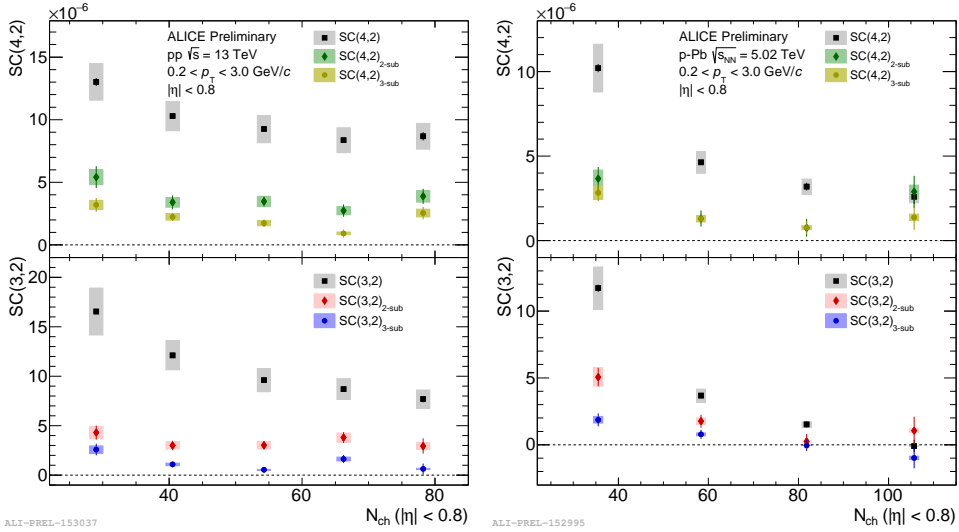


**Figure 6.10:** Multiplicity dependence of  $SC(4,2)$  (upper panels) and  $SC(3,2)$  (bottom panels) using the standard, 2- and 3-subevent method in 13 TeV pp collisions (left) and in 5.02 TeV p–Pb collisions (right). All measurements reveal a clear reduction of the strength of the  $v_n - v_m$  correlations with the subevent method.

### Summary of non-flow effects in multi-particle cumulant measurements

Similarly as was seen in the measurements of two-particle cumulants, no significant effect of the subevent method was observed in multi-particle cumulant results of large collision systems. An indication of a larger decrease of the  $SC(m,n)$  value with the 2-subevent method than with the 3-subevent method, which was compatible with the standard  $SC(m,n)$ , suggested decorrelations of  $v_n$  in pseudorapidity  $\eta$ .

Measurements in small collision systems increased the awareness of the importance of the subevent method. Further non-flow suppression was revealed in p–Pb collisions with the decrease of the  $c_2\{4\}$  to more negative values. A complete change of sign from positive to negative was discovered in pp collisions after the 3-subevent method was employed. A strong contamination of  $SC(m,n)$  with non-flow correlations was proven by the fact that the subevent method largely reduced the values of the measurements, both in pp and p–Pb collisions.

Therefore, it became clear that the influence of non-flow effects in the measurements of higher order cumulants is non-negligible, especially in small collision systems. It is crucial to measure the azimuthal particle correlations with the subevent method in order to prevent biased physics conclusions.

## 6.2 Comparison of results of $v_2\{m\}$ for $m \geq 2$

Figure 6.11 shows  $v_2\{m\}$  measurements as a function of  $N_{\text{ch}}$  in Xe–Xe collisions (panel (a)) and Pb–Pb collisions (panel (b)). The  $v_2$  measured with the two-particle cumulant is larger than the rest of the measurements using multi-particle cumulants:  $v_2\{2, |\Delta\eta| > 1.4\} >$

$v_2\{4\} \approx v_2\{6\} \approx v_2\{8\}$ . This is usually attributed to fluctuations of the underlying flow p.d.f. distribution [83]. In Pb–Pb collisions, the measurements of  $v_2\{m\}$  ( $m > 4$ ) seem to approach the  $v_2\{2, |\Delta\eta| > 1.4\}$  at very low multiplicity ( $N_{\text{ch}} < 100$ ), which is seen in small collision systems (shown below in Fig. 6.12). Unfortunately, the lack of data at low multiplicities does not allow to see whether the comparison between the two- and multi-particle cumulants becomes similar to what is observed in small collision systems at similar multiplicities.

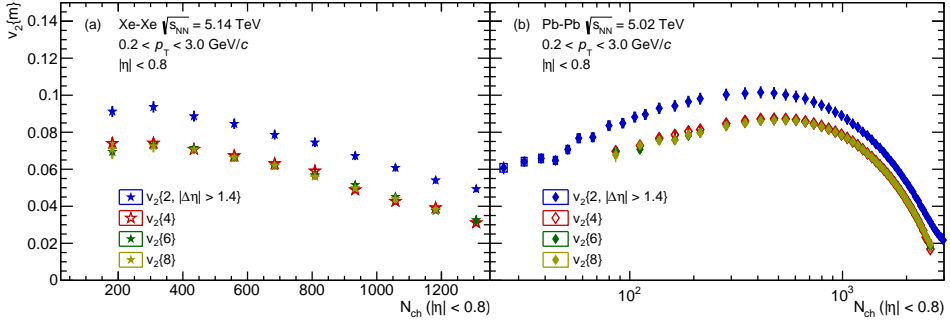


**Figure 6.11:** Multiplicity dependence of flow coefficient  $v_2$  using two-, four-, six- and eight-particle cumulant in 5.44 TeV Xe–Xe collisions (a) and in 5.02 TeV Pb–Pb collisions (b). The relation  $v_2\{2, |\Delta\eta| > 1.4\} \approx v_2\{4\} \approx v_2\{6\} \approx v_2\{8\}$  approximately holds for both collisions.

Measurements of  $v_2$  in small collision systems obtained from two-, four- and six-particle cumulant are compared in Fig. 6.12. A weak multiplicity dependence is observed for all the measurements shown for pp collisions in Fig. 6.12 (a). The  $v_2\{4\}$  could not be calculated due to the positive  $c_2\{4\}$  containing a large non-flow contamination. The measurements obtained with the two-, four- and six-particle cumulant are compatible with each other,  $v_2\{2, |\Delta\eta| > 1.4\} \approx v_2\{4\}_{3\text{-sub}} \approx v_2\{6\}$ , although  $v_2\{6\}$  is systematically higher across the whole multiplicity region. This can be caused by the remaining non-flow in  $v_2\{6\}$ , which has a positive contribution. The compatibility between  $v_2\{4\}_{3\text{-sub}}$  and  $v_2\{6\}$  can be improved with the 2-subevent method in the six-particle cumulants, which is expected to decrease the value of  $v_2\{6\}$ .

In Fig. 6.12 (b), the same measurements are presented in p–Pb collisions. Moreover, it was also possible to include results of  $v_2\{4\}$ , since flow-like effects start to prevail at large multiplicities, leading to a negative  $c_2\{4\}$ . Further suppression of non-flow effects with the 3-subevent method (causing the  $c_2\{4\}$  to decrease to more negative values) results in an increase of the  $v_2\{4\}_{3\text{-sub}}$ , as well as an extension of the available multiplicity range down to lower  $N_{\text{ch}}$ . Similarly as in pp collisions, there is an agreement between the  $v_2\{4\}_{3\text{-sub}}$  and  $v_2\{6\}$  within the uncertainties, which was achieved with the additional non-flow suppression with the 3-subevent method. Finally, the relation between  $v_2\{2, |\Delta\eta| > 1.4\}$  and  $v_2\{m\}$  for  $m > 2$  is similar to what is observed in large collision systems:  $v_2\{2, |\Delta\eta| > 1.4\} > v_2\{4\} \approx v_2\{6\}$ .

Similar comparison of  $v_2\{m\}$  measurements as a function of multiplicity was performed by the ATLAS and CMS experiments [50, 79]. The measured  $v_2$  using the di-hadron correlations appeared to be compatible with the higher order cumulants,  $v_2\{2\text{PC}\} \approx v_2\{4\} \approx v_2\{6\}$ , for CMS [50]. On the other hand, ATLAS did not confirm such an observation. Instead, they

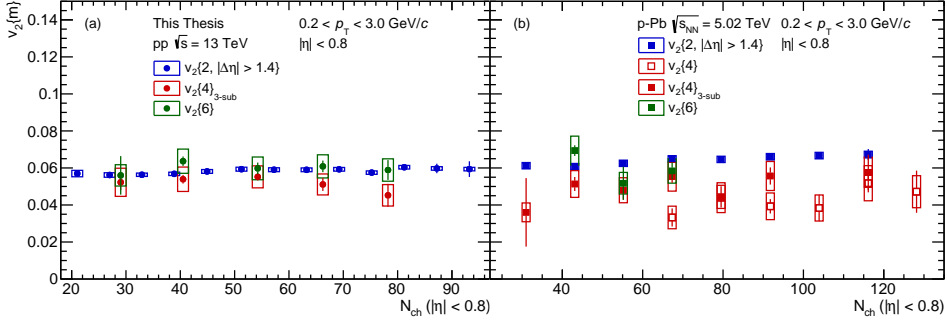


**Figure 6.12:** Multiplicity dependence of flow coefficient  $v_2$  using two-, four- and six-particle cumulant in 13 TeV pp collisions (a) and in 5.02 TeV p-Pb collisions (b). All measurements show weak multiplicity dependence. (a): Results from different order cumulants are compatible with each other  $v_2\{2, |\Delta\eta| > 1.4\} \approx v_2\{4\}_{3\text{-sub}} \approx v_2\{6\}$ . (b): The relation  $v_2\{2, |\Delta\eta| > 1.4\} > v_2\{4\}_{3\text{-sub}} \approx v_2\{6\}$  approximately holds for p-Pb collisions.

reported [79] that  $v_2\{2PC\} > v_2\{4\}_{3\text{-sub}}$ , which suggests similar type of the underlying flow p.d.f. as in p-Pb or Pb-Pb collisions. The difference between the results from these two experiments, apart from the possible effects of multiplicity fluctuations in CMS results, are due to different methods used for the subtraction of non-flow effects. These approaches to the calculation of the flow coefficient from two-particle correlations are yet different from the method used in ALICE results presented in this thesis. In addition, it should be noted that the measurements from other experiments and ALICE are obtained with different acceptances, and also with different selection of high multiplicity events: ATLAS and CMS select high multiplicity events based on the multiplicity at mid-rapidity, while ALICE uses the forward multiplicity selection.

### Summary from comparison of $v_2\{m\}$ (for $m \geq 2$ ) measurements

The difference between  $v_2\{2\}$  and  $v_2\{m\}$  ( $m > 2$ ) seen in Pb-Pb, Xe-Xe, and even in p-Pb collisions, although less pronounced, might arise from similar type of the underlying flow p.d.f. distribution [83]. A vanishing difference between  $v_2$  from the two- and four-particle cumulant is reported here in pp collisions. This might be interpreted with a different flow p.d.f., or with a small number of sources  $N_s = 4v_2\{2\}^4/v_2\{4\}^4 - 3$  [79, 83, 84], which would cause a negligible ratio of  $v_2\{4\}/v_2\{2\}$ , therefore  $v_2\{2\} \approx v_2\{4\}$ . Also, this observation might simply arise from biased measurements by the decorrelation of  $v_n$  in pseudorapidity, which would be connected to the large  $|\Delta\eta|$  gap used in the two-particle cumulant.

## 6.3 Direct comparison of small and large collision systems

### 6.3.1 Flow coefficients $v_n$ measured with two-particle cumulants

Measurements of flow coefficients  $v_2$ ,  $v_3$  and  $v_4$  calculated with the two-particle cumulant as a function of  $N_{ch}$  is shown in Fig. 6.13 for pp, p-Pb, Xe-Xe and Pb-Pb collisions in order to directly compare the measurements and assess the similarities between large and small

collision systems. Only results with the largest possible  $|\Delta\eta|$  gap with reduced contamination from non-flow effects are presented. Ordering of the flow coefficients,  $v_2 > v_3 > v_4$ , is common for all systems. In addition, weak multiplicity dependence of higher order flow coefficients,  $v_3$  and  $v_4$ , is also seen for both small and large collision systems. The distinct shape of  $v_2$  with multiplicity in Xe–Xe and Pb–Pb collisions, firstly decreasing at large  $N_{\text{ch}}$  and then increasing at low  $N_{\text{ch}}$ , is connected to the initial overlap geometry of the nuclei. The increasing trend of  $v_2$  with multiplicity is also observed in small collision systems, although it is much more modest compared to the large collision systems. At very low multiplicity,  $N_{\text{ch}} < 50$ ,  $v_2$  from small and large collision systems become compatible.

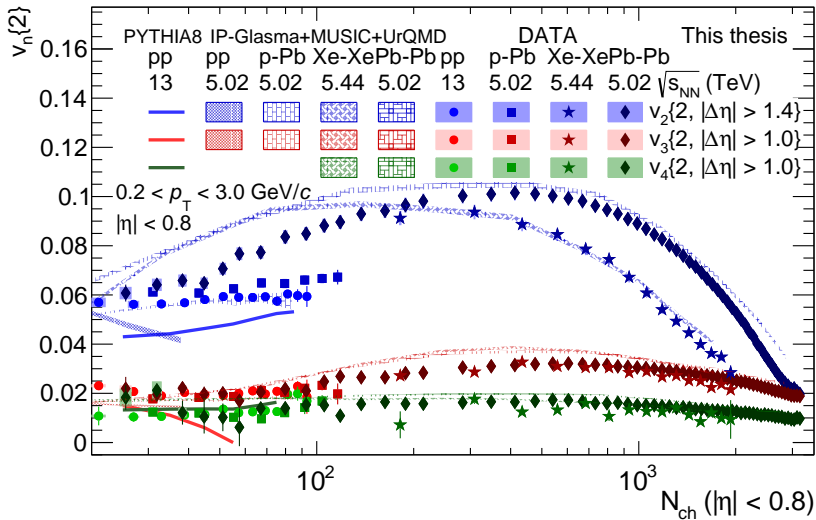


**Figure 6.13:** Multiplicity dependence of flow coefficients  $v_2$ ,  $v_3$  and  $v_4$  using two-particle cumulant with a  $|\Delta\eta|$  gap for small (pp and p–Pb) and large (Xe–Xe and Pb–Pb) collision systems. The measurements are compared to the PYTHIA 8 simulations [56, 57] of  $\sqrt{s} = 13$  TeV pp collisions, and the IP-Glasma+MUSIC+UrQMD [85, 86] simulations of all four collision systems.

Measurements in Fig. 6.13 are compared to PYTHIA 8 simulation [56, 57] of pp collisions at  $\sqrt{s} = 13$  TeV, which is a model that aims to describe the high energy collisions of elementary particles (e.g. protons), thus it does not include final state collective effects. The main source of azimuthal correlations in this model are jets or resonance decays, which we denote as non-flow. The simulation results were obtained with the ALICE software and computational resources, and calculated using the same procedure as in the real data analysis<sup>†</sup>.

PYTHIA calculations are represented with the coloured lines: blue for  $v_2$ , red for  $v_3$  and green for  $v_4$ . The model underestimates the  $v_2$  measurement in pp collisions. At the same time, it cannot catch the weak multiplicity dependence observed in data. Instead, a rising trend with multiplicity is reported in the simulation results. This observation alone

<sup>†</sup>For more details on the simulation setup see Appendix F

is not expected from a non-flow only model, but is probably caused by the forward high multiplicity selection. The third flow coefficient  $v_3$  cannot be reproduced by PYTHIA either; the calculation reveals a lower value of  $v_3$  compared to what is observed in data. In addition, the simulation result has a decreasing trend with multiplicity, until the signal vanishes at  $N_{\text{ch}} \approx 45$ , while the measurements from pp collisions have a weak multiplicity dependence. This strange decreasing trend of  $v_3$  in PYTHIA was noticed to be present only when large  $|\Delta\eta|$  gap was applied. The standard  $v_3$ , or  $v_3$  with only small pseudorapidity separation, appear to have similar behaviour as the rest of the flow coefficients. The reason for such behaviour remains to be understood. Finally, in contrast to the lower orders of flow coefficients, the  $v_4$  calculated with PYTHIA seems to be compatible with the measurement in pp collisions in the presented multiplicity range.

The IP-Glasma+MUSIC+UrQMD hydrodynamic model (including sub-nucleon fluctuations in the initial state) [85, 86], is also added for comparison in Fig. 6.13. Very recent extension of this model to the smallest collision system, the pp collisions, was shown at Quark Matter 2018 [87]. The authors provided the data points from their newest calculations, performed for all collision systems that are considered in this thesis. Their flow coefficients are obtained from two-particle correlations and are presented as a function of charged particle multiplicity at  $|\eta| < 0.8$  and with  $0.2 < p_T < 3.0$  GeV/c. The  $v_2$ ,  $v_3$  and  $v_4$  are provided in Pb–Pb and Xe–Xe collisions, while only  $v_2$  and  $v_3$  are calculated for small collision systems. The collision energies match those used in the experiment, except for pp collisions, where the energy is  $\sqrt{s} = 5.02$  TeV instead of 13 TeV. However, this should have a negligible effect on the final results, since the measurements of  $v_n$  in pp collisions were found to be independent on collision energy [49].

The hydrodynamic calculations are represented with coloured bands, with similar colour code as used for the representation of experimental results. The model can quantitatively reproduce the results from Pb–Pb and Xe–Xe collisions at high multiplicities. On the other hand, this agreement does not hold at low  $N_{\text{ch}}$ , where the model significantly overpredicts the data. The model calculations of p–Pb collisions can describe the weak multiplicity dependence of the  $v_2$  and  $v_3$  in experimental results. However, the value from the simulations slightly underestimates the measurements, which might suggest that non-flow has not been fully suppressed with  $|\Delta\eta| > 1.4$  in p–Pb collisions. Despite the ability of the model to continuously reproduce the p–Pb, Xe–Xe and Pb–Pb measurements, results in pp collisions are not reflected in the model: the magnitude is underestimated, and the overall trend of  $v_n$  from theoretical calculations is decreasing with increasing multiplicity, while the measurements are approximately constant in the whole multiplicity range. Further improvements in the theoretical description of pp collisions are ongoing by authors.

In summary, the presented flow coefficients measured with the two-particle cumulant method exhibit similarities between small and large collision systems at comparable multiplicity range. The  $v_n$  in pp collisions cannot be explained by non-flow only model. On the other hand, hydrodynamic calculations did not describe these measurements either, while the  $v_n$  from Pb–Pb, Xe–Xe and p–Pb collisions seem to be reproduced fairly well. At the same time,  $v_n\{2, |\Delta\eta|\}$  measurements might still contain some level of non-flow, which might bias the final conclusions. This calls for the usage of more robust observables, presented in the following sections.

### 6.3.2 Flow coefficients $v_n$ measured with multi-particle cumulants

Second order flow coefficient  $v_2$  calculated with  $m$ -particle cumulants (for  $m > 2$ ) is shown for all collision systems in Fig. 6.14. Standard multi-particle cumulant measurements are compared to measurements with the subevent method, which was calculated up to the eight-particle cumulant in Pb–Pb collisions. It is clear that large collision systems are collective: the fact that multi-particle cumulant measurements with the standard and the subevent method are compatible ( $v_2\{4\} \approx v_2\{4\}_{3\text{-sub}}$ ,  $v_2\{6\} \approx v_2\{6\}_{2\text{-sub}}$ ,  $v_2\{8\} \approx v_2\{8\}_{2\text{-sub}}$ ) shows that the correlations are long-range. At the same time, the results from all orders of multi-particle cumulants are consistent  $v_2\{4\} \approx v_2\{6\} \approx v_2\{8\}$ , which shows that the correlations are among many particles. Flow dominant large collision systems are compared to the IP-Glasma+MUSIC+UrQMD [85] hydrodynamic calculations in Fig. 6.14. The agreement between  $v_2\{4\}$  from experimental measurements and theory calculations is very good in Pb–Pb collisions, and within uncertainties also holds in Xe–Xe. Similarly as for the  $v_2$  obtained from two-particle cumulants shown above, the calculations from both collision systems become compatible at low multiplicity. The model description of experimental data at this region of  $N_{\text{ch}}$  gives better result when compared to multi-particle cumulant measurements than to two-particle cumulant results, suggesting that multi-particle cumulants are less sensitive to non-flow.

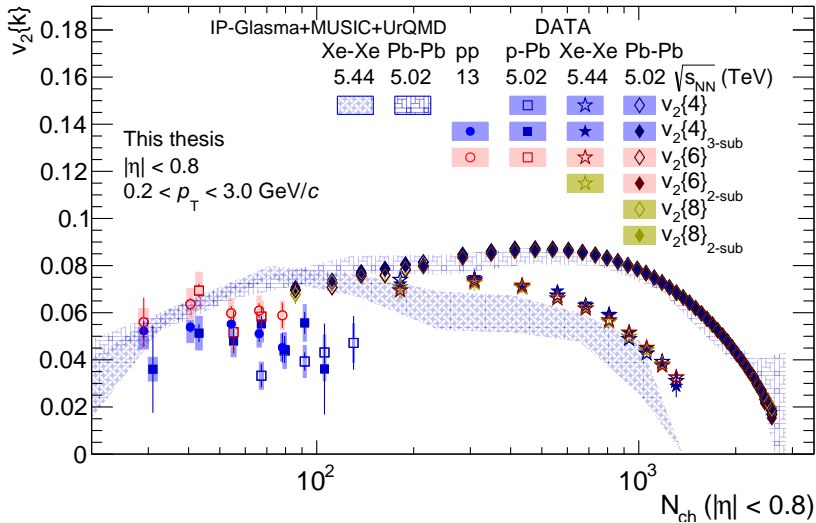


**Figure 6.14:** Multiplicity dependence of  $v_2\{m\}$  for  $m > 2$  with the standard and the subevent method for small (pp and p–Pb) and large (Xe–Xe and Pb–Pb) collision systems. The Xe–Xe and Pb–Pb results are compared to the IP-Glasma+MUSIC+UrQMD calculations [85, 86].

The four- and six-particle cumulant measurements in pp and p–Pb collisions are compatible with each other, similarly as was reported in Xe–Xe and Pb–Pb collisions. This could be achieved only after the non-flow suppression with the 3-subevent method in the four-particle cumulant, as discussed in section 6.1.2. Improved agreement could be done with

the  $v_2\{6\}_{2\text{-sub}}$ , which is expected to be slightly smaller than  $v_2\{6\}$ . Comparison of the hydrodynamic model to the measurements of multi-particle cumulants in small collision systems was not available at the time of writing this thesis. On the other hand, the large generated sample of PYTHIA 8 events allowed to obtain results from multi-particle cumulants in pp collisions at  $\sqrt{s} = 13$  TeV. A direct comparison to the  $v_2\{m\}$  measurements in Fig. 6.14 is not possible since the strong dominance of non-flow inhibits the calculation of real-valued  $v_2$  by inducing a positive sign of the four-particle cumulant in PYTHIA. Therefore, comparison to  $c_2\{m\}$  measurements is shown instead in Fig. 6.15, with  $c_2\{4\}$  on the left panel, and  $c_2\{6\}$  on the right panel. It is clear that PYTHIA is not able to describe the multi-particle cumulant measurements in pp collisions. A suppression of non-flow with the subevent method is apparent, however the  $c_2\{4\}_{3\text{-sub}}$  from PYTHIA simulations remains compatible with 0, while the data show a clear negative value. The  $c_2\{6\}$  simulation result is resembling the value of the measurement shown on the right panel, although PYTHIA calculations are systematically lower than the data. This might suggest that the  $v_2\{6\}$  measurement in small collision systems still contains some non-flow, supporting the necessity of the subevent method in  $v_2\{6\}$  measurements in order to reduce the influence of these effects and improve the agreement  $v_2\{4\}_{3\text{-sub}} \approx v_2\{6\}$  in small collision systems, that was discussed above.

To conclude, similarities than can be seen between the  $v_2$  measurements of multi-particle cumulants from small and large collision systems shown in Fig. 6.14, indicate the presence of collectivity in p–Pb and pp collisions. Furthermore, the disagreement of the results with PYTHIA 8 calculations supports this indication by showing that non-flow effects alone cannot explain the negative  $c_2\{4\}$ .

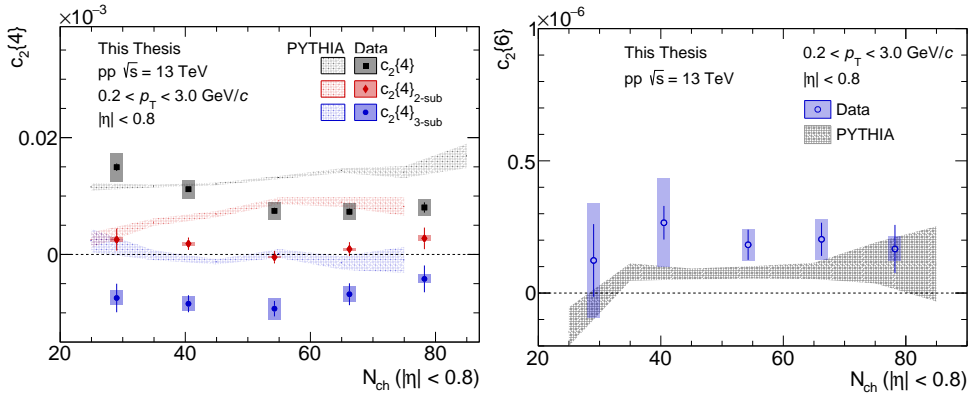


**Figure 6.15:** Left: Multiplicity dependence of  $c_2\{4\}$ ,  $c_2\{4\}_{2\text{-sub}}$  and  $c_2\{4\}_{3\text{-sub}}$  from pp collisions, compared to the PYTHIA calculations. The model does not describe the measurements. Right: Comparison of the  $c_2\{6\}$  measurement from pp collisions to the PYTHIA calculations [56, 57]. The model underestimates the data.

### Summary from measurements of flow coefficients

Measurements of flow coefficients using the two- and multi-particle cumulants shown here suggest the presence of collectivity in small collision systems. This is supported by the

observed similarities between the measurements of small and large collision systems (which are further compatible with hydrodynamic calculations in the whole multiplicity range), and the disagreement between the pp results and PYTHIA 8 calculations containing non-flow effects. On the other hand, the IP-Glasma+MUSIC+UrQMD calculations did not reproduce the reported pp results either. It is important to note that this does not immediately disfavor hydrodynamic description of this small collision system. Another hydrodynamic model using the superSONIC framework with UrQMD simulation of the hadronic phase actually showed an agreement with measurements of  $v_n$  from Pb–Pb, p–Pb and even pp collisions [88]. With the suitable title of “One fluid to rule them all”, this model justifies that hydrodynamics might be one of the explanations responsible for the observed collectivity also in small collision systems. Another possibility was introduced by an initial state model, which was able to reproduce the pattern of  $v_n\{m\}$  in p–Pb collisions [89]. Collectivity originating in the initial state indeed appears to be important in small collision systems, as was discussed in [87, 90]. Thus, more observables sensitive to the initial state effects, and their comparison to model calculations, are necessary to conclude about the origin of collectivity observed in data.

### 6.3.3 $SC(m, n)$ measured with multi-particle cumulants

The collectivity feature observed in small collision systems naturally raises a question: what is its origin? In large collision systems it is well understood that the observed collectivity comes from the hydrodynamically flowing QGP. However, the answer in small collision systems is not known yet.

Measurements of Symmetric Cumulants and normalised Symmetric Cumulants reflect the correlation between different orders of flow coefficients. It was shown that these measurements provide further constraints to model parameters in heavy-ion collisions [43]. In particular, flow coefficients  $v_2$  and  $v_3$  are believed to be directly connected to the initial spatial eccentricities,  $\epsilon_2$  and  $\epsilon_3$ . On the other hand,  $v_4$  coefficient, apart from the linear part which is connected to the cumulant-defined initial quadrangular eccentricity  $\epsilon_4$ , contains also non-linear flow modes from  $v_2$ , which build up during the QGP phase [40]. Thus, correlations between  $v_2$  and  $v_3$ , and between  $v_2$  and  $v_4$ , help constrain the initial conditions and the transport properties of the QGP. These capabilities of Symmetric Cumulants measurements propose a way to provide additional insight into the studies of the origin of collectivity in small collision systems.

It was shown in section 6.1.2 that non-flow effects largely affect measurements of Symmetric Cumulants, especially in non-flow dominated small collision systems. Therefore, only results with the 3-subevent method are chosen for comparison. Figure 6.16 shows  $SC(m, n)_{3\text{-sub}}$  as a function of multiplicity in pp, p–Pb, Xe–Xe and Pb–Pb collisions. The upper panel shows the correlation between  $v_2$  and  $v_4$ , and the bottom panel the correlation between  $v_2$  and  $v_3$ . Positive  $SC(4, 2)_{3\text{-sub}}$  is observed in all collision systems from small to large multiplicities. Large collision systems reveal an anti-correlation between  $v_2$  and  $v_3$  at intermediate and large multiplicities, similarly as was observed in [43, 91]. At low multiplicity region, the  $SC(3, 2)_{3\text{-sub}}$  from Pb–Pb collisions approaches 0, and eventually changes its sign from negative to positive. The positive correlation is reported in both pp and p–Pb collisions, too. In addition, the multiplicity trend indicating a crossing point at 0 seems to be followed by the small collisions systems.

Hydrodynamic calculations of IP-Glasma+MUSIC+UrQMD [85] are compared to the  $SC(m, n)$  measurements in large collision systems with the coloured bands. A qualitative

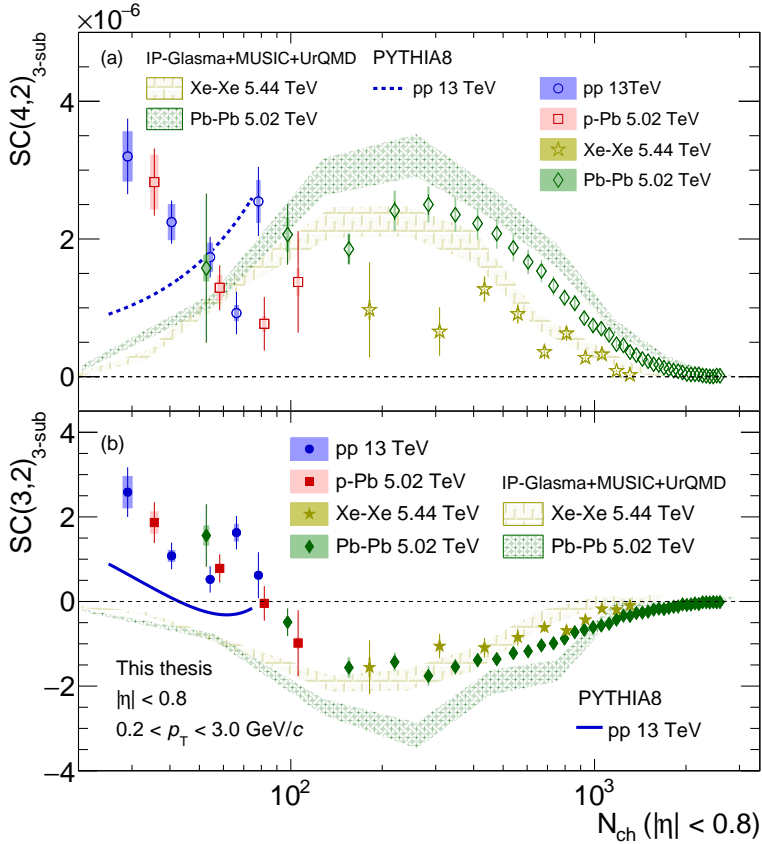


**Figure 6.16:** Top: Multiplicity dependence of  $SC(4,2)_{3-sub}$  for small (pp and p-Pb) and large (Xe-Xe and Pb-Pb) collision systems. Bottom: Measurements of  $SC(3,2)_{3-sub}$  for small (pp and p-Pb) and large (Xe-Xe and Pb-Pb) collision systems. Results from pp collisions are compared to PYTHIA 8 calculations [56, 57] (blue lines), and the coloured bands represent IP-Glasma+MUSIC+UrQMD [85] hydrodynamic calculations from Xe-Xe and Pb-Pb collisions.

agreement between the theory and experimental data is achieved at intermediate and large multiplicities, for both  $SC(4,2)$  and  $SC(3,2)$  observables. The low multiplicity region yields a different result. While the  $SC(4,2)_{3-sub}$  seems to be qualitatively reproduced by the hydrodynamic model, the negative  $SC(3,2)_{3-sub}$  from model is in disagreement with the crossing from negative to positive values seen in Pb-Pb collisions. This suggests that non-flow effects, dominant at this low multiplicity region, are not completely suppressed with the 3-subevent method.

Whether non-flow correlations are indeed responsible for the generally observed positive  $SC(m,n)_{3-sub}$  at low multiplicities can be studied with comparison to a non-flow model. Results from PYTHIA 8 [56, 57] are drawn in Fig. 6.16 for  $\sqrt{s} = 13 \text{ TeV}$  pp collisions as

blue lines. Even though a positive  $SC(4,2)_{3\text{-sub}}$  is seen both in theory calculations and data, the dependence on  $N_{\text{ch}}$  is different. The decreasing trend of  $SC(3,2)_{3\text{-sub}}$  with multiplicity is reflected in the PYTHIA 8 model. However, the strength of the correlation is not reproduced. Therefore, non-flow effects alone cannot be considered as the only explanation of experimental findings in  $SC(m,n)_{3\text{-sub}}$  measurements at low multiplicity.

Genuine correlations between  $v_n$  and  $v_m$  can be obtained by dividing the  $SC(m,n)_{3\text{-sub}}$  measurements with the product  $\langle v_n^2 \rangle \langle v_m^2 \rangle$ , called the normalised Symmetric Cumulants  $NSC(m,n)_{3\text{-sub}}$ . In particular,  $v_n \{2, |\Delta\eta|\}$  with the largest available pseudorapidity separation are chosen for the normalisation in order to reduce the effects from non-flow. With the normalisation, the correlations between flow coefficients can be compared among different collision systems without the influence of different magnitudes of  $v_n$  and its dependence on multiplicity. In addition, the sensitivity of  $v_n$  to the system dynamics is removed in  $NSC(m,n)$  measurements. Thus,  $NSC(3,2)$  puts tight constraints on the initial-state fluctuations, while  $NSC(4,2)$  on both initial conditions and medium transport coefficients [43].

The comparison of  $NSC(m,n)_{3\text{-sub}}$  between small and large collision systems is shown in Fig. 6.17, where  $NSC(4,2)_{3\text{-sub}}$  is presented on the upper panel, and  $NSC(3,2)_{3\text{-sub}}$  on the bottom panel. Both observables are compatible among all the collision systems, although large statistical fluctuations are present in  $NSC(4,2)_{3\text{-sub}}$ , probably caused by the large uncertainties in  $v_4$  results. The normalised Symmetric Cumulants reveal much stronger correlations at low than at large multiplicities, which was not caught by the  $SC(m,n)_{3\text{-sub}}$  results. In general, the good agreement within uncertainties between all collision systems invites to suggest a common origin of collectivity in both small and large collision systems. However, it is important to note that the  $SC(m,n)$  measurements were divided by the  $v_n$  results obtained from the two-particle cumulant, which is not robust against few-particle short-range correlations, even after applying a large  $|\Delta\eta|$  gap. Thus, this ratio introduces remnants of non-flow effects, which are more significant in small than in large collision systems.

The positive type of correlation between  $v_2$  and  $v_4$  among various sizes of collision systems is confirmed by the ATLAS and CMS experiments [80, 81]. However, the crossing of  $SC(3,2)_{3\text{-sub}}$  from negative to positive values at low multiplicities presented above is not seen by these experiments. On the contrary, they report a complete change of sign of  $SC(3,2)_{\text{sub}}$  from positive to negative correlation in the whole multiplicity region. This apparent difference between ALICE and ATLAS/CMS results probably has an origin in the different ranges of the detector acceptance used in the analyses. The longitudinal decorrelation of  $v_n$  might play a more significant role in ATLAS/CMS measurements compared to the almost three times smaller acceptance of ALICE.

### Summary from measurements of Symmetric Cumulants

The presented measurements of Symmetric Cumulants indicate that the origin of collectivity seen in small collision systems is universal with the one from large collision systems at similar multiplicities. However, neither PYTHIA 8, nor hydrodynamic IP-Glasma+MUSIC+UrQMD calculations were able to fully reproduce the measurements and interpret the observed collective phenomena. Apart from the presented theory calculations, AMPT model of p-Pb collisions [92] was able to reproduce CMS results of  $SC(m,n)$  [80] and predict the behaviour of these measurements with the subevent method, later shown by ATLAS [81]. Finally, model of p-Pb collisions based on initial state effects [89] qualitatively predicted positive correlation

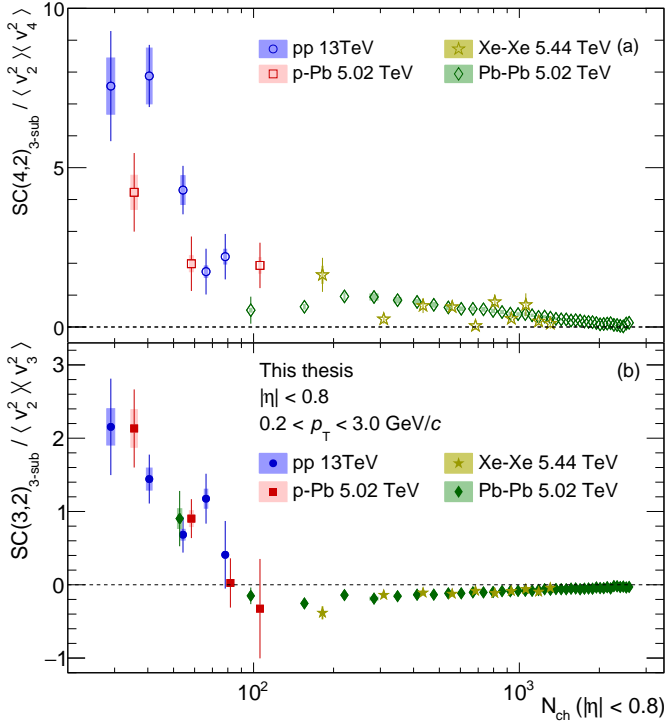
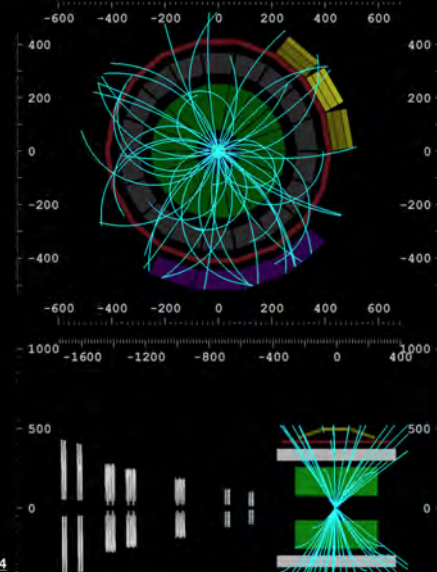
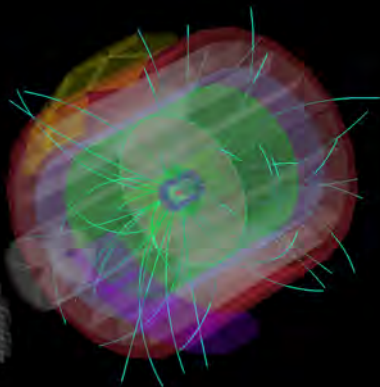


**Figure 6.17:** Multiplicity dependence of normalised  $SC(4,2)_{3\text{-sub}}$  (top) and  $SC(3,2)_{3\text{-sub}}$  (bottom) for small (pp and p-Pb) and large (Xe-Xe and Pb-Pb) collision systems. The  $v_n$  in the denominator are taken from the two-particle cumulant measurements with the largest available  $|\Delta\eta|$  gap.

between  $v_2$  and  $v_4$  and the crossing from negative to positive correlation between  $v_2$  and  $v_3$ , although the magnitude of results was overestimated and direct comparison to data is not possible due to unclear connection to the  $x$ -axis variable used in this model. Overall, there is no single framework that would describe the  $SC(m, n)$  in pp collisions, yet.



pp@13 TeV, ALICE, taken from: <https://cds.cern.ch/record/2020604>

## 7. Conclusions

The properties of the QGP created in the ultrarelativistic heavy-ion collisions has been scrutinised over the past years with the measurements of azimuthal anisotropy quantified by the flow coefficients  $v_n$ . It was found that the QGP is a strongly interacting, almost perfect fluid, which expands collectively. This collectivity can be observed in the form of long-range multi-particle azimuthal correlations. In the recent years, small collision systems have revealed features usually ascribed to the presence of the QGP in heavy-ion collisions, such as the ridge structure at near side in the two-particle correlations spanning long range in pseudorapidity  $\eta$ . Since this type of collisions was not expected to be collective, it became important to further investigate this topic and understand the mechanisms responsible for such observations in pp and p–Pb collisions.

This thesis presented the first ALICE results of flow coefficients  $v_n$ , and their correlations via  $SC(m, n)$ , as a function of charged particle multiplicity in  $\sqrt{s_{NN}} = 5.02$  TeV Pb–Pb,  $\sqrt{s_{NN}} = 5.44$  TeV Xe–Xe,  $\sqrt{s_{NN}} = 5.02$  TeV p–Pb and  $\sqrt{s} = 13$  TeV pp collisions from the LHC Run 2 data taking. The main goal of these measurements was to contribute to the investigation of collectivity in small collision systems and attempt to determine its origin.

Results were measured using the cumulant method with two- and multi-particle correlations, which was described in Chapter 2. Small collision systems are highly contaminated by the short-range few-particle correlations, called non-flow, which do not arise from the global correlations with respect to a common symmetry plane. The analysis techniques were therefore extended with the subevent method, which is successful in largely suppressing the contribution from non-flow. This was a crucial step forward in analyses of azimuthal correlations in small collision systems.

The influence of the subevent method on the measurements from pp, p–Pb, Xe–Xe, and Pb–Pb collisions was investigated in Chapter 6. No significant effect was observed in large collision systems due to the dominance of flow. The success of the subevent method became

apparent when it revealed a negative  $c_2\{4\}_{3\text{-sub}}$  in pp collisions, a first compelling indication of collectivity observed for the first time with ALICE experiment. Moreover, the subevent method largely reduced the non-flow contamination in  $c_2\{4\}$  in p–Pb collisions, which was displayed by a decrease of  $c_2\{4\}$  down to more negative values. Finally, measurements of Symmetric Cumulants in small collision systems have also proven to be significantly contaminated by non-flow effects, which was demonstrated by the large decrease of the strength of  $v_n - v_m$  correlations after applying the subevent method. These findings imply that the interpretation of results in small collision systems might be biased if non-flow contributions to the measurements are not treated properly.

Chapter 6 continued with the presentation of the comparison of measurements of flow coefficients in different collision systems. Hints of other than just non-flow effects in small collision systems were revealed with  $v_n\{2\}$  results, such as the weak multiplicity dependence, non-trivial ordering of  $v_n$  and values approaching those measured in large collision systems at similar multiplicities. Measurements of multi-particle cumulants probed the existence of collectivity in small systems further. Real-valued  $v_2\{4\}_{3\text{-sub}}$  in pp and p–Pb collisions was found to be compatible with  $v_2\{6\}$ , similar to the observations made in large collision systems ( $v_2\{4\} \approx v_2\{6\} \approx v_2\{8\}$ ). This strongly supports the idea of presence of collectivity in small collision systems. Measurements in pp collisions were compared to PYTHIA 8 and IP-Glasma+MUSIC+UrQMD calculations. Neither of the two models can describe the measurements seen in this type of collisions. On the other hand, hydrodynamic calculations were able to reproduce results from Pb–Pb, Xe–Xe and p–Pb collisions fairly well.

Investigations of the source of collectivity in small collision systems were brought forward with the measurements of  $SC(m, n)$  and normalised  $SC(m, n)$ . These observables determine the correlation between different orders of flow coefficients  $v_n$  and  $v_m$ . A positive correlation between  $v_2$  and  $v_4$  was observed for all systems. In Pb–Pb collisions, the anti-correlation between  $v_2$  and  $v_3$  changed to a positive correlation at small multiplicities, which was followed by both pp and p–Pb collisions. Such a comparable behaviour observed among different collision systems suggests a similar origin of the collectivity seen in large and small collision systems. The nature of these phenomena was further probed with comparison of PYTHIA 8 to results from pp collisions, and IP-Glasma+MUSIC+UrQMD calculations to results from large systems. The compatibility between the data and theory at large multiplicities in the later case clearly shows the dominance of hydrodynamic collectivity. The failure of this model to describe these measurements at multiplicities similar to those produced in small collision systems indicate remnants of other type of effects. Comparison of measurements in pp collisions to PYTHIA8 at this multiplicity range suggests that some non-flow contributions still persists in the measurements, although it cannot explain the results completely.

The puzzle about the origin of the collectivity in small collision systems is still waiting to be solved. Final state models [86, 88, 92] suggest that a small droplet of the QGP might be created in small collision systems. On the other hand, the collective phenomena revealed in the measurements of small collision systems can be also addressed with the initial state based models [89]. Finally, a compromise between the initial and final state effects, which contribute with similar strength to the final azimuthal anisotropies in small collision systems, appears to be a reasonable suggestion for the explanation of the collective behaviour in small collision systems [87, 90]. Further model comparisons, and further developments of observables sensitive enough to disentangle between various theoretical approaches, are crucial to find

---

a definite answer to the source of collective phenomena in various collision systems. The measurements presented in this thesis in a broad range of collision systems, using the latest methods to provide the least biased results, will help in the future studies of collectivity in small collision systems by putting constraints to model calculations.

The main measurements presented in this thesis are aiming for a publication in the *Phys. Rev. Lett.*. The proposal was approved by the collaboration and the paper draft is now being internally reviewed, so it is expected to be publicly available within few months. More detailed investigations with all the measurements presented here, extended with differential studies as a function of  $p_T$ , are planned to be contained in a long publication which is expected to be ready next year. In addition, this time will be used to include all the available ALICE data from pp, and probably even the new expected Pb–Pb collisions taken in the end of the year 2018. Apart from the significant increase of statistics, the new pp data will also provide a significant amount of high multiplicity events selected with the SPD trigger, that will be free from effects imposed by the forward high multiplicity event selection with the V0 detector.

Apart from completing the ALICE experimental measurements, a plan is to also release a publication summarising the application of the subevent method in the Generic Framework.





# Bibliography

- [1] “Standard model of elementary particles.”  
[https://commons.wikimedia.org/wiki/File:Standard\\_Model\\_of\\_Elementary\\_Particles.svg](https://commons.wikimedia.org/wiki/File:Standard_Model_of_Elementary_Particles.svg). Accessed: 30.06.2018.
- [2] R. Stock, “Relativistic Nucleus-Nucleus Collisions and the QCD Matter Phase Diagram,” arXiv:0807.1610 [nucl-ex].
- [3] J. D. Bjorken, “Highly Relativistic Nucleus-Nucleus Collisions: The Central Rapidity Region,” *Phys. Rev.* **D27** (1983) 140–151.
- [4] E. Iancu, “QCD in heavy ion collisions,” in *Proceedings, 2011 European School of High-Energy Physics (ESHEP 2011): Cheile Gradistei, Romania, September 7-20, 2011*, pp. 197–266. 2014. arXiv:1205.0579 [hep-ph].  
<http://inspirehep.net/record/1113441/files/arXiv:1205.0579.pdf>.
- [5] “The Frontiers of Nuclear Science, A Long Range Plan,” arXiv:0809.3137 [nucl-ex].
- [6] **HotQCD** Collaboration, A. Bazavov *et al.*, “Equation of state in (2+1)-flavor QCD,” *Phys. Rev.* **D90** (2014) 094503, arXiv:1407.6387 [hep-lat].
- [7] D. Keane, “The Beam Energy Scan at the Relativistic Heavy Ion Collider,” *J. Phys. Conf. Ser.* **878** no. 1, (2017) 012015.
- [8] F. Gelis, E. Iancu, J. Jalilian-Marian, and R. Venugopalan, “The Color Glass Condensate,” *Ann. Rev. Nucl. Part. Sci.* **60** (2010) 463–489, arXiv:1002.0333 [hep-ph].

- [9] E. Iancu and R. Venugopalan, “The Color glass condensate and high-energy scattering in QCD,” in *Quark-gluon plasma 4*, R. C. Hwa and X.-N. Wang, eds., pp. 249–3363. 2003. arXiv:hep-ph/0303204 [hep-ph].
- [10] L. McLerran, “A Brief Introduction to the Color Glass Condensate and the Glasma,” in *Proceedings, 38th International Symposium on Multiparticle Dynamics (ISMD 2008): Hamburg, Germany, September 15-20, 2008*, pp. 3–18. 2009. arXiv:0812.4989 [hep-ph].  
<http://inspirehep.net/record/806434/files/arXiv:0812.4989.pdf>.
- [11] **ZEUS, H1** Collaboration, A. M. Cooper-Sarkar, “Extraction of the proton parton density functions using a NLO-QCD fit of the combined H1 and ZEUS inclusive DIS cross sections,” in *Proceedings, 16th International Workshop on Deep Inelastic Scattering and Related Subjects (DIS 2008): London, UK, April 7-11, 2008*, p. 25. 2008. arXiv:0808.1854 [hep-ph].  
<http://inspirehep.net/record/793031/files/arXiv:0808.1854.pdf>.
- [12] M. L. Miller, K. Reygers, S. J. Sanders, and P. Steinberg, “Glauber modeling in high energy nuclear collisions,” *Ann. Rev. Nucl. Part. Sci.* **57** (2007) 205–243, arXiv:nucl-ex/0701025 [nucl-ex].
- [13] D. Kharzeev and M. Nardi, “Hadron production in nuclear collisions at RHIC and high density QCD,” *Phys. Lett.* **B507** (2001) 121–128, arXiv:nucl-th/0012025 [nucl-th].
- [14] H. J. Drescher and Y. Nara, “Effects of fluctuations on the initial eccentricity from the Color Glass Condensate in heavy ion collisions,” *Phys. Rev.* **C75** (2007) 034905, arXiv:nucl-th/0611017 [nucl-th].
- [15] B. Schenke, P. Tribedy, and R. Venugopalan, “Fluctuating Glasma initial conditions and flow in heavy ion collisions,” *Phys. Rev. Lett.* **108** (2012) 252301, arXiv:1202.6646 [nucl-th].
- [16] B. Schenke, P. Tribedy, and R. Venugopalan, “Event-by-event gluon multiplicity, energy density, and eccentricities in ultrarelativistic heavy-ion collisions,” *Phys. Rev.* **C86** (2012) 034908, arXiv:1206.6805 [hep-ph].
- [17] C. Gale, S. Jeon, B. Schenke, P. Tribedy, and R. Venugopalan, “Event-by-event anisotropic flow in heavy-ion collisions from combined Yang-Mills and viscous fluid dynamics,” *Phys. Rev. Lett.* **110** no. 1, (2013) 012302, arXiv:1209.6330 [nucl-th].
- [18] P. F. Kolb and U. W. Heinz, “Hydrodynamic description of ultrarelativistic heavy ion collisions,” arXiv:nucl-th/0305084 [nucl-th].
- [19] J.-Y. Ollitrault, “Relativistic hydrodynamics for heavy-ion collisions,” *Eur. J. Phys.* **29** (2008) 275–302, arXiv:0708.2433 [nucl-th].

- 
- [20] P. Romatschke, “Do nuclear collisions create a locally equilibrated quark-gluon plasma?,” *Eur. Phys. J.* **C77** no. 1, (2017) 21, arXiv:1609.02820 [nucl-th].
- [21] P. Kovtun, D. T. Son, and A. O. Starinets, “Viscosity in strongly interacting quantum field theories from black hole physics,” *Phys. Rev. Lett.* **94** (2005) 111601, arXiv:hep-th/0405231 [hep-th].
- [22] H. Song, S. A. Bass, and U. Heinz, “Elliptic flow in 200 A GeV Au+Au collisions and 2.76 A TeV Pb+Pb collisions: insights from viscous hydrodynamics + hadron cascade hybrid model,” *Phys. Rev.* **C83** (2011) 054912, arXiv:1103.2380 [nucl-th]. [Erratum: *Phys. Rev.* C87,no.1,019902(2013)].
- [23] J. E. Bernhard, J. S. Moreland, S. A. Bass, J. Liu, and U. Heinz, “Applying Bayesian parameter estimation to relativistic heavy-ion collisions: simultaneous characterization of the initial state and quark-gluon plasma medium,” *Phys. Rev.* **C94** no. 2, (2016) 024907, arXiv:1605.03954 [nucl-th].
- [24] J. E. Bernhard, *Bayesian parameter estimation for relativistic heavy-ion collisions*. PhD thesis, Duke U., 2018-04-19. arXiv:1804.06469 [nucl-th]. <http://inspirehep.net/record/1669345/files/1804.06469.pdf>.
- [25] S. Ryu, J. F. Paquet, C. Shen, G. S. Denicol, B. Schenke, S. Jeon, and C. Gale, “Importance of the Bulk Viscosity of QCD in Ultrarelativistic Heavy-Ion Collisions,” *Phys. Rev. Lett.* **115** no. 13, (2015) 132301, arXiv:1502.01675 [nucl-th].
- [26] S. A. Bass *et al.*, “Microscopic models for ultrarelativistic heavy ion collisions,” *Prog. Part. Nucl. Phys.* **41** (1998) 255–369, arXiv:nucl-th/9803035 [nucl-th]. [Prog. Part. Nucl. Phys.41,225(1998)].
- [27] Z.-W. Lin, C. M. Ko, B.-A. Li, B. Zhang, and S. Pal, “A Multi-phase transport model for relativistic heavy ion collisions,” *Phys. Rev.* **C72** (2005) 064901, arXiv:nucl-th/0411110 [nucl-th].
- [28] U. W. Heinz, “The Strongly coupled quark-gluon plasma created at RHIC,” *J. Phys.* **A42** (2009) 214003, arXiv:0810.5529 [nucl-th].
- [29] S. Voloshin and Y. Zhang, “Flow study in relativistic nuclear collisions by Fourier expansion of Azimuthal particle distributions,” *Z. Phys.* **C70** (1996) 665–672, arXiv:hep-ph/9407282 [hep-ph].
- [30] ALICE Collaboration, K. Aamodt *et al.*, “Harmonic decomposition of two-particle angular correlations in Pb-Pb collisions at  $\sqrt{s_{NN}} = 2.76$  TeV,” *Phys. Lett.* **B708** (2012) 249–264, arXiv:1109.2501 [nucl-ex].
- [31] ALICE Collaboration, K. Aamodt *et al.*, “Higher harmonic anisotropic flow measurements of charged particles in Pb-Pb collisions at  $\sqrt{s_{NN}}=2.76$  TeV,” *Phys. Rev. Lett.* **107** (2011) 032301, arXiv:1105.3865 [nucl-ex].

- [32] **ALICE** Collaboration, J. Adam *et al.*, “Anisotropic flow of charged particles in Pb-Pb collisions at  $\sqrt{s_{\text{NN}}} = 5.02$  TeV,” *Phys. Rev. Lett.* **116** no. 13, (2016) 132302, arXiv:1602.01119 [nucl-ex].
- [33] **CMS** Collaboration, A. M. Sirunyan *et al.*, “Non-Gaussian elliptic-flow fluctuations in PbPb collisions at  $\sqrt{s_{\text{NN}}} = 5.02$  TeV,” arXiv:1711.05594 [nucl-ex].
- [34] **ALICE** Collaboration, S. Acharya *et al.*, “Energy dependence and fluctuations of anisotropic flow in Pb-Pb collisions at  $\sqrt{s_{\text{NN}}} = 5.02$  and 2.76 TeV,” arXiv:1804.02944 [nucl-ex].
- [35] **ALICE** Collaboration, J. Adam *et al.*, “Pseudorapidity dependence of the anisotropic flow of charged particles in Pb-Pb collisions at  $\sqrt{s_{\text{NN}}} = 2.76$  TeV,” *Phys. Lett.* **B762** (2016) 376–388, arXiv:1605.02035 [nucl-ex].
- [36] **CMS** Collaboration, V. Khachatryan *et al.*, “Evidence for transverse momentum and pseudorapidity dependent event plane fluctuations in PbPb and pPb collisions,” *Phys. Rev.* **C92** no. 3, (2015) 034911, arXiv:1503.01692 [nucl-ex].
- [37] **ALICE** Collaboration, S. Acharya *et al.*, “Searches for transverse momentum dependent flow vector fluctuations in Pb-Pb and p-Pb collisions at the LHC,” *JHEP* **09** (2017) 032, arXiv:1707.05690 [nucl-ex].
- [38] **ATLAS** Collaboration, M. Aaboud *et al.*, “Measurement of longitudinal flow decorrelations in Pb+Pb collisions at  $\sqrt{s_{\text{NN}}} = 2.76$  and 5.02 TeV with the ATLAS detector,” *Eur. Phys. J.* **C78** no. 2, (2018) 142, arXiv:1709.02301 [nucl-ex].
- [39] **ALICE** Collaboration, S. Acharya *et al.*, “Anisotropic flow of identified particles in Pb-Pb collisions at  $\sqrt{s_{\text{NN}}} = 5.02$  TeV,” arXiv:1805.04390 [nucl-ex].
- [40] **ALICE** Collaboration, S. Acharya *et al.*, “Linear and non-linear flow modes in Pb-Pb collisions at  $\sqrt{s_{\text{NN}}} = 2.76$  TeV,” *Phys. Lett.* **B773** (2017) 68–80, arXiv:1705.04377 [nucl-ex].
- [41] **ATLAS** Collaboration, G. Aad *et al.*, “Measurement of the correlation between flow harmonics of different order in lead-lead collisions at  $\sqrt{s_{\text{NN}}}=2.76$  TeV with the ATLAS detector,” *Phys. Rev.* **C92** no. 3, (2015) 034903, arXiv:1504.01289 [hep-ex].
- [42] A. Bilandzic, C. H. Christensen, K. Gulbrandsen, A. Hansen, and Y. Zhou, “Generic framework for anisotropic flow analyses with multiparticle azimuthal correlations,” *Phys. Rev.* **C89** no. 6, (2014) 064904, arXiv:1312.3572 [nucl-ex].
- [43] **ALICE** Collaboration, J. Adam *et al.*, “Correlated event-by-event fluctuations of flow harmonics in Pb-Pb collisions at  $\sqrt{s_{\text{NN}}} = 2.76$  TeV,” *Phys. Rev. Lett.* **117** (2016) 182301, arXiv:1604.07663 [nucl-ex].
- [44] **ATLAS** Collaboration, G. Aad *et al.*, “Observation of Long-Range Elliptic Azimuthal Anisotropies in  $\sqrt{s} = 13$  and 2.76 TeV *pp* Collisions with the ATLAS Detector,” *Phys. Rev. Lett.* **116** no. 17, (2016) 172301, arXiv:1509.04776 [hep-ex].

- 
- [45] CMS Collaboration, V. Khachatryan *et al.*, “Observation of Long-Range Near-Side Angular Correlations in Proton-Proton Collisions at the LHC,” *JHEP* **09** (2010) 091, arXiv:1009.4122 [hep-ex].
- [46] CMS Collaboration, S. Chatrchyan *et al.*, “Observation of long-range near-side angular correlations in proton-lead collisions at the LHC,” *Phys. Lett.* **B718** (2013) 795–814, arXiv:1210.5482 [nucl-ex].
- [47] ALICE Collaboration, B. B. Abelev *et al.*, “Multiparticle azimuthal correlations in p-Pb and Pb-Pb collisions at the CERN Large Hadron Collider,” *Phys. Rev.* **C90** no. 5, (2014) 054901, arXiv:1406.2474 [nucl-ex].
- [48] CMS Collaboration, V. Khachatryan *et al.*, “Evidence for Collective Multiparticle Correlations in p-Pb Collisions,” *Phys. Rev. Lett.* **115** no. 1, (2015) 012301, arXiv:1502.05382 [nucl-ex].
- [49] ATLAS Collaboration, M. Aaboud *et al.*, “Measurement of multi-particle azimuthal correlations in pp, p+Pb and low-multiplicity Pb+Pb collisions with the ATLAS detector,” *Eur. Phys. J.* **C77** no. 6, (2017) 428, arXiv:1705.04176 [hep-ex].
- [50] CMS Collaboration, V. Khachatryan *et al.*, “Evidence for collectivity in pp collisions at the LHC,” *Phys. Lett.* **B765** (2017) 193–220, arXiv:1606.06198 [nucl-ex].
- [51] A. Bilandzic, *Anisotropic flow measurements in ALICE at the large hadron collider*. PhD thesis, Utrecht U., 2012. <http://inspirehep.net/record/1186272/files/CERN-THESIS-2012-018.pdf>.
- [52] N. Borghini, P. M. Dinh, and J.-Y. Ollitrault, “A New method for measuring azimuthal distributions in nucleus-nucleus collisions,” *Phys. Rev.* **C63** (2001) 054906, arXiv:nucl-th/0007063 [nucl-th].
- [53] N. Borghini, P. M. Dinh, and J.-Y. Ollitrault, “Flow analysis from multiparticle azimuthal correlations,” *Phys. Rev.* **C64** (2001) 054901, arXiv:nucl-th/0105040 [nucl-th].
- [54] N. Borghini, P. M. Dinh, and J.-Y. Ollitrault, “Flow analysis from cumulants: A Practical guide,” in *International Workshop on the Physics of the Quark Gluon Plasma Palaiseau, France, September 4-7, 2001*. 2001. arXiv:nucl-ex/0110016 [nucl-ex].
- [55] A. Bilandzic, R. Snellings, and S. Voloshin, “Flow analysis with cumulants: Direct calculations,” *Phys. Rev.* **C83** (2011) 044913, arXiv:1010.0233 [nucl-ex].
- [56] T. Sjöstrand, S. Ask, J. R. Christiansen, R. Corke, N. Desai, P. Ilten, S. Mrenna, S. Prestel, C. O. Rasmussen, and P. Z. Skands, “An Introduction to PYTHIA 8.2,” *Comput. Phys. Commun.* **191** (2015) 159–177, arXiv:1410.3012 [hep-ph].
- [57] “Pythia 8 manual.”  
<http://home.thep.lu.se/~torbjorn/pythia82html/Welcome.html>.  
Accessed: 20.07.2018.

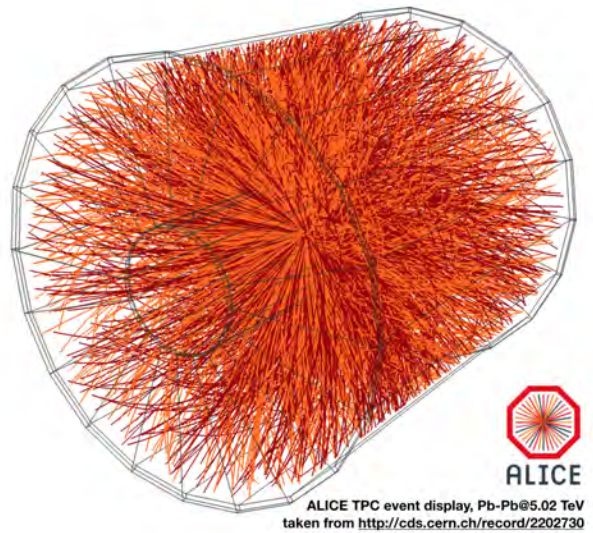
- [58] J. Jia, M. Zhou, and A. Trzupek, “Revealing long-range multiparticle collectivity in small collision systems via subevent cumulants,” *Phys. Rev.* **C96** no. 3, (2017) 034906, arXiv:1701.03830 [nucl-th].
- [59] P. Huo, K. Gajdošová, J. Jia, and Y. Zhou, “Importance of non-flow in mixed-harmonic multi-particle correlations in small collision systems,” *Phys. Lett.* **B777** (2018) 201–206, arXiv:1710.07567 [nucl-ex].
- [60] L. Evans and P. Bryant, “LHC Machine,” *JINST* **3** (2008) S08001.
- [61] “Lhc, taking a closer look at lhc.” [https://www.lhc-closer.es/taking\\_a\\_closer\\_look\\_at\\_lhc/1.lhc](https://www.lhc-closer.es/taking_a_closer_look_at_lhc/1.lhc). Accessed: 20.05.2018.
- [62] M. Brice, “Aerial View of the CERN taken in 2008..” Jul, 2008.
- [63] ALICE Collaboration, K. Aamodt *et al.*, “The ALICE experiment at the CERN LHC,” *JINST* **3** (2008) S08002.
- [64] A. Tauro, “ALICE Schematics.” General Photo, May, 2017.
- [65] ALICE Collaboration, G. Dellacasa *et al.*, “ALICE technical design report of the inner tracking system (ITS),”.
- [66] P. Kuijter, “The inner tracking system of the alice experiment,” *Nuclear Instruments and Methods in Physics Research Section A: Accelerators, Spectrometers, Detectors and Associated Equipment* **530** no. 1, (2004) 28 – 32. <http://www.sciencedirect.com/science/article/pii/S0168900204010289>. Proceedings of the 6th International Conference on Large Scale Applications and Radiation Hardness of Semiconductor Detectors.
- [67] ALICE Collaboration, G. Dellacasa *et al.*, “ALICE: Technical design report of the time projection chamber,”.
- [68] J. Alme *et al.*, “The ALICE TPC, a large 3-dimensional tracking device with fast readout for ultra-high multiplicity events,” *Nucl. Instrum. Meth.* **A622** (2010) 316–367, arXiv:1001.1950 [physics.ins-det].
- [69] A. Maire, “ALICE TPC sectors and pad rows.” General Photo, Oct, 2011.
- [70] ALICE Collaboration, E. Abbas *et al.*, “Performance of the ALICE VZERO system,” *JINST* **8** (2013) P10016, arXiv:1306.3130 [nucl-ex].
- [71] P. Billoir, “Progressive track recognition with a Kalman like fitting procedure,” *Comput. Phys. Commun.* **57** (1989) 390–394.
- [72] M. Krivda *et al.*, “The ALICE trigger system performance for p-p and Pb-Pb collisions,” *JINST* **7** (2012) C01057.
- [73] “Worldwide lhc computing grid.” <http://wlcg-public.web.cern.ch/>. Accessed: 20.05.2018.

- 
- [74] R. Brun, F. Carminati, and S. Giani, “GEANT Detector Description and Simulation Tool,” *CERN Program Library Long Write-up, W5013* (1994).
- [75] **ALICE Collaboration** Collaboration, “The ALICE definition of primary particles,” <https://cds.cern.ch/record/2270008>.
- [76] S. Roesler, R. Engel, and J. Ranft, “The Monte Carlo event generator DPMJET-III,” in *Advanced Monte Carlo for radiation physics, particle transport simulation and applications. Proceedings, Conference, MC2000, Lisbon, Portugal, October 23-26, 2000*, pp. 1033–1038. 2000. [arXiv:hep-ph/0012252](https://arxiv.org/abs/hep-ph/0012252) [hep-ph]. <http://www-public.slac.stanford.edu/sciDoc/docMeta.aspx?slacPubNumber=SLAC-PUB-8740>.
- [77] X.-N. Wang and M. Gyulassy, “HIJING: A Monte Carlo model for multiple jet production in p p, p A and A A collisions,” *Phys. Rev.* **D44** (1991) 3501–3516.
- [78] W. Zhao, Y. Zhou, H. Xu, W. Deng, and H. Song, “Hydrodynamic collectivity in proton-proton collisions at 13 TeV,” *Phys. Lett.* **B780** (2018) 495–500, [arXiv:1801.00271](https://arxiv.org/abs/1801.00271) [nucl-th].
- [79] **ATLAS Collaboration**, M. Aaboud *et al.*, “Measurement of long-range multiparticle azimuthal correlations with the subevent cumulant method in  $pp$  and  $p + Pb$  collisions with the ATLAS detector at the CERN Large Hadron Collider,” *Phys. Rev.* **C97** no. 2, (2018) 024904, [arXiv:1708.03559](https://arxiv.org/abs/1708.03559) [hep-ex].
- [80] **CMS Collaboration**, A. M. Sirunyan *et al.*, “Observation of Correlated Azimuthal Anisotropy Fourier Harmonics in  $pp$  and  $p + Pb$  Collisions at the LHC,” *Phys. Rev. Lett.* **120** no. 9, (2018) 092301, [arXiv:1709.09189](https://arxiv.org/abs/1709.09189) [nucl-ex].
- [81] **ATLAS Collaboration**, M. Aaboud *et al.*, “Correlated long-range mixed-harmonic fluctuations measured in  $pp$ ,  $p+Pb$  and low-multiplicity  $Pb+Pb$  collisions with the ATLAS detector,” [arXiv:1807.02012](https://arxiv.org/abs/1807.02012) [nucl-ex].
- [82] **ALICE Collaboration**, K. Gajdšová, “ALICE measurements of flow coefficients and their correlations in small (pp and p-Pb) and large (Xe-Xe and Pb-Pb) collision systems,” in *27th International Conference on Ultrarelativistic Nucleus-Nucleus Collisions (Quark Matter 2018) Venice, Italy, May 14-19, 2018*. 2018. [arXiv:1807.02998](https://arxiv.org/abs/1807.02998) [nucl-ex].
- [83] L. Yan and J.-Y. Ollitrault, “Universal fluctuation-driven eccentricities in proton-proton, proton-nucleus and nucleus-nucleus collisions,” *Phys. Rev. Lett.* **112** (2014) 082301, [arXiv:1312.6555](https://arxiv.org/abs/1312.6555) [nucl-th].
- [84] A. Bzdak, P. Bozek, and L. McLerran, “Fluctuation induced equality of multi-particle eccentricities for four or more particles,” *Nucl. Phys.* **A927** (2014) 15–23, [arXiv:1311.7325](https://arxiv.org/abs/1311.7325) [hep-ph].
- [85] B. Schenke, P. Tribedy, and R. Venugopalan, “Multiplicity distributions in p+p, p+A and A+A collisions from Yang-Mills dynamics,” *Phys. Rev.* **C89** no. 2, (2014) 024901, [arXiv:1311.3636](https://arxiv.org/abs/1311.3636) [hep-ph].

- [86] H. Mäntysaari, B. Schenke, C. Shen, and P. Tribedy, “Imprints of fluctuating proton shapes on flow in proton-lead collisions at the LHC,” *Phys. Lett.* **B772** (2017) 681–686, arXiv:1705.03177 [nucl-th].
- [87] B. Schenke, C. Shen, and P. Tribedy, “Features of the IP-Glasma,” in *27th International Conference on Ultrarelativistic Nucleus-Nucleus Collisions (Quark Matter 2018) Venice, Italy, May 14-19, 2018*. 2018. arXiv:1807.05205 [nucl-th].
- [88] R. D. Weller and P. Romatschke, “One fluid to rule them all: viscous hydrodynamic description of event-by-event central p+p, p+Pb and Pb+Pb collisions at  $\sqrt{s} = 5.02$  TeV,” *Phys. Lett.* **B774** (2017) 351–356, arXiv:1701.07145 [nucl-th].
- [89] K. Dusling, M. Mace, and R. Venugopalan, “Multiparticle collectivity from initial state correlations in high energy proton-nucleus collisions,” *Phys. Rev. Lett.* **120** no. 4, (2018) 042002, arXiv:1705.00745 [hep-ph].
- [90] M. Greif, C. Greiner, B. Schenke, S. Schlichting, and Z. Xu, “Importance of initial and final state effects for azimuthal correlations in p+Pb collisions,” *Phys. Rev.* **D96** no. 9, (2017) 091504, arXiv:1708.02076 [hep-ph].
- [91] **ALICE** Collaboration, S. Acharya *et al.*, “Systematic studies of correlations between different order flow harmonics in Pb-Pb collisions at  $\sqrt{s_{NN}} = 2.76$  TeV,” *Phys. Rev.* **C97** no. 2, (2018) 024906, arXiv:1709.01127 [nucl-ex].
- [92] M.-W. Nie, P. Huo, J. Jia, and G.-L. Ma, “Multi-particle azimuthal cumulants in p+Pb collisions from a multiphase transport model,” arXiv:1802.00374 [hep-ph].
- [93] **ALICE** Collaboration, K. Gajdošová, “Investigations of anisotropic collectivity using multi-particle correlations in pp, p?Pb and Pb?Pb collisions,” *Nucl. Phys.* **A967** (2017) 437–440.
- [94] **ATLAS** Collaboration, M. Zhou, “Measurement of multi-particle azimuthal correlations with the subevent cumulant method in pp and p +Pb collisions with the ATLAS detector,” *Nucl. Phys.* **A967** (2017) 472–475.

# **Appendices**





# A. Non-uniform acceptance

The procedure to obtain the non-uniform acceptance correction was described in Chapter 5.1: the correction factor is calculated from the event-averaged  $\phi$  distribution. It was shown for pp collisions, that this correction should be dependent on the period, but not on the run number. Similar checks performed in the rest of the collision systems, which will be summarised here, have shown that a run-dependent correction is necessary in p-Pb and Pb-Pb data.

## A.1 p-Pb collisions

The data from p-Pb collisions are divided into two periods: LHC16q and LHC16t. The event-averaged  $\phi$  distributions from each period are compared to each other in Fig. A.1. The left panel shows the normalised distributions with the number of entries (i.e. tracks), and the right panel shows the ratio of the distribution from the LHC16t to the LHC16q period. It is clear that the inefficiencies are different in different periods, thus the correction should be period-dependent.

In addition to the dependence on the period, a run-dependent correction is necessary for the LHC16q period in p-Pb collisions. The comparison of  $\phi$  distribution from different runs of the LHC16q and the LHC16t period is shown in Fig. A.2 and A.3, respectively. The ratios of the distributions from each run to the first run of p-Pb collisions are shown together in one plot. The LHC16t period did not reveal any dependence of the inefficiencies on the run number.

## A.2 Xe-Xe and Pb-Pb collisions

The data from Xe-Xe and Pb-Pb collisions are contained within one period. The LHC15o, with around 80 different runs, represents Pb-Pb collisions, while Xe-Xe collisions only have

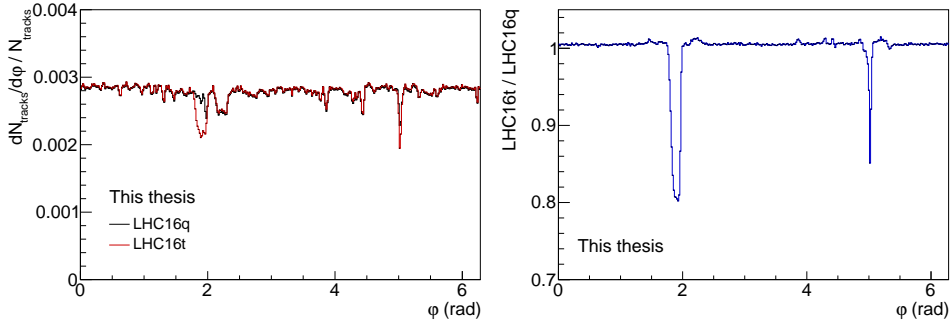


**Figure A.1:** Left:  $\phi$  distribution from different periods of p–Pb collisions. The distributions are normalised with the number of entries. The  $\phi$  distributions from different periods are incompatible. Right: Ratio of  $\phi$  distributions of the LHC16t period to the LHC16q period. The distributions are first normalised with number of entries. The necessity for a period dependent acceptance correction is apparent.

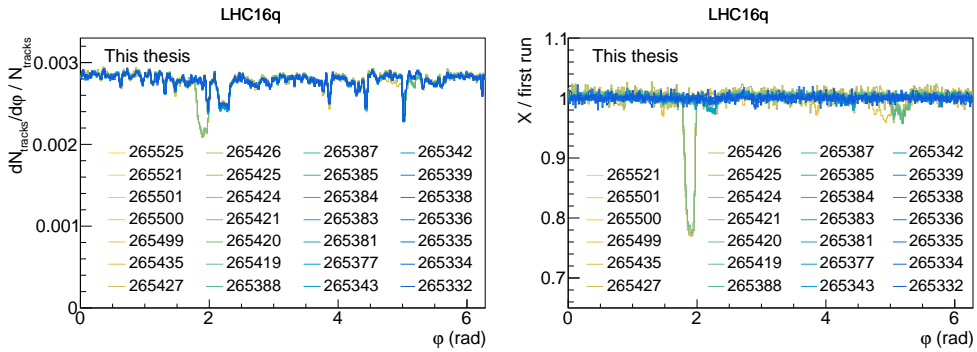


**Figure A.2:** Left:  $\phi$  distribution from different runs of the LHC16q period. The distributions are normalised with the number of entries. Right: Ratio of  $\phi$  distributions of various runs to the first run of the LHC16q period. The distributions are first normalised with number of entries. The correction is not dependent on the run number.

2 runs in the LHC17n period. Thus, only the dependence on the run number was investigated in these collisions. The event-averaged  $\phi$  distributions from different runs are compared with each other in Fig. A.4 and A.5. Differences between the  $\phi$  distributions from different runs are observed for Pb–Pb collisions. Therefore, run-dependent correction is applied. On the contrary, Xe–Xe collisions do not show any difference between the two runs.

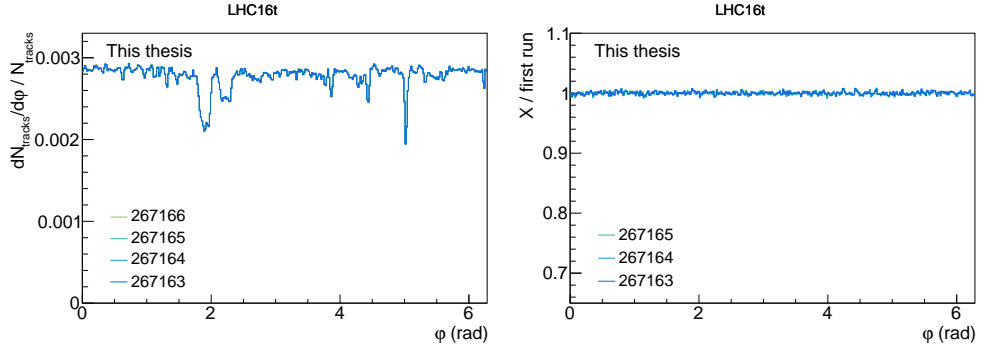


**Figure A.3:** Left:  $\phi$  distribution from different runs of the LHC16t period. The distributions are normalised with the number of entries. Right: Ratio of  $\phi$  distributions of various runs to the first run of the LHC16t period. The distributions are first normalised with number of entries. The correction is not dependent on the run number.

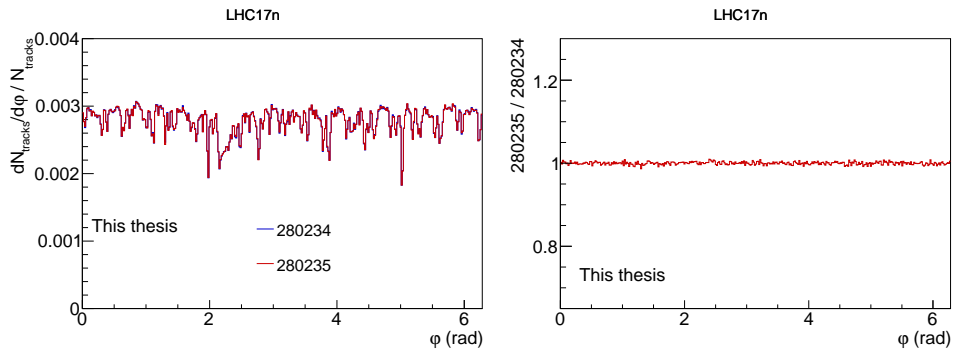


**Figure A.4:** Left:  $\phi$  distribution from different runs of Xe–Xe collisions. The distributions are normalised with the number of entries. Right: Ratio of  $\phi$  distributions of various runs to the first run of Xe–Xe collisions. The distributions are first normalised with number of entries.

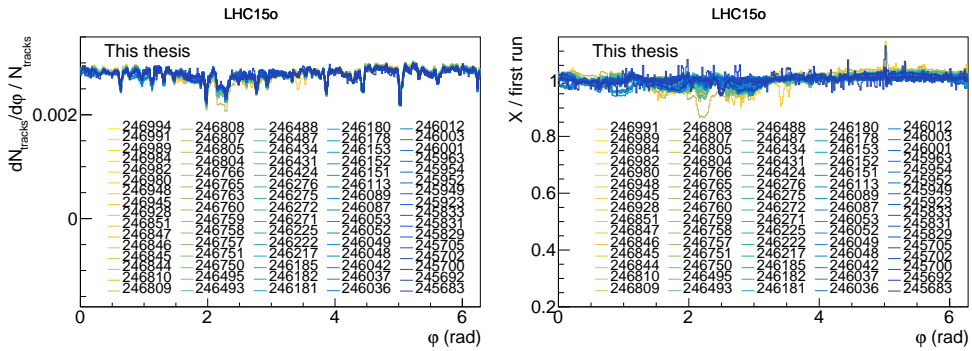
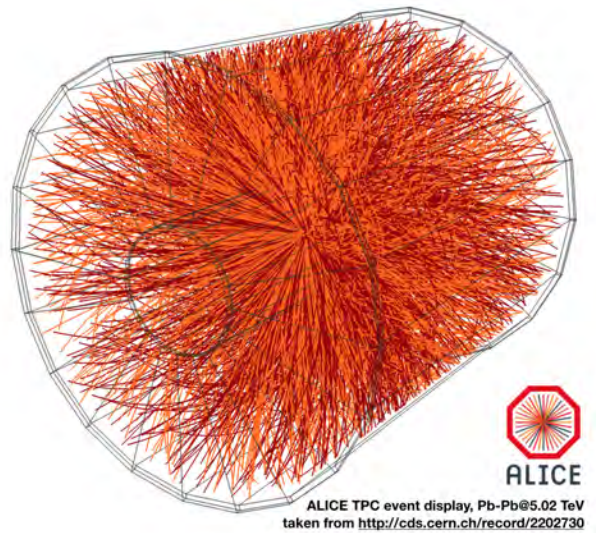


**Figure A.5:** Left:  $\phi$  distribution from different runs of Pb–Pb collisions. The distributions are normalised with the number of entries. Right: Ratio of  $\phi$  distributions of various runs to the first run of Pb–Pb collisions. The distributions are first normalised with number of entries.



## B. Efficiency correction

The procedure to obtain the efficiency correction from Monte Carlo simulation was described in Chapter 5.2: the correction factor is calculated as the ratio of particle distributions from the MC-reconstructed to the MC-truth samples. It was shown for pp collisions, that this correction should be dependent on the period, as well as on  $p_T$ ,  $\eta$  and  $V_z$ . Similar checks were performed for the rest of the collision systems, which will be summarised here. Different models most suitable to the given type of the collision system were used to obtain the efficiency correction. In particular, the DPMJET [76] was used in p–Pb collisions, while HIJING [77] was employed in Xe–Xe collisions, and the AMPT [27] model in Pb–Pb collisions.

### B.1 p–Pb collisions

The data from p–Pb collisions are divided into two periods: LHC16q and LHC16t. The ratio of the efficiency from LHC16t to LHC16q period as a function of  $p_T$ ,  $\eta$  and  $V_z$  is shown in Fig. B.1. The detector inefficiencies are different in different periods, thus the correction should be period-dependent.

In addition to the dependence on the period, a run-dependent efficiency was noted in the LHC16q period in p–Pb collisions. The comparison of efficiencies from different runs of the LHC16q period in p–Pb collisions is shown in Fig. B.2. The LHC16t period did not reveal any dependence on the run number, as can be seen in Fig. B.3.

### B.2 Xe–Xe and Pb–Pb collisions

The data from Xe–Xe and Pb–Pb collisions are contained within one period. The LHC15o, with around 80 different runs, represents Pb–Pb collisions, while Xe–Xe collisions only have 2 runs in the LHC17n period. Thus, only the dependence on the run number was investigated

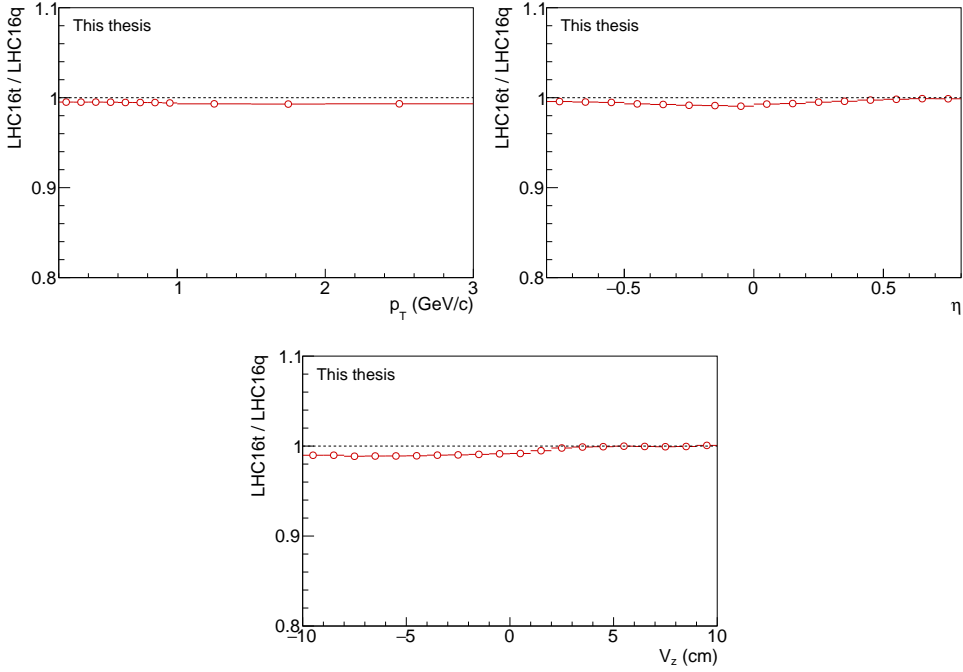


**Figure B.1:** Ratio of efficiency as a function of  $p_T$  (left),  $\eta$  (right) and  $V_z$  (bottom) from the LHC16t period to the LHC16q period.

in these collisions. The detector efficiencies from different runs are compared with each other in Fig. B.4 and B.5 for Xe–Xe and Pb–Pb collisions, respectively. Differences between the efficiencies from different runs are observed in Pb–Pb collisions. Therefore, run-dependent correction is applied. On the contrary, Xe–Xe collisions do not show any difference between the two runs.

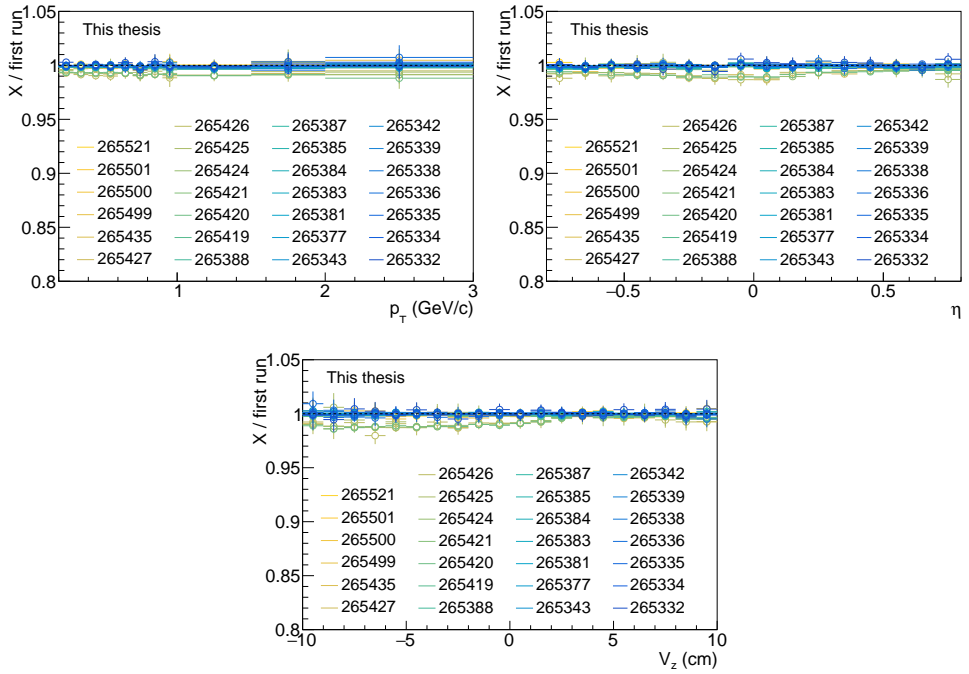


**Figure B.2:** Ratio of detector efficiency as a function of  $p_T$  (left),  $\eta$  (right) and  $V_z$  (bottom) from different runs of the LHC16q period in p–Pb collisions to the first run of that period.

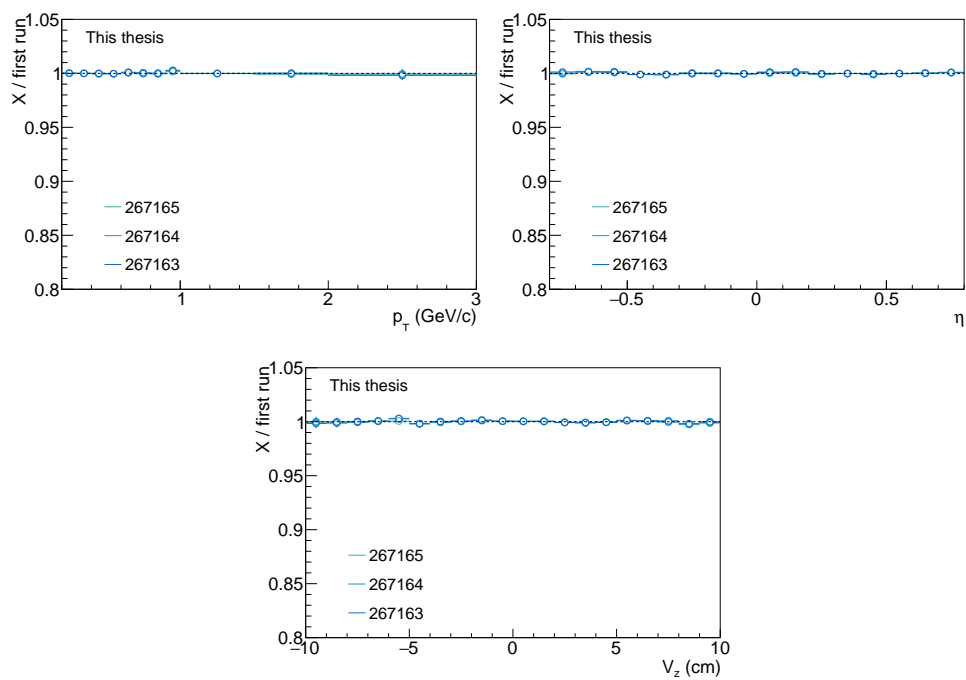


**Figure B.3:** Ratio of detector efficiency as a function of  $p_T$  (left),  $\eta$  (right) and  $V_z$  (bottom) from different runs of the LHC16t period in p–Pb collisions to the first run of that period.

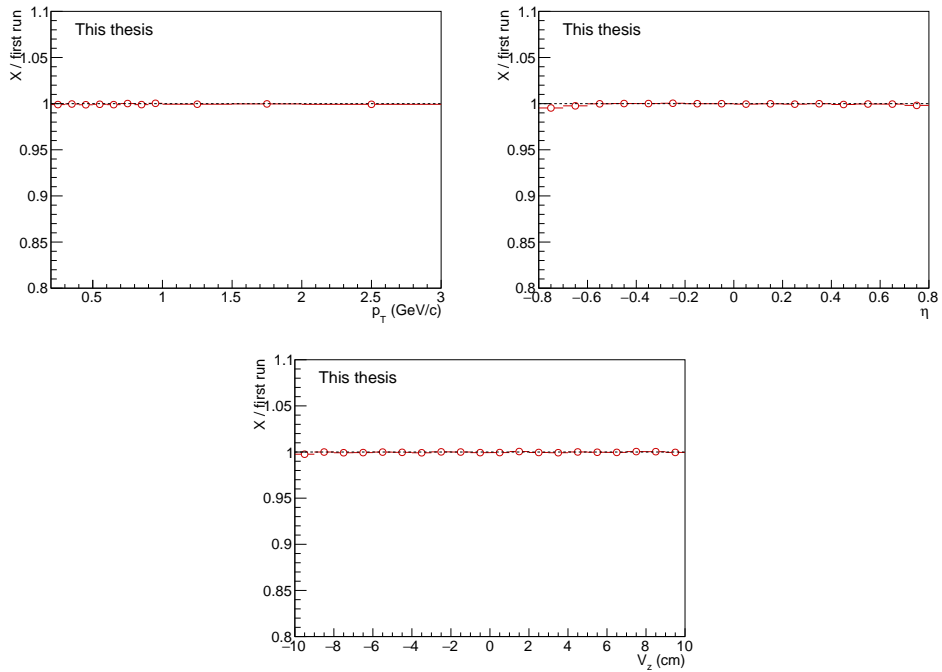


**Figure B.4:** Ratio of detector efficiency as a function of  $p_T$  (left),  $\eta$  (right) and  $V_z$  (bottom) from different runs in the LHC17n period in Xe–Xe collisions to the first run of that period.

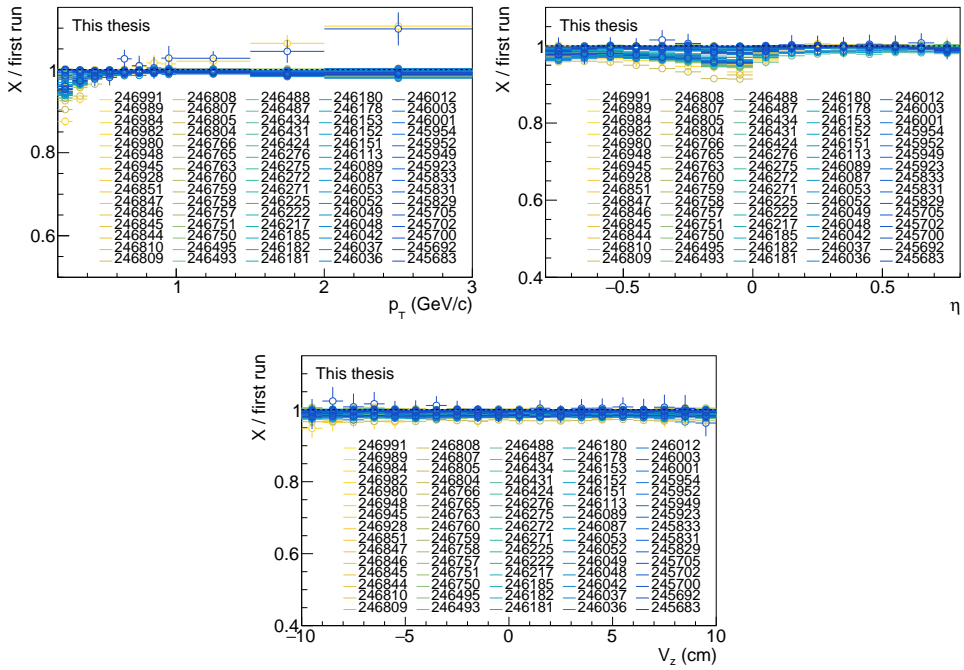
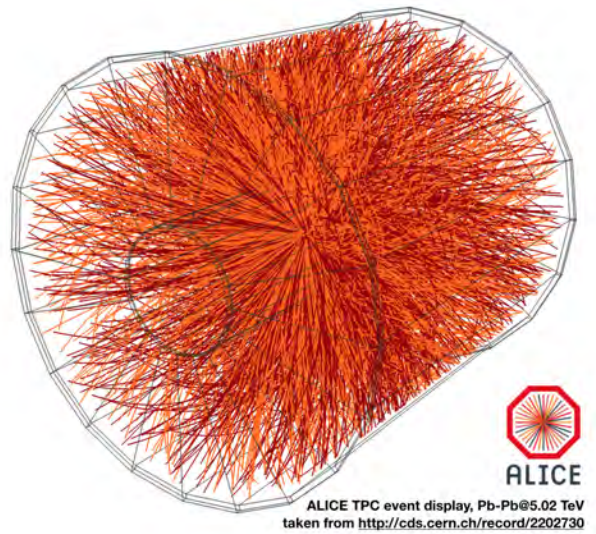


**Figure B.5:** Ratio of detector efficiency as a function of  $p_T$  (left),  $\eta$  (right) and  $V_z$  (bottom) from different runs in the LHC15o period in Pb–Pb collisions to the first run of that period.



## C. Correction of the $x$ -axis

The procedure to correct the  $x$ -axis of the final results from the number of reconstructed tracks to the number of charged particles  $N_{\text{ch}}$  was described in Chapter 5.3: a response matrix representing the correlation between the number of true charged particles in the MC-truth sample,  $N_{\text{ch}}^{\text{truth}}$ , and the number of reconstructed tracks from the MC-reconstructed sample,  $N_{\text{trk}}^{\text{reco}}$ , is obtained from the Monte Carlo simulations. The same procedure was repeated for the rest of the collision systems. The response matrices are shown here for p-Pb collisions in Fig. C.1, Xe-Xe collisions in Fig. C.2 and Pb-Pb collisions in Fig. C.3. Different models most suitable to the given type of the collision system were used to obtain the efficiency correction. In particular, the DPMJET [76] was used in p-Pb collisions, while HIJING [77] was employed in Xe-Xe collisions, and the AMPT [27] model in Pb-Pb collisions.

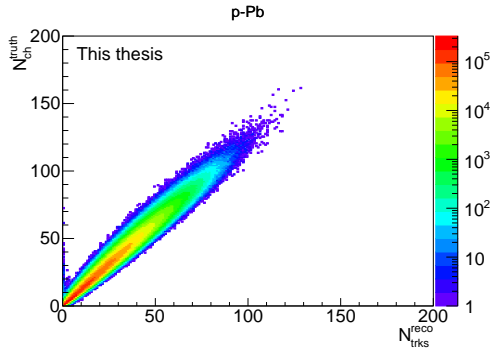


**Figure C.1:** Response matrix from p–Pb collisions. It is the correlation between the number of true charged particles in the MC-truth sample and the number of reconstructed tracks from the MC-reconstructed sample.

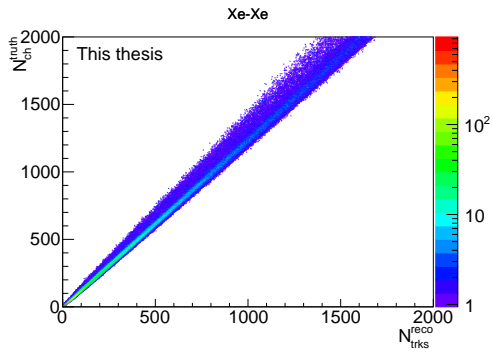


**Figure C.2:** Response matrix from Xe–Xe collisions. It is the correlation between the number of true charged particles in the MC-truth sample and the number of reconstructed tracks from the MC-reconstructed sample.

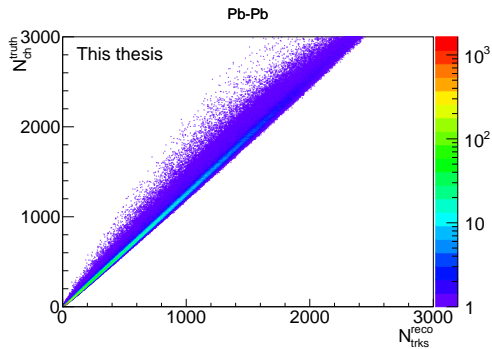
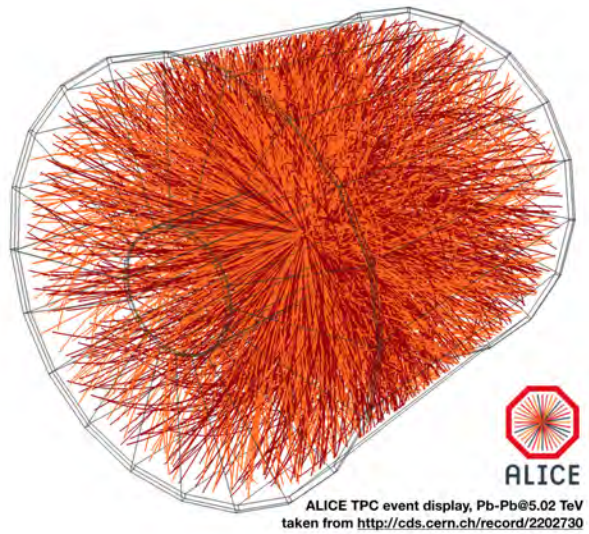


**Figure C.3:** Response matrix from Pb–Pb collisions. It is the correlation between the number of true charged particles in the MC-truth sample and the number of reconstructed tracks from the MC-reconstructed sample.



## D. Systematic uncertainties

Final systematic uncertainties of all observables from all collision systems that were used in the analysis presented in this thesis are summarised here in the form of a maximum relative uncertainty in %. The list of systematic uncertainties from  $\sqrt{s} = 13$  TeV pp collisions is shown in Table D.1,  $\sqrt{s_{NN}} = 5.02$  TeV p-Pb collisions in Table D.2,  $\sqrt{s_{NN}} = 5.44$  TeV Xe-Xe collisions in Table D.3, and  $\sqrt{s_{NN}} = 5.02$  TeV Pb-Pb collisions in Table D.4.

Observable	Final	Observable	Final
$v_2\{2\}$	1.7%	$c_2\{4\}$	12.5%
$v_2\{2,  \Delta\eta  > 0.0\}$	1.5%	$c_2\{4,  \Delta\eta  > 0.0\}$	12.5%
$v_2\{2,  \Delta\eta  > 0.2\}$	1.5%	$c_2\{4, 3\text{-sub}\}$	12.5%
$v_2\{2,  \Delta\eta  > 0.4\}$	1.0%	$v_2\{4, 3\text{-sub}\}$	16.0%
$v_2\{2,  \Delta\eta  > 0.8\}$	1.0%	$v_2\{6\}$	11.0%
$v_2\{2,  \Delta\eta  > 1.0\}$	1.0%	$SC(4, 2)$	12.0%
$v_2\{2,  \Delta\eta  > 1.4\}$	1.0%	$SC(4, 2)_{2\text{-sub}}$	12.0%
$v_3\{2\}$	3.0%	$SC(4, 2)_{3\text{-sub}}$	12.0%
$v_3\{2,  \Delta\eta  > 0.0\}$	2.5%	$SC(3, 2)$	12.0%
$v_3\{2,  \Delta\eta  > 0.2\}$	2.0%	$SC(3, 2)_{2\text{-sub}}$	12.0%
$v_3\{2,  \Delta\eta  > 0.4\}$	2.0%	$SC(3, 2)_{3\text{-sub}}$	12.0%
$v_3\{2,  \Delta\eta  > 0.8\}$	2.0%	$NSC(4, 2)$	12.5%
$v_3\{2,  \Delta\eta  > 1.0\}$	2.0%	$NSC(4, 2)_{2\text{-sub}}$	12.5%
$v_4\{2\}$	3.5%	$NSC(4, 2)_{3\text{-sub}}$	12.5%
$v_4\{2,  \Delta\eta  > 0.0\}$	2.5%	$NSC(3, 2)$	12.5%
$v_4\{2,  \Delta\eta  > 0.2\}$	2.0%	$NSC(3, 2)_{2\text{-sub}}$	12.5%
$v_4\{2,  \Delta\eta  > 0.4\}$	2.0%	$NSC(3, 2)_{3\text{-sub}}$	12.5%
$v_4\{2,  \Delta\eta  > 0.8\}$	2.0%		
$v_4\{2,  \Delta\eta  > 1.0\}$	2.0%		

**Table D.1:** List of final systematic uncertainties in  $\sqrt{s} = 13$  TeV pp collisions.

Observable	Final	Observable	Final
$v_2\{2\}$	1.5%	$c_2\{4\}$	17.0%
$v_2\{2,  \Delta\eta  > 0.0\}$	1.5%	$c_2\{4,  \Delta\eta  > 0.0\}$	17.0%
$v_2\{2,  \Delta\eta  > 0.2\}$	2.0%	$c_2\{4, 3\text{-sub}\}$	17.0%
$v_2\{2,  \Delta\eta  > 0.4\}$	2.0%	$v_2\{4\}$	16.0%
$v_2\{2,  \Delta\eta  > 0.8\}$	2.0%	$v_2\{4\}_{2\text{-sub}}$	16.0%
$v_2\{2,  \Delta\eta  > 1.0\}$	2.5%	$v_2\{4\}_{3\text{-sub}}$	12.5%
$v_2\{2,  \Delta\eta  > 1.4\}$	2.5%	$v_2\{6\}$	12.5%
$v_3\{2\}$	2.0%	$SC(4, 2)$	16.0%
$v_3\{2,  \Delta\eta  > 0.0\}$	5.0%	$SC(4, 2)_{2\text{-sub}}$	16.0%
$v_3\{2,  \Delta\eta  > 0.2\}$	5.0%	$SC(4, 2)_{3\text{-sub}}$	16.0%
$v_3\{2,  \Delta\eta  > 0.4\}$	5.0%	$SC(3, 2)$	14.0%
$v_3\{2,  \Delta\eta  > 0.8\}$	5.0%	$SC(3, 2)_{2\text{-sub}}$	14.0%
$v_3\{2,  \Delta\eta  > 1.0\}$	5.0%	$SC(3, 2)_{3\text{-sub}}$	14.0%
$v_4\{2\}$	4.0%	$NSC(4, 2)$	13.0%
$v_4\{2,  \Delta\eta  > 0.0\}$	3.0%	$NSC(4, 2)_{2\text{-sub}}$	13.0%
$v_4\{2,  \Delta\eta  > 0.2\}$	3.0%	$NSC(4, 2)_{3\text{-sub}}$	13.0%
$v_4\{2,  \Delta\eta  > 0.4\}$	3.0%	$NSC(3, 2)$	12.0%
$v_4\{2,  \Delta\eta  > 0.8\}$	3.0%	$NSC(3, 2)_{2\text{-sub}}$	12.0%
$v_4\{2,  \Delta\eta  > 1.0\}$	3.0%	$NSC(3, 2)_{3\text{-sub}}$	12.0%

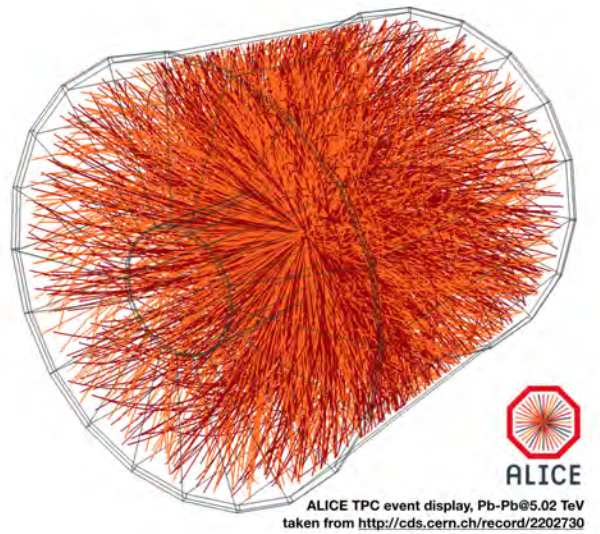
**Table D.2:** List of final of systematic uncertainties in  $\sqrt{s} = 5.02$  TeV p–Pb collisions.

Observable	Final	Observable	Final
$v_2\{2\}$	3.0%	$c_2\{6\}$	11.0%
$v_2\{2,  \Delta\eta  > 0.0\}$	3.0%	$c_2\{8\}$	15.0%
$v_2\{2,  \Delta\eta  > 0.2\}$	3.0%	$v_2\{4\}$	3.0%
$v_2\{2,  \Delta\eta  > 0.4\}$	3.0%	$v_2\{4\}_{2\text{-sub}}$	3.0%
$v_2\{2,  \Delta\eta  > 0.8\}$	3.0%	$v_2\{4\}_{3\text{-sub}}$	3.0%
$v_2\{2,  \Delta\eta  > 1.0\}$	3.0%	$v_2\{6\}$	3.0%
$v_2\{2,  \Delta\eta  > 1.4\}$	3.0%	$v_2\{8\}$	3.5%
$v_3\{2\}$	5.0%	$SC(4, 2)$	14.0%
$v_3\{2,  \Delta\eta  > 0.0\}$	4.0%	$SC(4, 2)_{2\text{-sub}}$	14.0%
$v_3\{2,  \Delta\eta  > 0.2\}$	4.0%	$SC(4, 2)_{3\text{-sub}}$	14.0%
$v_3\{2,  \Delta\eta  > 0.4\}$	4.0%	$SC(3, 2)$	14.0%
$v_3\{2,  \Delta\eta  > 0.8\}$	4.0%	$SC(3, 2)_{2\text{-sub}}$	14.0%
$v_3\{2,  \Delta\eta  > 1.0\}$	4.0%	$SC(3, 2)_{3\text{-sub}}$	14.0%
$v_4\{2\}$	7.0%	$NSC(4, 2)$	16.5%
$v_4\{2,  \Delta\eta  > 0.0\}$	6.0%	$NSC(4, 2)_{2\text{-sub}}$	16.5%
$v_4\{2,  \Delta\eta  > 0.2\}$	6.0%	$NSC(4, 2)_{3\text{-sub}}$	16.5%
$v_4\{2,  \Delta\eta  > 0.4\}$	6.0%	$NSC(3, 2)$	20.0%
$v_4\{2,  \Delta\eta  > 0.8\}$	6.0%	$NSC(3, 2)_{2\text{-sub}}$	20.0%
$v_4\{2,  \Delta\eta  > 1.0\}$	6.0%	$NSC(3, 2)_{3\text{-sub}}$	20.0%
$c_2\{4\}$	11.0%		
$c_2\{4\}_{2\text{-sub}}$	11.0%		
$c_2\{4\}_{3\text{-sub}}$	11.0%		

**Table D.3:** List of final of systematic uncertainties in  $\sqrt{s} = 5.44$  TeV Xe–Xe collisions.

Observable	Final	Observable	Final
$v_2\{2\}$	3.0%	$c_2\{6\}$	15.0%
$v_2\{2,  \Delta\eta  > 0.0\}$	3.0%	$c_2\{6\}_{2\text{-sub}}$	15.0%
$v_2\{2,  \Delta\eta  > 0.2\}$	3.0%	$c_2\{8\}$	18.0%
$v_2\{2,  \Delta\eta  > 0.4\}$	3.0%	$c_2\{8\}_{2\text{-sub}}$	18.0%
$v_2\{2,  \Delta\eta  > 0.8\}$	3.0%	$v_2\{4\}$	3.0%
$v_2\{2,  \Delta\eta  > 1.0\}$	3.0%	$v_2\{4\}_{2\text{-sub}}$	3.0%
$v_2\{2,  \Delta\eta  > 1.4\}$	3.0%	$v_2\{4\}_{3\text{-sub}}$	3.0%
$v_3\{2\}$	5.0%	$v_2\{6\}$	3.0%
$v_3\{2,  \Delta\eta  > 0.0\}$	4.0%	$v_2\{6\}_{2\text{-sub}}$	3.0%
$v_3\{2,  \Delta\eta  > 0.2\}$	4.0%	$v_2\{8\}$	3.0%
$v_3\{2,  \Delta\eta  > 0.4\}$	4.0%	$v_2\{8\}_{2\text{-sub}}$	3.0%
$v_3\{2,  \Delta\eta  > 0.8\}$	4.0%	$SC(4, 2)$	11.0%
$v_3\{2,  \Delta\eta  > 1.0\}$	4.0%	$SC(4, 2)_{2\text{-sub}}$	11.0%
$v_4\{2\}$	7.0%	$SC(4, 2)_{3\text{-sub}}$	11.0%
$v_4\{2,  \Delta\eta  > 0.0\}$	5.5%	$SC(3, 2)$	12.0%
$v_4\{2,  \Delta\eta  > 0.2\}$	5.5%	$SC(3, 2)_{2\text{-sub}}$	12.0%
$v_4\{2,  \Delta\eta  > 0.4\}$	5.0%	$SC(3, 2)_{3\text{-sub}}$	12.0%
$v_4\{2,  \Delta\eta  > 0.8\}$	5.0%	$NSC(4, 2)$	11.0%
$v_4\{2,  \Delta\eta  > 1.0\}$	5.0%	$NSC(4, 2)_{2\text{-sub}}$	11.0%
$c_2\{4\}$	14.0%	$NSC(4, 2)_{3\text{-sub}}$	11.0%
$c_2\{4\}_{2\text{-sub}}$	14.0%	$NSC(3, 2)$	12.0%
$c_2\{4\}_{3\text{-sub}}$	14.0%	$NSC(3, 2)_{2\text{-sub}}$	12.0%
		$NSC(3, 2)_{3\text{-sub}}$	12.0%

**Table D.4:** List of final of systematic uncertainties in  $\sqrt{s} = 5.02$  TeV Pb–Pb collisions.



## E. Earlier studies of collectivity

In this section, former results on the investigation of collectivity in small collision systems are presented. These results were shown at Quark Matter 2017 conference, which resulted in a conference proceedings [93]. However, these studies were not presented in the main text of the thesis, because since then, the amount of newly collected data has increased significantly, and in addition, new data from Pb–Pb, Xe–Xe and p–Pb collisions from Run 2 were available for analysis. Nevertheless, the results summarised here represent the beginnings of the investigation of collectivity in small collision systems using two- and multi-particle cumulants with ALICE with fresh new ideas. One of the examples would be the development of the subevent method in multi-particle cumulants, which later appeared to be an important part of the measurements of anisotropic flow in small collision systems. Thus, these results deserve a dedicated section.

At the time when this analysis was performed it was not clear whether collectivity is observed in high multiplicity pp collisions or not. The negative  $c_2\{4\}$  observed by CMS was contaminated by multiplicity fluctuations, and no other clear signature of collectivity has been revealed so far.

### E.1 Data sets

The data set used in the following analysis consisted of a pp, p–Pb and Pb–Pb collisions at  $\sqrt{s} = 13$  TeV,  $\sqrt{s_{NN}} = 5.02$  TeV and  $\sqrt{s_{NN}} = 2.76$  TeV, respectively. A minimum-bias trigger was used in all the results. In addition, a high multiplicity trigger was available for pp data sample. This trigger selected high multiplicity collisions based on the multiplicity in the SPD detector. Therefore, it differs from the high multiplicity trigger used for the main analysis presented in this thesis, which selected events based on the multiplicity in the forward V0 detector. The advantage of the SPD high multiplicity trigger is that the events are a direct

subsample of the minimum-bias events, thus they can be used to enhance the statistics at high multiplicity. This is going to be illustrated in the following.

The multiplicity distributions of the minimum-bias and the SPD high multiplicity triggers are shown in Fig. E.1 (left). The distributions are normalised with the integral between  $M = (60, 80)^*$  in order to demonstrate that the SPD high multiplicity trigger data match the minimum-bias data at high multiplicity. In particular, the SPD high multiplicity trigger starts to reproduce the minimum-bias approximately at  $M \approx 55$ . The ratio of these two distributions is shown in the right panel. At the region where the multiplicity distributions from the two triggers seemed to overlap, their ratio is roughly constant. Due to the lack of statistics in the minimum-bias trigger at high multiplicity, these comparisons suffer from statistical fluctuations. However, a constant fit to the ratio in the region of  $M = (55, 90)$  shows that the constant approximation is reasonable. This property of the SPD high multiplicity trigger allows to enhance the statistics in the high multiplicity region, and hence, extend the measurements from the minimum-bias trigger.

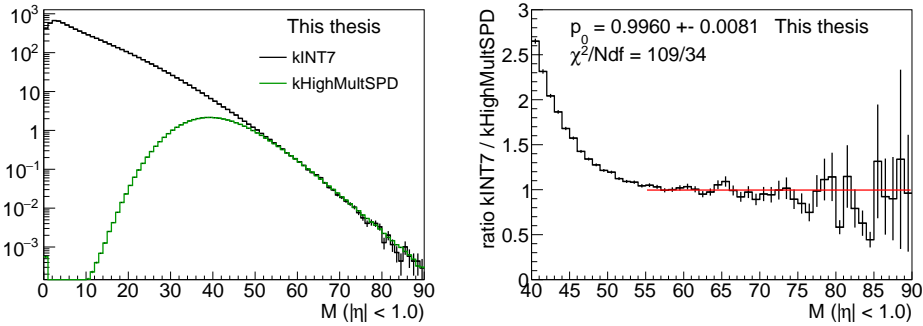


**Figure E.1:** Left: Multiplicity distributions from  $\sqrt{s} = 13$  TeV pp collisions from minimum-bias (kINT7) and SPD high multiplicity trigger (kHighMultSPD). Distributions are normalised with the integral between  $M = (60, 80)$ . The distributions start to overlap from approximately  $M \approx 55$ . Right: Ratio of the distribution from the minimum-bias trigger to the SPD high multiplicity trigger. The ratio is fitted with a constant function in the range where the multiplicity distributions seemed to overlap.

An example of a  $c_2\{2\}$  measurement as a function of multiplicity, obtained from the minimum-bias and the SPD high multiplicity trigger data samples, is shown in Fig. E.2. It can be seen that the measurements become compatible at similar range of multiplicity that was inferred from the multiplicity distributions shown above. Therefore, minimum-bias results will be used at the low multiplicity region below  $M < 55$ , since they overwhelm the statistics of the SPD high multiplicity trigger at this region. Above this threshold, the lack of statistics in the minimum-bias trigger, which would impede the realisation of the measurements, will be recovered by the SPD high multiplicity trigger. This trigger will increase the maximum multiplicity reach of the results by  $M \approx 30$ .

The selected region of the transverse momentum  $p_T$  is similar as was used in the main

\* $M$  is the uncorrected number of tracks within  $|\eta| < 1.0$  and  $0.2 < p_T < 3.0$  GeV/c.

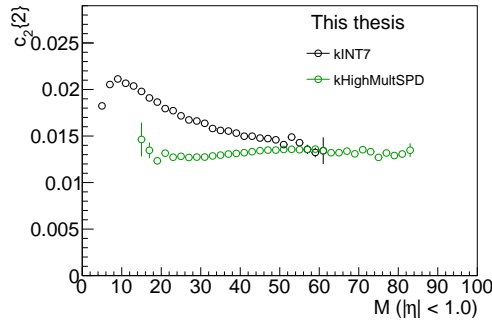


**Figure E.2:** Measurements of  $c_2\{2\}$  as a function of multiplicity from  $\sqrt{s} = 13$  TeV pp collisions from the minimum-bias (kINT7) and the SPD high multiplicity trigger (kHighMultSPD). The measurements start to overlap at  $M \approx 55$ .

measurements presented in this thesis:  $0.2 < p_T < 3.0$  GeV/ $c$ . However, the acceptance of the detector in pseudorapidity was chosen to be larger here:  $|\eta| < 1.0$ . This choice was made in order to be able to compare the measurements to the ALICE publication [47], which used the same data sets as this analysis, and results of which will be used to compare to the newly extracted pp measurements. This choice of the detector acceptance will lead to larger inefficiencies near the detector edges. However, this was accounted for by weighting the  $Q$ -vectors within the Generic Framework [42], as was done in the main analysis presented in this thesis.

## E.2 Results

The multiplicity dependence<sup>†</sup> of two-particle cumulant from pp, p–Pb and Pb–Pb collisions, calculated with the standard method without the pseudorapidity gap, is shown in the left panel of Fig. E.3. The  $c_2\{2\}$  measurements from all collision systems show a decreasing trend with multiplicity, which is more pronounced in p–Pb and pp collisions than in Pb–Pb collisions. At the same time, the  $c_2\{2\}$  is clearly higher in pp collisions than in the other two collision systems. This might suggest large contamination of the  $c_2\{2\}$  with short-range few-particle correlations.

In order to suppress such effects, the  $|\Delta\eta| > 1.4$  gap is applied to the  $c_2\{2\}$  measurements, and shown in the right panel of Fig. E.3. A significant decrease of the signal is observed in Pb–Pb and p–Pb collisions, suggesting a successful reduction of non-flow effects. The measurements from both collision systems are now increasing with multiplicity, which is in contrast to the expected  $\propto 1/M$  dependence of non-flow correlations, suggesting presence of other effects. A significant non-flow suppression can be also seen in pp collisions. The magnitude of  $c_2\{2, |\Delta\eta| > 1.4\}$  decreased down to a value that is compatible with p–Pb collisions at high multiplicity. Only a weak dependence of  $c_2\{2, |\Delta\eta| > 1.4\}$  on  $N_{ch}$  is

<sup>†</sup>Results are shown as a function of  $N_{ch}$ , which is the number of tracks within  $|\eta| < 1.0$  and  $0.2 < p_T < 3.0$  GeV/ $c$ , corrected for inefficiencies.

reported in pp collisions, as opposed to the increasing trend seen in the rest of the collision systems. Nevertheless, such a monotone trend is not expected from solely non-flow effects.

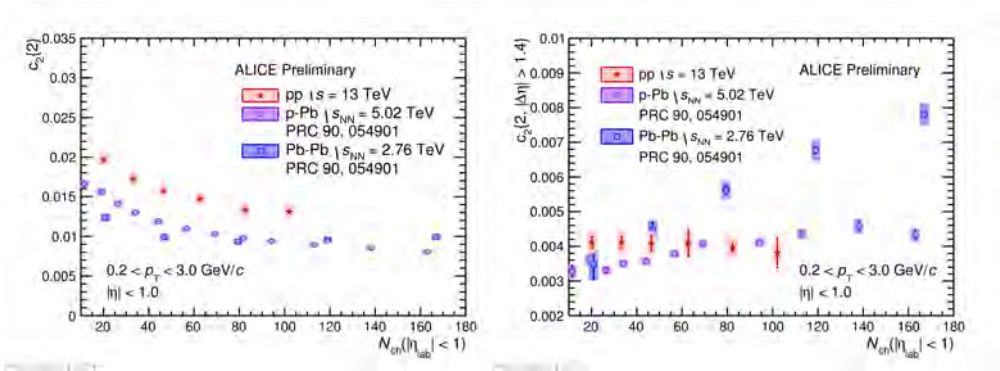


**Figure E.3:** Left: Multiplicity dependence of  $c_2\{2\}$  in pp, p–Pb and Pb–Pb collisions. A decreasing trend with multiplicity can be seen. Right: Multiplicity dependence of  $c_2\{2, |\Delta\eta| > 1.4\}$  from pp, p–Pb and Pb–Pb collisions. The  $|\Delta\eta|$  gap induces a decrease of the measurements. The measurements from p–Pb and Pb–Pb collisions are taken from [47].

The measurement of  $c_2\{2, |\Delta\eta| > 1.4\}$  has suggested the presence of other than just non-flow correlations in pp collisions. However, collectivity should be further probed with multi-particle correlation measurements in order to test, whether particles exhibit a common correlation with respect to a global symmetry plane; a typical way how collectivity displays itself in a flow dominant system. Therefore, measurement of the four-particle cumulant,  $c_2\{4\}$ , is a suitable observable to study collective phenomena. In particular, its value has to be negative in order to allow for the calculation of real-valued flow coefficient  $v_2$ . On the other hand, pure non-flow correlations are believed to give only a positive sign of  $c_2\{4\}$ , as is shown in this thesis in Fig. 6.15, or in [47] for heavy-ion collisions.

Figure E.4 presents the  $c_2\{4\}$  calculated as a function of multiplicity. A clear negative sign can be seen in Pb–Pb collisions, as expected. Moreover, a significant negative  $c_2\{4\}$  is measured in p–Pb collisions, too. However, the sign of  $c_2\{4\}$  in pp collisions is positive at a similar multiplicity range. Based on such an observation, no indication of collective behaviour in small collision systems can be confirmed with the standard measurement of the four-particle cumulant.

### E.2.1 Enhancing the flow signal

Differential measurements of  $v_n$  as a function of transverse momentum  $p_T$  have been obtained in flow dominant systems, like Pb–Pb collisions [32]. In particular,  $v_n$  is increasing as a function of  $p_T$ , which can be used as a prerequisite for one of the ideas to reveal collectivity in small collision systems: to enhance the possible flow signal. The increasing trend of  $v_n$  with  $p_T$ , translated in terms of the two-particle cumulant measurement as a function of multiplicity, is sketched in Fig. E.5. On the left, a typical dependence of a  $v_n$  measurement on  $p_T$  can be seen. In order to obtain this result as a function of multiplicity, one has to choose a  $p_T$  range in which cumulants will be measured. The blue colour represents the

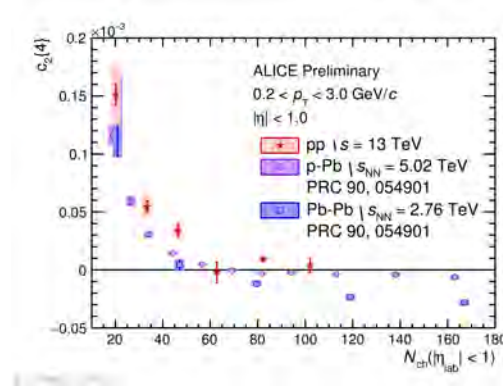


**Figure E.4:** Multiplicity dependence of  $c_2\{4\}$  in pp, p-Pb and Pb-Pb collisions. While a negative  $c_2\{4\}$  is observed in p-Pb and Pb-Pb data, a positive  $c_2\{4\}$  is seen in pp collisions in the whole multiplicity range. The measurements from p-Pb and Pb-Pb collisions are taken from [47].

$0.2 < p_T < 3.0$  GeV/c range, the red colour denotes the  $0.5 < p_T < 3.0$  GeV/c range where the minimum  $p_T$  threshold has been increased, and finally, the green colour stands for the  $p_T$  range with the highest minimum  $p_T$  cut,  $0.7 < p_T < 3.0$  GeV/c. The integral of the coloured areas underneath the  $v_n$  curve would increase with increasing minimum  $p_T$  threshold. This would reflect in the measurements of two-particle cumulants presented as a function of multiplicity in a way that is illustrated in the second picture of Fig. E.5. The definition of colours is similar as was just described above. If the  $v_n$  as a function of  $p_T$  increases, then the integrated  $c_n\{2\}$  as a function of multiplicity is expected to increase with increasing minimum  $p_T$  threshold. An opposite behaviour is expected from measurements of the four-particle cumulant as a function of multiplicity due to the requirement of a negative  $c_n\{4\}$  in order to obtain a real-valued  $v_n$ . This is sketched in the last picture in Fig. E.5. It is expected that with increasing minimum  $p_T$  threshold, a decreasing  $c_n\{4\}$  to more negative values will be observed as a function of multiplicity.

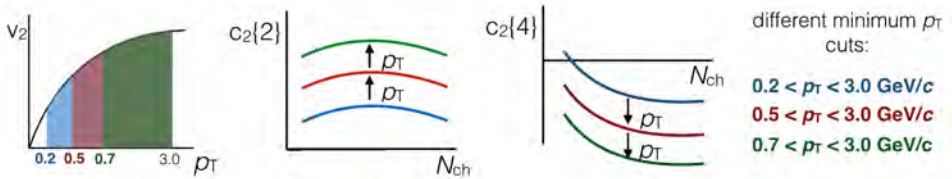


**Figure E.5:** Illustration of the attempt to enhance flow in the measurements of  $m$ -particle cumulants.

In this context, it is important to note that non-flow correlations are also affected by the increase of the minimum  $p_T$  threshold. With larger minimum  $p_T$ , one might enhance the abundance of particles originating from a jet, or particles from high- $p_T$  resonance decays,

which would result in smaller opening angles between the decay particles. These effects would contribute with a positive sign to the two-particle cumulant. However, larger contribution from non-flow would not decrease the  $c_2\{4\}$  to more negative values. Instead, the  $c_2\{4\}$  would remain positive, or even increase to larger positive values. Therefore, the four-particle cumulant seems to be a more suitable observable in this study.

First, the idea of the enhancement of flow was tested on the measurements from Pb–Pb collisions. The multiplicity dependence of  $c_2\{2\}$  and  $c_2\{4\}$  for different ranges of  $p_T$  is shown in the left and the right panel of Fig. E.6, respectively. An increasing trend of  $c_2\{2\}$  can be seen with increasing minimum  $p_T$  threshold. However, as was mentioned above, this might also increase the non-flow contribution to the two-particle cumulant measurement. On the other hand, the right panel of Fig. E.6 shows more evident demonstration of the expected effects of the flow enhancement study. At larger multiplicities where flow dominates, a clear decrease of  $c_2\{4\}$  to more negative values is observed with increasing the minimum  $p_T$ . The measurements approach each other towards lower multiplicities, until they cross to positive  $c_2\{4\}$  at similar multiplicity  $N_{ch} \approx 50$ , indicating a transition from flow dominated region to a non-flow dominated region. At low multiplicities, the  $c_2\{4\}$  seems to increase with increasing minimum  $p_T$ , as expected from non-flow correlations. These measurements from Pb–Pb collisions thus set an ideal example of flow enhancement effects.

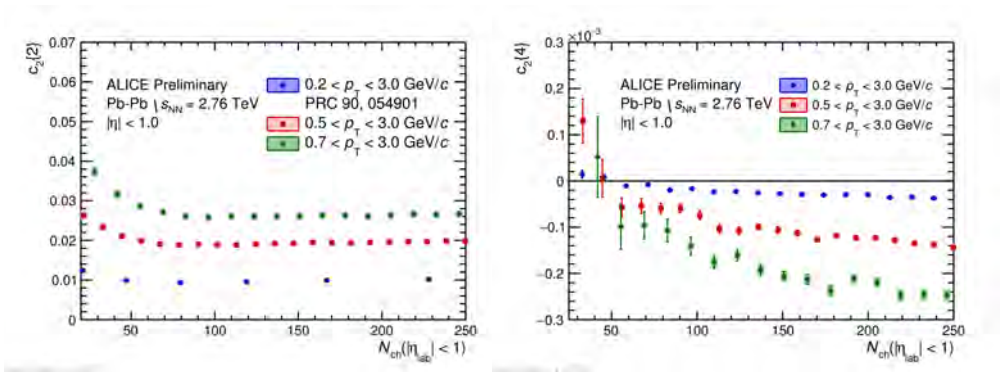


**Figure E.6:** Multiplicity dependence of  $c_2\{2\}$  (left) and  $c_2\{4\}$  (right) in Pb–Pb collisions for different regions of  $p_T$ . An increase of  $c_2\{2\}$  with minimum  $p_T$  thresholded is seen. A decreasing trend of  $c_2\{4\}$  with increasing minimum  $p_T$  is observed at large multiplicity, while a crossing to positive values and an increasing trend of  $c_2\{4\}$  with minimum  $p_T$  is seen at low  $N_{ch}$ . The measurement of  $c_2\{2\}$  with  $0.2 < p_T < 3.0$  GeV/c from p–Pb collisions is taken from [47].

Collisions of a proton and a lead ion have already shown a hint of collectivity, especially by revealing a negative sign of  $c_2\{4\}$  [47]. At the same time, this collision system is largely affected by non-flow, as opposed to the Pb–Pb collisions shown above. Therefore, it is tempting to see what effects will the change of the minimum  $p_T$  have on the measurements in p–Pb collisions.

The left panel of Fig. E.7 shows the  $c_2\{2\}$  as a function of multiplicity for various ranges of  $p_T$  in p–Pb collisions. Similarly as seen in the large collision system, there is a general increasing trend of  $c_2\{2\}$  with increasing the minimum  $p_T$  threshold. However, more can

be revealed by studying the evolution of the  $c_2\{4\}$  with different  $p_T$  ranges, which is shown in the right panel of Fig. E.7. The interplay of flow and non-flow effects is apparent. A decreasing trend of  $c_2\{4\}$  with increasing minimum  $p_T$  cut can be seen at large multiplicities. A common crossing point to positive values is observed at  $N_{\text{ch}} \approx 65$ . The dominance of non-flow effects at low multiplicities is clear: the  $c_2\{4\}$  has a strong positive signal, which further increases with increasing minimum  $p_T$ . Overall, the method of enhancing flow has the expected effect in p–Pb collisions.

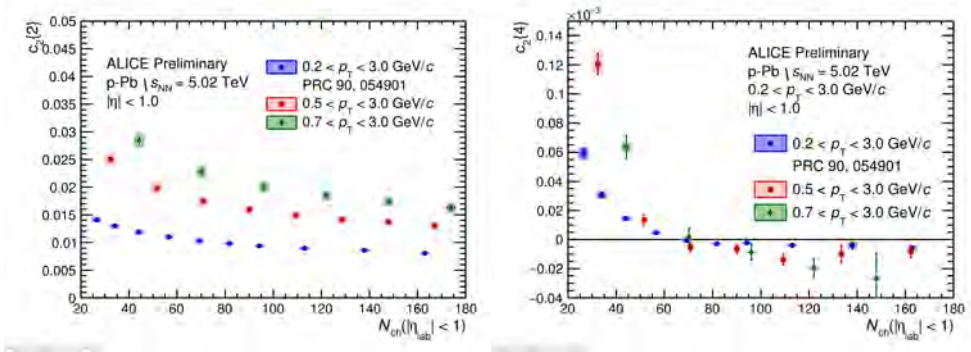


**Figure E.7:** Multiplicity dependence of  $c_2\{2\}$  (left) and  $c_2\{4\}$  (right) in p–Pb collisions for different regions of  $p_T$ . An increase of  $c_2\{2\}$  with minimum  $p_T$  thresholded is seen. A decreasing trend of  $c_2\{4\}$  with increasing minimum  $p_T$  is observed at large multiplicity, and an increase of  $c_2\{4\}$  with minimum  $p_T$  at low  $N_{\text{ch}}$ . The measurements from p–Pb collisions with  $0.2 < p_T < 3.0$  GeV/c are taken from [47].

Since this approach was able to enhance the abundance of collective effects both in Pb–Pb and p–Pb collisions, it is now applied to pp collisions in order to see whether collectivity would be revealed there. The strong increasing  $c_2\{2\}$  with increasing minimum  $p_T$  threshold shown in the left panel of Fig. E.8 is not conclusive, since both flow and non-flow have a positive contribution to the two-particle cumulant. The four-particle cumulant as a function of multiplicity is shown in the right panel of Fig. E.8 for various ranges of  $p_T$ . As opposed to Pb–Pb or p–Pb collisions, the measurement in pp interactions is increasing with increasing minimum  $p_T$  threshold. Most notable, this occurs at the multiplicity range where p–Pb and Pb–Pb collisions showed a clear enhancement of collective effects.

To conclude, this method did not reveal collective effects in pp collisions, even though it seemed to yield the desired effect in both Pb–Pb and p–Pb collisions.

## E.2.2 Suppression of non-flow effects

After the unsuccessful search for collective effects in pp collisions with enhancing the possible flow signal by increasing the minimum  $p_T$  threshold, another approach will be described in this section. This method is rather opposite than the one shown above: instead of enhancing flow, a method for a suppression of non-flow will be used now.

This method was described in Chapter 2. Its main purpose is to suppress non-flow effects, which arise from correlations between particles from a jet, or resonance decays. It consists of

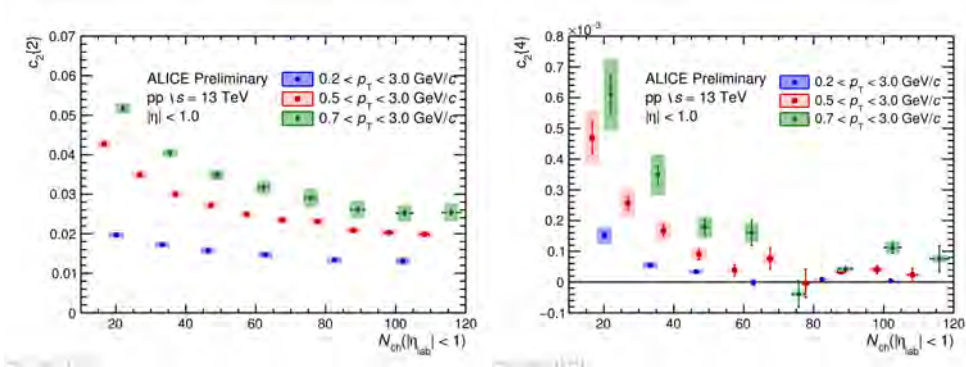


**Figure E.8:** Multiplicity dependence of  $c_2\{2\}$  (left) and  $c_2\{4\}$  (right) from pp collisions for different regions of  $p_T$ . Both  $c_2\{2\}$  and  $c_2\{4\}$  increase with the minimum  $p_T$  threshold in the whole multiplicity range.

dividing the detector acceptance into two or more subevents and performing correlations only between particles from these subevents. In this way, one enforces a space separation between the particles that are being correlated. This is already widely used in the measurements of two-particle cumulants. Its application to the higher order cumulants was not used, because higher order cumulants are by construction less sensitive to non-flow effects from lower order correlations. However, they still might be contaminated by remaining non-flow correlations of the same order. This fact has gained its importance especially in the studies of small collision systems, which are largely influenced by non-flow effects. Thus, the subevent method has been extended to multi-particle cumulants [58, 59].

At the time of performing this analysis, the subevent method in multi-particle cumulants was not known yet. Thus, these results are the first measurements using such a method (presented together with ATLAS [94] at Quark Matter 2017).

Multiplicity dependence of  $c_2\{4\}$  and  $c_2\{4, |\Delta\eta|\}$  in Pb–Pb collisions is shown in Fig. E.9 (left). Apart from the default subevent method where the detector acceptance is split into two subevents, corresponding to  $c_2\{4, |\Delta\eta| > 0.0\}$ , measurements with increasing  $|\Delta\eta|$  gap between the subevents are shown as well. The small amount of statistics did not allow to calculate the results with larger pseudorapidity separation. Nevertheless, a sign of a signal suppression is observed at low multiplicities already with the  $|\Delta\eta| > 0.0$  case. On the other hand, no significant difference is observed between the  $c_2\{4\}$  measurements at large multiplicities. Considering that this is a flow dominant region with multi-particle long-range correlations, which wouldn't feel the effect of the subevent method, such an observation is expected.

Similar measurements in p–Pb collisions are shown in the right panel of Fig. E.9. Here, a clear decrease of the  $c_2\{4\}$  at low multiplicities is apparent, showing the ability of the  $|\Delta\eta|$  gap to further suppress non-flow correlations in four-particle cumulant measurements. In the flow dominant region at large multiplicities, where the  $c_2\{4\}$  is negative, a systematic additional decrease of the signal is observed too, although with less strength compared to the low multiplicity region.

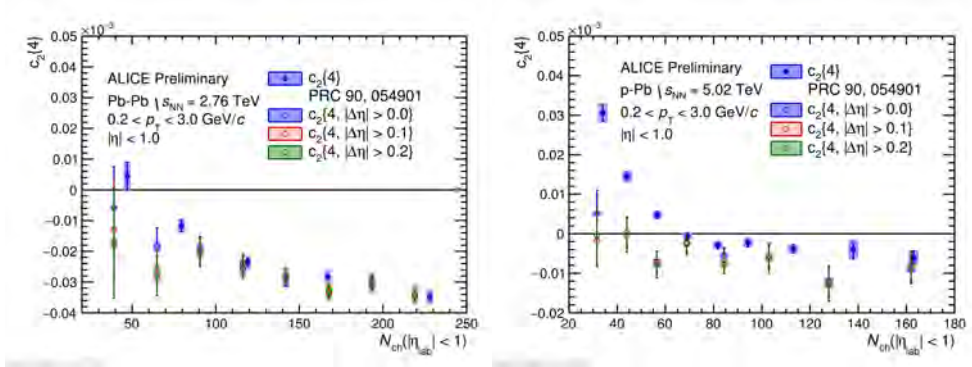


**Figure E.9:** Left: Multiplicity dependence of  $c_2\{4\}$  and  $c_2\{4, |\Delta\eta|\}$  in Pb–Pb collisions. No significant differences between the measurements are observed, apart from the lowest multiplicity region. Right: Multiplicity dependence of  $c_2\{4\}$  and  $c_2\{4, |\Delta\eta|\}$  in p–Pb collisions. A significant decrease of  $c_2\{4\}$  can be observed in p–Pb collisions, which is more pronounced at low multiplicities.

Finally, this method is applied to the measurements in pp collisions. The results of  $c_2\{4\}$  and  $c_2\{4, |\Delta\eta|\}$  as a function of multiplicity are shown in Fig. E.10. Similarly as in p–Pb collisions, a clear further suppression of non-flow is observed in pp collisions too, demonstrated by the strong decrease of the  $c_2\{4\}$  value. However, no significant negative  $c_2\{4\}$  is observed in pp collisions, even after the suppression of non-flow contribution.

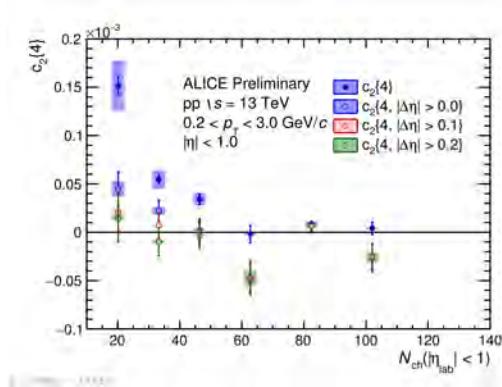


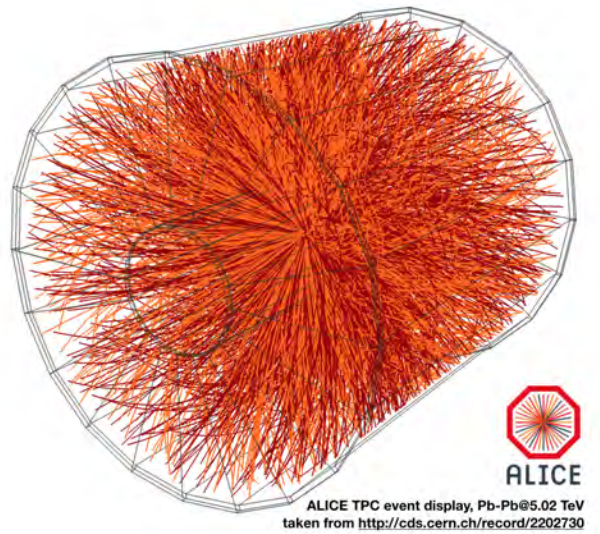
**Figure E.10:** Multiplicity dependence of  $c_2\{4\}$  and  $c_2\{4, |\Delta\eta|\}$  from pp collisions. A significant decrease of  $c_2\{4\}$  can be observed in the whole multiplicity region.

### E.2.3 Summary

In summary, investigation of collectivity in small collision systems, performed prior to the main discussion shown in this thesis, was presented here. The measurements from

pp collisions at  $\sqrt{s} = 13$  TeV were compared to the Run 1 data of Pb–Pb collisions at  $\sqrt{s_{NN}} = 2.76$  TeV and p–Pb collisions at  $\sqrt{s_{NN}} = 5.02$  TeV. Two different approaches were employed to reveal the possible collectivity in pp collisions. First was based on a method to enhance flow contribution, which consisted in increasing the minimum value of the  $p_T$  threshold. The second approach was based on the suppression of non-flow effects by employing the new subevent technique in multi-particle cumulants. While both methods yielded expected effects on the Pb–Pb and p–Pb collisions, neither of them revealed a negative sign of  $c_2\{4\}$  in pp collisions, which would signal an indication of collectivity.

As was later realised, a selection of high multiplicity events based on the signal in the forward V0 detector, together with the sensitivity of the 3-subevent method, is capable of reducing non-flow effects such that collectivity is revealed even in pp collisions within the ALICE acceptance. This is described in the main text of the thesis.



## F. PYTHIA 8 simulation setup

The so-called “on-the-fly” event generation was performed to obtain the simulation results, which consists of generating a PYTHIA event with a subsequent calculation of  $m$ -particle correlations. In particular, PYTHIA version 8.210 [56, 57] was used with `SoftQCD:inelastic = on`. This parameter switches on all soft QCD processes except for elastic collisions. This setting is used by ALICE because it resembles the standard minimum-bias collisions the most. Results of  $v_n$  and  $SC(m, n)$  were calculated with the same kinematic cuts that were used in the real data analysis:  $0.2 < p_T < 3.0$  GeV/ $c$  and  $|\eta| < 0.8$ . Since the pp data were selected with the high-multiplicity trigger, PYTHIA calculations were performed with simulated high-multiplicity trigger conditions. As was explained in section 4.1.3, the high multiplicity trigger can be mimicked by applying a cut on multiplicity in the forward V0 detector:  $V0M/\langle V0M \rangle > 4$ . Similar condition was applied to PYTHIA simulations, as is described below.

### Selection of collisions with high multiplicity

Conditions similar to the high multiplicity trigger selection in data were recreated in PYTHIA simulation in the following way:

1. Distribution of charged primary particles (based on ALICE definition [75]) with  $p_T > 0$  GeV/ $c$  within the acceptance of the V0 detector ( $2.8 < \eta < 5.1$  and  $-3.7 < \eta < -1.7$ ) was obtained, denoted as  $M_{\text{forward}}$ .
2. The value of the cut marking the threshold for the high multiplicity event selection was determined as  $M_{\text{forward}} = 4 \cdot \langle M_{\text{forward}} \rangle$
3. Generated collisions with  $M_{\text{forward}} < 4 \cdot \langle M_{\text{forward}} \rangle$  were rejected

The particle multiplicity distribution in the forward region,  $M_{\text{forward}}$ , is shown in Fig. F.1 (left). The region of collisions satisfying the high multiplicity cut is highlighted with the blue color. The selected high multiplicity collisions represent 1% of the overall generated event sample ( $367 \cdot 10^6$  out of  $3.3 \cdot 10^{10}$  events). The effect of this cut on the measurements is examined in the right panel of Fig. F.1. PYTHIA 8 calculation of  $c_2\{2\}$  as a function of multiplicity at mid-rapidity,  $N_{ch}(|\eta| < 0.8)$ , is shown for two sets of generated collisions: the high multiplicity collisions selected with the cut on forward multiplicity, and all generated collisions, which represent the minimum-bias trigger in real data taking. A clear difference between the measurements from the two different collision samples is observed, similar to what was reported in real data in section 4.1.3. Thus, the mimicked selection of high multiplicity collisions in PYTHIA 8 is able to at least qualitatively reproduce the high multiplicity trigger in pp collisions.

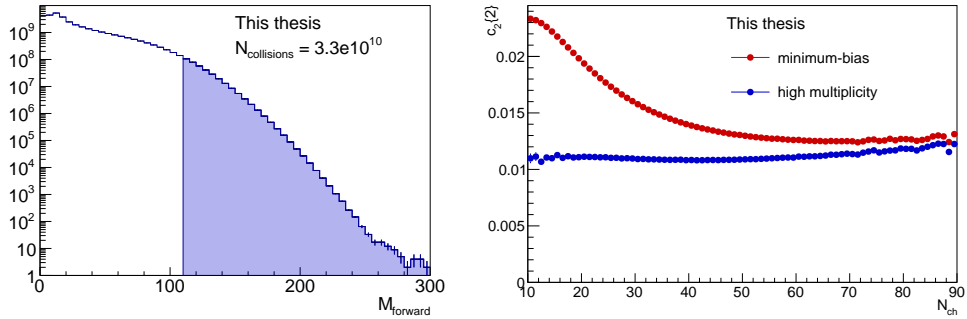
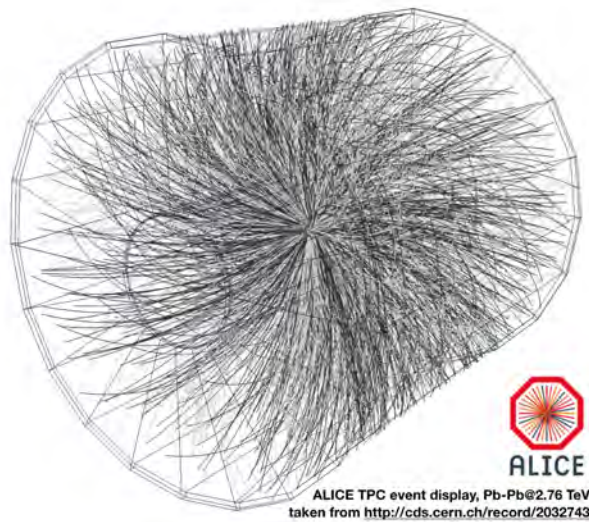


**Figure F.1:** Left: Distribution of multiplicity in the forward region of the V0 detector acceptance. The blue area represents the region of high multiplicity events used for the comparison with data. Right: Measurement of  $c_2\{2\}$  as a function of multiplicity at mid-rapidity for all PYTHIA 8 generated collisions (representing the minimum-bias events in real data) and high multiplicity events obtained based on the forward multiplicity selection. Similar effect of the trigger selection as in real data is observed.



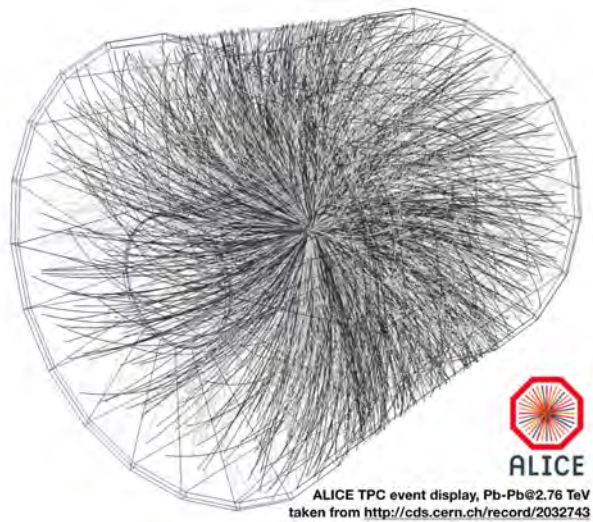
## List of Figures

1.1	Standard Model of elementary particles. . . . .	4
1.2	Diagram of the evolution of a heavy-ion collision. . . . .	5
1.3	Phase diagram of nuclear matter. . . . .	6
1.4	Initial energy densities if the overlapping region of the colliding heavy nuclei. . . . .	8
1.5	Initial energy densities if the overlapping region of the colliding heavy nuclei. . . . .	10
1.6	. . . . .	13
1.7	Di-hadron correlations in 2.76 TeV Pb–Pb collisions. . . . .	14
1.8	Flow coefficients as a function of collision centrality in $\sqrt{s_{NN}} = 5.02$ TeV Pb–Pb collisions. . . . .	15
1.9	Measurements of Symmetric Cumulants $SC$ and normalised $SC$ in Pb–Pb collisions at $\sqrt{s_{NN}} = 2.76$ TeV. . . . .	16
1.10	Di-hadron correlations in 13 TeV pp collisions. . . . .	18
1.11	Di-hadron correlations in 5.02 TeV p–Pb collisions. . . . .	19
1.12	Four-particle cumulant as a function of multiplicity in Pb–Pb and p–Pb collisions. . . . .	20
1.13	Multiplicity dependence of four-particle cumulant in pp, p–Pb and Pb–Pb collisions measured by ATLAS. . . . .	20
2.1	Measurements of $c_2\{m\}$ in $\sqrt{s_{NN}} = 5.02$ TeV Pb–Pb collisions. . . . .	27
2.2	Sketch of an example of two-particle correlation without the subevent method. . . . .	29
2.3	Sketch of an example of two-particle correlation with the 2-subevent method. . . . .	29
2.4	Sketch of an example of four-particle correlation with the 2-subevent method. . . . .	30
2.5	Sketch of an example of four-particle correlation with the 3-subevent method. . . . .	31
2.6	Sketch of an example of six-particle correlation with the 2-subevent method. . . . .	32
2.7	Sketch of an example of eight-particle correlation with the 2-subevent method. . . . .	32

2.8	PYTHIA 8 results of $c_2\{m\}$ to test the subevent method. . . . .	35
2.9	PYTHIA 8 results of $SC(m, n)$ to test the subevent method. . . . .	36
3.1	The layout of the Large Hadron Collider (LHC). . . . .	38
3.2	Schematic view of the ALICE detector during the Run2 data taking. . . . .	39
3.3	Schematic view of the Inner Tracking System (ITS) detector. . . . .	40
3.4	Schematic view of the Time Projection Chamber (TPC) detector. . . . .	42
3.5	Illustration of the signal readout in the TPC. . . . .	43
3.6	Illustration of the layout of the V0 detector. . . . .	44
4.1	Correlation between the multiplicity at mid-rapidity, $M( \eta  < 0.8)$ , and $V0M/\langle V0M \rangle$ . . . . .	51
4.2	Distribution of multiplicity at mid-rapidity in different triggers in pp collisions. . . . .	52
4.3	Measurement of $c_2\{2\}$ from different triggers in pp collisions. . . . .	53
4.4	Measurement of $c_2\{2,  \Delta\eta  > 1.4\}$ from different triggers in pp collisions. . . . .	53
4.5	Track distributions of $\eta$ , $p_T$ and $\phi$ in pp collisions. . . . .	54
4.6	Measurement of $c_2\{2\}$ and $V0M/\langle V0M \rangle$ in different periods of pp collisions. . . . .	55
4.7	Measurement of $c_2\{2\}$ and $V0M/\langle V0M \rangle$ in different periods of p–Pb collisions. . . . .	56
5.1	$\phi$ in pp collisions before and after the non-uniform acceptance correction. . . . .	58
5.2	Comparison of $\phi$ distribution for different periods in pp collisions. . . . .	59
5.3	$\phi$ distributions dependent on $\eta$ and $V_z$ in LHC16k period. . . . .	59
5.4	Efficiency as a function of $p_T$ , $\eta$ and $V_z$ in pp collisions. . . . .	61
5.5	Response matrix from PYTHIA8 MC simulation of pp collisions. . . . .	62
5.6	Parameters of a Gaussian fit to the y-axis projection of the response matrix in each bin of $N_{\text{trk}}^{\text{reco}}$ . . . . .	63
5.7	Extended response matrix from PYTHIA 8 MC simulation of pp collisions. . . . .	63
5.8	$\phi$ distribution for different variations of the cuts for estimation of systematic uncertainties. . . . .	65
5.9	Monte Carlo efficiency as a function of $p_T$ , $\eta$ and $V_z$ for different variations of the cuts. . . . .	66
5.10	Comparison of $v_2\{2\}$ results from pp collisions with variation of cuts for systematic studies. . . . .	67
5.11	Ratio of $v_2\{2\}$ results from pp collisions with variation of cuts to the results with default cuts. . . . .	68
5.12	Comparison of $v_2\{2\}$ results from MC-reconstructed and MC-truth sample from PYTHIA 8 simulation of pp collisions. . . . .	69
6.1	Multiplicity dependence of $v_2\{2\}$ , $v_3\{2\}$ and $v_4\{2\}$ for various pseudorapidity gaps in Xe–Xe and Pb–Pb collisions. . . . .	73
6.2	Multiplicity dependence of $v_n\{2\}$ compared to $v_n\{2,  \Delta\eta \}$ in Xe–Xe and Pb–Pb collisions. . . . .	73
6.3	Multiplicity dependence of $v_2\{2\}$ , $v_3\{2\}$ and $v_4\{2\}$ for various pseudorapidity gaps in pp and p–Pb collisions. . . . .	75

6.4	Multiplicity dependence of $v_n\{2\}$ compared to $v_n\{2,  \Delta\eta \}$ in pp and p–Pb collisions. . . . .	75
6.5	Multiplicity dependence of $c_2\{m\}$ and $c_2\{m\}_{\text{sub}}$ in Xe–Xe and Pb–Pb collisions. . . . .	77
6.6	Multiplicity dependence of $SC(m, n)$ in Xe–Xe and Pb–Pb collisions. . . . .	78
6.7	Multiplicity dependence of $c_2\{4\}$ , $c_2\{4\}_{2\text{-sub}}$ and $c_2\{4\}_{3\text{-sub}}$ in pp and p–Pb collisions. . . . .	79
6.8	Comparison of $c_2\{4\}$ measurements from minimum-bias and high multiplicity trigger in pp collisions. Multiplicity dependence of $c_2\{4\}$ , $c_2\{4\}_{2\text{-sub}}$ , $c_2\{4\}_{3\text{-sub}}$ and $c_2\{4\}_{3\text{-sub},  \Delta\eta >0.2}$ in pp collisions. . . . .	80
6.9	Multiplicity dependence of $c_2\{6\}$ in pp and p–Pb collisions. . . . .	81
6.10	Multiplicity dependence of $SC(m, n)$ in pp and p–Pb collisions. . . . .	82
6.11	Multiplicity dependence of $v_2\{m\}$ in Xe–Xe and Pb–Pb collisions. . . . .	83
6.12	Multiplicity dependence of $v_2\{m\}$ in pp and p–Pb collisions. . . . .	84
6.13	Measurements of $v_2\{2\}$ , $v_3\{2\}$ and $v_4\{2\}$ with $ \Delta\eta $ gap for all collision systems, compared to the PYTHIA 8 and IP-Glasma+MUSIC+UrQMD calculations. . . . .	85
6.14	Measurements of $v_2\{m\}$ for $m > 2$ with the standard and the subevent method for all collision systems, compared to IP-Glasma+MUSIC+UrQMD calculations. . . . .	87
6.15	Comparison of $c_2\{4\}$ and $c_2\{6\}$ from pp collisions to PYTHIA calculation. . . . .	88
6.16	Measurements of $SC(m, n)_{3\text{-sub}}$ for all collision systems. . . . .	90
6.17	Measurements of normalised $SC(m, n)_{3\text{-sub}}$ for all collision systems. . . . .	92
A.1	Comparison of $\varphi$ distribution for different periods in p–Pb collisions. . . . .	108
A.2	Comparison of $\varphi$ distribution for different runs in p–Pb collisions. . . . .	108
A.3	Comparison of $\varphi$ distribution for different runs in p–Pb collisions. . . . .	109
A.4	Comparison of $\varphi$ distribution for different runs in Xe–Xe collisions. . . . .	109
A.5	Comparison of $\varphi$ distribution for different runs in Pb–Pb collisions. . . . .	110
B.1	Detector efficiency as a function of $p_T$ , $\eta$ and $V_z$ in p–Pb collisions. . . . .	112
B.2	Comparison of detector efficiencies for different runs in the LHC16q period in p–Pb collisions. . . . .	113
B.3	Comparison of detector efficiencies for different runs in the LHC16t period in p–Pb collisions. . . . .	114
B.4	Comparison of detector efficiencies for different runs in the LHC17n period in Xe–Xe collisions. . . . .	115
B.5	Comparison of detector efficiencies for different runs in the LHC15o period in Pb–Pb collisions. . . . .	116
C.1	Response matrix from p–Pb collisions. . . . .	118
C.2	Response matrix from Xe–Xe collisions. . . . .	118
C.3	Response matrix from Pb–Pb collisions. . . . .	118
E.1	Multiplicity distributions from $\sqrt{s} = 13$ TeV pp collisions from the minimum-bias (kINT7) and the SPD high multiplicity trigger (kHighMultSPD). . . . .	124

E.2	Measurements of $c_2\{2\}$ as a function of multiplicity from $\sqrt{s} = 13$ TeV pp collisions from the minimum-bias (kINT7) and the SPD high multiplicity trigger (kHighMultSPD). . . . .	125
E.3	Multiplicity dependence of two-particle cumulant in pp, p-Pb and Pb-Pb collisions.	126
E.4	Multiplicity dependence of four-particle cumulant from pp, p-Pb and Pb-Pb collisions. . . . .	127
E.5	Illustration of the attempt to enhance flow in the measurements of $m$ -particle cumulants. . . . .	127
E.6	Multiplicity dependence of $c_2\{4\}$ from Pb-Pb collisions for different regions of $p_T$ . . . . .	128
E.7	Multiplicity dependence of $c_2\{4\}$ from p-Pb collisions for different regions of $p_T$ .	129
E.8	Multiplicity dependence of $c_2\{4\}$ in pp collisions for different regions of $p_T$ . . . . .	130
E.9	Multiplicity dependence of $c_2\{4\}$ and $c_2\{4,  \Delta\eta \}$ from Pb-Pb and p-Pb collisions.	131
E.10	Multiplicity dependence of $c_2\{4\}$ and $c_2\{4,  \Delta\eta \}$ in pp collisions. . . . .	131
F.1	. . . . .	134



# List of Tables

4.1	List of collision systems and corresponding periods. . . . .	48
5.1	Table of event and track cuts that were varied for systematic studies. . . . .	64
D.1	List of final of systematic uncertainties in $\sqrt{s} = 13$ TeV pp collisions. . . . .	119
D.2	List of final of systematic uncertainties in $\sqrt{s} = 5.02$ TeV p-Pb collisions. . . . .	120
D.3	List of final of systematic uncertainties in $\sqrt{s} = 5.44$ TeV Xe-Xe collisions. . . . .	121
D.4	List of final of systematic uncertainties in $\sqrt{s} = 5.02$ TeV Pb-Pb collisions. . . . .	122